THE RATIO OF INCLUSIVE JET CROSS SECTIONS AT $\sqrt{s} = 630$ GeV AND $\sqrt{s} = 1800$ GeV

by

John Krane

A DISSERTATION

Presented to the Faculty of
the Graduate College at the University of Nebraska
in Partial Fulfillment of the Requirements for
the Degree of Doctor of Philosophy

Under the Supervision of Professor Gregory R. Snow

Lincoln, Nebraska

1998
Second Printing

THE RATIO OF INCLUSIVE JET CROSS SECTIONS AT $\sqrt{s} = 630$ GeV AND $\sqrt{s} = 1800$ GeV

John Krane, Ph.D.

A Dissertation submitted in partial fulfillment of
the requirements for the degree of
Doctor of Philosophy

Approved:

Gregory R. Snow
Professor of Physics
Thesis Committee Chair

Edward C. Jones
Professor of Physics

Timothy J. Gay
Professor of Physics

Ronald J. Bonstetter
Professor of Education

Gerald C. Blazey
Professor of Physics
Northern Illinois University
Honorary Committee Member

THE RATIO OF INCLUSIVE JET CROSS SECTIONS AT
$\sqrt{s} = 630$ GeV AND $\sqrt{s} = 1800$ GeV

John Krane, Ph.D.

University of Nebraska, 1998

Advisor: Gregory R. Snow

This dissertation presents an analysis of hadronic jet production from proton-antiproton collisions at two center–of–mass energies. Measurements were performed in the central region ($|\eta| < 0.5$) of the DØ detector at Fermi National Accelerator Laboratory (Batavia, IL). Results are compared to next–to–leading–order QCD predictions generated with JETRAD and EKS Monte Carlo. Several techniques reduce the uncertainty in the ratio of cross sections to as low as 5%. The observed normalization difference results in a low probability that the data and predictions describe the same distribution.

Contents

List of Figures

viii

List of Tables

Preface

> *"Listen, buddy, if I could tell you in a minute what I
> did, it wouldn't be worth the Nobel Prize!"*
> — Richard Feynman, to a journalist

High Energy Physics (HEP) is the search for, and description of, fundamental particles. Protons and neutrons in the nuclei of atoms are not fundamental because they are composed of smaller elements: quarks and gluons. This dissertation represents one of many possible measurements of these proton constituents.

Analyses in experimental HEP may be split into two distinct enterprises: searches for new phenomena and tests of theories that describe previously observed phenomena. This analysis serves both purposes to a degree; it is a search for yet smaller components that may comprise quarks, and it provides a benchmark for theories that describe the interactions between quarks and gluons.

This dissertation is arranged in eight chapters, which could be grouped into three general categories:

- Background material: introduction to the theory, the experiment, and data collection
- Primary analysis: the jet energy scale and details of the cross section analysis, including all corrections
- Error analysis: calculation and cancellation of error, final results, and a quantitative comparison to theoretical predictions.

Chapter 1 briefly introduces the field of high energy particle physics and the nature of the measurement described in later chapters. Although many of the details of the theoretical predictions for the inclusive jet cross section are too lengthy to present in this work,

some of the tools used in the calculation are presented to clarify the different associated uncertainties and to describe the open theoretical questions. Chapter 2 describes the research laboratory and detector where the measurement was performed. It attempts to present, with a reasonable degree of detail, the underlying principles and hardware specifications of the Fermilab accelerator complex and the DØ detector. The actual data collection process is briefly described in Chapter 3, and illustrated with several event displays. (While important to a self–contained document, these first three chapters are quite standard in HEP theses; readers already familiar with HEP and the DØ experiment may wish to skip them entirely.)

In addition to providing the largest correction to the data set, the jet energy scale correction produces the largest single source of uncertainty in the analysis. Chapter 4 is devoted to a detailed summary of this crucial determination. Chapter 5 describes the calculation of the inclusive jet cross section, including luminosity and efficiencies. Chapter 6 describes the "unsmearing" process, by which the cross section distribution is corrected for the effect of stochastic fluctuations in jet energy.

Chapter 7 calculates the uncertainty in the jet cross section ratio that results from all of the effects and corrections of the prior chapters. Because the final result of the analysis is a ratio of cross sections, uncertainties common to both the $\sqrt{s} = 630$ GeV and 1800 GeV data sets will cancel to some degree. The cancellation of errors in the ratio is the true strength of this analysis. Comparison of data to next-to-leading-order QCD predictions is reserved for Chapter 8. The data sample in this dissertation is the largest sample collected to date, spans a wider range of center–of–mass energy than any prior measurement, and was collected with a single detector to minimize experimental uncertainties.

The appendices provide several parenthetical discussions. Definitions of coordinate systems, units, and variables that are useful in high energy physics are placed in Appendix A for easy reference. The heavy emphasis on error analysis in this dissertation required several discussions of statistical methods. Again for convenience in reference, these discussions have been collected in Appendix B. Computation of the W boson cross section provides a

cross-check on the total integrated luminosity; a brief description of the results is available in Appendix C.

Each chapter includes one or more summary sections. Readers unfamiliar with this analysis may wish to read through the chapter summaries before reading the full document. Readers unfamiliar with HEP will definitely want to look over Appendix A immediately, if only to discover the meaning of "$\sqrt{s}$."

Informal Acknowledgments

Hundreds of physicists and engineers worked in concert to build the detector and collect the data that made this work possible. Tens of people in the various analysis groups at DØ guided and educated me, looked over my work, and, in some cases, did the hard work for me. A handful of people worked hard just to keep me sane. I want to take the time to single out a few people whose efforts exceeded their duty in these regards.

I learned a great deal in a short time while fixing problems. In many cases, the problems with my analysis weren't noticed until someone actually pointed them out; thus, I owe a great debt to those people who kicked holes in my work. Mark Strovink, Heidi Schellman, and Harry Weerts all did a little kicking, but more than their share of patching up the resulting holes. Nikos Varelas shared my office for nearly a year; in that time he taught me the all–important skill of *cross–checking*. I also thank Horst Wahl (Chair of my Editorial Board) and Bob McCarthy, who taught me about covariance matrices more clearly than any textbook or article ever could.

The people working on jet analyses received a large dose of Krane, and their patience and guidance were invaluable. I refer specifically to Daniel Elvira (Godfather of this analysis), Robert Hirosky (the Duke of Jets), Iain Bertram (Mr. Monte Carlo), and Jerry Blazey (who taught me the meaning of the word *concise*). These people also aim a mean kick.

The grad students I had the pleasure getting to know also deserve credit here. Not only did they teach me a great deal about the computing systems we use and the physics we study, but they also allowed me to teach them what I know in return. Surrounded by so

many people that obviously know exactly what to do and therefore have little use for you, it is immensely gratifying to be able to help someone as you yourself are being helped. For this mutual relationship, I thank Richard Genik, Kevin P. Davis, Robert Snihur, Thomas Rockwell, and especially Gian Di Loreto, who (because of his proximity) overheard many a curse, snarl, or primal scream, depending on the nature of my day.

Terry Heuring wasted more of his time educating me than anyone else on the experiment. I pestered this poor guy constantly. He, willingly or unwillingly, became my surrogate advisor during my time at Fermilab, and I owe him a great debt.

Finally, and most of all, I want to thank my advisor Greg Snow for opening this door for me. And for not smashing my sense of wonder prematurely.

Special Thanks

To my parents, John and Aileen, and to my friends from South Dakota (Ray, Judy, Jason, Carrie, Kyle, Randi, Dez, Heather, Mott, Steve, Monte, Mike), Nebraska (Brian, Brad, Michelle, Gary, Frog, Donna, Patrick), Minnesota (Amy, Patrick, Tim), and Illinois (Eric, Mike, Linda, Amy). In the time we have known one another, we have spread across the continent and claimed almost every field of endeavor. Thank you for helping me to believe that physics was mine to claim.

A Note on the Second Printing

The prolonged interest in this work has resulted in the need for additional bound copies. This second printing provides a good opportunity to rectify a dangerous error: the sole content change in the second printing of this dissertation occurs in Table 3.2, page 60. Historically, the "apparent" online luminosity of the $\sqrt{s} = 630$ GeV triggers was 40% higher than the true, or "physics," luminosity—an important but very confusing distinction. The numbers in the table (and thus the entire document) now reflect the physics luminosity, as intended. The numbers quoted in Chapter 5 and Appendix C are now, and have always been, the correct ones for physics calculations.

About the Author

John Krane ███████████████████████████████████ After twelve short months of island living, his family moved to Arlington Heights, Illinois, then to Sioux Falls, South Dakota in 1975. Krane attended the University of South Dakota, earning a B.S. in Management from the School of Business Administration in 1991 and a B.S. in Physics from the College of Arts and Sciences in 1992. He attended graduate school at the University of Nebraska–Lincoln, working first in Condensed Matter physics and then in High Energy Physics under the tutelage of Professor Gregory R. Snow. Krane received his M.S. in physics in 1995 and has worked in residence at Fermilab since July of that year. At the time, he had never programmed in FORTRAN, had never been exposed to PAW (the physics analysis software), and needed thirty minutes to open his first terminal window because he was waiting for it to pop open by itself.

External Publications Arising from this Document

1. J.Krane, J.Bantly, D.Owen, "The DØ Luminosity Monitor Constant for $\sqrt{s} = 630$ GeV," Fermilab Technical Memorandum 2000, Apr. 15, 1997.

2. J.Bantly, J.Krane, D.Owen, R.Partridge, L.Paterno, "DØ Luminosity Monitor Constant for the 1994-1996 Tevatron Run," Fermilab Technical Memorandum 1995, Feb. 1, 1997.

3. B.Abbott *et al.*, "Determination of the Absolute Jet Energy Scale in the DØ Calorimeters", submitted to Nucl. Instrum. and Methods A, 1998 (630 GeV portion). Available as preprints FERMILAB-pub-97/330-E and hep-ex/9805009.

4. B.Abbott *et al.*, "The DØ Collaboration," *The Ratio of Inclusive Jet Cross Sections at $\sqrt{s} = 630$ and 1800 GeV*, Phys. Rev. Lett., to be submitted.

5. B.Abbott *et al.*, "The DØ Collaboration," *A Measurement of $\sigma\left(p\bar{p} \to W + X\right) \cdot B\left(W \to e\nu\right)/\sigma\left(p\bar{p} \to Z + X\right) \cdot B\left(Z \to ee\right)$*, Phys. Rev. D, to be submitted (630 GeV W boson cross section portion).

xx

Chapter 1

The Structure of Matter

> *"Why sometimes I've believed as many as six*
> *impossible things before breakfast."*
>   — The Red Queen in *Through the*
>   *Looking-Glass,* by Lewis Carroll

As early as 1200 B.C., Indian philosophers formulated the concept of the granular structure of matter. The idea was further developed in the fifth century B.C. by Leucippus and his student Democritus, who proposed that matter consisted of indestructible atoms. Such speculations remained purely philosophical in nature until 1811, when the Italian physicist Avogadro developed a theory of atoms and molecules that would later form the basis of chemistry.

Physicists believed atoms to be indivisible until 1897, when J. J. Thomson discovered the electron. While measuring the velocity of cathode rays by directing them through crossed electric and magnetic fields, he concluded the "rays" were in fact composed of charged particles with very small mass. Thomson's ability to liberate light–weight charged particles from initially neutral atoms implied a heavy and positively charged remainder, later revealed (by Rutherford) to be a tiny massive nucleus.*

Physicists believed atoms were indivisible until 1901, when Becquerel discovered the source of natural radioactivity. His study of uranium indicated that the β rays he had

---

* Disappointingly, the most widespread description of the atom continues to be the "planetary" atomic model that was developed in 1914.

observed were electrons, and, from energy considerations, they must originate from deep within the nucleus. By 1932, Fermi had associated β radiation with neutron decay, which produces a proton, an electron, and a new particle, the neutrino. Also, Dirac had predicted the existence of antiparticles and received confirmation from cosmic ray experiments. Only five years passed before the discovery of the muon; by 1956, the particle beastiary would grow to include three pions, the Λ, the kaons, the Σ, and the $\bar{\rho}$. The known particles were classified into three groups, *leptons* (light–weight), *mesons* (middle–weight), and *baryons* (heavy–weight), but a more cohesive understanding had to wait until 1961 with Gell–Mann's geometrical model, the *Eightfold Way*, and the group theory model that followed.

In one of several attempts to organize the ever–expanding family of "elementary" particles, in 1964, Gell–Mann and Zweig independently proposed [1] that all hadrons (*i.e.* the mesons and baryons) were composed of several particles. These constituents, *quarks*, possess fractional charge and seemed to violate Pauli's exclusion principle. Initially, three quark varieties, called *flavors,* were proposed to fully explain the decay mechanisms of the known particles. A new quantum number, whimsically called *color*, was created to accommodate the exclusion principle inconsistency.

Since the proposal of quarks, many experiments have investigated the structure of the proton and other hadrons. To date, not one experiment has disproven a prediction of the quark model. Despite some discomfort with the failure to isolate single quarks, this theory has remained strong enough to be dubbed the *Standard Model*.

The remainder of this chapter describes the fundamental particles and forces[†] of the Standard Model (SM), and introduces Feynman diagrams as a descriptive tool. The theory of the strong subatomic forces will be described at some length, culminating in the concept of a hadronic "jet." Finally, a description of scaling behavior shall be presented to motivate the physics analysis in later chapters.

---

† Although numerous extensions to the Standard Model have been proposed, their lack of confirmation places them beyond the scope of this chapter.

Force	Carrier	Rest Mass	Spin	Charge	Range	Strength
Strong	gluon	0	1	0	10^{-13} cm	1
Electromagnetic	photon	0	1	0	∞	10^{-2}
Weak	W$^{\pm}$	80.2 GeV	1	± 1	10^{-16} cm	10^{-13}
	Z	91.2 GeV		0		
Gravitational	graviton (?)	0	2 (?)	0	∞	10^{-42}

Table 1.1: Parameters of the four forces of nature. Strengths are relative.

1.1 The Standard Model and Feynman Diagrams

At the most fundamental level, four distinct forces exist in nature. In descending order of strength, these forces are: the strong (or nuclear) force, the electromagnetic force, the weak force, and the gravitational force. Table 1.1 lists [2] the relative strengths of the forces and the mediators of each. Despite its overwhelming role in the macroscopic world, the gravitational force is negligible in the microcosm of particle physics.

Table 1.2 lists the six fundamental quarks and leptons of the Standard Model (SM hereafter). While the previously described force carriers are bosonic (integer spin), the quarks and leptons are all fermions (half–integer spin). All matter is composed of a combination of these fundamental particles, or their antimatter twins. By definition, any particle composed of three quarks is a baryon, and any particle composed of a quark and an antiquark is a meson. For instance, a bound state of two up quarks and a down quark (uud) forms a proton. Similarly, the neutron is composed of two down quarks and an up (udd). Table 1.3 lists the composition and masses for these two hadrons and also for the lightest and most common mesons, the pions. By convention, an antiquark is denoted with a bar over the symbol. In contrast, antimatter leptons are denoted by specification of their charge; the electron, denoted e^{-}, complements the positron, e^{+}.

The charged leptons interact via electromagnetic and weak forces. Neutrinos, having no charge, can interact only through the weak force. Quarks primarily interact via the strong force, though they also undergo weak and electromagnetic interactions. These interactions are limited to particular topologies, easily described with Feynman diagrams.

	Fundamental Particle	Symbol	Charge	Mass (MeV)
	electron	e^-	-1	0.511
	electron neutrino	ν_e	0	$\leq 5 \times 10^{-6}$
	muon	μ^-	-1	106.6
Leptons	muon neutrino	ν_μ	0	≤ 0.17
	tau	τ^-	-1	1784
	tau neutrino	ν_τ	0	≤ 30
	down	d	$-\frac{1}{3}$	7.5
	up	u	$\frac{2}{3}$	4.2
	strange	s	$-\frac{1}{3}$	150
Quarks	charm	c	$\frac{2}{3}$	1300
	bottom	b	$-\frac{1}{3}$	4300
	top	t	$\frac{2}{3}$	172000

Table 1.2: The six fundamental leptons and the six fundamental quarks. Antiparticles exist for each table entry, differing only in the sign of their charge. Note: the d, u, and s quark masses are highly speculative.

Particle	Composition	Mass (MeV)
proton	uud	938.28
neutron	udd	929.57
π^+	$u\bar{d}$	139.57
π^-	$\bar{u}d$	139.57
π^0	$(u\bar{u}\text{-}d\bar{d})/\sqrt{2}$	134.96

Table 1.3: The most common hadronic particles.
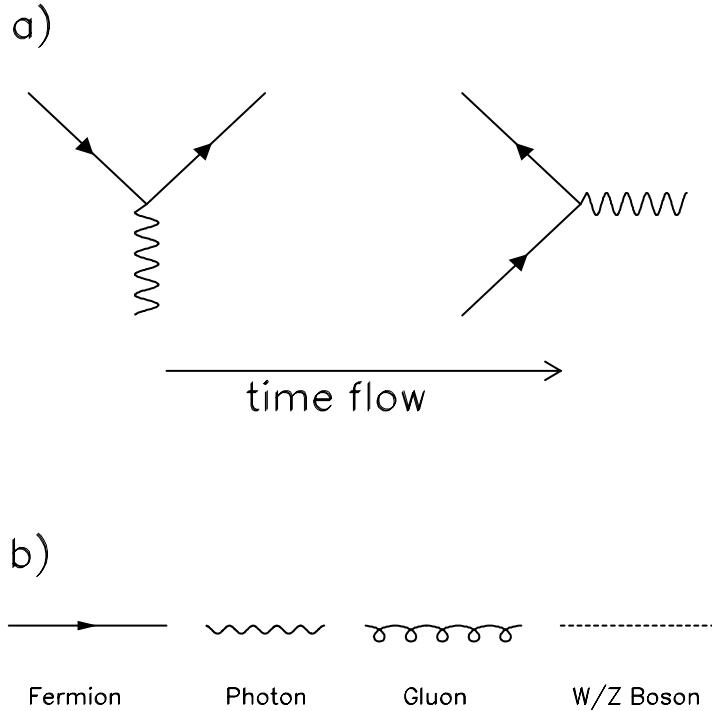
Figure 1.1: (a) The two primitive QED vertices, electron-photon scattering and e^+e^- annihilation. As indicated by the time arrow, initial conditions lie at the left edge of the diagrams by convention. (b) Generally, solid arrow-lines can indicate either quarks or leptons while the mediators of the three forces each have their own symbols.

To illustrate the use of Feynman diagrams, consider the basic quantum electrodynamics (QED) vertex, where two fermion lines meet a photon line, and assume the most common QED situation: let the fermion lines represent electrons or positrons. The rotational orientation of the vertex indicates the two possible conditions: an electron interacts with a virtual photon, or an electron and positron annihilate to form a photon.

Consider Figure 1.1(a), illustrating the two primitive vertices. Time flows from left to right by convention, so the initial condition of the first diagram indicates a single electron. The two lines in the diagram on the right show two fermions, but the top fermion arrow points in the direction opposite the time flow. This reversed arrow indicates an antimatter particle moving forward in time, not a matter particle moving backward through time. The second diagram thus depicts an electron and a positron annihilating to form a photon. The
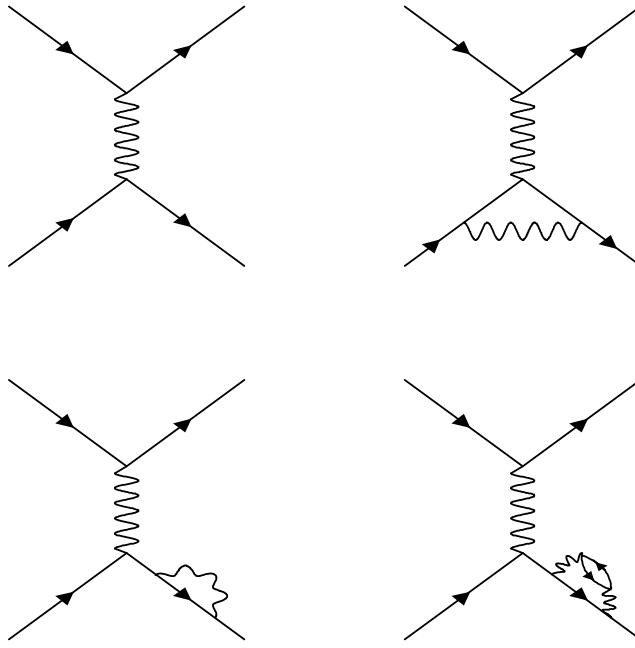
Figure 1.2: The lowest-order diagram for Möller scattering, and several higher-order contributions.

photon can only mediate interactions between fermions with non–zero charge; therefore, the fermion lines in the primitive QED vertices could also represent quarks, muons, or taus, but not neutrinos. Use of the additional symbols in Figure 1.1(b) extends the formalism from electromagnetism to include the strong and weak forces. Although some vertex combinations are forbidden, the solid arrow–lines can indicate any of the fermions listed in Table 1.2 (or their antimatter counterparts). More than cartoon sketches, these diagrams are real calculational tools that compactly represent four–dimensional quantum mechanics scattering equations. By diagramming many variations of a particular process, one is really computing a type of Taylor expansion of the *scattering amplitude* (the "matrix element") and the corresponding *density of final states* (the "phase space element"). The simplest diagrams represent the leading–order terms and more complicated diagrams depict second– and higher–order terms.

In the Feynman formalism, any real interaction must include at least two primitive

vertices to conserve energy and momentum. As an example, Figure 1.2 displays several diagrams for Möller ($e^+e^- \rightarrow e^+e^-$) scattering. In the simplest diagram (upper left), two electrons interact elastically by exchanging a photon. Only lines that propagate to the exterior of the diagram are observable; the photon describing the mechanism of the exchange, completely contained within the diagram, cannot be observed. Non–observable particles in an interaction are termed *virtual*. The other diagrams include more than one virtual photon and the final case includes a virtual fermion pair. Not limited to electrons and positrons, the fermion lines in the figure could represent other charged leptons or quarks.

In a full calculation of Möller scattering, all diagrams contribute, not only the ones in the figure, but the infinity of diagrams that were not included. Fortunately, each additional vertex carries a factor of α with it, where the coupling constant $\alpha \approx \frac{1}{137}$. Thus, in QED, the more complicated a diagram becomes, the less it contributes to the final result. For most applications, calculations achieve suitable accuracy using only the simplest few diagrams.

1.2   Characteristics of Strong Interactions

In direct analogy to the QED formalism, strong interactions between quarks are meditated by gluons. Additional vertices are available in strong interactions because, unlike QED, the strong force mediator is capable of coupling to itself (Figure 1.3) with important ramifications.

For strong interactions, a new quantum number, similar to electric charge, must be introduced. This "strong charge," originally used only as a bookkeeping device [2] to satisfy the Pauli exclusion principle, later became an integral part of the theory with great predictive power. Because there exist three orthogonal strong charges, the label *color* was applied to them; the three colors for quarks are red, green, and blue, along with three corresponding "anticolors" to indicate a negative strong charge on antiquarks.

The study of strong interactions, called *quantum chromodynamics* (QCD), initially consisted of the search for bare quarks emerging from particle collisions. No quarks have ever been observed, leading theorists to postulate [3] the principle of *confinement*. This prin-
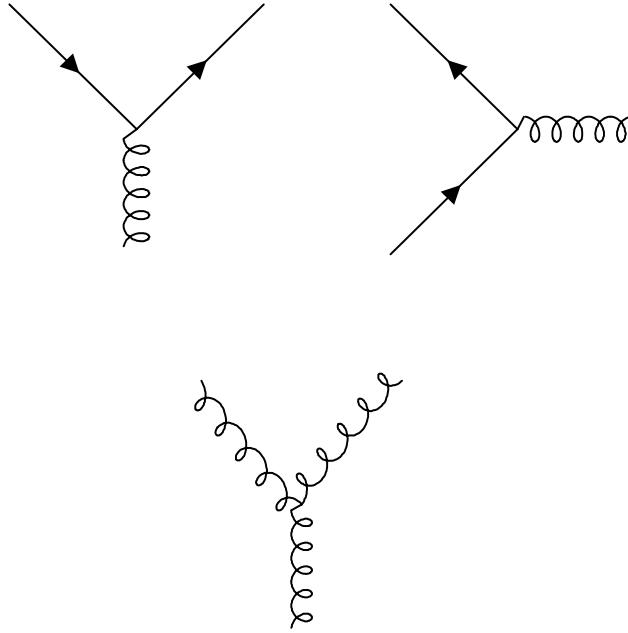
Figure 1.3: The primitive QCD vertices. For these diagrams, the fermion lines represent quarks only. Unlike the photon, the gluon is capable of interacting with other gluons.

ciple states that the net color charge of all macroscopically observable particles must be zero. Following the (figurative) color formulation, a proton must contain a *red* quark, a *blue* quark, and a *green* quark, resulting in a net color $r + b + g = white$. Of the two quarks within a pion, one must carry the anticolor of the other, for instance, $r + \bar{r} = white$. Solitary quarks cannot be observed because they each carry a single quantum of color. In the QCD formalism, the confinement principle is explained by assigning color to gluons. When the force mediators possess a "strong charge," they can interact with themselves, making QCD a non–Abelian formalism. The self–interactions of the gluons tend to anti–screen the quark's color charge and the strong force between two quarks *increases* with distance, as opposed to QED, where photons posses no electric charge and the force between electrons decreases with distance.

The confinement principle may be expressed mathematically in the value of the strong coupling parameter, α_s, by the variance of its strength with distance (or, equivalently,

energy). For historical reasons, α_s is called a *running coupling constant* rather than a coupling variable or coupling parameter. At very short distances or very high energies, the value of α_s remains small, allowing quarks within hadrons to "rattle around" nearly freely. As the distance between quarks becomes larger, the quickly–increasing coupling strength causes the potential energy between them to grow very rapidly, trapping quarks (and gluons) within the confines of the particle radius $\left(\sim 10^{-15}\ \mathrm{m}\right)$. The running coupling constant takes the form:

$$\alpha_\mathrm{s}\left(\mathrm{Q}^2\right) = \frac{\alpha_\mathrm{s}\left(\mu^2\right)}{1 + \frac{\alpha_\mathrm{s}(\mu^2)}{12\pi}\left(11c - 2n_f\right)\log\left(\frac{\mathrm{Q}^2}{\mu^2}\right)}, \tag{1.1}$$

where Q is the magnitude of the momentum transferred in the interaction, n_f indicates the number of quark varieties (6 in the SM), and c is the number of quark colors (3 in the SM). The expression has been renormalized in terms of the coupling constant at some reference energy μ, called the renormalization scale. Without renormalization, calculation of Feynman diagrams that contain loops result in divergent integrals. For the price of introducing a new arbitrary parameter μ, these divergent integrals either become finite or vanish entirely. Although the renormalization scale can differ for each divergent diagram, in perturbative QCD calculations, the *minimal subtraction* scheme[*] requires a constant μ for all diagrams, and usually, $\mu \propto \mathrm{Q}$. Alternately, the strong coupling constant could be re–expressed in terms of a scale factor Λ:

$$\alpha_\mathrm{s}\left(\mathrm{Q}^2\right) = \frac{12\pi}{\left(11c - 2n_f\right)\log\left(\frac{\mathrm{Q}^2}{\Lambda^2}\right)}, \tag{1.2}$$

where

$$\Lambda^2 = \mu^2 \exp\left[\frac{-12\pi}{\left(11c - 2n_f\right)\alpha_\mathrm{s}\left(\mu^2\right)}\right]. \tag{1.3}$$

Figure 1.4 depicts the inverse log behavior of the strong coupling constant. The most recent analysis of all HEP results yields an optimum value at $\Lambda = 0.3$ GeV [4] (lower curve in the figure). For Q^2 values above 15 GeV^2, α_s takes a value of ~ 0.1, and perturbative

---

[*] Specifically, QCD predictions employ a "modified minimum subtraction scheme," denoted $\overline{\mathrm{MS}}$ [4].

The QCD Coupling Strength
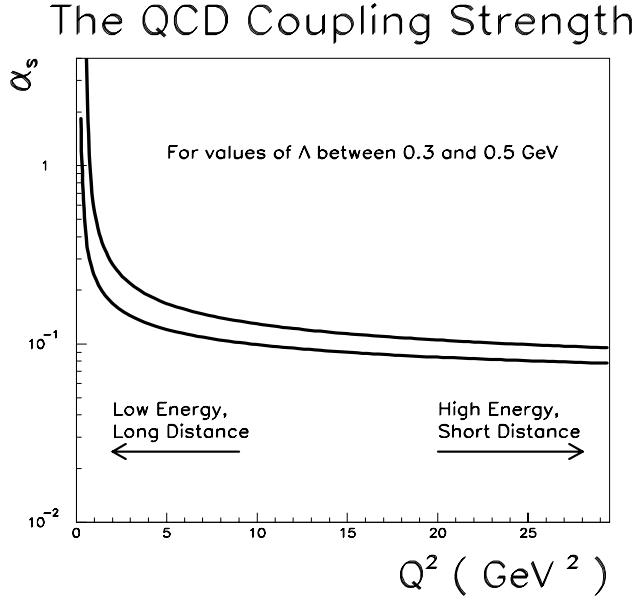
Figure 1.4: The "running" of α_s as a function of Q^2.

expansions in terms of α_s become valid. Essentially, the usefulness of perturbative expansions defines the high–energy regime of physics. At these energies, the stability and low value of the coupling constant results in *asymptotic freedom* for quarks: the coupling to the surrounding quarks and gluons may be neglected. For sufficiently low Q^2, perturbative expansions no longer apply and quarks no longer exhibit free behavior; instead, the proton acts like a single structureless particle.

The triumph of QCD lies in its ability to explain parton confinement and asymptotic freedom simultaneously, as explicitly expressed in the running coupling constant. The difficulties in QCD calculations result from their non-Abelian nature; the theoretical framework is only valid where the coupling is perturbatively small. As should be evident from Figure 1.4, different choices of scale (either μ or Λ) result in different values of the coupling constant and change the threshold for free behavior. Additionally, different choices of renormalization scale change theoretical predictions of cross sections, as shall be illustrated in a later section.

1.3 Jet Production

In a collision with sufficient momentum transfer, quarks can be ejected from the proton and antiproton. Because gluons carry color charge, they are also "objects" that can collide and be ejected from a hadron. Sometimes quarks and gluons are collectively called *partons*, to generically indicate a constituent of a hadron. As the distance between an ejected parton and the parent hadron increases, the strong coupling potential grows large enough to spontaneously generate dozens of new gluons and quark–antiquark pairs that subsequently recombine into stable, colorless groupings. This process of *hadronization* ultimately results in a "jet" of relatively stable particles with a total momentum vector nearly equal to the initial parton momentum. In the limit of complete freedom of quarks and gluons within the proton, particle masses much smaller than their momenta, and perfect collimation, the jet vector is exactly equal to that of the final state parton. Figure 1.5 illustrates a common leading–order $\left(\mathcal{O}(\alpha_s^2)\right)$ dijet mechanism. One quark from the proton and one quark from the antiproton annihilate to form a virtual gluon. The gluon subsequently produces a quark–antiquark pair which then hadronizes.

The expression for the momentum of each initial state quark or gluon in the primary interaction is separated into two factors: the parton distribution function (PDF), and the hard–scattering coefficient. The boundary between the two factors divides short–distance effects from long–distance effects and is set with a scale parameter μ_f. The *factorization scale*, μ_f, is not to be confused with the renormalization scale, μ; although they may conveniently be set to the same value, the two scales do not serve the same purpose. The renormalization scale determines how divergent integrals are replaced with finite expressions, the factorization scale isolates the non-perturbative cross section contributions (the PDF) from the calculable perturbative portion (the hard–scattering coefficient).

A PDF describes the probability to observe a specific parton of given momentum. Each PDF is specific to an initial hadron (*e.g.*, the PDF for a proton differs from that of a pion); the PDF contains all information that cannot be calculated perturbatively and must be
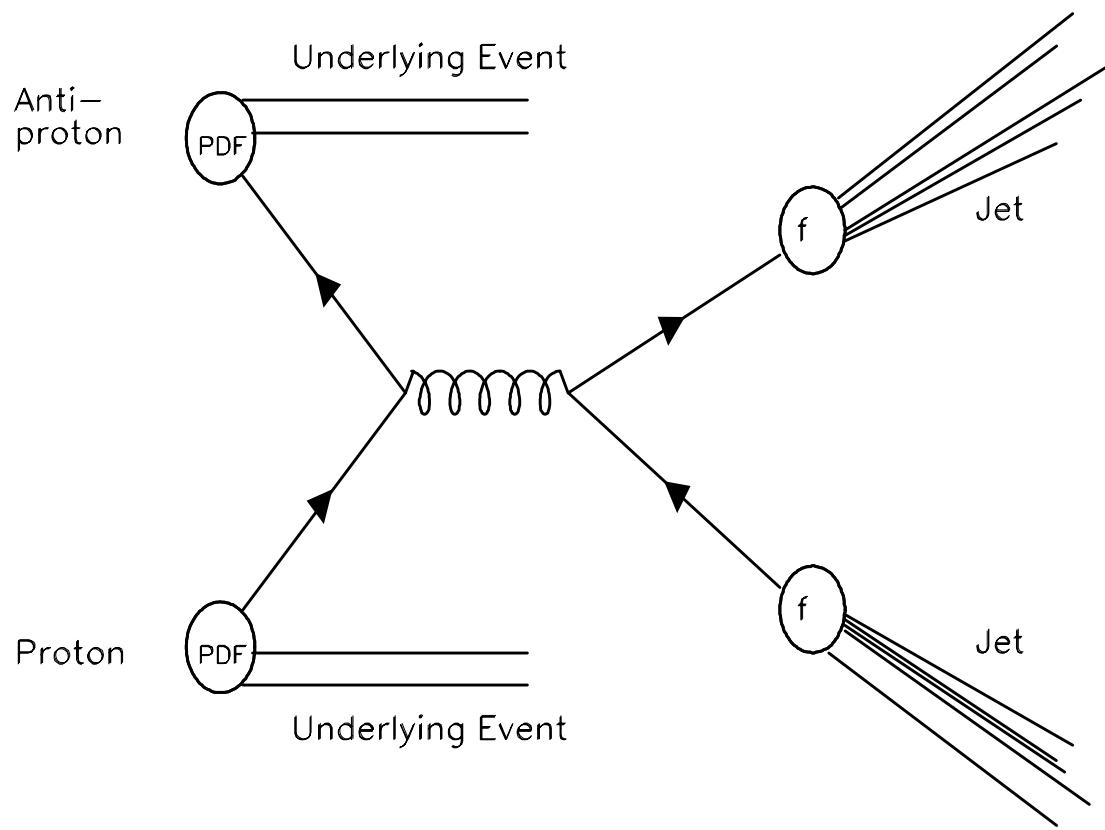
Figure 1.5: An augmented Feynman diagram for a leading-order proton-anitproton interaction resulting in two jets.

entirely determined by experiment. The PDF is independent of the specific interaction and its momentum transfer, but does depend on choice of renormalization scale μ, coupling strength $\alpha_s(\mu)$, and the order of the theoretical calculation (leading–order, $\mathcal{O}(\alpha_s^3)$, etc.). The PDF's are best–fits to the results of preceding experiments; variations result from the exclusion of conflicting results and from different extrapolations to momentum regions where data does not exist.

In contrast, the hard–scattering coefficients, represented by Feynman diagrams, are perturbatively calculable. The coefficients do not vary with respect to the identity of the initial hadron, whether it be a proton, neutron, or pion. In essence, these coefficients are the elastic scattering cross section for a given set of initial partons. The coefficients are functions of momentum transfer Q^2, renormalization scale, and coupling strength.

The details of hadronization are sometimes modelled with a fragmentation function and associated coefficients, denoted $\mathbf{f}$ in Figure 1.5. Fragmentation functions have not been studied in great detail, but operate contralaterally to PDF's: they use empirical data to parameterize the incalculable portions of hadronization. Because no distinction is made between jets of differing compositions, fragmentation functions have no effect on the QCD predictions of this dissertation.

Quarks and gluons interact non-perturbatively with one another within hadrons, so the initial momentum of the partons in a hard–scattering interaction will vary according to the PDF. Figure 1.6 depicts the momentum fractions carried by partons within the proton, where

$$x = \frac{p_{parton}}{p_{proton}} \tag{1.4}$$

This collection of parton distribution functions, one of several sets prepared by the CTEQ group,* reflects the expected number of quarks at a given x for each flavor. Because the

---

* PDF's are primarily prepared from global analyses by one of three collaborations: The Coordinated Theoretical-Experimental Project on QCD (CTEQ), Martin, Roberts, and Stirling (MRS), or Gluck, Reya, and Vogt (GRV). More information may be found in [5], [6], and [7].
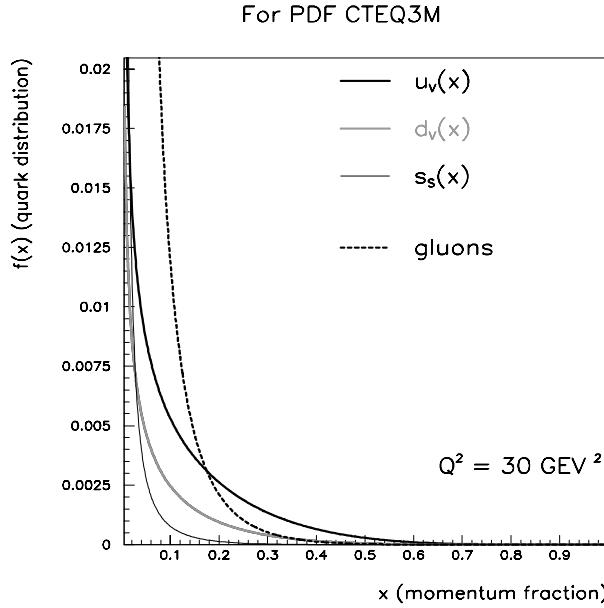
Figure 1.6: True distributions for the up quark (valence only), down quark (valence only), and strange quark for $Q^2 = 30$ GeV^2. Dashed line indicates the gluon distribution.
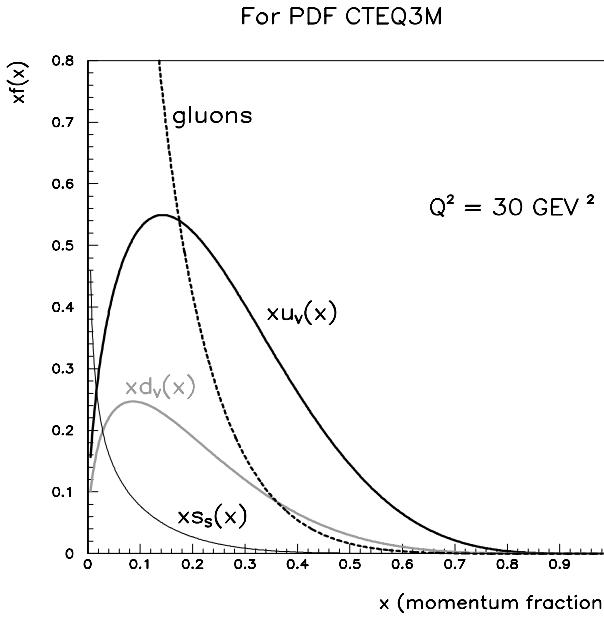
Figure 1.7: Parton distribution functions in standard form, $xf(x)$. While less intuitive, this format highlights differences in the shapes of the distributions.

proton is composed of two up quarks and a down quark, by definition,

$$\int_0^1 u_v(x)\,dx = 2 \tag{1.5}$$

and

$$\int_0^1 d_v(x)\,dx = 1. \tag{1.6}$$

Additionally, there remains a non–zero possibility of virtual quark pair formation, as previously illustrated in the lower right diagram of Figure 1.2. These *sea quarks* may be any of the six flavors, but up, down, and strange are most common due to their small masses. (The requisite two up quarks and down quark are differentiated from the virtual types with the term *valence quark,* hence the subscript v in Equations 1.5 and 1.6.) The light sea quarks and antiquarks have nearly identical distributions, thus,

$$s_s(x) \approx u_s(x) \approx d_s(x) \approx \bar{s}_s(x) \approx \bar{u}_s(x) \approx \bar{d}_s(x). \tag{1.7}$$

By direct integration of $s_s(x)$, the expected number of sea quarks in a proton is approximately $6 \times 0.8 + h$, where h, the contribution from heavy flavors (charm, bottom, and top), is very small. Also shown in Figure 1.6, the gluon distribution dominates the quark distributions at small x. This nearly divergent distribution indicates that a very large number of gluons have vanishingly small momentum. The distribution of "soft gluons" is difficult to measure and therefore poorly known at this time. The rarity of high–momentum gluons ("hard gluons") results in a large uncertainty in the high–x region of the gluon distribution as well. For the parameterization in Figure 1.6, an average of 15 gluons exist in the proton at any given moment. In summary, the proton consists of three valence quarks, a sea of quark–antiquark pairs that "wink" into and out of existence, and a collection of gluons that hold all the quarks together.

Because the many distributions are similar, authors normally present graphs of $x \cdot f(x)$ versus x (Figure 1.7), a formulation that highlights the differences between the functional forms. Only in this format is the term *parton distribution function* properly applied. Despite the confusion caused by the convention, the form $x \cdot f(x)$ is more useful in relating

experimental results to theoretical predictions because the area under the curves represents the total momentum fraction carried by a particular set of partons.

Given empirical determination of a PDF at one momentum scale, QCD determines the *evolution* of the PDF to any other momentum scale with the Dokshitzer–Gribov–Lipatov–Altarelli–Parisi (DGLAP) evolution equations.* In essence, the DGLAP equations quantify the probability that a parton of given momentum will "split" by radiating one or more partons. Naïvely, the number of partons at a given x would be the same without regard for the momentum of the proton. In fact, as its momentum increases, a parton is more likely to radiate a gluon; thus, the high-x region of the PDF becomes more depleted as proton momentum increases. A second way to simplify the DGLAP result is to state that higher–energy collisions "resolve" more substructure within the proton; a quark with $x = 0.6$ could resolve into an $x = 0.55$ quark and an $x = 0.05$ gluon when the absolute momentum increases.

After a hard interaction, the initial hadrons have lost the color charge associated with the interacting partons; therefore, the parent hadrons are no longer stable, colorless objects. As a result, the remainders of the initial proton and antiproton undergo hadronization also. The additional hadronic products resulting from the "spectator partons" are collectively called the *underlying event*. To study jets, the additional energy deposits from the underlying event must be removed, as shall be described in Chapter 4.

Figure 1.8 (a) depicts the two leading–order quark–quark dijet processes and a gluon–quark dijet process. Part (b) shows two examples of next–to–leading–order (NLO) dijet processes. Finally, part (c) describes two NLO mechanisms that result in a three–jet final state (gluon bremsstrahlung diagrams). Many additional next–to–leading–order diagrams exist, as well as analogous QED dijet mechanisms and weak dijet mechanisms where many of the virtual gluons may be replaced with photons or Z bosons. At the time of this writing, QCD predictions for inclusive jet production stop at NLO: calculations at the next level of precision, $\mathcal{O}(\alpha_s^4)$, have not yet been completed.

---

* Formerly known as the Altarelli–Parisi evolution equations.
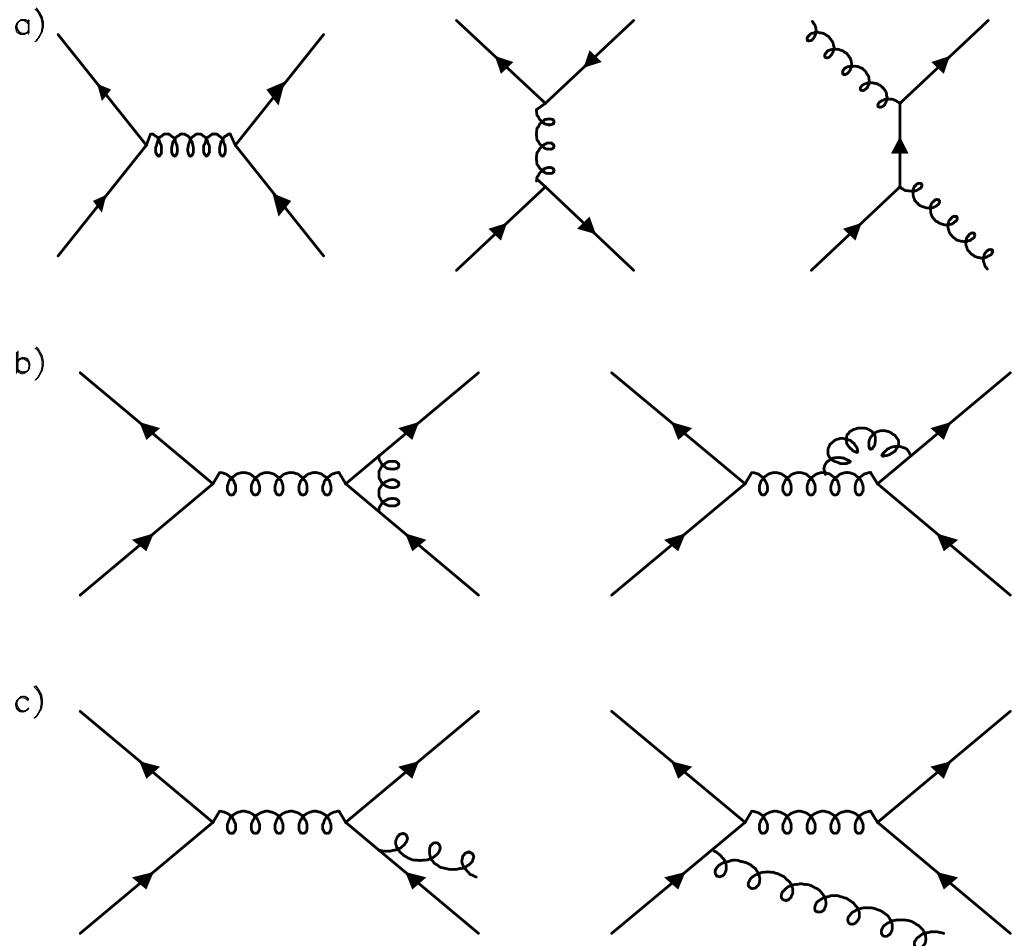
Figure 1.8: Selected Feynman diagrams for: (a) leading-order dijet events, (b) next-to-leading-order dijet events, (c) three-jet events. By convention, underlying event and final-state hadronization are omitted.
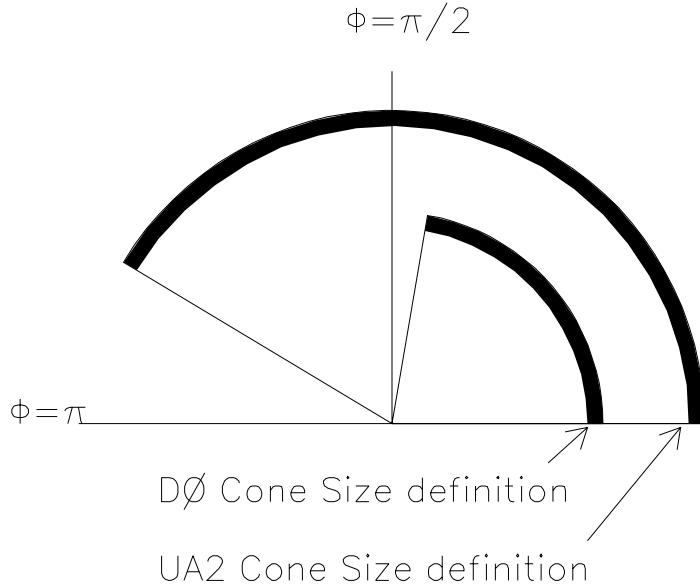
Figure 1.9: Difference between the 0.7 jet cone definition (DØ, present) and the 1.3 definition (used by the UA2 Collaboration, 1991).

1.4   The Inclusive Jet Cross Section

Although any hadronic shower constitutes a jet, several non–equivalent definitions of jet energy exist. When QCD predictions included only leading order contributions, jets were defined [12] as the energy deposited in an $\eta - \phi$ cone of dimensionless radius 1.3. (Here, ϕ is an azimuthal angle and η is a measure of the colatitude; *cf* Appendix A for details on DØ coordinates and definitions.) The jet cone radius of 1.3 tends to reduce a many–jet topology to a dijet topology, which is subject to a leading–order description. With NLO predictions available, the cone size definition for inclusive measurements can be narrowed to $R = 0.7$ (or less) to allow valid comparisons to both two– and three–jet events. Figure 1.9 illustrates the difference in azimuth subtended by the two jet cone definitions. The 1.3 radius cone encompasses nearly half the arc of a circle while the 0.7 cone can accommodate the presence of many additional jets. In addition to changes in jet multiplicity, the 0.7 radius cone also results in increased precision of measurement (increased energy resolution) and slightly lower energy for each jet.

At DØ, jet cone centroids are defined by the summed four–momenta of its cells. When any two jet cones overlap, ambiguity is removed with a merging and splitting algorithm (M/S hereafter), summarized in Table 1.4. Any study involving more than one jet in the final state requires the use of M/S in the data analysis. For the theoretical predictions, the energy–weighted center of the final–state partons defines the jet center (Snowmass definition), and final state partons within the same $\eta - \phi$ cone form a single jet. To reproduce theoretically the behavior of the M/S algorithm in the data the size of the theoretical cone must be reduced. A new parameter, R_{sep}, defines the cone–size reduction necessary for good matching, where the maximum allowed parton separation is then $R_{theory} = R_{sep} \cdot R$. The best empirically determined value [8] for R_{sep} is 1.3, which is valid for all cone sizes.

The inclusive jet cross section may be expressed in several ways. While theoretical calculations are normally expressed in terms of the *invariant cross section*

$$\text{E} \cdot \frac{d^3\sigma}{dp^3},\tag{1.8}$$

the measurable variables in collider physics are the transverse energy and the pseudorapidity (*cf* Appendix A for definitions). In terms of these variables, the cross section is expressed as

$$\frac{d^2\sigma}{dp_\text{T}\,d\eta},\tag{1.9}$$

where Equations 1.8 and 1.9 are related by

$$\text{E} \cdot \frac{d^3\sigma}{dp^3} = \frac{1}{2\pi p_\text{T}} \times \frac{d^2\sigma}{dp_\text{T}\,d\eta}.\tag{1.10}$$

Figure 1.10 depicts the spectrum of the jet cross section, as defined by Equation 1.9. For most measurements, the cross section is integrated over some range of pseudorapidity, in this case, $|\eta| < 0.5$ (*i.e.* the central region). The cross section, kinematically limited to zero at 315 GeV, decreases approximately exponentially over many orders of magnitude.

If the Overlap Region Contains:	Then:
$> 50\%$ of the smaller jet's E_T	Merge jets into one jet
$< 50\%$ of the smaller jet's E_T	Split jets into two jets

Table 1.4: Criteria of the merging and splitting algorithm.
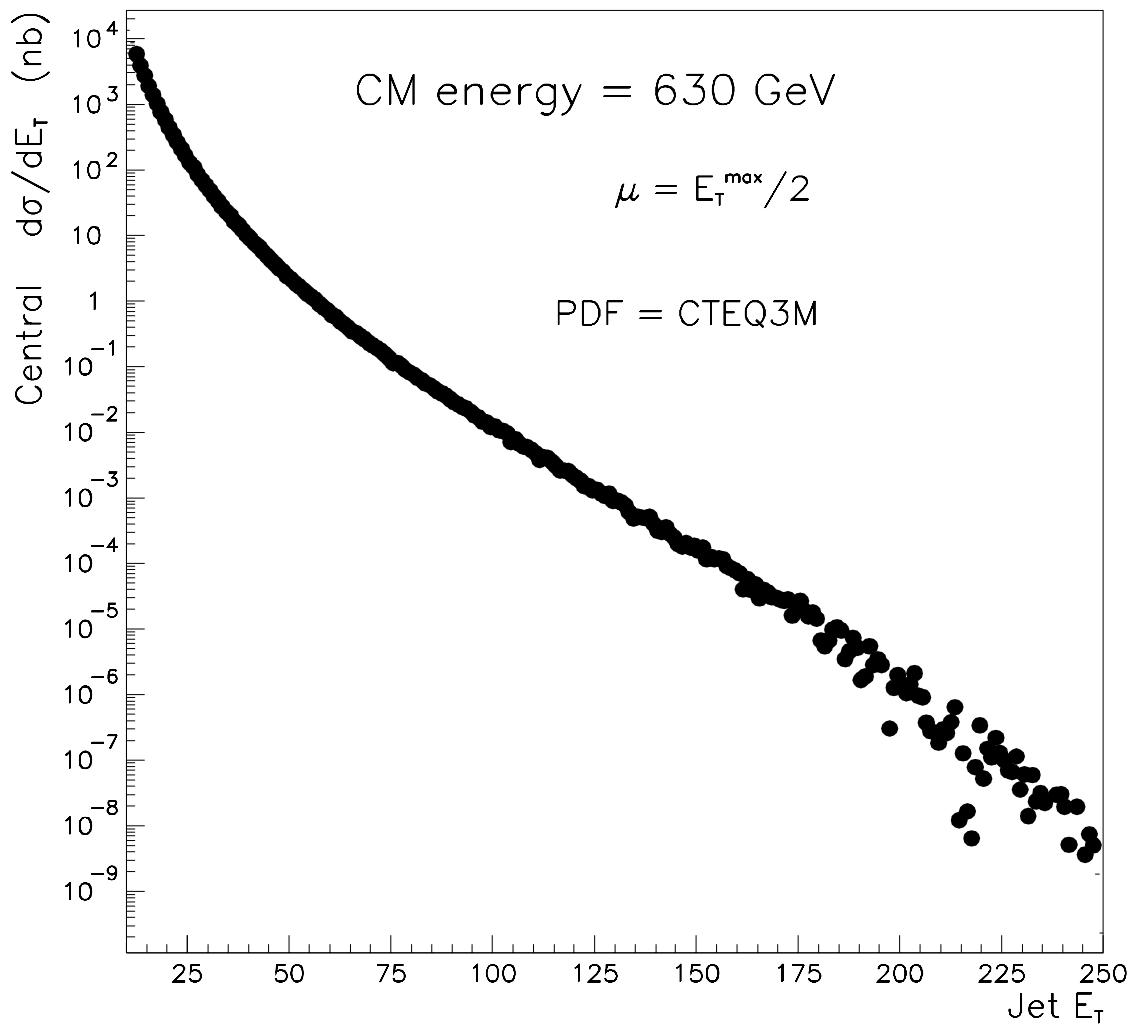
Figure 1.10: QCD prediction for the spectrum of the inclusive jet cross section as a function of transverse jet energy. Discontinuities at high E_T values are caused by statistical fluctuations, not by a feature of the theory.

The inclusive jet cross section measures the probability of observing at least one hadronic jet in a hard p$\bar{\text{p}}$ collision. The term *inclusive* indicates that the presence or absence of additional non-jet objects in an event does not concern this analysis. Moreover, an event which contains three jets will appear in the cross section three times. The inclusive measurement is sometimes denoted $\sigma(\text{p}\bar{\text{p}} \to Jet + x)$. Because it is measured many times over different discreet intervals of p_{T}, the measurement could also be described as a *differential* cross section in the limit the bin widths approach zero.

The theoretical NLO prediction is generated event–by–event, much like the data the DØ experiment collects. For each generated event, the strength of the coupling constant α_s has been renormalized by $\mu = 0.5$ times the E$_{\text{T}}$ of the most energetic jet, denoted E$_{\text{T}}^{max}$. (Note that E$_{\text{T}}^{max}$ is not the only possible measure of the momentum transfer Q and is thus not the only possible choice for μ.) The selected PDF, CTEQ3M, has demonstrated its ability [9] to reproduce experimental results from DØ, CDF, and the many fixed–target experiments at Fermilab. The Monte Carlo event generator, a program [10] called JETRAD, can produce fluctuations in the spectrum due to low statistics, especially at extreme values of jet E$_{\text{T}}$, as visible in Figure 1.10. Due to detector limitations and statistical limits in the data, the cross section measurement performed at the DØ Experiment will have a lower domain limit near 25 GeV and an upper limit near 160 GeV; thus, no increase in the statistical power of the prediction will be required.

As mentioned in the previous section, different choices of theoretical parameters will result in different spectra for the inclusive cross section. Defining the spectrum in Figure 1.10 as the standard, consider the variations in Figure 1.11, which depicts cross section differences in the ratio. In part (a), two different PDF's result in a shape change in the cross section. Because the fit of PDF's to experimental data includes a subjective component, different fitting groups find different "best" fits. Alternately, different factorization scale choices (b) could shift the cross section in the opposite direction. Parts (c) and (d) illustrate the shifts that result from new selections of renormalization scale and effective cone size. The uncertainty in the cross section from any given parameter can become as large as 30%.
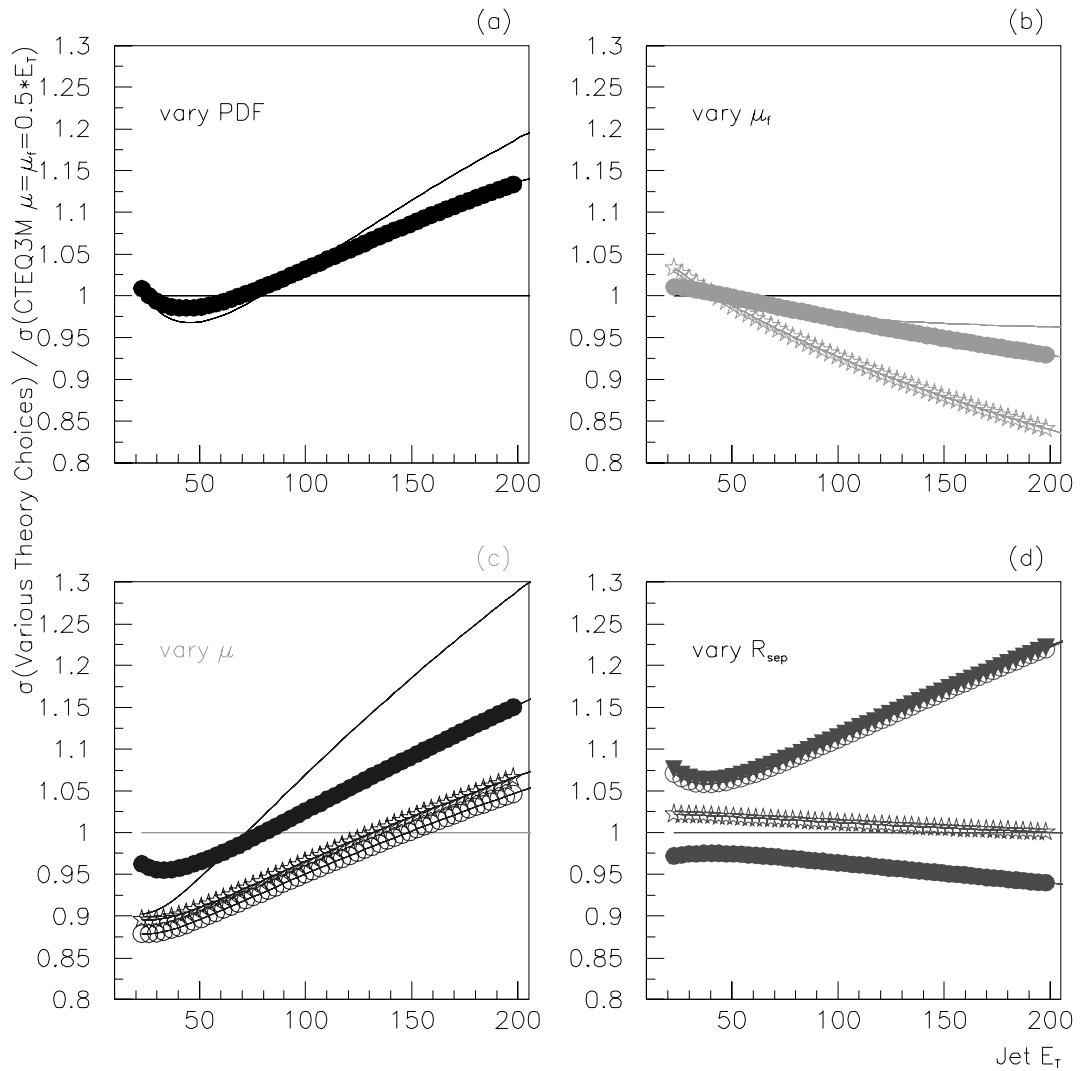
Figure 1.11: Theoretical uncertainties in the NLO QCD prediction for the inclusive jet cross section result from (a) changes in the PDF, (b) changes in renormalization scale, (c) changes in factorization scale, and (d) changes in the effective cone size for partons.
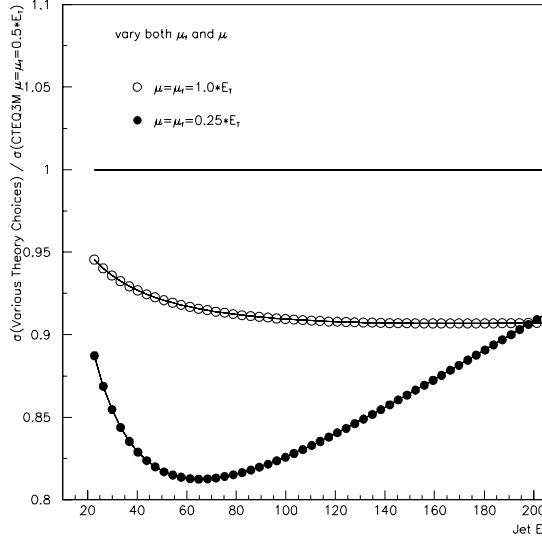
Figure 1.12: Variations in the cross section when illustrate the principle of minimum sensitivity. Here, the comparison line at unity is formed by $\mu = \mu_f = \frac{1}{2}E_T$; both other selections (circles) result in a lower cross section.

For the special case when the renormalization and factorization scales are set equal to one another, the standard choice of $\mu = \mu_f = 0.5 \cdot E_T^{max}$ appears to be a saddle point, all other choices [11] (both larger and smaller) result in smaller values for the cross section. This effect, referred to as the principle of minimum sensitivity, provides the only reason to prefer 0.5 as a scale over the other possibilities.

The large variance between the theoretical predictions indicates a potential for current experiments to constrain the theoretical choices mentioned above. While direct cross section measurements will accomplish this goal to some degree, a more powerful measurement can be performed by comparing the jet E_T spectra at two different collision energies.

1.5   The Ratio of Scaled Invariant Cross Sections

By expressing the cross section in terms of dimensionless variables, the inclusive jet spectrum is, to first–order, independent of center–of–mass energy. A simple sketch of the scaled invariant cross section (Figure 1.13) reveals the advantages of the new formulation. While

it is possible to compare $E \cdot \frac{d^3\sigma}{dp^3}$ versus E_T for both energies, the data will differ greatly in both magnitude and range in E_T. In contrast, the cross sections as functions of $E_T^4 \cdot E \cdot \frac{d^3\sigma}{dp^3}$ versus $x_T \equiv \frac{2 \cdot E_T}{\sqrt{s}}$ are somewhat linearized and lie very close to one another; the dimensionless[*] cross section is said to "scale" with center–of–mass energy. To yield an expression in terms of collider variables, the scaled invariant cross section must be transformed according to Equation 1.10.

Deviations from scaling behavior result from higher–order QCD effects, particularly gluon emission processes, as described by the DGLAP evolution equations. Measurement of the ratio of dimensionless invariant cross sections thus provides a sensitive and direct test of NLO QCD without masking the high–order effects with the leading–order contribution. As an additional benefit, much uncertainty in the cross section predictions cancels in the ratio; most notably, the ratio is nearly insensitive to choice of PDF.

1.6   Summary

This chapter introduced the Standard Model of particle physics and illustrated the fundamental interactions with Feynman diagrams, a primary tool of high energy physics. Basic terminology and specific features of the theory of strong interactions were described, including the concepts of renormalization and factorization, the role of parton distributions, and the cone definition of jets.

The jet cross section cannot be determined analytically: the theoretical calculations are next–to–leading–order approximations. Even perturbative calculations require a renormalization scale (μ) to handle divergent integrals; the best value for the constant cannot be determined from the theory alone, resulting in large theoretical uncertainties in the perturbative QCD cross section calculation. Parton distribution functions, determined by prior experiments, describe the incalculable initial states of the interacting partons. Incomplete or contradictory data in PDF global analyses result in additional uncertainties in the prediction. Freedom to select a factorization scale, which determines precise momentum where

---

[*] The cross section is dimensionless in terms of *natural units* (*cf* Appendix A).
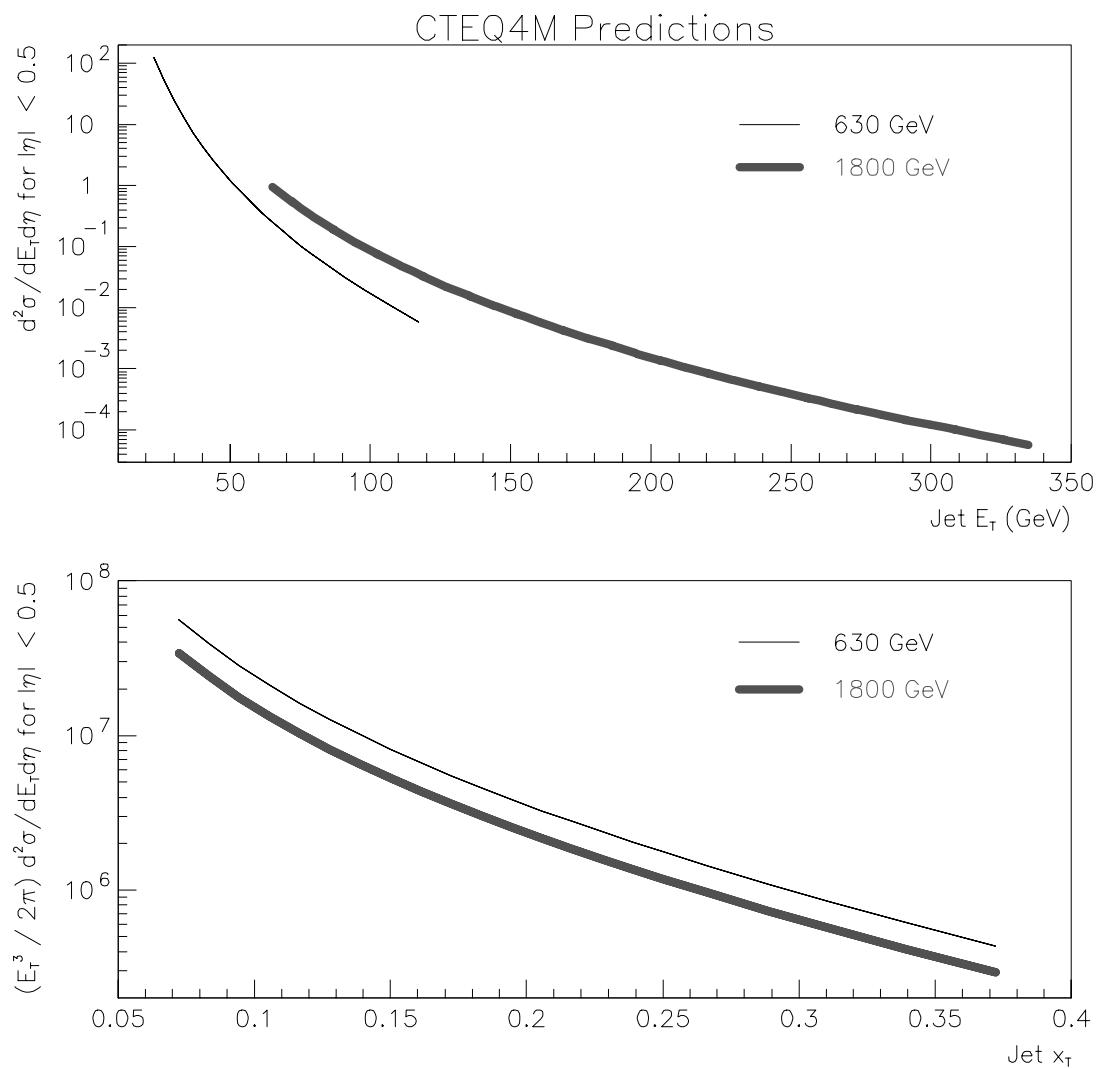
Figure 1.13: Different presentations of the inclusive jet cross sections at (thin line) $\sqrt{s} = $ 630 GeV and (thick line) 1800 GeV. Theoretically, the scaled dimensionless cross sections should be nearly linear and lie very close to one another.

the PDF ends and the perturbative QCD calculations begin, adds additional uncertainty to the calculation. Comparisons of NLO cross section predictions, with different choices of renormalization scale and PDF, reveal the uncertainties inherent in the calculation (approximately 30%).

The high energy physics expression for the cross section differs slightly from the non–relativistic quantum mechanics definition to better accommodate the physics of a collider detector. The scaled invariant cross section varies slightly with center–of–mass energy as described by the DGLAP evolution equations. The ratio of scaled invariant cross sections, the measurement described in this dissertation, was presented as a powerful test of perturbative QCD.

The following two chapters describe the laboratory, detector, and control systems used to collect the jet data. The subsequent four chapters relate the analysis of the jet data, including jet corrections, distribution corrections, and error analysis. The final chapter will present the results of this work.

Chapter 2

The Experiment

To best probe proton substructure and search for new particles, collisions with high center–of–mass energy ($\sqrt{s}$) are required. Consider the antiproton creation process $p + p \rightarrow 3p + \bar{p}$. For a proton incident on a fixed target, much of the initial energy must remain in the form of momentum relative to the lab frame. Thus, the total initial beam energy required [2] for the process is

$$E_i^{\mathrm{FT}} = 7 \ m_p c^2. \tag{2.1}$$

Now consider two protons colliding with equal but opposite momenta. The threshold energy condition for the antiproton creation process occurs when all products are produced at rest. For this case, the initial energy *for each proton* is

$$E_i^{\mathrm{C}} = 2 \ m_p c^2, \tag{2.2}$$

a significant advantage over the fixed target result. Although the specific coefficients of Equations 2.1 and 2.2 will vary for different processes, the threshold energy advantage of the collider will always remain. Searches for new heavy particles require high center–of–mass energies that can only be provided by a collider.

The first hadron accelerator complex, the Intersecting Storage Rings at CERN, collided protons at $\sqrt{s} = 63$ GeV, later switching to $p\bar{p}$ collisions. The full center–of–mass energy was insufficient [3] to produce real W bosons ($M_W \approx 80$ GeV) at the ISR, although jets were eventually detected. The later CERN Super Proton Synchrotron improved matters in 1981,

running first at $\sqrt{s} = 540$ GeV, and later increasing to 630 GeV. The UA2 experiment[*] performed comprehensive measurements of the inclusive jet cross section at both CM energies and examined the ratio between them. This ratio, an early test of jet scaling, motivated the DØ analysis presented in this thesis.

The DØ experiment[†] is located at Fermi National Accelerator Laboratory (FNAL, or Fermilab), near Batavia, Illinois. At Fermilab, protons and antiprotons counter–rotate in a superconducting collider ring 1 km in radius. As will be detailed in the first half of this chapter, the 1800 GeV center–of–mass collision energy of the Fermilab Tevatron is attained via a number of discrete steps. The following sections summarize the methods used to generate antiprotons as well as the techniques used to accelerate protons and antiprotons to 900 GeV and collide them at the center of the two collider detectors resident at Fermilab. The second half of this chapter describes the components of the DØ detector: the central tracking region, the calorimeter, the muon spectrometer, and the Level Ø hodoscopes. Each detector region consists of several subsystems designed to make specialized measurements. Jet physics analyses focus on calorimetery; other detector subsystems play minor roles.

2.1   The Fermilab Accelerator Complex

"The road to truth has many turns."

The Fermilab accelerator complex consists of several distinct devices, each with its own effective energy regime (Figure 2.1). While the Tevatron is capable of accelerating particles from 150 GeV to 900 GeV, it is not designed to manage particle energies below 150 GeV. Starting with hydrogen gas, five different devices are needed to prepare protons for injection into the Tevatron. The first two devices, the plasma source and the Cockcroft–Walton generator, share the same housing and are often collectively called the preaccelerator system. The remaining systems, the Linac, the Booster, and the Main Ring, will successively increase particle momenta while narrowing momentum variance.

Successful Tevatron operation results in a collision between a proton and an antiproton

---

[*] The UA2 experiment was named for its location on the SPS collider ring, "Underground Area 2"...
[†] ...and the DØ Experiment was named in the same tradition, for its location on the Tevatron collider ring.
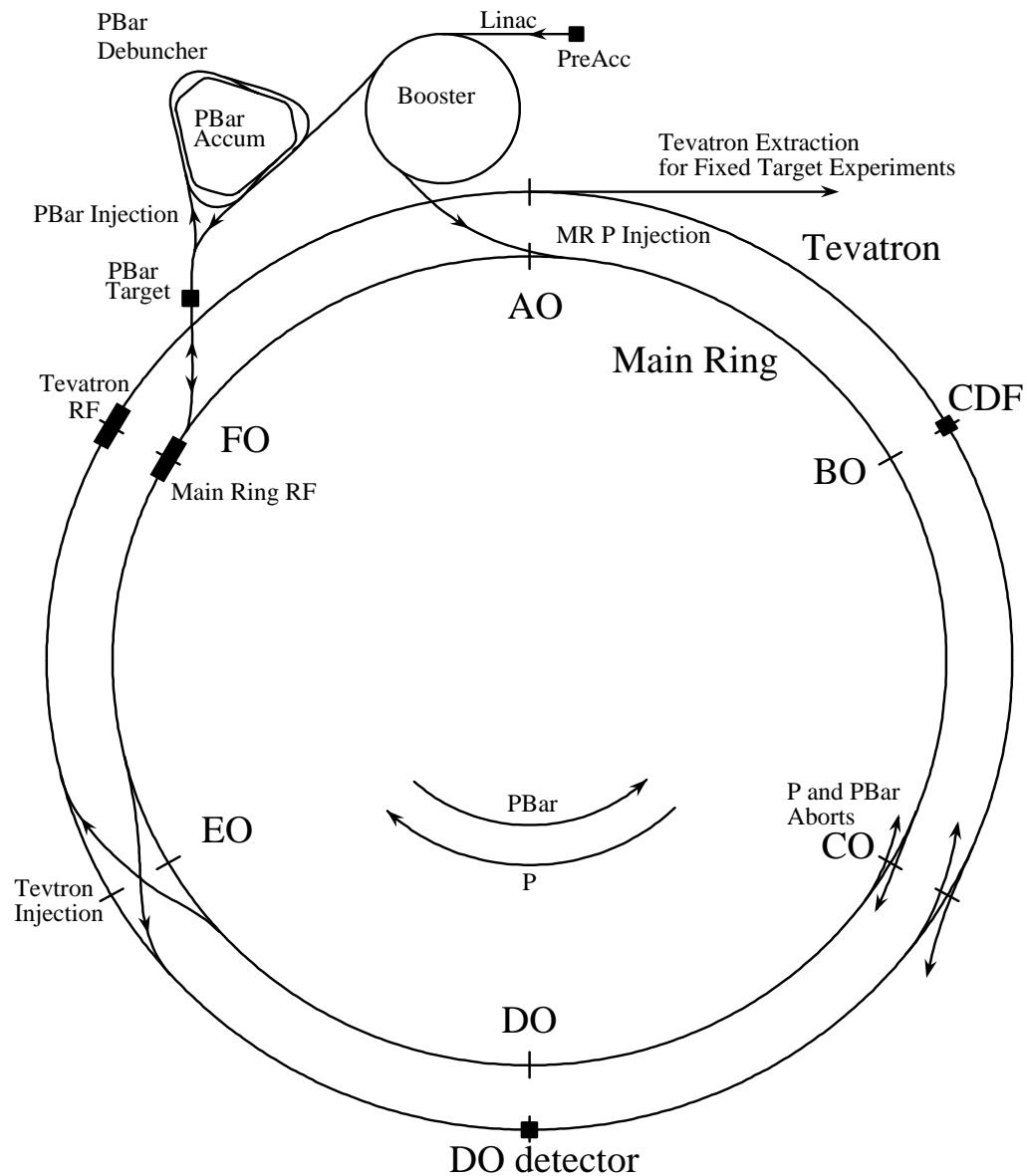
Figure 2.1: Schematic overview of the Fermilab accelerator complex. The Main Ring and the Tevatron have the same radius but have been drawn concentrically to reveal injection system details.
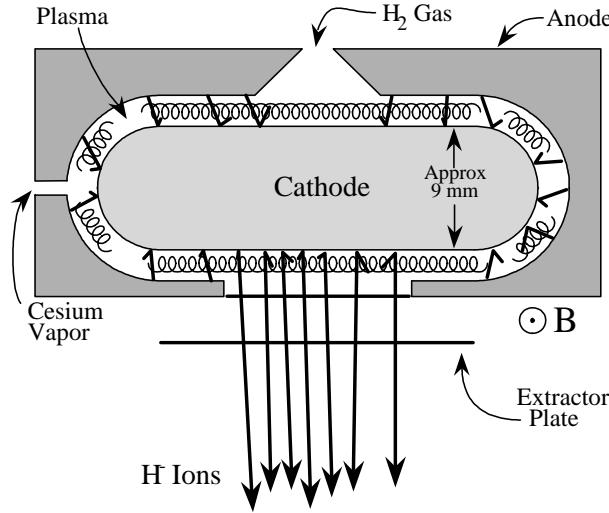
Figure 2.2: The magnetron plasma source. The magnetic field is perpendicular to the plane of the image.

with a center–of–mass energy of 1800 GeV. The beams consist of discrete bunches rather than a smooth continuum, so precise timing is essential. Because many of the more technical details of the accelerator system are beyond the scope of this work, the interested reader should consult Reference [13] for further discussion of the Fermilab accelerator complex.

2.1.1 The Plasma Source

Starting with hydrogen gas, the magnetron surface–plasma source generates negative hydrogen ions. The magnetron consists of an ovoid cathode, a surrounding anode, and an external magnetic field (Figure 2.2). Pulses of hydrogen gas enter the 1 mm gap between the anode and cathode with a typical pressure of $\sim$ 100 mTorr. Many H_2 molecules become adsorbed to the cathode, while free electrons and positive ions travel in a helical path in the anode–cathode gap. The crossed electric and magnetic fields ensure high–density for this spiraling plasma. When positive ions and energetic particles collide with the adsorbed hydrogen, they eject, or "sputter," hydrogen atoms and a small number of H^- ions. A charged plate extracts the produced H^- ions through an anode aperture with a typical energy of 18 keV. A small admixture of cesium vapor boosts operating efficiency by lowering
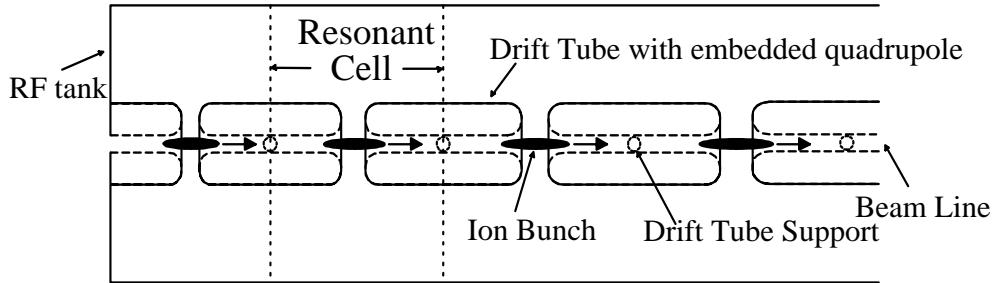
Figure 2.3: A simplified view of an Alvarez drift tube linac.

the work function of the cathode: the likelihood of a sputtered hydrogen atom to associate with an extra electron increases from 0.2% to 10%. A steering magnet directs the extracted ions into a right–angle turn, filtering the beam of electrons.

Similar devices can create H^+ ions and eliminate the need to strip electrons from the ions later, but positive ion sources require higher current and therefore longer pulse times. The fast–pulsing negative ion source improves beam quality dramatically for the downstream accelerators because a small spread in creation time will translate to precision in particle position downstream.

2.1.2 The Cockcroft–Walton Generator

The Cockcroft–Walton high–voltage generator, a solid state device, generates high voltage by charging capacitors in parallel and discharging them in series. With five stages of voltage multiplication, the generator boosts the input voltage of 75 kV by a factor of ten with very little fluctuation. Once H^- ions have been created by the magnetron, a positively charged plate accelerates them to an energy of 750 keV.

2.1.3 The Linac

Emerging from the Cockcroft–Walton generator, the hydrogen ions enter a linear accelerator. The first stage, a 70 m long Alvarez drift–tube linac, employs five electrically resonant copper–clad steel tanks. Each tank contains 23 to 59 drift tubes configured as shown in Figure 2.3. Particles in the narrow sections between drift tubes experience an accelerating
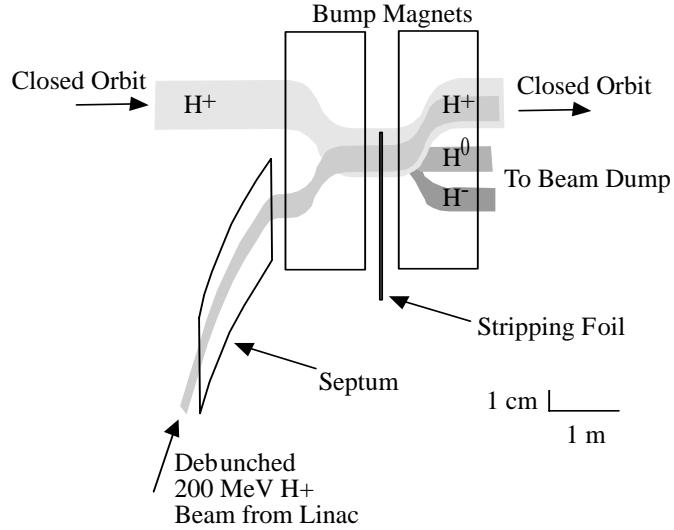
Figure 2.4: Booster injection schematic. A carbon foil removes both electrons from the H$^-$ ions. Beam merging is accomplished with two "orbital bump magnets."

field whereas particles inside the tubes are shielded. The drift tubes within the tanks are thus designed with successively increasing lengths to ensure that the applied electric field (cycling at 201.24 MHz) maintains a constant phase angle with respect to the particle's position in the tubes. Because the oscillation frequency of the applied field lies in the radio frequency range, the drift–tube assembly is often called an RF tank.

The second stage of the linac has a slightly different tube design but operates similarly. The gaps between drift tubes are smaller and more efficient, and the tanks resonate at 805 MHz, with particles every fourth cycle. The entire length of the linac system is 146 m, the H$^-$ ions emerge with an energy of 400 MeV and drift an additional 46 m before injection into the booster.

2.1.4 The Booster

H$^-$ ions enter the Booster, a rapidly cycling synchrotron with a radius of 250 feet. Paired bump magnets direct the ions through a carbon foil that strips the electrons, leaving bare protons. Simultaneously, the magnets merge the new protons with any existing protons in

the booster (Figure 2.4).

At maximum capacity, the Booster holds 84 proton bunches, each consisting of 6 merged linac bunches. Once the Booster is full, it accelerates the protons from 400 MeV to 8 GeV. As the protons become more relativistic, the electric and magnetic fields vary synchronously with the changing particle momentum to maintain a closed orbit.

The proton's destination must be designated as either the antiproton target or the Tevatron. If antiprotons are required, all 84 bunches in the Booster are directed into the Main Ring with a "kicker magnet." Because of the finite rise time in the kicker, one bunch is lost during this procedure. If the protons are destined for the Tevatron, only 11, 13, or 15 bunches will be injected into the Main Ring; the rest are directed into a beam dump.

2.1.5   The Main Ring

Prior to the construction of the Tevatron, the Main Ring was the highest energy synchrotron in the world, accelerating particles to 400 GeV. The Main Ring has a 1000 m radius, uses 774 dipole magnets to bend the beam and maintain closed orbits, and refocuses the beam with 240 quadrupole magnets. Within the Tevatron complex, the Main Ring serves two purposes: it directs a proton beam to a target to create antiprotons, and it injects particles into the Tevatron.

Antiproton Creation

Before the Tevatron can operate in collider mode, antiprotons must be created. Because antiprotons accumulate slowly, the Main Ring continues the antiproton generation process even while the Tevatron collides proton and antiproton beams. To generate antiprotons, the Main Ring accelerates 83 proton bunches to an energy of 120 GeV and directs them at a nickel target disk. This incident proton energy optimizes the number of antiprotons generated with 8 GeV of energy (matching the Booster injection energy). The proton beam strikes the target along the plane of the disk so the target depth along a chord may be easily selected with small lateral movements (Figure 2.5). The yield is 10^7 antiprotons for every 10^{12} protons.
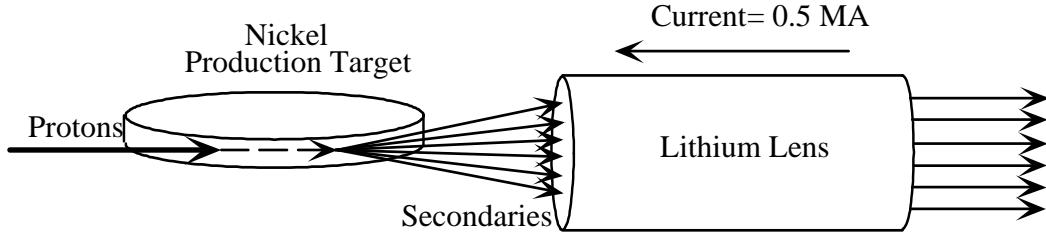
Figure 2.5: The antiproton creation process.

All resulting particles pass through a lithium cylinder that carries a longitudinal pulsed current of 0.5 MA. The induced azimuthal magnetic field focuses the charged particles along the axis of the cylinder. An optimal material choice due to its low density and high conductivity, Lithium provides little energy absorption or multiple scattering while still accommodating a high magnetic field.

A pulsed dipole magnet selects 8 GeV antiprotons, directing them into a debuncher ring that reduces the longitudinal and transverse spread of the beam. The "cooled" antiprotons are then added to any antiprotons already stored in the Accumulator ring for later injection into the Tevatron via the Main Ring.

Tevatron Injection

Once in the Main Ring, 11 to 15 proton or antiproton bunches destined for the Tevatron are coalesced into a single bunch by superimposing phased RF waveforms. The resulting waveform decelerates forward particles relative to the centroid of the bunches while accelerating the lagging bunches (Figure 2.6). Once the particles have been collected at the centroid, new RF waveforms are applied to reposition the bunch in the ring for injection. This "cogging" process ensures good time separation between the other bunches and allows collisions to occur at the designated Tevatron ring positions.

The Tevatron, constrained by a need to fit within the existing beam tunnel, is suspended two feet below the Main Ring. Because Main Ring operation would disturb detectors studying collisions in the Tevatron, the Main Ring beam pipe was bent vertically upward
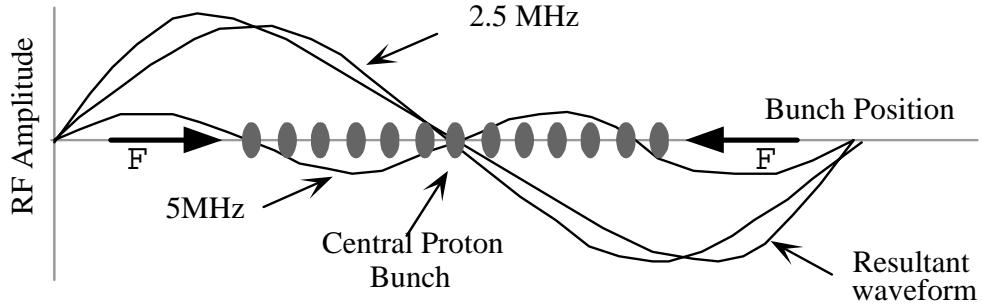
Figure 2.6: Phased RF waveforms coalesce proton bunches. Bunches ahead of the centroid receive a net decelerating force and vice versa.

to arch over ring location BØ (home of the CDF detector). A prototype "overpass" was first built at location DØ with the intent that a second collider detector would eventually take advantage of the separation. Because there was no second detector at the time of the overpass construction, the prototype had a separation of 89.2 inches and fit within the existing beam tunnel. In contrast, the BØ overpass required major tunnel reconstruction, achieving a separation of 19 feet. As a result of the design of the DØ overpass, the current DØ calorimeter is perforated by the Main Ring beampipe, complicating physics analyses.

2.1.6   The Tevatron

Similar in design to the Main Ring, the Tevatron accelerates particles from 150 to 900 GeV, steering and focusing the beams with dipole and quadrupole magnets. In contrast to the water–cooled Main Ring, the superconducting Tevatron magnets require liquid helium to achieve an operating temperature of 4.6 K. Due to their equal masses and opposite charges, protons and antiprotons can share the same accelerating fields and thus the same beampipe, permitting an elegant and economical design.

With the exception of several test runs in December of 1995, Fermilab has operated the Tevatron with six proton bunches counter–rotating with six antiproton bunches. A small vertical displacement between the beams minimizes the number of collisions at the 10 of 12 possible collision areas that are not occupied by a detector. At the occupied sites, specially

designed quadrupole magnets placed on either side of the collision area focus the beams together and reduce the beam spot size to $\sigma_{x,y} \approx 40~\mu m$. These magnets, the "low–beta quads," maximize luminosity $\left([\mathcal{L}] = \frac{particle~crossings}{cm^2 \cdot sec}\right)$ at the center of the detectors and subsequently defocus the beams after collisions to maximize beam lifetime.

In the Tevatron, small perturbations about the circular closed path tend to increase in amplitude with time. The resulting particle displacements lead to collisions with the beampipe, causing luminosity attenuation and "beam halo" (see Chapter 5). To maintain beam quality, both beams are periodically directed into their respective dump sites and fresh bunches are injected. A period of uninterrupted running, usually 12 to 18 hours, is called a "store."

Flexibility in the Tevatron design allowed the beam energy to be decreased during December of 1995. The reduced center–of–mass energy, $\sqrt{s} = 630$ GeV, matches the energy of the SPS accelerator used by the UA2 experiment. As discussed in later chapters, a comparison of the "low–energy" data to the full energy data allows a powerful QCD measurement that would not be possible with data from a single center–of–mass energy.

2.1.7 Future Prospects for Fermilab

Currently, magnet technology limits the center–of–mass energy of the beams. The superconducting bend magnets "quench" above a critical current load and therefore produce a limited maximum angle of deflection per magnet. Because the maximum center–of–mass energy is constrained by the need to keep the beam in a closed orbit, an increase would require either a larger ring (as is being built in Europe) or more powerful magnets.

In the next several years, Fermilab will incorporate a new injection system into the Tevatron accelerator complex, increasing both the number of particles per bunch and also the number of bunches in each beam (from the current six to as many as 128). Additionally, the center–of–mass energy limit will be finessed slightly: by squeezing more magnets into the Tevatron ring the collision energy will be raised from 1800 GeV to 2000 GeV.
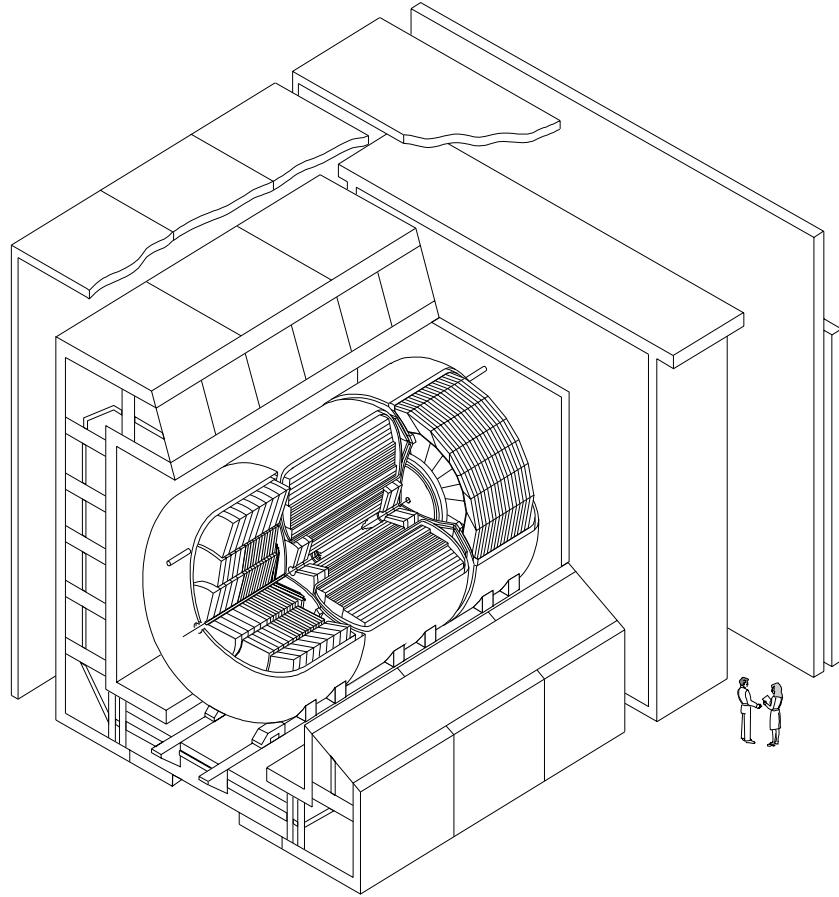
Figure 2.7: Isometric view of the DØ detector.

2.2 The DØ Detector

> *"The answer to any question starting 'Why don't they...?' is almost always, 'Money.'"*
>
> — From "Shooting *Destination Moon*," by Robert
>   A. Heinlein

During a store, protons and antiprotons collide near the center of the DØ detector. The central detector and calorimeter are cylindrically symmetric in design; the surrounding muon system was designed with a simpler box–like structure (Figure 2.7). Discussion of detector components requires definition of coordinate systems. For convenience of reference, a full discussion of all DØ coordinate systems is provided in Appendix A.

The detector volume closest to the beampipe measures the position of collision products non–destructively. This central tracking region exploits two effects: ionization and transition radiation. The drift chambers collect ionization electrons liberated when charged particles pass through the active medium. The energy lost through ionization represents a very small fraction of the total energy of a relativistic particle. The transition radiation detectors measure X–rays produced when very relativistic charged particles cross the boundary between materials with different dielectric constants. The tracking detectors are collectively called the Central Detector (CD).

Surrounding the CD, the calorimeter is designed to measure particles destructively. Particle energies are successively absorbed and remeasured by alternating layers of inert and active material. Because of size constraints, optimization of this sampling technique requires very dense absorbing materials, specifically radiation–depleted uranium, copper, and stainless steel. The active ionization medium, liquid argon, requires well–insulated cryostats. Bremsstrahlung and subsequent pair production, which occur when a particle traverses the absorber plates, create showers of particles in the calorimeter. These processes may proceed electromagnetically, via the usual Coulomb mechanism with photons and e^+e^- pairs, or hadronically, via the strong force with gluons that subsequently hadronize.

The outermost sections of the detector identify and measure muons. Because muons do not interact via the strong force, have low photon bremsstrahlung probability, and (at relativistic speeds) do not decay within the distance scale of the detector ($c\tau = 650$ m), these particles do not suffer significant energy loss in the calorimeter. Three layers of proportional drift tube chambers measure muon position. Toroidal magnets between the first and second layer induce a bend in muon trajectory, providing a method of measuring muon momentum.

A layer of scintillating material placed above the detector differentiates $p\bar{p}$ collisions from cosmic ray activity. Additional scintillators placed between the calorimeter cryostats increase instrumentation in the seams.

The following sections describe the detector subsystems in more detail, providing a first–principles description of the way in which they work. Reference [14] is an excellent
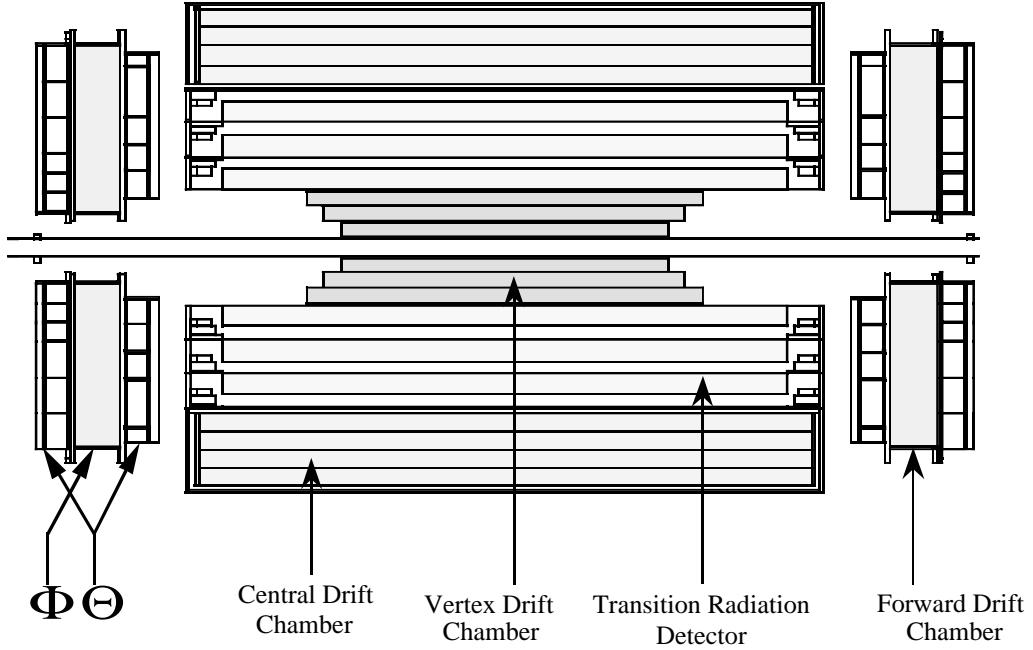
Figure 2.8: Side view of the central tracking system. The CD is composed of a transition radiation detector and several drift chambers.

supplemental resource for the interested reader.

2.2.1 The Central Detector (CD)

Completely enclosed by the Calorimeter, the CD occupies a volume bounded by 3.7 cm $<$ $r <$ 78 cm and $|z| <$ 135 cm (Figure 2.8). The Vertex Detector, the innermost subsystem, was designed to resolve tracks to 50 μm. The Central and Forward Drift Chambers have a resolving power of $150 - 200$ μm. The subsystems in the CD were designed to non–destructively measure particle positions.

The Vertex Detector (VTX)

The Vertex Detector provides fine vertex position resolution. The VTX consists of three concentric cylindrical drift chambers, holding arrays of sense wires parallel to the beampipe. The sense wires operate at an electrical potential of +2.5 kV. CO_2 doped [15] with 5% ethane and 0.5% H_2O functions as the active medium. Drawn to the sense wires, ionization
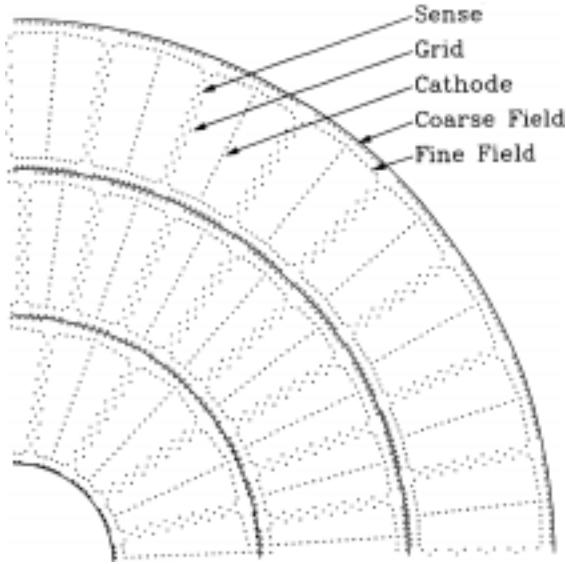
Figure 2.9: An r–ϕ view of the VTX chambers, revealing sense wire configuration.

electrons provide $r - \phi$ information with their non–zero drift times, while their z positions are determined using a charge division technique using pulse measurements from each end of the sense wire. Because the electric field in the cells is strong enough to cause electron cascades, no information can be gained from the magnitude of the collected charge.

The innermost layer of the VTX employs 16 cells in azimuth and the other two layers have 32 cells. The information from each cell inherently contains a left–right ambiguity; thus, from one layer to the next, the cell positions are staggered in ϕ to improve resolution and avoid uninstrumented regions (Figure 2.9).

The Transition Radiation Detector (TRD)

Although ionization electrons are liberated in the active medium, the TRD was designed to collect electron pairs produced by transition X–rays. As a heuristic illustration, consider a charged particle approaching a dielectric boundary. The image charge approaches the interface from the opposite side, forming an electric dipole. When the particle crosses the dielectric boundary, the image charge crosses in the other direction and the dipole has oscillated. For ultra–relativistic particles, this strong dipole oscillation results in a radiated

CROSS–SECTION OF TRD LAYER 1

OUTER CHAMBER SHELL

70μm GRID WIRE

ALUMINIZED MYLAR

8mm

65mm

2mm   15mm

2π/256

2mm   4mm

RADIATOR STACK

N₂

CONVERSION
STAGE

30μm ANODE WIRE

100μm POTENTIAL WIRE

23μm MYLAR WINDOWS

HELICAL CATHODE STRIPS
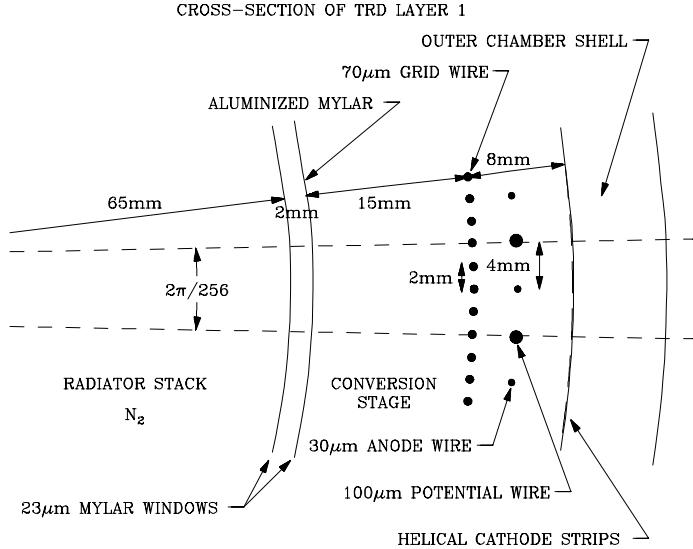
Figure 2.10: Detail of the Transition Radiation Detector. Transition X-rays typically produce electron pairs in the first few millimeters of the conversion gap.

X–ray with energy proportional [16] to the relativistic γ of the particle, allowing the TRD to differentiate particles by their masses. The TRD is primarily used to distinguish electrons from pions.

The energy spectrum of the X–rays is also dependent on the number and thickness of the radiating foils. At DØ, the radiator section of each TRD unit consists of 393 foils of 18 μm thick polypropylene suspended in nitrogen gas. 150 μm gaps were created between the foils by embossing a mesh pattern onto each before wrapping them all into a cylinder. The radiators and nitrogen gas are sealed within a mylar "window" and surrounded by an array of sense wires suspended in an active medium of [17] Xenon doped with 7% CH_4 and 2% C_2H_6. This pattern (Figure 2.10) is repeated for each of the three concentric layers of the TRD.

Central Drift Chamber (CDC) and Forward Drift Chambers (FDC)

Four layers of structurally independent drift chambers comprise the CDC. Each layer consists of 32 ϕ segments and is offset by one half cell from the previous layer (Figure 2.11).
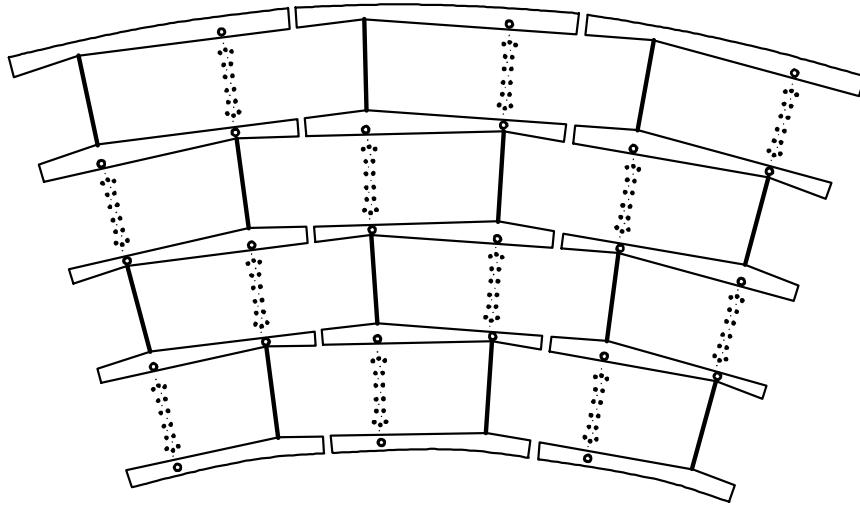
Figure 2.11: Central Drift Chamber detail. Sense wires, ground wires, and delay lines are strung into and out of the plane of the image.

Each segment contains seven sense wires (the small wires in the figure) with two grounded potential wires between them. Two delay lines lie inside the inner and outer cell walls. Charge accumulated on the inner– and outer–most sense wires induces a charge on the delay lines as well. Time measurement of the delay lines at both ends determines the z position of the ionized track. An extra ground wire at the inner and outer positions ensures induced charges originate only from the extreme sense wires. The CDC uses [17] argon doped with $CH_4(4\%)$, $CO_2(3\%)$, and $H_2O(0.5\%)$ as the active medium.

The Forward Drift Chambers measure θ and ϕ position of charged tracks via delay lines (Figure 2.12) much like the CDC. The cells of each module contain 16 sense wires and uses the same active medium as the CDC. The first and third layers of the FDC measure the θ position of particle trajectories, while the second layer measure the ϕ position. Because the θ–layers are four–fold symmetric, a 45° angle between them maximizes the position resolution of the FDC.
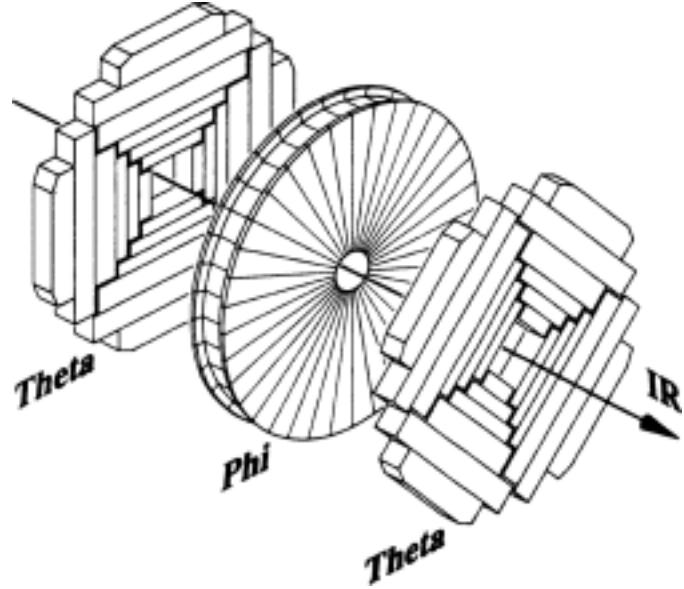
Figure 2.12: Exploded view of the Forward Drift Chamber modules. Interior construction is similar to the CDC.

2.2.2 The Calorimeter

In the parlance of chemistry, a calorimeter is a well–insulated device that measures the energy stored within foods. By completely capturing all the heat energy released from burning compounds, the calorimeter precisely measures the stored chemical energy. Analogously in high energy physics, a calorimeter precisely measures the energy released in particle interactions by completely containing all product particles (except muons, neutrinos, and particles that escape down the beampipe).The DØ calorimeter (Figure 2.13) consists of many dense layers of material, interspaced with layers of ionization medium. The physics of the calorimeter is most easily described in terms of *radiation lengths* and *nuclear interaction lengths* for electromagnetic and hadronic particles, respectively. These quantities, X_0 and λ, describe the energy loss of a particle versus distance according to

$$E(d) = E_0 e^{-\frac{d}{X_0}} \text{ and} \tag{2.3a}$$

$$E(d) = E_0 e^{-\frac{d}{\lambda}}. \tag{2.3b}$$

44

DØ LIQUID ARGON CALORIMETER

END CALORIMETER

Outer Hadronic
(Coarse)

Middle Hadronic
(Fine & Coarse)

**CENTRAL
CALORIMETER**

Electromagnetic
Fine Hadronic

Inner Hadronic
(Fine & Coarse)

Coarse Hadronic

Electromagnetic

1m
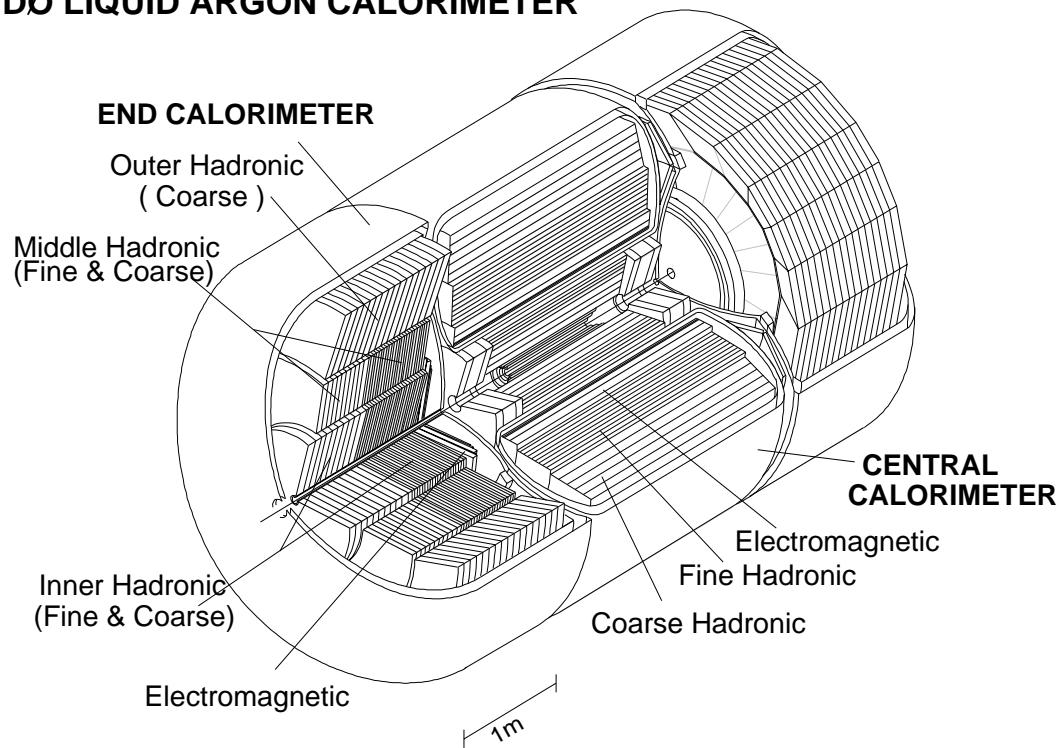
Figure 2.13: The DØ calorimeter, consisting of three modules (two endcalorimeters and a central calorimeter). Each module is divided into electromagnetic and hadronic sections.
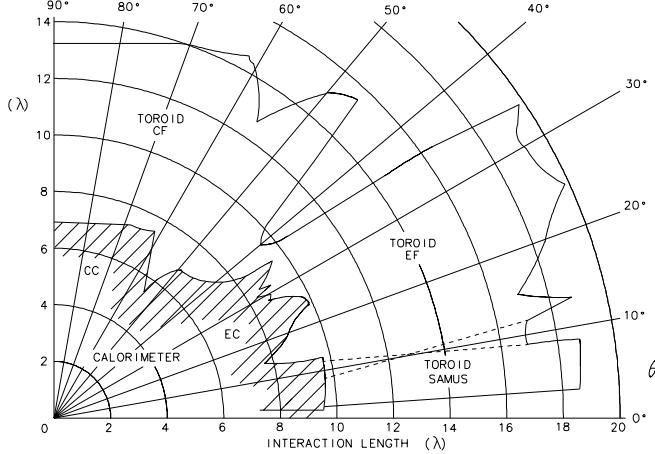
Figure 2.14: Thickness of the DØ detector as a function of colatitude, expressed in number of nuclear interaction lengths of material.

Radiation length, defined as the free path for emitting bremsstrahlung radiation, depends on the Compton wavelength of the particle and therefore on the inverse square of the particle mass. Because they are 200 times heavier than electrons, muons do not suffer significant Compton losses while passing through the calorimeter; instead, they escape easily, leaving only a minimum ionization trail. Neutrinos, interacting only through the weak force, also escape. In contrast, all electrons passing through the calorimeter will produce copious electromagnetic showers. For electrons, radiation length may be parameterized [16] in terms of atomic mass (A) and atomic number (Z), yielding

$$X_0 \sim 180 \frac{A}{Z^2}. \tag{2.4}$$

This rough 1/Z dependence justifies the use of depleted uranium ($X_0 \approx 3.2$ mm) as an absorbing material in the EM section of the calorimeter.

The nuclear interaction length scales as $A^{\frac{1}{3}}$, reducing the advantage of exotic high–density materials for hadronic measurements. In gluon bremsstrahlung, pions are the most copiously produced secondaries because they are the lightest hadronic particles. Given equal probability to produce π^0, π^+, π^-, the products should be $\frac{1}{3}$ neutral and $\frac{2}{3}$ charged. The neutral pions quickly convert to two photons, which cascade electromagnetically. The

charged pions continue through the calorimeter, producing more hadronic products, roughly one third of which [16] are neutral pions. This process continues until the energy of the charged products becomes insufficient to pass through the absorbing material into the next active region. Except for the ionization energy deposited by the charged hadrons, only the neutral portions of the hadronic shower are measured (because they result in an electromagnetic shower). As a result of fluctuations in π^0 production relative to charged pions (particularly in the first inelastic interaction), the energy measurement of hadronic particles has a much larger inherent uncertainty than that of purely electromagnetic particles.

Additionally, a sizeable amount of the available energy in a hadronic shower is lost to binding energy effects in the absorber plates. Energy expended to excite or break nuclei apart in the absorbing material normally will not result in detectable energy. In most materials, a small fraction of the energy is recovered when nuclei de–excite, but the resulting slow neutron or photon may not be measured [16] until a later beam crossing. With uranium 238 as the absorber, it was thought that energy normally lost to nuclear effects would instead yield neutron–induced fission products with their own signal in the calorimeter; then, the resulting measured energy from the hadronic fraction of a shower would more closely match the energy from the electromagnetic portion. Unfortunately, the expected fission products materialized only in small numbers. The response was instead balanced by varying the thicknesses of the absorbing plates and the active regions between them. Usually expressed as the *response ratio*, the DØ calorimeter value of

$$\frac{R_{electrons}}{R_{hadrons}} \approx 1.1 \tag{2.5}$$

compares favorably [18] to the ratio of 1.4 for most other calorimeters. The small compensation effect due to nuclear fission and the graduated thickness of the plate and gap layers partially offsets the damage caused by neutral pion fluctuations. The stochastic nature of pion production and the residual binding energy effects result in a loss of *energy resolution*, to be discussed further in Chapter 5 in the context of its effect on the jet cross section.

Collision products from a p$\bar{\text{p}}$ interaction are contained within 20 radiation lengths (X$_0$)

of material followed by 7.2 nuclear interaction lengths (λ) of material (Figure 2.14); in this sense, the calorimeter is very "well–insulated," allowing less than 2% of all collision energy to escape. The scales of the electromagnetic (X_0) and hadronic (λ) interactions are quite different; the 20 radiation length thickness of the EM calorimeter constitutes roughly half of a nuclear interaction length.

The DØ calorimeter was assembled in three pieces: a cylindrical central piece (the CC) and two end caps (north EC and south EC), as shown in Figure 2.13. Each section is divided into a large number of cells that are identified by location in azimuth, pseudorapidity, and layer (roughly, the distance from the vertex). There are 64 divisions in ϕ and 80 divisions in the pseudorapidity region $-4.0 < \eta < 4.0$; thus, each cell covers an area in $\eta - \phi$ of approximately 0.1×0.1, with exceptions described in the following sections. Seventeen unique layers in the calorimeter vary in thickness depending on the specific purpose of the layer (electromagnetic particle detection or hadronic particle detection). A *sampling calorimeter* by design, each layer consists of a dense absorption plate followed by a liquid argon gap (Figure 2.15). During operation, copper readout pads, in the center of each gap and 2.3 mm from the absorber plates on each side, are held at a potential of 2 kV while the absorber plates are grounded. Drift time for ionization electrons across the gap is 450 ns.

The calorimeter was designed with a pseudo–projective geometry; cells are aligned so their centers are arranged radially with respect to the interaction vertex, forming towers of cells with identical positions in η and ϕ (Figure 2.16). By design, the seams between the CC and EC's cut across these towers rather than parallel with them to prevent uninstrumented regions. The full instrumentation of the DØ detector between $-4.0 < \eta < 4.0$ is sometimes referred to as hermetic coverage. Although the material composition of the Central and End Calorimeters differs slightly, the performance of the calorimeters is equivalent.

To accommodate the DØ detector, the Main Ring, normally within two feet of the Tevatron, arcs upward several meters. While the Main Ring overpass clears the central tracking region, the pipe actually travels *through* the calorimeter, near the top (visible in Figure 2.16). Activity in the Main Ring often interferes with normal operation of the outermost hadronic
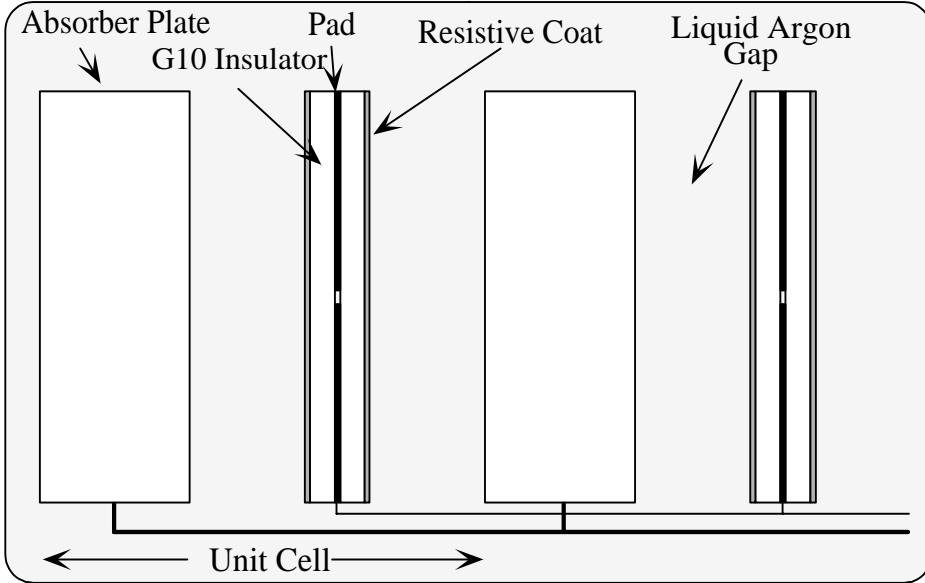
Figure 2.15: Two unit cells of the DØ calorimeter.

layer of the calorimeter, requiring special treatment during data analysis.

The following subsections detail the individual subsystems of the calorimeter, with concise summaries in tabular form. The information in the tables (which originates primarily from [19]) includes dimensions, segmentation, sampling weights, and the number of readout channels for each subsystem.

Central Calorimeter (CC)

The Central Calorimeter is coaxially subdivided into the electromagnetic (EM) layers, several fine hadronic (FH) layers, and a coarse hadronic (CH) layer (*cf* Figure 2.16). Because maximum EM shower development occurs after 10 radiation lengths of material, the third electromagnetic layer is more finely segmented than all others, increasing accuracy in the measurement of shower location and shape.

End Calorimeter (EC)

The structure of the End Calorimeter differs slightly from the CC. The EM portion extends radially [20] from 5.7 cm to 104 cm. The Inner Hadronic module, placed behind (larger
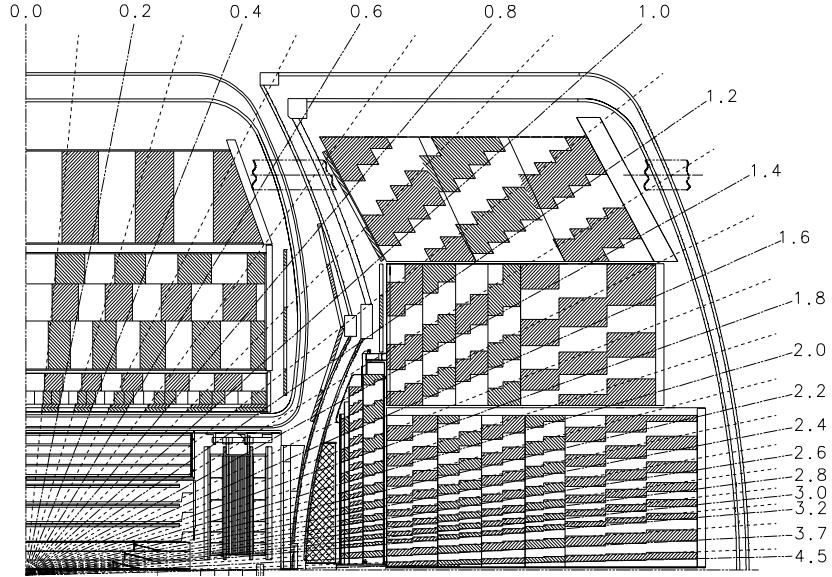
Figure 2.16: One–quarter η–view of the calorimeter and Central Detector, illustrating the pseudoprojective tower geometry. Radial lines indicate detector pseudorapidity. The Inter–Cryostat Detectors are visible as thin tiles between $0.8 < \eta < 1.2$. The Main Ring beampipe pierces the calorimeter near the top.

CC Module	EM	FH	CH
Rapidity Range ($|\eta| \leq$)	1.2	1.0	0.6
Absorbing Material	Uranium	Uranium (1.7% Nb)	Copper
Absorber Plate Thickness	2.3 mm	2.3 mm	46.5 mm
Total Depth (X_0)	20.5	96	32.9
Total Depth (λ)	0.76	3.2	3.2
Number of Layers	4	3	1
Depth per Layer	2, 2, 7, 10 X_0	1.3, 1.0, 0.9 λ	3.2 λ
Segmentation	0.1×0.1 (Layers 1, 2, 4) 0.5×0.5 (Layer 3)	0.1×0.1	0.1×0.1
Sampling Fraction	11.79%	6.79%	1.45%
Channels	10,368	3,000	1,224

Table 2.1: Parameters for the Central Calorimeter.

EC Module	EM	Inner FH	Inner CH
Rapidity Range	$\pm\|1.3-3.7\|$	$\pm\|1.6-4.5\|$	$\pm\|2.0-4.5\|$
Absorbing Material	Uranium	Uranium (1.7% Nb)	Steel
Absorber Thickness	4.0 mm	6.0 mm	6.0 mm
Total Depth (X_0)	20.5	121.8	32.8
Total Depth (λ)	0.95	4.9	3.6
Number of Layers	4	4	1
Segmentation for $\|\eta\| < 2.6$	0.1×0.1 (Layers 1, 2, 4) 0.5×0.5 (Layer 3)	0.1×0.1	0.1×0.1
for $2.6 < \|\eta\| < 3.2$	0.1×0.1 (all Layers)	0.1×0.1	0.1×0.1
for $\|\eta\| > 3.2$	0.2×0.2 or more	0.2×0.2 or more	0.2×0.2 or more
Sampling Fraction	11.9%	5.7%	1.5%
Channels	7,488	5,216	

Table 2.2: Parameters for the EM and Inner End Calorimeter modules.

EC Module	Middle FH	Middle CH	Outer CH
Rapidity Range	$\pm\|1.0-1.7\|$	$\pm\|1.3-1.9\|$	$\pm\|0.7-1.4\|$
Absorbing Material	Uranium (1.7% Nb)	Steel	Steel
Absorber Plate Thickness	6.0 mm	46.5 mm	46.5 mm
Total Depth (X_0)	115.5	37.9	65.1
Total Depth (λ)	4.0	4.1	7.0
Number of Layers	4	1	3
Segmentation	0.1×0.1	0.1×0.1	0.1×0.1
Sampling Fraction	6.7%	1.6%	1.6%
Channels	1,856		960

Table 2.3: Parameters for the Middle and Outer End Calorimeter modules.

z) the EM module, consists of four FH layers and one CH layer. Surrounding the Inner Hadronic module coaxially, the Middle Hadronic module also consists of four FH layers and a CH layer. The Outer Hadronic module in turn surrounds the Middle section; it possesses only coarse hadronic layers and was designed with angled cells with respect to the beam axis to improve η coverage (*cf* Figure 2.16).

Because the physical size of a 0.1×0.1 cell goes to zero as the cell's pseudorapidity location approaches infinity, the segmentation of all End Calorimeter cells changes near the beampipe. The parameters of the End Calorimeters are summarized in Tables 2.2 and 2.3.

Inter–Cryostat Region (ICR)

The pseudorapidity region between 0.8 and 1.4 suffers from depleted instrumentation because this volume is occupied by the insulating bulkheads of the calorimeters, the module endplates, and necessary support structures. To improve sensitivity in this region, two independent systems were installed: the Inter–Cryostat Detector (ICD) and the Massless Gap detectors (MG). Although these systems cannot replace the full sampling modules present in other areas, they prevent the ICR from becoming "dead space."

The ICD, visible between the two bulkheads in Figure 2.16, consists of two annular scintillating tile arrays mounted on the outer EC walls. Grooves cut into each scintillating tile (of dimension 0.1×0.1 in $\eta - \phi$) guide wavelength–shifting optic fibers that channel the scintillation photons to photomultiplier tubes (PMT's) for readout. The tile arrays, symmetric in ϕ, cover the entire rapidity range from 0.8 to 1.4.

The MG detectors, mounted on the inside bulkhead surface of both the CC and EC cryostats, supplement the ICD coverage (again, Figure 2.16). Identical to the readout pads in the standard calorimeter modules, the copper MG readout boards collect electrons liberated from the liquid argon medium. Unlike the calorimeter cells, the absorber plates are absent.

2.2.3 The Muon Spectrometer

Three layers of proportional drift tube chambers (PDT's) surround the calorimeter, comprising the Muon Spectrometer. The innermost rack, the A layer, consists of four decks of PDT surrounded by toroidal magnets. The iron toroids, carrying a magnetic field strength of 2 Tesla, induce a bend in muon trajectory. Two additional PDT layers, B and C, measure the muon direction after the bend. The initial vector, formed with the vertex and A layer hits, combined with the final vector, formed with the B and C layer hits, determines the muon momentum. Detection of a minimum ionization trace in the calorimeter can confirm the presence of a muon. Timing information from the layer of scintillator above the detector can reject spurious hits caused by cosmic ray showers.
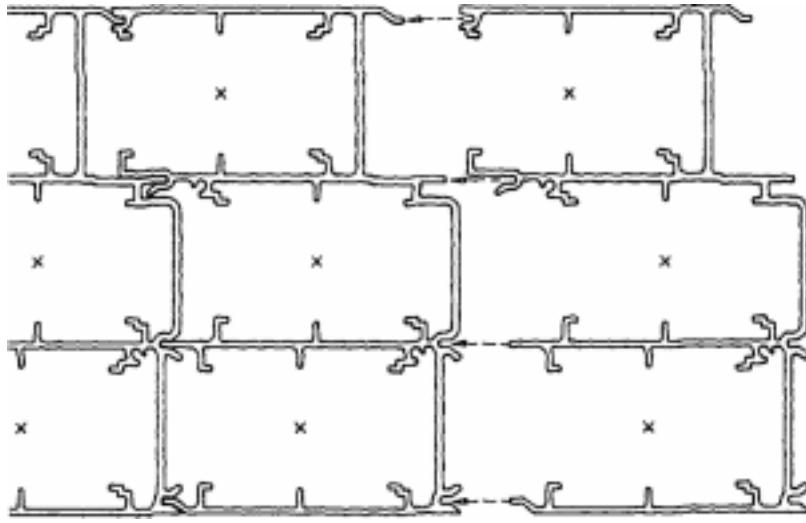
Figure 2.17: Muon chamber detail of the B layer. The C layer is identical but the A layer has four decks instead of three.

2.2.4 Level Ø

A scintillating hodoscope array was placed between each end calorimeter and the central calorimeter, approximately [24] 140 cm from the center of the detector and perpendicular to the beam axis. In this forward position, the arrays intercept most collision products. The tiled construction provides nearly full coverage in the pseudorapidity range $2.2 < |\eta| < 3.9$ and partial η–coverage as low as 1.9 and as high as 4.3. With very high efficiency, these hodoscopes identify inelastic $p\overline{p}$ collisions when both arrays detect charged particles within a small time interval. Because inelastic collisions comprise the majority of the events DØ studies, the hits in coincidence within the hodoscopes are a prerequisite for physics triggers (as described in Chapter 3). The hardware and software triggers are respectively named Level 1 and Level 2, so the twin hodoscopes are called Level Ø.

By monitoring the interaction rate, the Level Ø system also provides a measure of the instantaneous particle luminosity ($\mathcal{L}$) within the Tevatron. Additionally, the hodoscopes measure the rate at which spurious particles escape from the beam (such particles are called "beam halo"). Details of the luminosity calculation are provided in Chapter 5, along
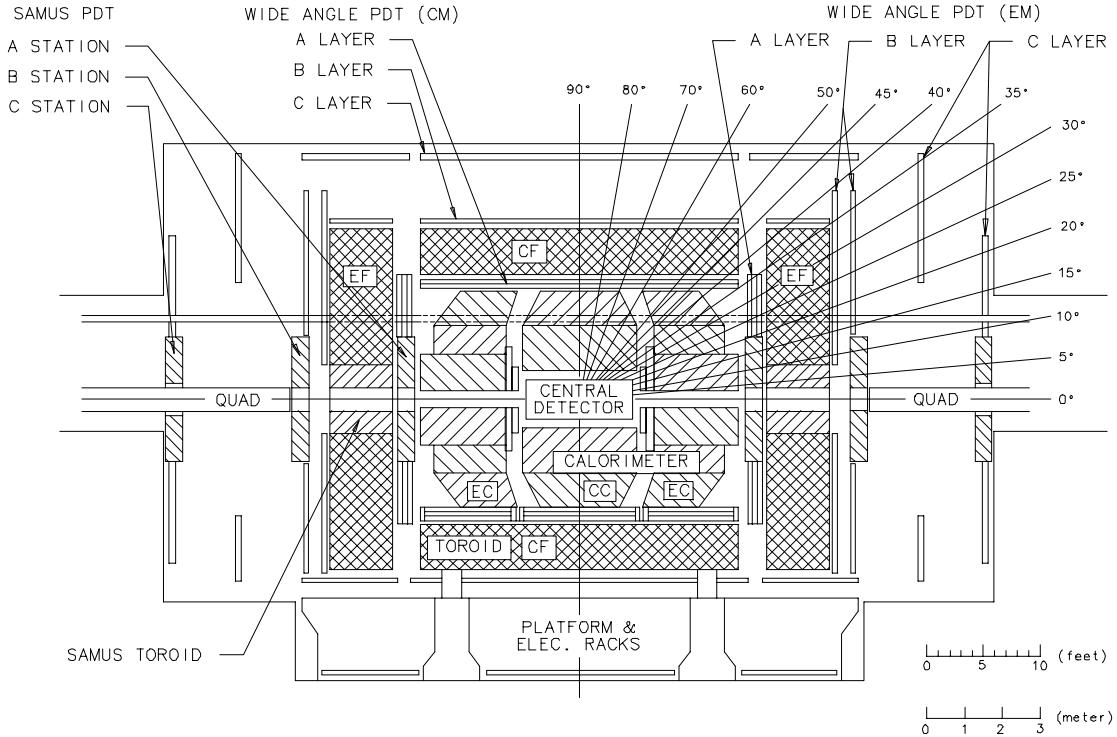
Figure 2.18: The DØ detector, showing the placement of the Central Detector, the Calorimeter, the Muon Detector layers (A, B, and C), and the iron toroids (CF and EF).

with discussion of beam quality issues.

2.2.5 Detector Summary

The detector systems measure particle energies in different ways. Ionization products, liberated primarily through elastic scattering with atomic electrons, are collected onto sense wires. Transition photons convert to e^+e^- pairs and are collected with a proportional wire chamber. Absorbing plates in the calorimeter initiate showers of electrons. Scintillating materials become excited by charged particles and emit photons which are subsequently measured in photomultiplier tubes. Working in concert, the disparate systems comprise a very versatile general purpose detector, capable of:

- Excellent identification and measurement of electrons and muons,
- Good measurement of jets with large E_T using highly segmented calorimetry and good energy resolution,

54

- Detection of neutrinos (and other non–interacting particles) via [14] missing E_T measurement.

The fully assembled detector (Figure 2.18) stands approximately 13 m in height and 20 m in length. The total weight of the system is approximately 5500 tons. Two hydraulic rams push the entire structure between assembly area and collision hall along hardened steel tracks; the detector reaches a top speed of two inches per hour. Cooling the calorimeter cryostats to operating temperature (78 K) requires approximately 10 days.

Chapter 3

Data Collection

*"Divide each difficulty into as many parts as is
feasible and necessary to resolve it."*

— Rene Descartes

With every Tevatron bunch crossing inside the DØ detector, signals are sent to an array
of digital logic circuits. Consisting of logical AND/OR gates, these logic boards quickly
analyze the information of each beam crossing, searching for *events* that satisfy preset
criteria. The parameters of the events that pass the requirements are sent to one of many
VAX workstations, where a software search algorithm applies additional constraints to each
event. Any event that meets or exceeds the final requirements is written to tape. The set
of hardware and software event criteria is known as a *trigger list*.

During a collider run, the DØ detector collects data almost continuously. A crew of
five physicists mans the control room 24 hours per day, seven days per week. While the
Tevatron collides protons and antiprotons, the physicist in charge of data acquisition (the
DAQ shifter) loads predetermined trigger lists, monitors the hardware and software of the
DAQ system, and follows the flow of data from the detector to disk to tape. A detector
shifter ensures that all the individual systems of the detector behave as expected, resetting
high-voltage when necessary and looking for failing components. A Fermilab operator from
the Research Division monitors the cryogenic fluids and drift gasses of the detector, easing
the load of the detector shifter. The global monitor, sometimes called the "last line of
defense," studies selected events in detail, looking for any hint of detector malfunction.

55

Finally, a shift captain determines when trigger lists must change, when special runs should occur, and acts as liaison between the experiment and Fermilab personnel. Even when the Tevatron is idle, the crew collects data from cosmic rays to recalibrate the detector or test new trigger lists. Other times, small maintenance tasks are performed. In the absence of unusual failures, an eight-hour shift can be quite uneventful; when things go wrong, the crew may not be enough. For this reason, one designated expert for each detector system always remains on call.

The data collection process is entirely dependent on the trigger list in use. Because the bandwidth (the rate at which events may be written to tape) is limited, the DØ collaboration must decide the composition of the trigger list well in advance of the actual run. A typical list selects a mixture of several classes of event; including events with high E_T jets, photons, electrons, or muons, events with large missing E_T, or events with high multiplicity of jets. Selection is performed in several stages, designated Level Ø, Level 1, and Level 2. The raw event rate of nearly 300 kHz must be successively decreased after each stage, finally meeting the bandwidth limit after Level 2 (approximately 2-10 events per second). A good trigger must therefore identify and accept a particular class of event and yet reject enough background events to yield an acceptable event rate. Trigger experts design the lists with an eye for balance between the many physics processes worthy of study.

Despite data buffers between the trigger levels, occasionally a combination of high luminosity and loose trigger criteria results in more accepted events per second than the system's bandwidth can handle. When the bottleneck in the system occurs in the Level 1 stage the condition is termed *front-end busy*. If the bottleneck occurs in Level 2, the condition is called *Level 2 disable.* Both cases result in discarded events. Activity in the Main Ring will veto many beam crossings as well, resulting in more discarded events. The final luminosity calculations must reflect all of these conditions (collectively known as "dead time").

The next sections of this chapter review the event triggering and data acquisition process in terms of the three trigger stages. Afterward, the jet triggers used in this analysis will be described, including the number of events collected for each. The number of events may

be expressed in terms of the *luminosity exposure*, as described below. Many aspects of the triggering and data acquisition process have direct consequences in the data analysis stage. Full discussion of some details must therefore be reserved for Chapter 5.

3.1 The Level Ø Trigger

The scintillating hodoscope arrays discussed in Chapter 2 serve as the prerequisite to the majority of DØ's data triggers and from this use they take their name. Final state particles from spectator partons in a p$\bar{\text{p}}$ collision tend to have low–angle trajectories. The scintillating tiles are placed near the beampipe to intercept these collision products with high probability. If both arrays detect particles within a small time window, most likely a p$\bar{\text{p}}$ collision has occurred; thus, Level Ø passes the event to the Level 1 trigger system. During the run, a small subset of the DØ trigger list bypassed the Level Ø requirement entirely, automatically passing each beam crossing to Level 1. Data without the Level Ø requirement plays a crucial role in studies of trigger behavior. Additionally, some special triggers collect diffractive events that have low probability of meeting the Level Ø requirement (see also Chapter 5 for details of diffractive cross sections and Level Ø).

If all triggers lacked the Level Ø requirement, the event rate into Level 1 would be equal to the beam crossing rate, 286 kHz. With Level Ø, the rate is reduced to approximately 17 kHz for luminosities typical of the low energy run $\left(\mathcal{L} = 0.5 \times 10^{30} \frac{beam\ crossings}{cm^2 \cdot sec} \right)$, a much more manageable level.

3.2 The Level 1 Trigger

Consisting of hardware logic circuits, the Level 1 trigger system quickly filters the data stream, searching for potentially interesting physics events. Because tracking information from the central detector requires too much time to generate and analyze before the next beam crossing (3.5 μsec), Level 1 uses only calorimeter tower information and muon hit information as criteria. The calorimeter towers are ganged into 2×2 arrays, called a *trigger tower*. A jet trigger might require a trigger tower with at least 2 GeV of transverse energy

in the event. The vector sum of all trigger towers yields the missing E_T magnitude, a requirement of W boson triggers (see also Appendix C). The energy in the electromagnetic portion of a trigger tower is used to make photon and electron triggers. As a recent innovation, entire quadrants of the detector have been ganged together to form *large tiles.* Very high E_T jet triggers use large tile information rather than trigger tower information in the Level 1 decision.

Events that pass the Level 1 decision are passed to Level 2, while events that fail to meet the Level 1 requirement are discarded. A very simple muon selection is performed at Level 1, and candidates are then passed to a special sublevel dubbed Level 1.5. This system calculates muon momentum from the bend angle between the hit centroid in the muon A layer and the centroids in the muon B and C layers. Unlike the rest of the Level 1 system, Level 1.5 cannot generate tracking information within the beam crossing time, and therefore cannot make its event decision at the Level 1 rate; thus, the entire detector suffers dead time during the Level 1.5 decision process.

3.3   The Level 2 Trigger

A "farm" of 48 VAX workstation nodes comprises the Level 2 system. Working in parallel, the Level 2 nodes identify objects in an event as electrons, jets, muons, or photons, using a host of custom-designed software algorithms. All detector information contributes to the Level 2 decision, although the object reconstruction is somewhat approximate to minimize the decision time. For example, offline a jet is defined as hadronic and electromagnetic energy deposited in an $\eta - \phi$ cone with radius 0.7. For the fast online reconstruction, a jet is any calorimeter energy deposit in a 7×7 tower square.

A trigger list at Level 2 (sometimes called the "Level 2 filters" to distinguish them from the "Level 1 triggers") contains up 128 independent sets of requirements. The filter requirements could be as simple or complicated as required. For example, a jet filter might require a single jet with E_T greater than 30 GeV, while a W boson filter might require an electromagnetic cluster with E_T greater than 25 GeV with a shower shape that matches the

Trigger Name	Level 1 requirement	Level 2 requirement
Jet_12-LNR	One trigger tower with 2 GeV E_T	One jet with 12 GeV E_T
Jet_12b-LNR	Two trigger towers, each with 2 GeV E_T	One jet with 12 GeV E_T
Jet_30-LNR	One large tile with 15 GeV E_T	One jet with 30 GeV E_T

Table 3.1: Triggers used in the inclusive jet cross section analysis.

electron shape determined with a test beam, and a missing E_T greater than 25 GeV.

The trigger list downloaded from the database implicitly includes a set of *prescales*. These prescale sets manage the total output rate from Level 2 to disk. To achieve a balance between common events and rare events, the trigger system is designed to deliberately discard some fraction of otherwise acceptable events. A trigger for low E_T jet events will receive a high prescale value so the common jet events will not consume the majority of the available bandwidth. Each trigger receives a prescale roughly proportional to the total cross section for its signal relative to the most rare process on the trigger list. Because the event rate is a function of instantaneous luminosity, prescale sets are changed as Tevatron luminosity attenuates over the course of a store.

Events that pass Level 2 are written to disk in partitions of 2000 events each, where each event is approximately 500 kilobytes in size. A cluster of seven disk drives holding between two and four gigabytes each serves as a buffer area from which partitions are written to 8mm tape. These tapes are transported to the Feynman Computing Center (near site BØ) for processing and storage.

3.4 The Jet Triggers

This analysis makes use of three triggers from the low energy (630 GeV) run. Table 3.1 names each trigger and compactly specifies the Level 1 and Level 2 requirements for each. All triggers required hits in both Level Ø hodoscopes as usual. Note the simplicity of the triggers in each case. As per DØ convention, the trigger suffix indicates the class of each trigger; in this case, "LNR" indicates the low CM energy trigger set. The number designates the nominal E_T threshold above which jets are accepted.

Trigger Name	Luminosity Exposure	Number of Events
Jet_12-LNR	4.82 nb^{-1}	439,769
Jet_12b-LNR	30.4 nb^{-1}	1,673,259
Jet_30-LNR	537 nb^{-1}	179,832

Table 3.2: Total luminosity exposure of the inclusive jet triggers and the number of events collected for each.

The inclusive jet cross section, a steeply and monotonically falling function of E_T, produces a much different event rate for each trigger. This can be expressed as

$$\int_{12 \text{ GeV}}^{\infty} \frac{d\sigma_{jet}}{dE_T} dE_T \gg \int_{30 \text{ GeV}}^{\infty} \frac{d\sigma_{jet}}{dE_T} dE_T. \tag{3.1}$$

Without a prescale, the Jet_12 triggers would have a rate larger than Jet_30-LNR by several orders of magnitude. During the run, Jet_12-LNR was prescaled by as much as a factor of 630. Jet_30-LNR was never prescaled. At very low luminosities, the global event rate was low enough to run all three jet triggers without prescales.

During the low energy running, the trigger rate from Jet_12-LNR took too large a share of the bandwidth out of Level 1, only to have the majority of the events rejected by Level 2. A large prescale applied to the trigger would not afford a statistically significant number of events by the end of the run, so a new algorithm was designed to be more selective in the hardware portion of the trigger. While Jet_12b-LNR has the same Level 2 requirement as the original, the stricter Level 1 condition reduces the number of spurious events (caused by noisy calorimeter cells) passed to Level 2. The result of the modification is a sacrifice in trigger turn-on efficiency (discussed in Chapter 5).

Table 3.2 lists the luminosity *exposure* for each trigger. The luminosity exposure reflects the prescale of each trigger for each run and any deadtime caused by Main Ring activity and front-end busy conditions. Because it was never prescaled, the Jet_30-LNR exposure reflects the total luminosity collected by DØ at $\sqrt{s} = 630$ GeV.

3.5   A Selected Data Event

The event displays in this section depict actual DØ data; they all display the same three-jet event, selected from the Run 1b data set ($\sqrt{s} = 1800$ GeV). Although event displays do not contribute to the data analysis, they provide an additional level of understanding to the processes under study.

Consider Figures 3.1 and 3.2. These side and end views of the DØ calorimeter reveal a very high E_T jet with substructure in the $+x$ central region, a high E_T jet in the $-x$ central region, and a third jet in the $-x$ ICR. Jet substructure is somewhat more obvious when only the active cells are drawn, as in Figure 3.3, a three dimensional rendering of the same event. Finally, a "lego plot" of the event is displayed in Figure 3.4; the grid represents the calorimeter coordinates remapped from a cylinder to a plane. In the figure, IPHI and IETA indicate calorimeter tower coordinates multiplied by ten; IPHI, the "integer phi," spans the range 0 to 64 with each integer corresponding to a tower. Similarly, IETA ranges from -40 to 40; any given calorimeter tower is specified with two integers. The blocks in the figure indicate the jet positions and energies, both hadronic and electromagnetic components. The lego plot is the most useful display for analysis of events. Note that the z-axis in this figure is energy and not E_T.

3.6   Summary

The data acquisition system of the DØ detector consists of three distinct subsystems. The Level Ø trigger, two simple scintillating hodoscope arrays, ensures the presence of a $p\bar{p}$ interaction before other systems examine detector signals. The Level 1 trigger forms fast sums of detector signals and applies minimal criteria to achieve fast rejection of common events. Nearly full event reconstruction at Level 2 allows excellent rejection of common events and background signals through the use of complicated software criteria. Working in series, the three trigger systems reduce the event rate from nearly 300 kHz to less than 3 Hz.
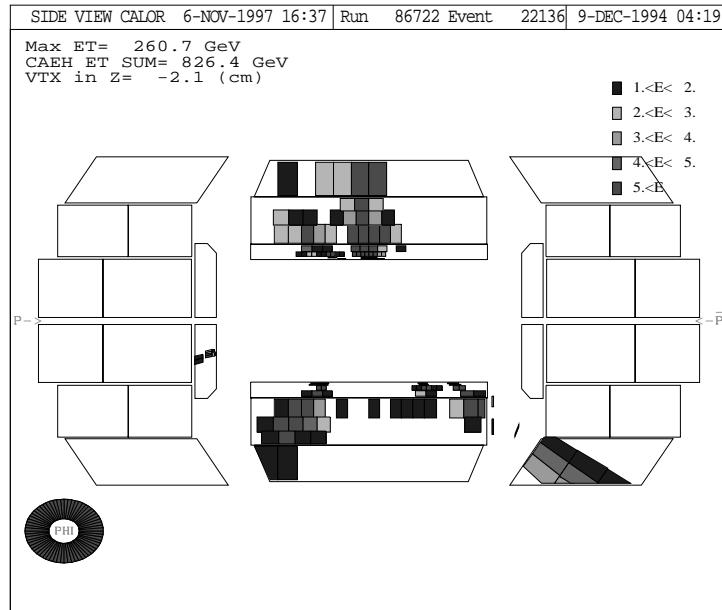
Figure 3.1: Calorimeter side view of a DØ event.
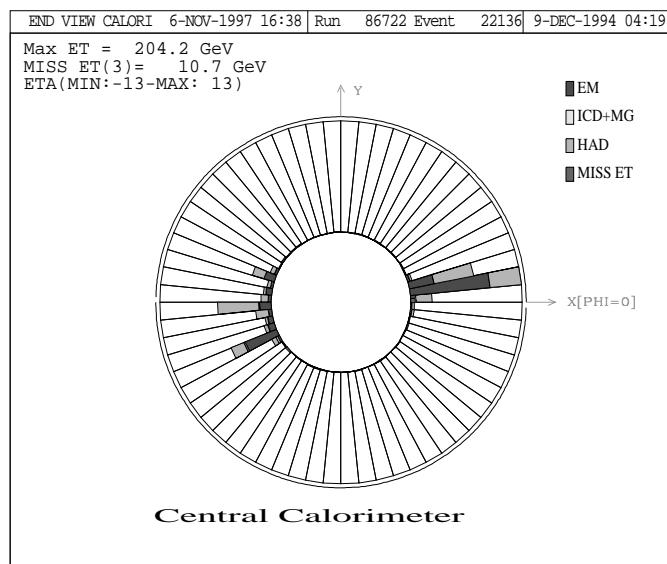
Figure 3.2: Calorimeter end view for the same DØ event.
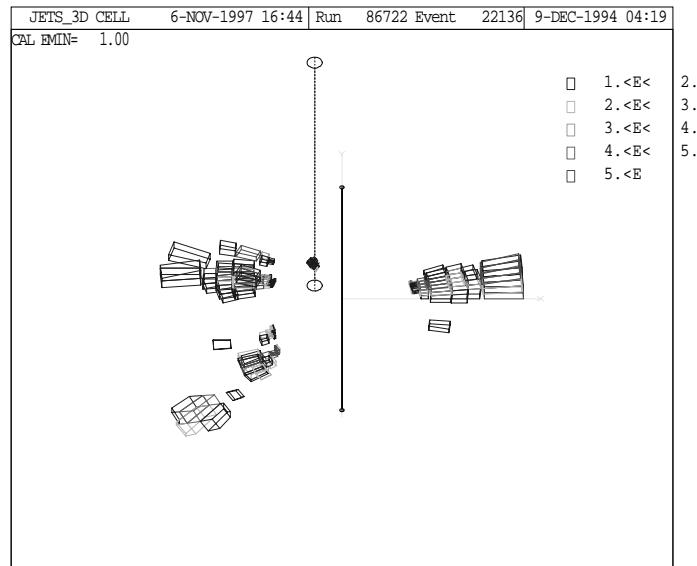
Figure 3.3: Cell-only view of the event.
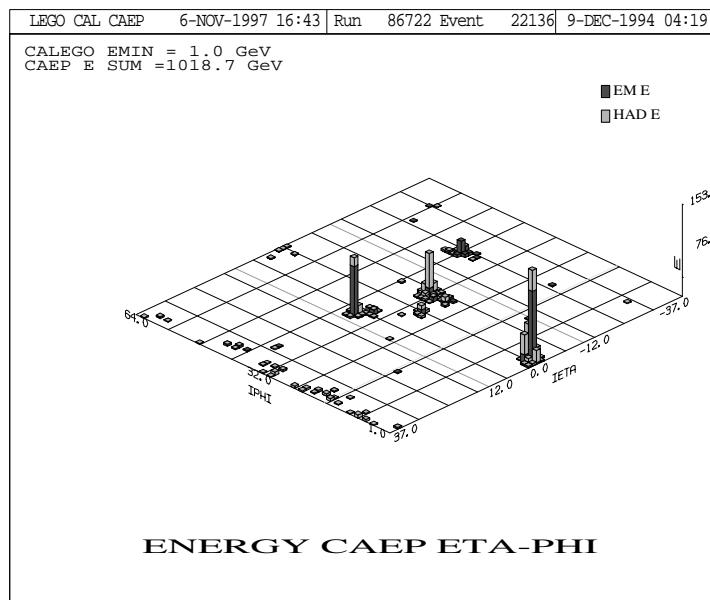
Figure 3.4: "Lego plot" of the DØ event.

Inclusive jet triggers, simple by design, consider only the E_T deposited within a well defined region. Because the probability of low E_T jet events far exceeds the probability of high E_T jet events, several jet triggers with different E_T thresholds collect data simultaneously. Each trigger has its own prescale such that the trigger rate from each is roughly comparable.

Event displays reproduce the appearance of a jet event as perceived by the DØ detector. Direct inspection of a representative sample of events ensures data quality and allows optimization of jet selection criteria, which are discussed in Chapter 5.

Chapter 4

The Jet Energy Scale

"Smooth seas do not make skillful sailors."
— African Proverb

While the DØ detector was still under construction, the collaboration tested several calorimeter modules, directing particles of known energy into the cells. This "test beam data" was used to calibrate the absolute scale of measured cell charge relative to true particle energy in the calorimeter. Several effects prevent test beam data from completely describing the *in situ* behavior of the calorimeter: off-center cell hits, pileup, underlying event energy, noise suppression, and out-of-cone showering. The algorithms in the online software and event reconstruction software sacrifice these adjustments for the sake of expedience, so additional corrections must be applied in the analysis stage.

Starting with reconstructed jet energy, E^{meas}, the corrected jet energy takes the form

$$E = \frac{E^{meas} - O}{R \cdot S},\tag{4.1}$$

where R is the overall response correction, S is the out-of-cone showering correction, and the offset O is the measured average jet energy resulting from noise and underlying events. The remainder of this chapter describes each of these corrections in detail. Although the majority of the energy scale correction is identical for both 1800 GeV and 630 GeV running, the underlying event energy differs, as described in the next section.[*]

---

[*] Major portions of this chapter were originally published as DØ Note 3288, "Jet Energy Scale at DØ for $\sqrt{s} = 630$ GeV," A.Goussiou and J.Krane, August, 1997.

Energy Distibution of Noise in a Calorimeter Cell
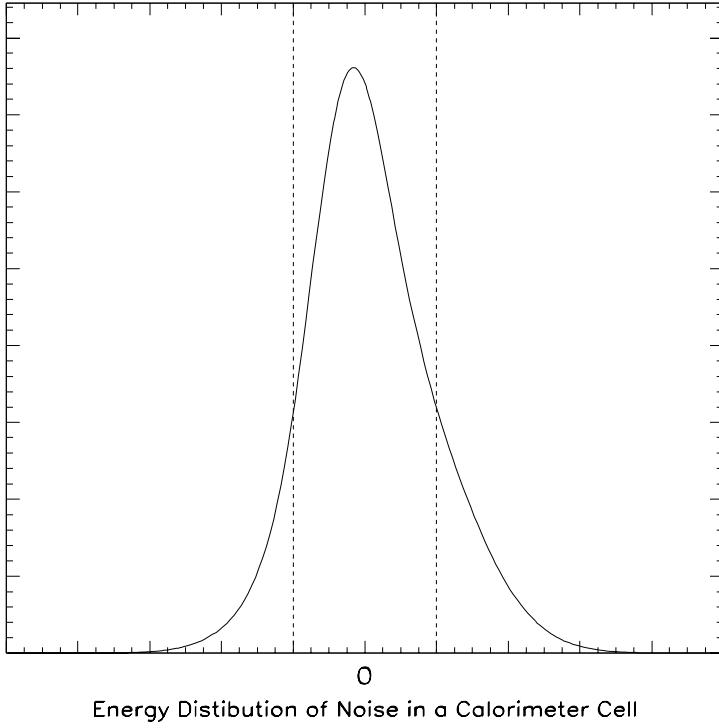
Figure 4.1: Example of a skewed Gaussian: the mean is zero despite the off–center peak. Removal of the portion between the vertical lines results in a non–zero mean for the remaining distribution.

4.1 The Offset Correction

Before scaling the reconstructed energy by multiplicative factors, the offset subtraction must compensate for effects not present in test beam data and remove energy resulting from spectator partons. The subtraction removes only the portion of a jet's measured energy which results from sources other than the final-state particles of the hard collision. Four distinct processes contribute extraneous energy to the calorimeter cells: noise, pileup, underlying event, and extra interactions.

Calorimeter noise, the first source of offset energy, results from two separate effects. *Suppression noise* results from background nuclear activity in the uranium absorber plates. To minimize the storage size and bandwidth needs of each event, the online system only considers energy deposits from calorimeter cells that are not consistent with uranium noise.

Calibration of the calorimeter sets the average uranium noise energy as the zero point for all measurements, then during data taking, the cells consistent with noise are *suppressed*, and not included in the data stream. Here, "consistent" indicates that the measured energy falls within a two standard deviation window about the average noise in a cell. Because uranium noise fluctuations do not quite follow a Gaussian distribution, the energy density outside the suppression window centered on the mean is not symmetric. As a result, unsuppressed noise fluctuations will not average to zero and noise will contribute a net positive energy to the average jet. Figure 4.1 illustrates the origin of suppression noise. Suppression noise is constant with respect to luminosity, but will vary with pseudorapidity differences in the construction of the detector. *Electronics noise* is generated in the calorimeter by the presence of the p and p̄ beams. Because calibration occurs during "quiet times" without beam, the true zero point for all measurements becomes slightly offset when the Tevatron is active.

Pileup, a second offset source, results from pp̄ interactions in previous beam crossings. The energy of each calorimeter cell is measured with a baseline subtraction scheme (BLS), in which the accumulated charge on the cell readout pad is sampled both immediately before and after a beam crossing. The *change* in charge density then maps to measured cell energy. Unfortunately, the ionization electrons in each cell have a non-zero collection time; some electrons liberated from the liquid argon during an event may linger for several beam crossings. This capacitor-like discharge effect, coupled with the BLS measurement scheme, results in a net negative energy contribution from prior events. Because the probability of a physics event during the prior beam crossing varies with luminosity, the pileup effect is both luminosity and pseudorapidity dependent.

Hadronization of spectator partons in the pp̄ collision (the *underlying event*) also contributes to the offset energy. Although the removal of underlying event energy has become a standard procedure, some theorists argue [21] that the colliding partons interact with the rest of the pp̄ system in a non-negligible manner; thus, analyses that include underlying event energy in the jet definition may contribute to theoretical understanding. In contrast,

most theorists and experimenters agree that underlying event removal extracts the primary physics from the nearly extraneous effects of the spectators. Because the fractional contribution of underlying event energy is negligible at high E_T, but may be as large as 3% at low E_T, failure to remove the additional energy will impart a shape-change to the cross section spectrum, which will be exacerbated by smearing effects (*cf* Chapter 6). Because underlying event energy was removed from the jet cross section analysis described in later chapters, the determination of its energy contribution is detailed below.

The fourth and final offset energy source, the energy resulting from additional $p\bar{p}$ interactions during a single beam crossing, exhibits a strong luminosity dependence. Multiple interactions comprise a small fraction of the 630 GeV data set, but the high instantaneous luminosity typical of 1800 GeV running resulted in a large fraction of multiple interactions in the data. The second (third, etc.) interactions do not usually result in measurably large jets; instead, smoothly distributed, low-energy particles contribute energy to jets from the primary interaction. When single interactions can be differentiated from multiple interactions, the luminosity dependence vanishes and an integer number of additional interactions results in an integer number of additional underlying events.

Although the four offset contributions are easily identified, the quantities must be extracted from measurements that involve several of the effects at once. The following subsections make use of two special data sets. "Minbias" data is collected when the Level Ø hodoscopes indicate a hard $p\bar{p}$ collision has occurred. No additional trigger criteria are applied. Very soft jets below reconstruction threshold (8 GeV) comprise the majority of this data sample. "Zerobias" data is collected during a beam crossing without regard to Level Ø information. As a result, many zerobias events consist of "empty events" where no hard collision occurred. While the DØ DAQ system primarily collected data in suppressed mode, the special data types were collected in both suppressed and unsuppressed modes at various instantaneous luminosities.

Experimenters at DØ developed several software algorithms to distinguish multiple inter-
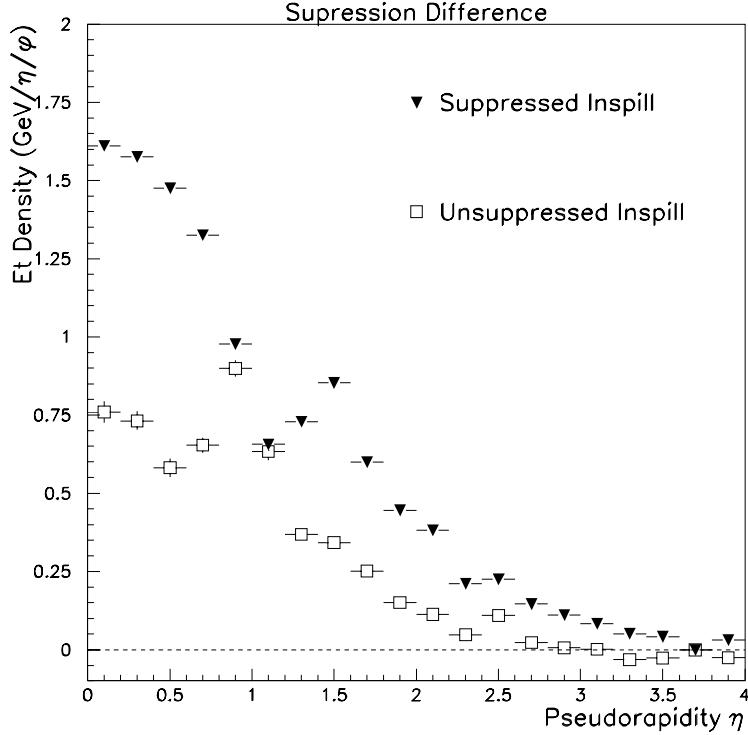
Figure 4.2: Difference in E_T density between suppressed and unsuppressed data.

actions from single interactions. These so-called MI_TOOL algorithms*use vertex, tracking, and calorimeter information to flag multiple interactions, with an efficiency [22] approaching 95%. The offset calculations exploit these tools to derive the extra interaction correction, verify the underlying event result, and further restrict events for the remaining corrections.

4.1.1 Suppression Noise

Residual energy resulting from incomplete noise suppression is most easily modelled with zerobias data. In the limit of zero instantaneous luminosity, the probability of a hard interaction during a beam crossing approaches zero and the effect of pileup becomes negligible. The following requirements ensure each zerobias event under study reflects only the effects of suppression noise:

- No hits in the Level Ø hodoscopes

---

* Two software routines exist, one for each center-of-momentum energy:
MULTIPLE_INTERACTION_TOOL_RUN1.FOR, and MULTIPLE_INTERACTION_TOOL_630.FOR.

- No jets in the event
- No main ring activity
- MI_TOOL indicates zero interactions
- Lowest instantaneous luminosity available

Figure 4.2 depicts the E_T distribution in "empty" beam crossings versus pseudorapidity. The upper curve (filled triangles) represents both electronics noise and suppression noise contributions, while the lower curve (unfilled squares) lacks suppression noise effects. Lack of uranium absorber plates in the ICR result in low levels of suppression noise between pseudorapidity values of 0.8 and 1.2.

Calibration ensures that cells with "real" energy deposits from particles have nearly zero noise contribution on average; thus, the magnitude of the suppression noise correction is a function of the number of cells without energy deposits from particles. Comparison of the number of struck cells in zerobias data to the number in jet data (Figure 4.3) indicates that the cell *occupancy* describes the difference in suppression noise with:

$$\text{Sup } E_T^{Jets} = \text{Sup } E_T^{zerobias} \times \frac{Occ^{zerobias}}{Occ^{Jets}} \tag{4.2}$$

Absolute confirmation of the occupancy model in Equation 4.2 is complicated by the large statistical scatter of the jet data, resulting in a 250 MeV uncertainty to the suppression noise calculation. This uncertainty dominates the error on the entire offset correction.

4.1.2   Underlying Event

Because minbias events primarily consist of below-threshold jets, they satisfactorily model the underlying event in physics data. Subtracting the empty crossing noise (from zerobias data) reveals the underlying event distribution.

In the limit of very low instantaneous luminosity, the distribution will accurately reflect the average energy distribution resulting from spectator partons in the proton and antiproton. Multiple interactions occur with higher frequency at high luminosity, and would contribute to the observed energy. To verify the accuracy of the underlying event result, MI_TOOL differentiates single and double interactions in minbias data. The underlying
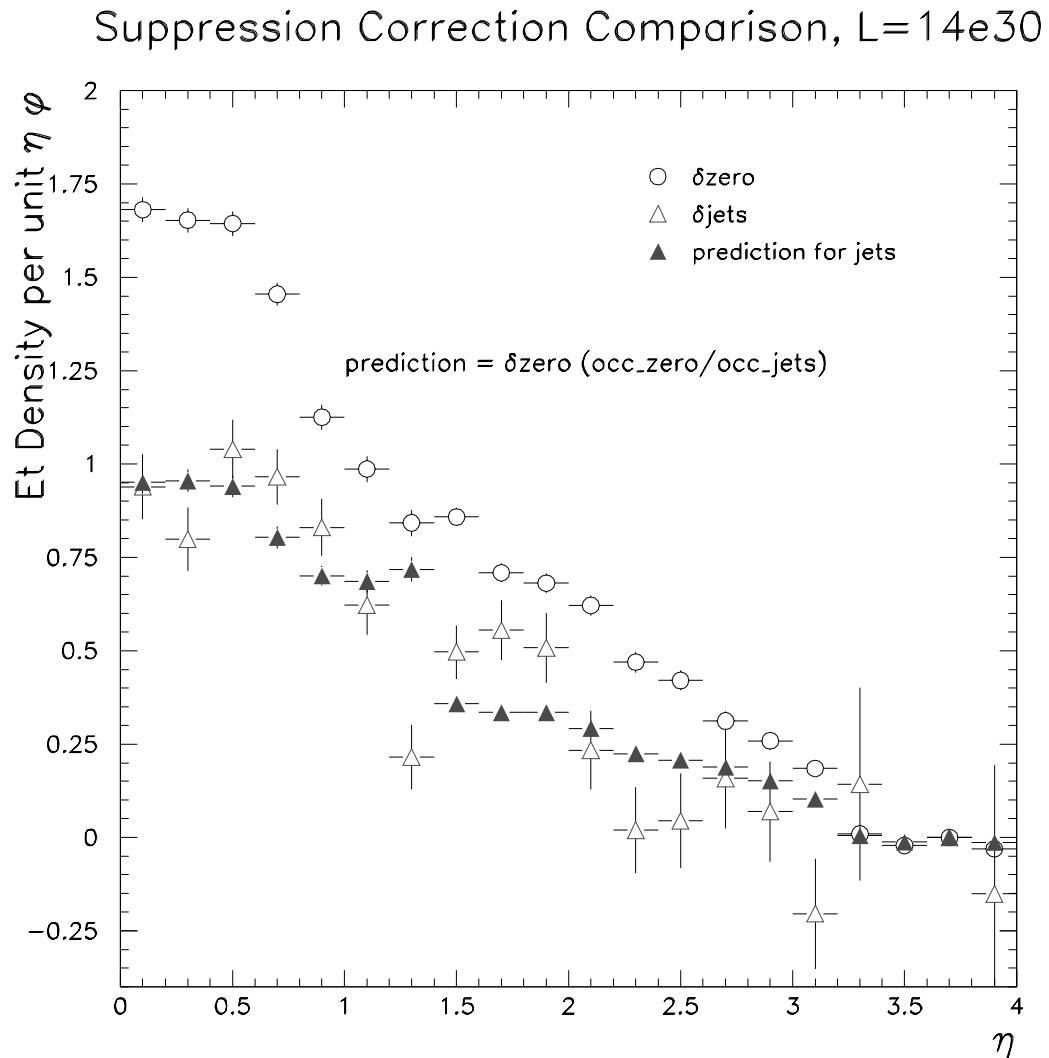
Figure 4.3: Suppression noise in zerobias data (open circles) and jet data (open triangles). Large statistical uncertainties in the jet data may be avoided by applying Equation 4.2 to the zerobias data (solid triangles).
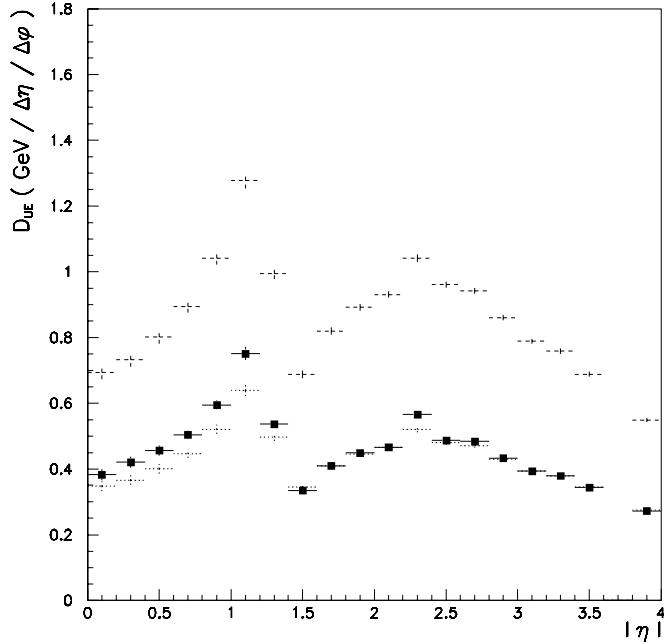
Figure 4.4: The physics underlying event. Square markers indicate the E_T density deposited in a single interaction versus pseudorapidity. Dashed lines represent E_T density deposited in events with two, three, or more interactions. The dotted lines are the multiple interaction result divided by two, showing good agreement with the single interaction result.

event energy density found in double interactions should be roughly twice that found in the single interactions. Figure 4.4 depicts the result of this single versus multiple interaction comparison for $\sqrt{s} = 630$ GeV.

The underlying event increases with increasing center–of–mass energy in two ways: the average particle multiplicity in the event increases and the average energy of each particle increases. The underlying event at $\sqrt{s} = 1800$ GeV is compared to that at 630 GeV in Figure 4.5 and the ratio is given by Figure 4.6.

4.1.3   Extra Interactions and Pileup

Using the multiple interaction tools to divide the minbias data sample into single and multiple interaction events isolates the contribution from extra interactions. The difference between the distributions is identical to the underlying event, as expected from Figure 4.4.
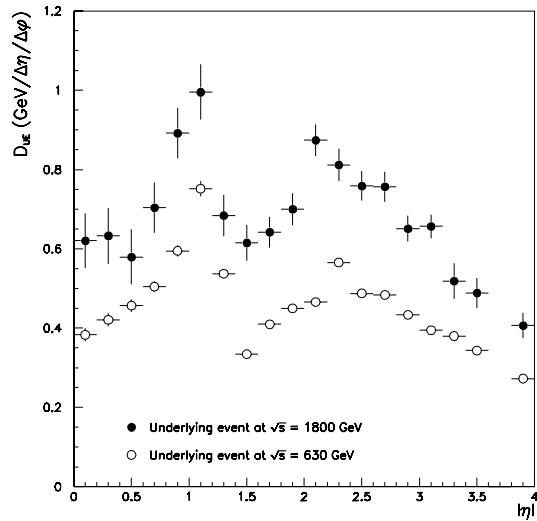
Figure 4.5: The underlying event E_T density for $\sqrt{s} = 630$ and 1800 GeV as functions of pseudorapidity.
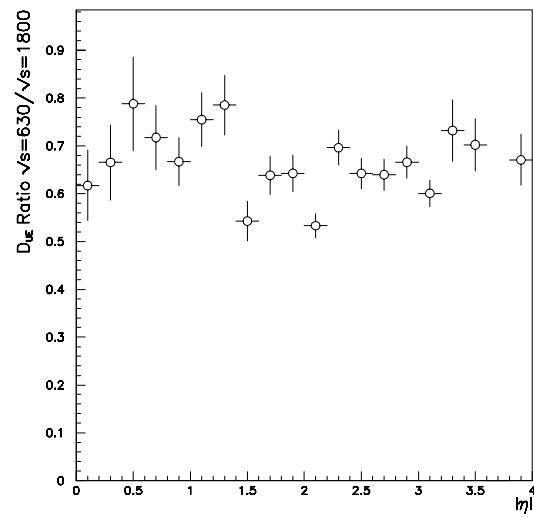
Figure 4.6: The ratio of underlying event E_T densities for $\sqrt{s} = 630$ and 1800 GeV as a function of pseudorapidity.

Total Offset, No Physics Underlying Event
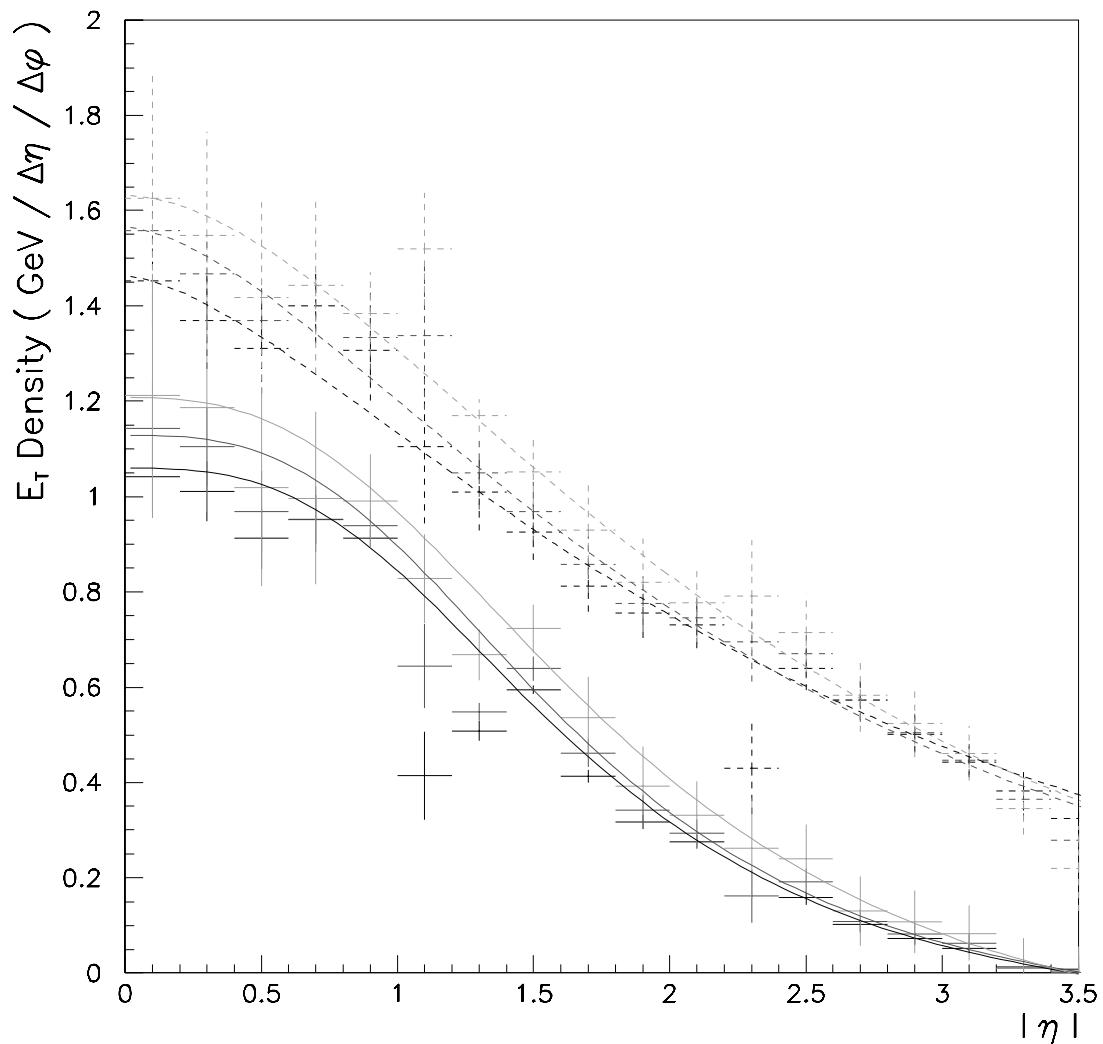
Figure 4.7: Data and fits to the combined noise, extra interaction, and pileup correction ($\sqrt{s}$ = 630 GeV). Lower three curves: single interactions and three representative luminosities. Upper three curves (dashed): multiple interactions, same three luminosities.

The total effect of noise, extra interactions, and pileup decreases with increasing pseudorapidity (Figure 4.7). The lower set of curves indicates the correction for single interactions while the upper curves (dashed lines) indicate the multiple interaction correction ($\sqrt{s} = 630$ GeV for both sets). Because the pileup effect is luminosity–dependent, three curves in each set demark three representative luminosities for each correction. The correction at $\sqrt{s} = 1800$ GeV is the same at comparable (*i.e.* low) luminosities, but can become twice as large at the highest luminosities.

The sum of Figures 4.5 and 4.7 results in the "total offset correction." Figure 4.8 depicts the various uncertainties of the correction. The underlying event uncertainty is the difference between the multiple and single interaction results in Figure 4.5. The Occupancy/Suppression uncertainty is valid only for $\sqrt{s} = 630$ GeV, and results from the extrapolation of 1800 GeV jet results to the low center–of–mass energy. The dashed line in Figure 4.8 indicates the covariant uncertainty from the fit to the pileup, noise, and extra interaction curves of Figure 4.7. The solid line represents the quadrature total of all these uncertainties. The largest uncertainty (not shown) results from a the parameterization of suppression noise, as discussed in a prior subsection.

4.1.4 Proof of Principle

Although the individual underlying event, pileup, and noise components become inextricable, direct study of dijet events can verify the magnitude of the total offset. The E_T deposits far from the two jet centroids will not include energy from the primary interaction, only the extraneous deposits that are azimuthaly homogeneous [23] throughout the calorimeter. Given jets with pseudorapidites of η_1 and η_2, and back–to–back azimuths ϕ_1 and ϕ_2, define "control cones" at positions:

$$\eta_a = \eta_b = \frac{\eta_1 + \eta_2}{2} + \kappa\pi \tag{4.3a}$$

$$\phi_{\substack{a \\ b}} = \phi_1 \pm \left(\frac{\pi}{2} - \kappa\,|\eta_1 - \eta_2|\right), \tag{4.3b}$$
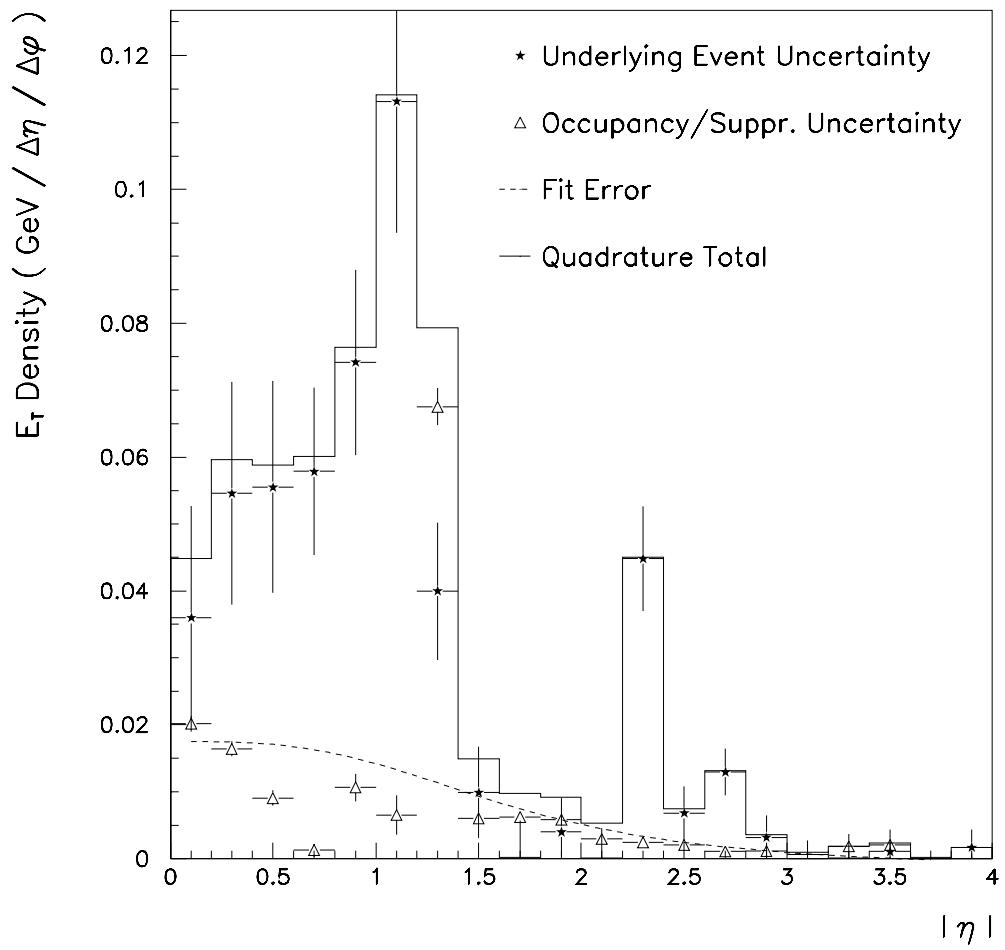
Figure 4.8: Uncertainties in the offset correction. Not shown: a 0.25 GeV effect, which is constant with respect to η, resulting from ambiguity in the choice of suppression parameterization.
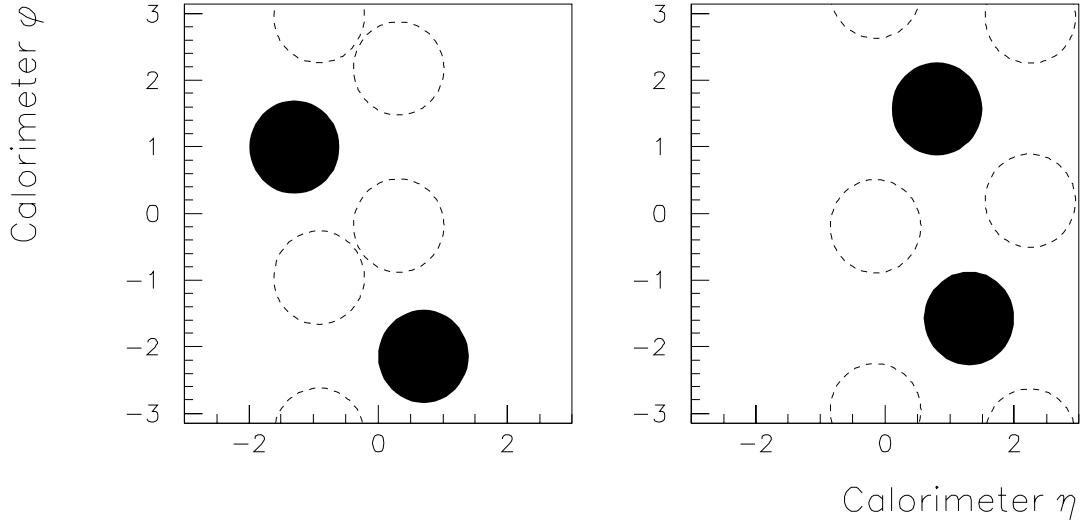
Figure 4.9: Typical control cones (unfilled circles) for different dijet topologies.

where

$$\kappa = \sqrt{\frac{4}{\pi^2 + (\eta_1 - \eta_2)^2} - \frac{1}{4}}. \tag{4.4}$$

These control cones are located $90°$ from each jet in ϕ and off the $\eta - \phi$ line that runs between the jets. In the limit of truly back–to–back jets, the prescription places each control cone 2.0 $\eta - \phi$ units from each jet. In the study sample, the dijet events were limited to single interactions and the two jets were separated in ϕ by at least 2 radians. Of four possible control cone positions (Figure 4.9), the two most central cones were selected.

The energy in the control cones compares favorably to the model used by the energy scale correction (Figure 4.10), renewing confidence in the jet offset, even in the limit of low jet E_T where the correction becomes important. In the figure, the stars represent the energy scale offset (as described prior this subsection) prediction for noise and underlying event in a 0.7 radius cone, the error band results from the occupancy model, and the vertical error bars include the rest of the CAFIX 5.1 uncertainties. The circles indicate the E_T versus η distribution of the control cones as found in jet events. The statistical uncertainties of the measurement are not visible on this scale.
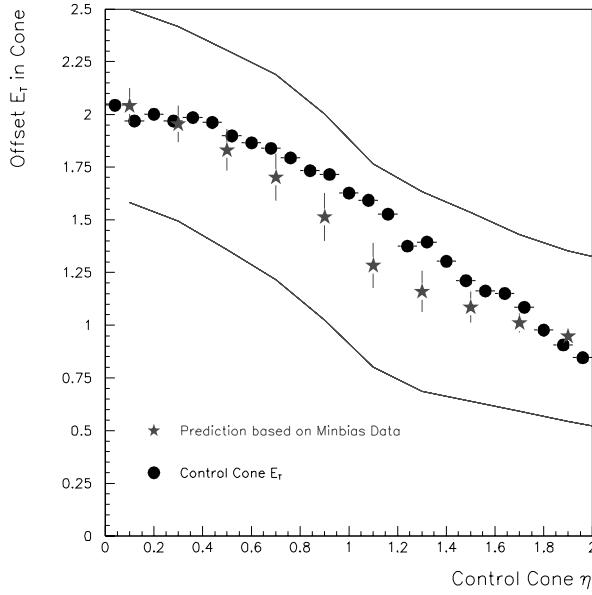
Figure 4.10: Comparison of underlying event predictions with observed energy in jet data. Stars: Underlying event and noise (CAFIX 5.1 correction) integrated over 0.7 cone. Circles: Actual energy in "control cones" located far from jets in the $\sqrt{s} = 630$ GeV data sample.

4.1.5   Offset Summary

The offset correction removes the effects of calorimeter noise, underlying events, energy from prior beam crossings (pileup), and extra interactions. Manipulation of two special data sets isolates these individual components: minbias data, collected when LØ indicates an interaction, and zerobias data, collected at random beam crossings. The data sets average one or zero p$\bar{\text{p}}$ events per beam crossing, respectively; thus, the difference in calorimeter energy between the two samples isolates the underlying event energy. The zerobias data alone provides a measure of the noise and pileup. Small corrections scale the offset from the special data sets to the correction necessary for jet data.

4.2   The Response Correction

Unlike test beam data, in p$\bar{\text{p}}$ collision data, resulting clusters of hadronic particles incident on the calorimeter will not always strike the centers of the calorimeter cells, nor will they

always strike at a 90° angle. Some particles may instead pass through a crack between cells or travel diagonally through only a portion of a cell. In addition, low E_T particles respond non-linearly, in contrast to the more linear energy deposition of high E_T particles. Finally, the cryostat modules differ slightly in construction. The response correction adjusts the reconstructed energy to remove these effects on average.

Because the energy variance of photons (and other electromagnetic particles) is negligible compared to that from jets, events containing only one photon and one jet provide an excellent measure the jet's lost energy, the *response*. The photon energy scale is precisely set by the well-measured Z (to e^+e^-), J/ψ, and π_0 resonances. The response in the jet energy scale demands that the transverse energy in the calorimeter balances the well–measured photon on average, such that $\vec{\rlap{/}{E}}_T = 0$. Jet to jet fluctuations about the mean can still result in mismeasured energy; this residual effect is called jet energy resolution, and shall be discussed in Chapter 6.

4.2.1 The Missing E_T Projection Fraction Method

Using the transverse energies of the photon and jet as vector quantities, the response correction R, the missing E_T vector ($\vec{\rlap{/}{E}}_T$), and the photon and jet E_T's are related by

$$\vec{E}_T^\gamma + R\,\vec{E}_T^{jet} = -\vec{\rlap{/}{E}}_T. \tag{4.5}$$

Defining the unit vector $\hat{n}_\gamma$ along the transverse direction of the photon, Equation 4.5 becomes

$$E_T^\gamma + R\,\hat{n}_\gamma \cdot \vec{E}_T^{jet} = -\hat{n}_\gamma \cdot \vec{\rlap{/}{E}}_T. \tag{4.6}$$

For a two-body system, conservation of momentum in the transverse direction demands $E_T^\gamma = -\hat{n}_\gamma \cdot \vec{E}_T^{jet}$, thus

$$R = 1 + \frac{\hat{n}_\gamma \cdot \vec{\rlap{/}{E}}_T}{E_T^\gamma} = 1 + MPF. \tag{4.7}$$

The Missing E_T Projection Fraction (MPF) expresses the response in terms of well-measured photon quantities. Application of the response correction becomes complicated because particle responses vary with *energy* rather than *transverse energy*. Additionally, photon-jet

events may contain additional jets with sub-threshold energy, which result in mismeasured $\vec{\rlap{E}\,}_{\mathrm{T}}$. Finally, jet energy measurements can suffer from poor resolution, resulting in large smearing effects (as discussed in Chapter 6). Simple topology cuts can remove the effect of additional jets in the data sample, but the other biases must be removed in a less direct manner.

To eliminate the smearing effects of jet resolution, the response correction must be expressed in terms of a variable that is strongly correlated to jet E^{meas}, yet is measured with much higher accuracy. The jet energy estimator

$$E' = \mathrm{E}_{\mathrm{T}}^{\gamma} \cdot \cosh\left(\eta^{jet}\right) \tag{4.8}$$

satisfies both criteria. Freed of resolution biases, the response as a function of E' then maps to E^{meas} bin by bin. More specifically, the response on an interval $[E'_1, E'_2]$ equals the response at the average value of E^{meas} on that same E' interval, as illustrated in Figure 4.11.

4.2.2 MPF Results

Calculated in each region of the calorimeter, the MPF response exhibits great stability throughout the entire pseudorapidity range. Displayed as a function of jet energy, the response curve (Figure 4.12) behaves in a highly linear manner above 100 GeV but decreases sharply at lower energies. The uncertainty on the response parameterization (solid lines) dominates the energy scale error at high energy.

Figure 4.12 derives from the $\sqrt{s} = 1800$ GeV data set. A comparison of 630 GeV data to this larger sample (Figure 4.13) reveals no significant change with different center–of–mass energy.

4.3 The Showering Correction

After the final-state partons of an interaction hadronize, the resulting particles strike the DØ detector and initiate a cascade of secondary particles that propagates through the calorimeter. A cone surrounding the initial particles may not be large enough to contain all the secondaries. Conversely, particles with vectors outside the cone may initiate a
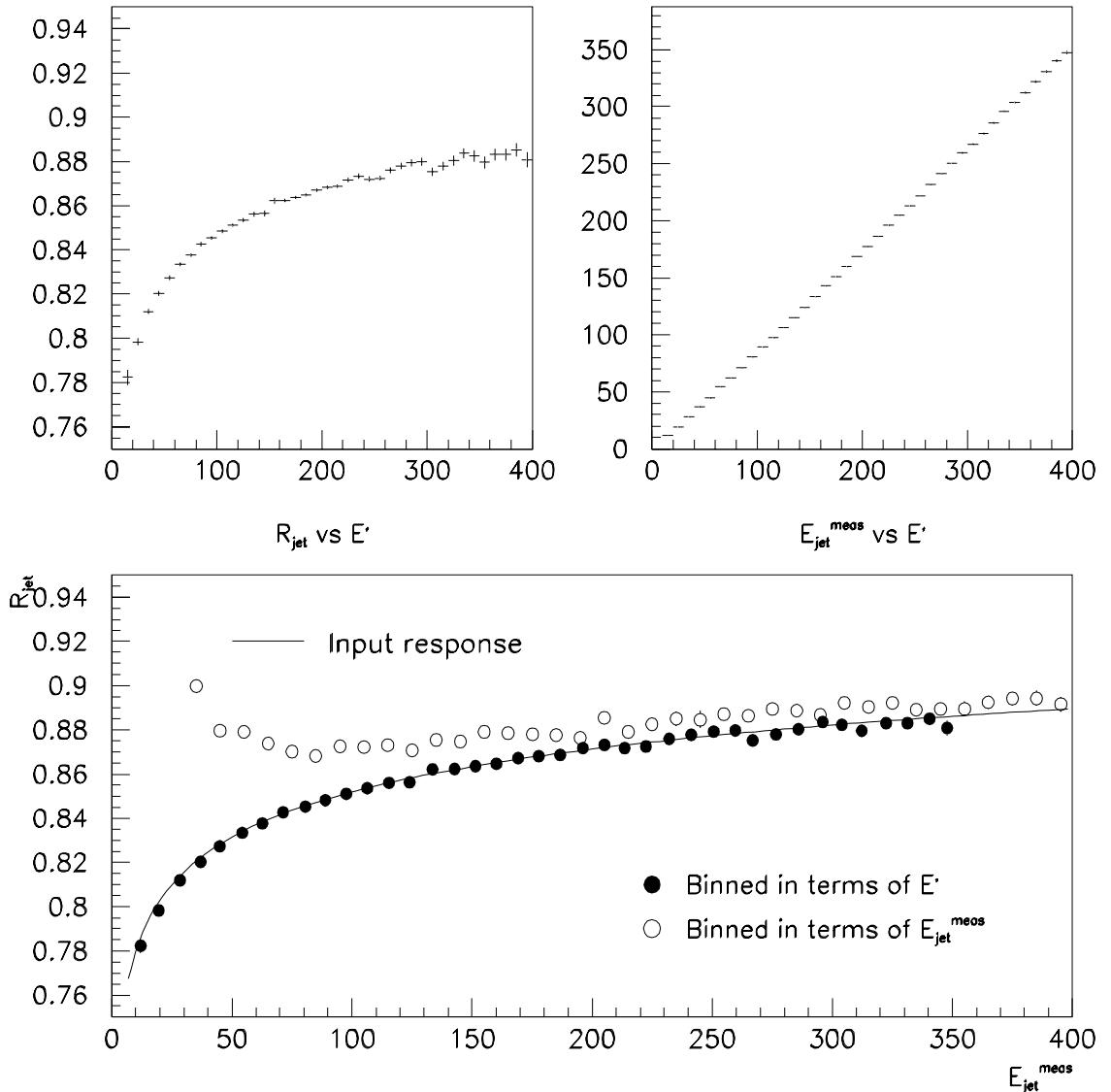
Figure 4.11: (Top) Mappings of response to the energy estimator, and of the measured jet energy to the energy estimator. (Bottom) Parametric simulation of jet response. Random misrepresentations of the jet energy (open circles) simulate the effects of finite jet resolution on the response determination. Use of the energy estimator E' (filled circles) eliminates the resolution effect relative to the input distribution (solid line).
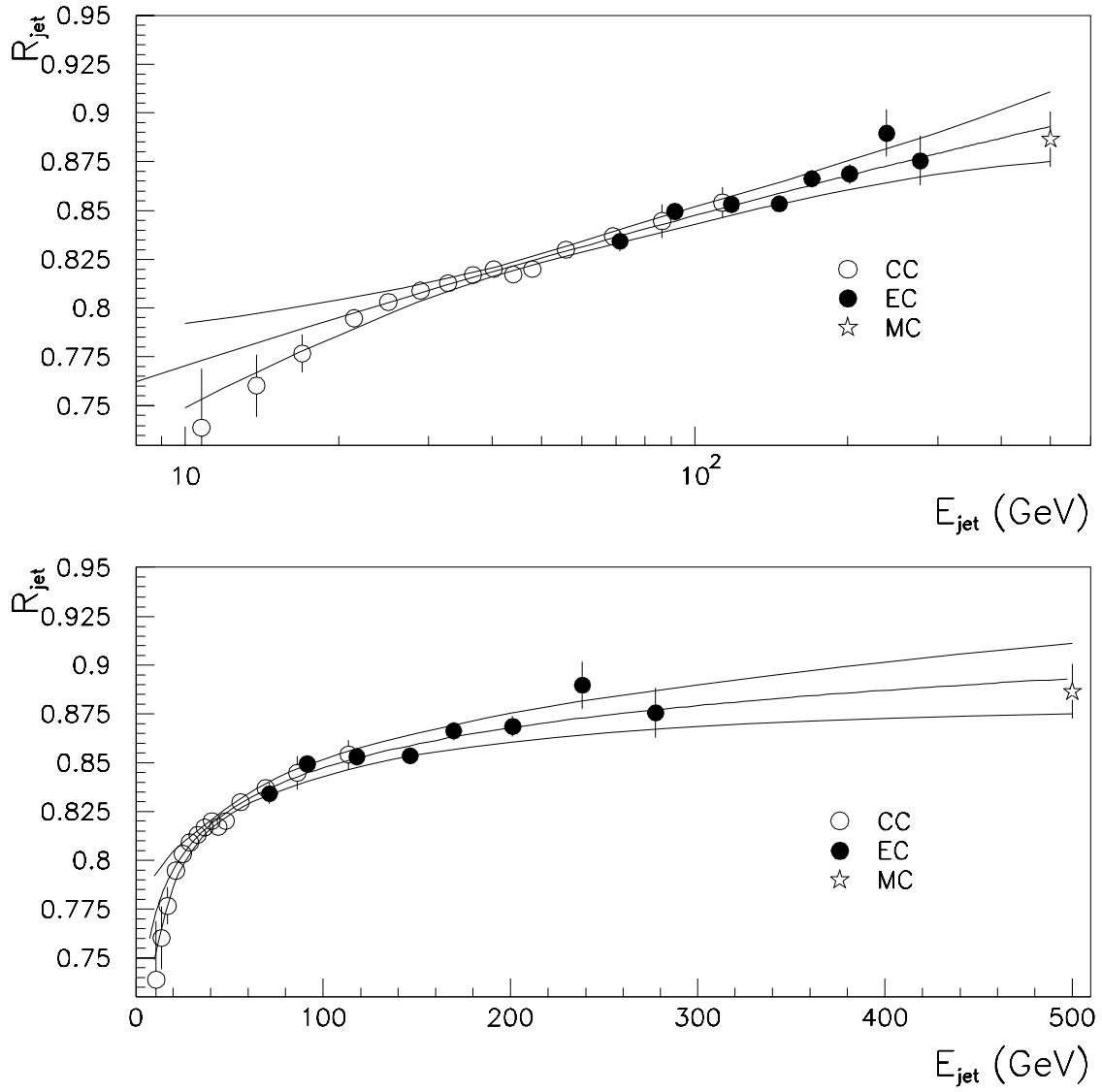
Figure 4.12: The DØ calorimeter response (R) for the central (open circles) and end regions (filled circles). Data for the top and bottom plots are identical, only the scale of the x-axis has changed. A single Monte Carlo point (star) constrains the high-E_T behavior of the response parameterization.
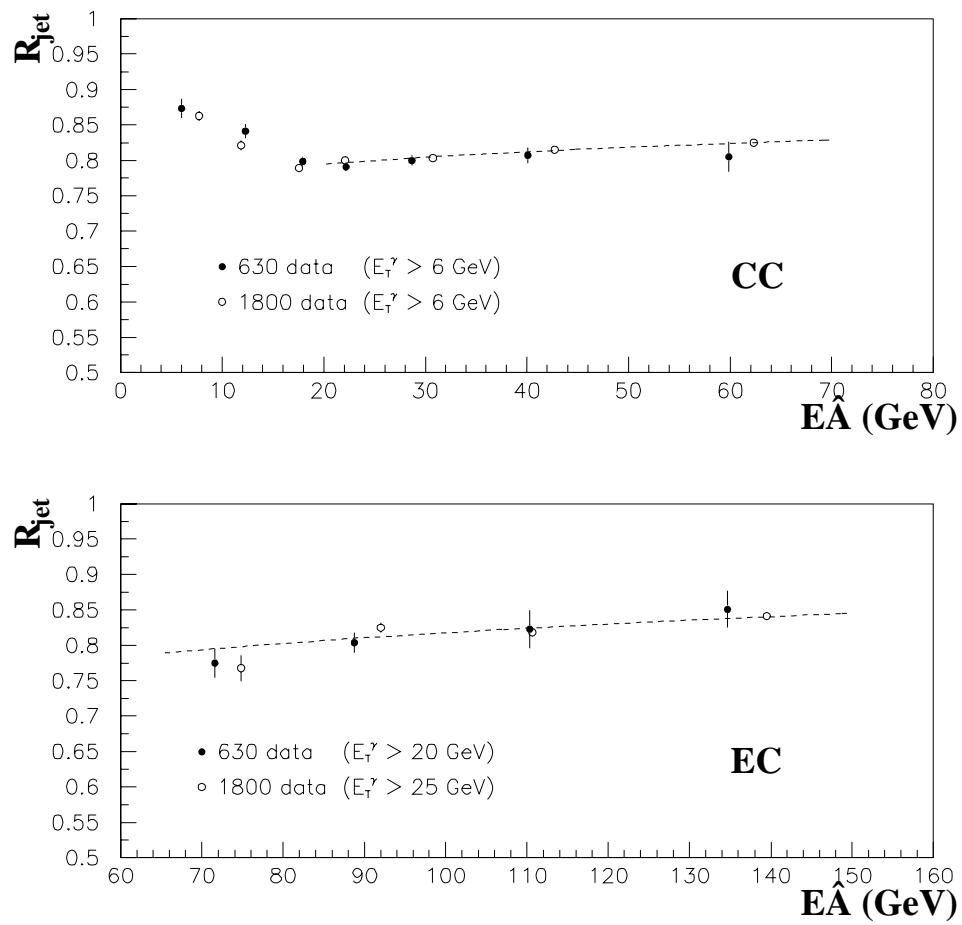
Figure 4.13: Comparison of the response between center–of–mass energies. In the region above 20 GeV (which includes all of the inclusive jet cross section data) the two data sets match.

cascade that ultimately deposits energy inside the cone. Because theoretical jet cross section predictions consider jets without showering effects, the data must be corrected back to this same level (the so–called "particle level"). The showering correction compensates for the flow of energy into and out of the jet cone during the cascade through the calorimeter, yielding only the energy of the particles that began within the cone.

The ratio of energy within a 0.7 cone to the energy in a larger cone determines the fraction of energy escaping the jet cone definition, provided the second radius is sufficiently large to encompass all shower energy. Test beam data demonstrates that on average a single hadron will deposit more than 99.5% of its energy within a 0.4 radius cone (corresponding to approximately $20°$ in azimuthal angle). This measurement and the RMS widths of jets in physics data (Figure 4.14) indicate a second cone of radius 1.0 will contain all secondary particles.

Physics data alone cannot reveal the amount of outriding energy due to particles outside the cone before showering; instead, a Monte Carlo event generator (HERWIG) resolves the ambiguity. Studying the data in two jet cone sizes, define

$$F_{Data} = \frac{E_{R=1.0}}{E_{R=0.7}}, \tag{4.9}$$

such that the expression represents

$$F_{Data} = \frac{J_7 + \text{true out–of–cone} + \text{net showering Loss}}{J_7} \tag{4.10}$$

$$= \frac{J_7 + Out + L}{J_7}. \tag{4.11}$$

Here, J_7 is, by definition, the energy within the $R = 0.7$ cone. The term "true out–of–cone" indicates the energy from particles whose vectors were not inside the cone boundary, and thus should *not* be recovered. Direct measurements of F_{Data} indicate that 96.7% of all energy in $R = 1.0$ lies within the 0.7 cone boundary.

To determine the showering correction with the form

$$\frac{1}{S} = \frac{J_7 + L}{J_7}, \tag{4.12}$$

the Monte Carlo events must provide

$$F_{MC} = \frac{J_7 + Out}{J_7}. \tag{4.13}$$

By adding and subtracting J and Out from Equation 4.12, it may be transformed to

$$\frac{1}{S} = F_{Data} - F_{MC} + 1. \tag{4.14}$$

Figure 4.15 depicts the showering correction factor (S) for $R = 0.7$ cones at several pseu-dorapidities (as determined at $\sqrt{s} = 1800$ GeV). At $\sqrt{s} = 630$ GeV, the observed average width of jets decreases; thus, the expected showering correction is smaller than that at 1800 GeV. The small size of the correction factor in the central region indicates that little (if any) change could occur with a change in $\sqrt{s}$ energy.

4.4   Summary

The jet energy scale correction takes the form

$$E = \frac{E^{meas} - O}{R \cdot S}, \tag{4.15}$$

where the detector energy is modified by the *Offset, Response,* and *Showering* terms. The offset corrects for calorimeter effects, extra interactions, and underlying event energy. As the primary correction, the response rescales measured jet energy to account for slightly non–linear charge deposition in liquid argon and the effect of uninstrumented material in the calorimeter. Finally, the showering correction returns to the jet any energy that may have cascaded outside the nominal cone boundary.

The energy scale correction dominates the uncertainty of the final jet cross section. At low E_T, the ~ 250 MeV uncertainty on the offset correction drives the total error, while at the other end of the spectrum, the uncertainty is driven by the response uncertainty. (Extended discussions of the uncertainties in the cross section determination are reserved for Chapter 7.)
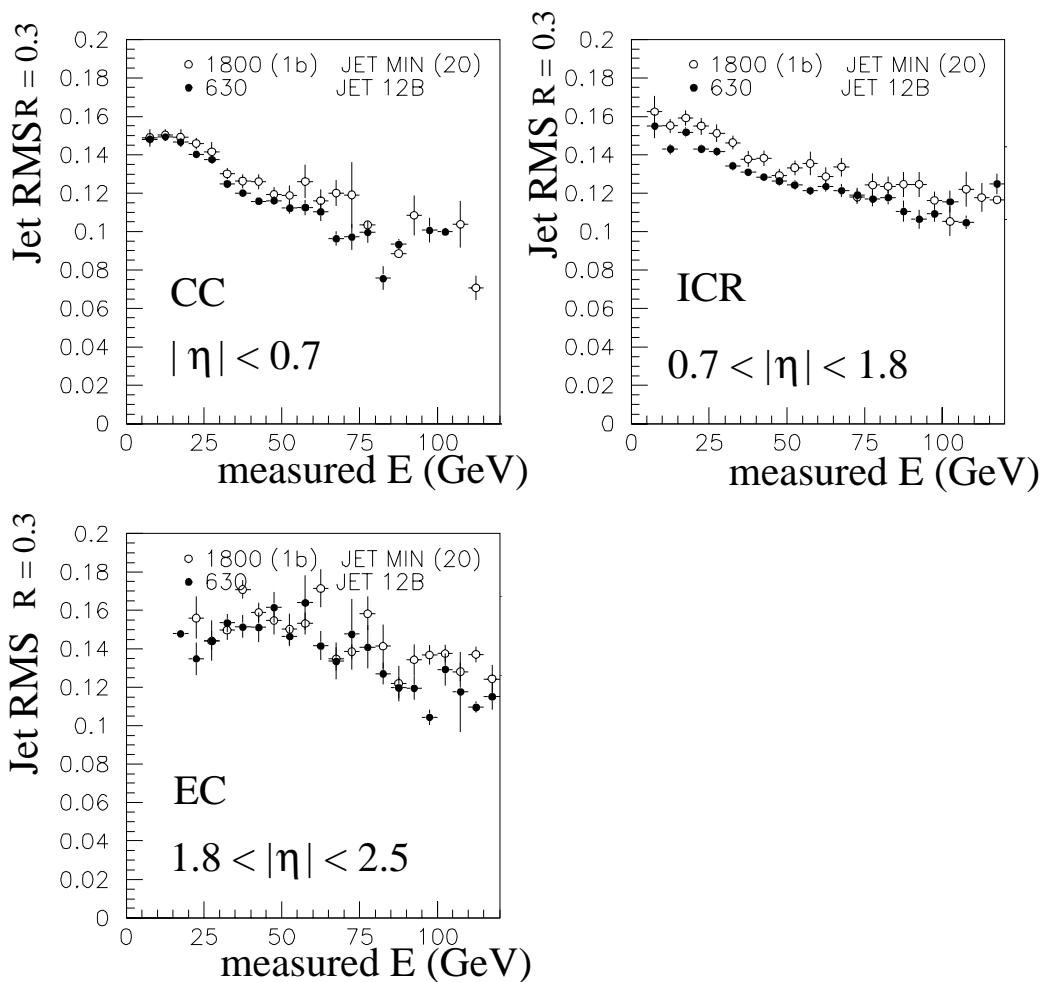
Figure 4.14: Jet RMS width versus measured jet energy, for both center–of–mass energies.
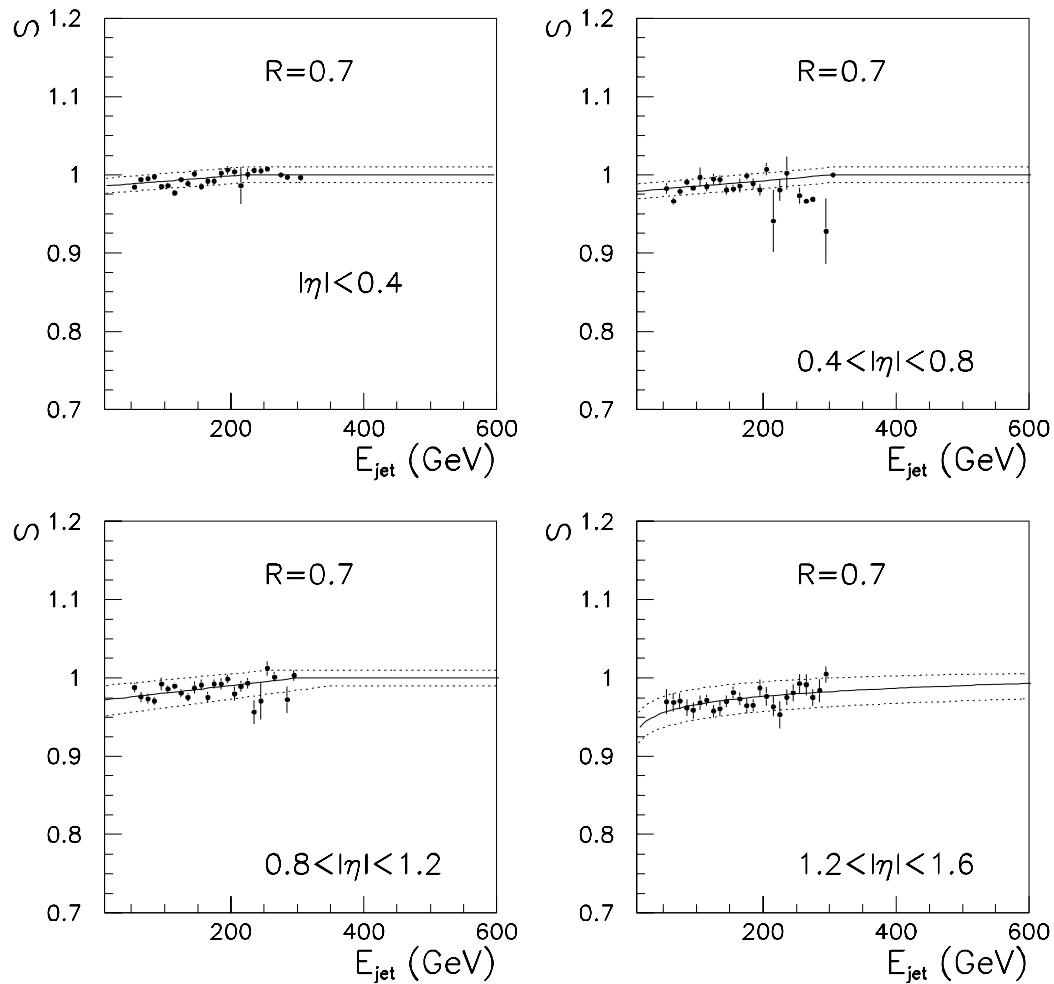
Figure 4.15: Showering correction as a function of jet energy for both center–of–mass energies. The correction increases slightly as a function of jet pseudorapidity.

Chapter 5

Cross Section Analysis

> *"Cowards can go no further."*
> — Narukagami

This chapter focuses on the full analysis of jet data. For both $\sqrt{s} = 630$ and 1800 GeV, events pass through the reconstruction, energy scale correction, and post–processing algorithms. To minimize redundancy, the individual discussions in this chapter will focus on data from either one $\sqrt{s}$ energy or the other, describing the more complicated of the two.

The inclusive differential jet cross section describes the probability of producing a hadronic jet with a given E_T. Because data are collected as discrete events, the analysis is performed in terms of histogram bins. The experimental formula for the cross section is thus given by

$$\left| \frac{d^2 \sigma_{jet}}{d\eta \; dE_T} \right|_{-0.5 < \eta < 0.5} = \frac{N}{\int \mathcal{L} \; dt \cdot \epsilon \cdot \Delta E_T \cdot \Delta \eta}, \qquad (5.1)$$

where the number of jets in a bin (N), is scaled by the time–integrated luminosity ($\int \mathcal{L} \; dt$), the data selection efficiency (ϵ), and the bin size in E_T and η. This result yields the "raw" cross section, which must subsequently be corrected for smearing effects (Chapter 6).

5.1 The Luminosity Calculation

This section[*] discusses the methodology used to calculate the *instantaneous luminosity* and the *time-integrated luminosity*. The first quantity describes the number of p$\bar{\text{p}}$ crossings that

---

[*] Major portions of this section were originally published as Fermilab Technical Memorandum 2000, "The DØ Luminosity Monitor Constant for $\sqrt{s} = 630$ GeV," J.Krane, J.Bantly, D.Owen, Apr. 15, 1997 and as DØ Note 3222 with same date and title.

occur in the beam per second. The second quantity is a measure of the total number of crossings that were potentially observable by the detector during the full data collection period.

Because of the finite acceptance of the DØ detector and the finite total p$\bar{\text{p}}$ cross section, not every p$\bar{\text{p}}$ crossing results in an observed event. The Luminosity Monitor Constant, $\sigma_{\text{LØ}}$, scales the measured interactions per second into the luminosity (given in *crossings·cm^{-2}·sec^{-1}*). As described in later chapters, the normalization uncertainty of the inclusive jet cross section is primarily driven by $\sigma_{\text{LØ}}$. This constant represents both the probability of an interaction and the likelihood of the detector to observe the interaction.

The Level Ø detector consists of two arrays of scintillating tiles surrounding the Tevatron beampipe and placed 140 cm from the center of the detector along the beam axis. These hodoscopes intercept low–angle particles generated by inelastic p$\bar{\text{p}}$ collisions. Nearly simultaneous hits in the innermost tiles of Level Ø (called "good FAST Z hits") determine the presence of a hard scattering interaction near the center of the DØ detector. The outermost tiles increase the geometric acceptance of the hodoscopes slightly and "good SLOW Z hits" are used in offline analyses.

The instantaneous luminosity is given by

$$\mathcal{L} = \frac{R}{\sigma_{\text{LØ}}}, \tag{5.2}$$

where R is the average number of (FAST Z) interactions per second and

$$\sigma_{\text{LØ}} = \epsilon_{\text{LØ}} f_{\text{halo}} f_{\text{MSD}} (\epsilon_{\text{SD}} \sigma_{\text{SD}} + \epsilon_{\text{DD}} \sigma_{\text{DD}} + \epsilon_{\text{HC}} \sigma_{\text{HC}}). \tag{5.3}$$

Here, the inelastic p$\bar{\text{p}}$ cross section has been split into three components (single diffractive, double diffractive, and hard-core) because the geometric acceptance (ϵ_i) for each process differs greatly. The halo and multiple single diffractive correction factors (f_{halo} and f_{MSD}) are almost negligible in the range of low luminosities experienced during the low-energy run, but they are included for completeness. Finally, the hardware efficiency ($\epsilon_{\text{LØ}}$) was calculated as a constant with respect to luminosity due to the limited luminosity range.

The luminosity monitor constant may be interpreted as the portion of the inelastic cross section observable by the DØ detector, thus $\sigma_{\mathrm{L}\varnothing}$ is sometimes called the Level Ø visible cross section.

During each bunch crossing, zero interactions, one interaction, or more than one interaction may occur. Because the Level Ø hodoscopes cannot distinguish between one interaction and several interactions, the actual event rate R must be inferred from the Level Ø counting rate $R_{\mathrm{L}\varnothing}$. From Poisson statistics, given the average number of interactions[*] per beam crossing μ, the probability of zero interactions in one crossing is

$$P_0 = e^{-\mu},\tag{5.4}$$

and Level Ø counting rate is then

$$R_{\mathrm{L}\varnothing} = \frac{1 - P_0}{\tau},\tag{5.5}$$

where τ is the time between bunch crossings, 350 μsec. Combining Equations 5.4 and 5.5, the true rate may be expressed as

$$R = \frac{\mu}{\tau} = \frac{-\ln\left(1 - R_{\mathrm{L}\varnothing}\tau\right)}{\tau},\tag{5.6}$$

and the instantaneous luminosity, in terms of measurable values, becomes

$$\mathcal{L} = \frac{-\ln(1 - R_{\mathrm{L}\varnothing}\tau)}{\sigma_{\mathrm{L}\varnothing}\tau}.\tag{5.7}$$

5.1.1 Calculation of p$\bar{\mathrm{p}}$ Cross Section Values

Calculation of the Level Ø cross section requires a measurement of the single diffractive, elastic, and total cross sections (σ_{SD}, σ_{EL}, and σ_{TOT}) at the intended center of mass energy. For $\sqrt{s} = 1800$ GeV, the world average cross section values were computed using published data [25][26] from CDF and E710. Because the results of the two experiments do not agree well, the uncertainty on the average value was increased [27] by a factor of χ. The calculation of the luminosity monitor constant for the low energy run, while similar [27][28]

---

[*] The actual number of interactions per beam crossing remains indeterminate for this calculation. Given an instantaneous luminosity, the average number of expected visible interactions is $\mu = \mathcal{L}\tau\sigma_{\mathrm{L}\varnothing}$.

	a	b	$\mathrm{Cov}(a, b)$
σ_{TOT}	0.2447 ± 0.0535	22.554 ± 8.711	-0.464
σ_{EL}	2.541 ± 0.545	-19.070 ± 6.992	-3.84
σ_{SD}	0.538 ± 0.413	1.471 ± 6.010	-2.48

Table 5.1: Fit parameters, errors, and covariance for the World Average cross sections.

σ_{TOT}	63.223 ± 0.829 mb
σ_{EL}	13.683 ± 0.290 mb
σ_{SD}	8.432 ± 0.641 mb

Table 5.2: Calculated cross sections and uncertainties at $\sqrt{s} = 630$ GeV.

to the 1800 GeV calculations, suffered from a slightly different complication: a complete set of three cross sections does not exist at $\sqrt{s} = 630$ GeV.

The nearest complete set of measurements [25][29][30] was obtained at a center-of-mass energy of 546 GeV. This section details the methodology used to interpolate the cross section values between 546 and 1800 for use at 630 GeV.

In the literature, the total $\mathrm{p\overline{p}}$ cross section is expected [30][31] to follow a $\ln^2 s$ dependence. In contrast, the elastic and single diffractive cross sections obey an observed [32] $\ln s$ dependence. A two parameter form $(a \ln^n s + b)$ was used to interpolate each cross section, where n had a value of 2 to fit the total cross section and 1 otherwise. Because the target point of the interpolation is very close to one end-point of the fit, the error at 630 GeV is largely driven by the error at 546 GeV. Figure 5.1 displays the results of the fits. Table 5.1 lists the fit parameters, the uncertainty on the parameters, and the covariance between a and b for the three cross sections. Table 5.2 summarizes the values and uncertainties found for σ_{SD}, σ_{EL}, and σ_{TOT} at $\sqrt{s} = 630$ GeV.

The fit to the total cross section was compared to the result obtained by the UA4/2 Collaboration [31] using a more complicated 8 parameter fit. UA4/2 modeled the $\sqrt{s}$ evolution of the total $\mathrm{p\overline{p}}$ cross section from 5 to 546 GeV with dispersion relations and 103 data points. They extrapolated their best fit to all data to LHC and SSC energies; their intermediate points are shown in Figure 5.2. The UA4/2 best fit points at 546, 900, and 1800 GeV are in excellent agreement with the simpler fit to the total cross section used
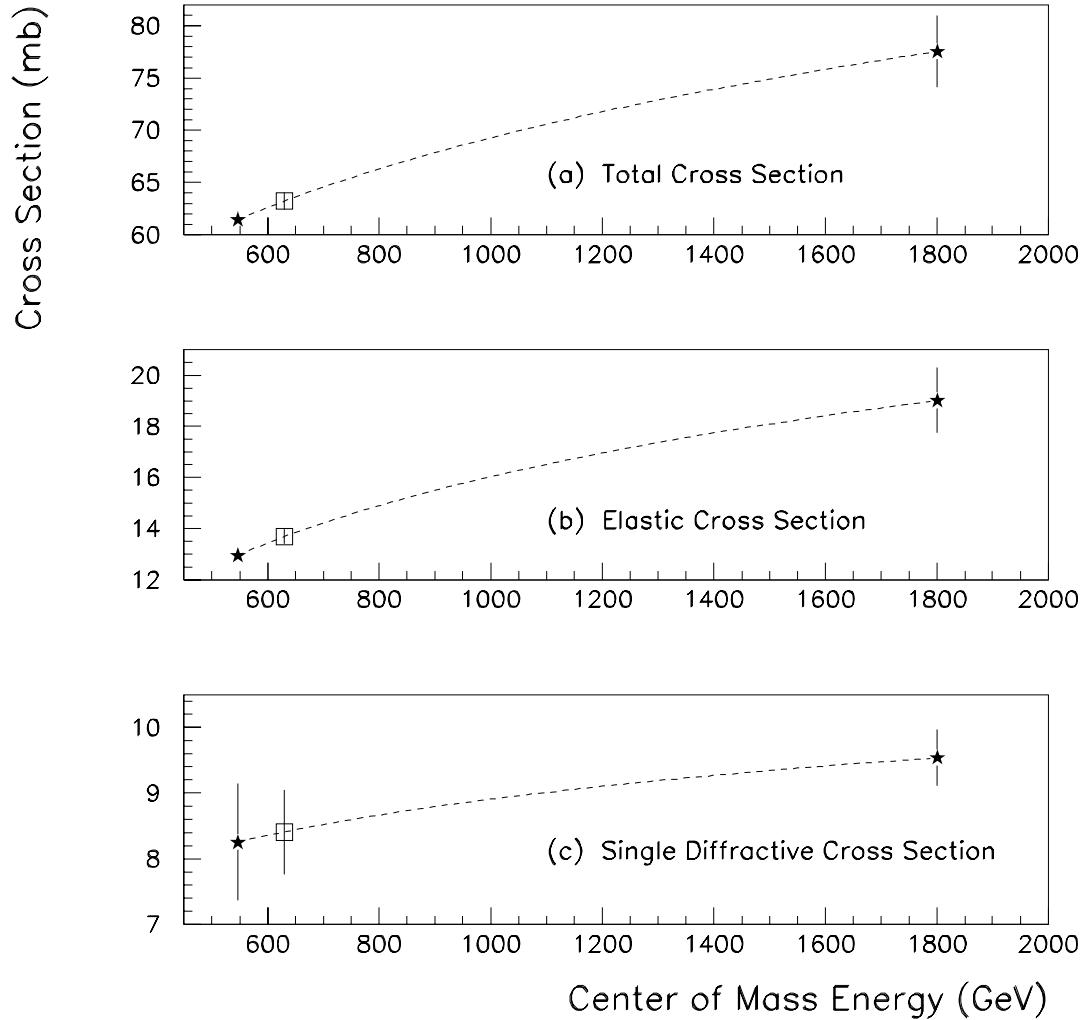
Figure 5.1: The results of interpolation for the (a) total, (b) elastic, and (c) single diffractive p$\overline{\text{p}}$ cross sections. The stars denote the world average cross sections at 546 and 1800 GeV, while the squares indicate the interpolated points at $\sqrt{s}$ = 630 GeV. The dashed line represents the two parameter fit.

σ_{SD}	8.432 ± 0.641 mb
σ_{DD}	1.299 ± 0.238 mb
σ_{HC}	39.810 ± 1.113 mb

Table 5.3: The calculated components of the inelastic $p\bar{p}$ cross section.

for the $\sigma_{\text{L}\emptyset}$ calculation. To estimate the uncertainty of interpolation due to the simple functional form of the model used in the $\sigma_{\text{L}\emptyset}$ calculation, the variance between the UA4/2 extrapolation and the simple interpolation (0.23%) is included as an error in quadrature with the other fitting uncertainties..

As detailed in reference [27], the double–diffractive and hard–core components of the p$\bar{\text{p}}$ cross section are calculated from the world average cross sections. The resulting values are presented in Table 5.3.

5.1.2   Geometric Acceptance of Level Ø

Monte Carlo studies determine the acceptance of the Level Ø hodoscopes by calculating the probability that one or more charged particles will pass through the scintillating tiles. The probabilities were calculated [25][33] with MBR and DTUJET, two minbias event generators. Samples of 6000 events each were generated for each of the three inelastic processes and passed through DØGEANT [34] and DØRECO [35] (the DØ detector simulator and reconstruction algorithms, respectively). The results are summarized in Figure 5.4. The MBR Monte Carlo program randomly selects a diffracted particle in SD interactions, while DTU-JET generates events with either the proton or the antiproton diffracted each time. Some events are "lost" during the GEANT or RECO stage, but the final sample size in each case is nominally 6000 events.

The results indicate a small decrease in acceptance when compared to the results of the $\sqrt{s} = 1800$ GeV study. For each subprocess, the geometric acceptance decreased by 1–3 percent. The decrease results from lower particle multiplicity of collision products at $\sqrt{s} = 630$ GeV.
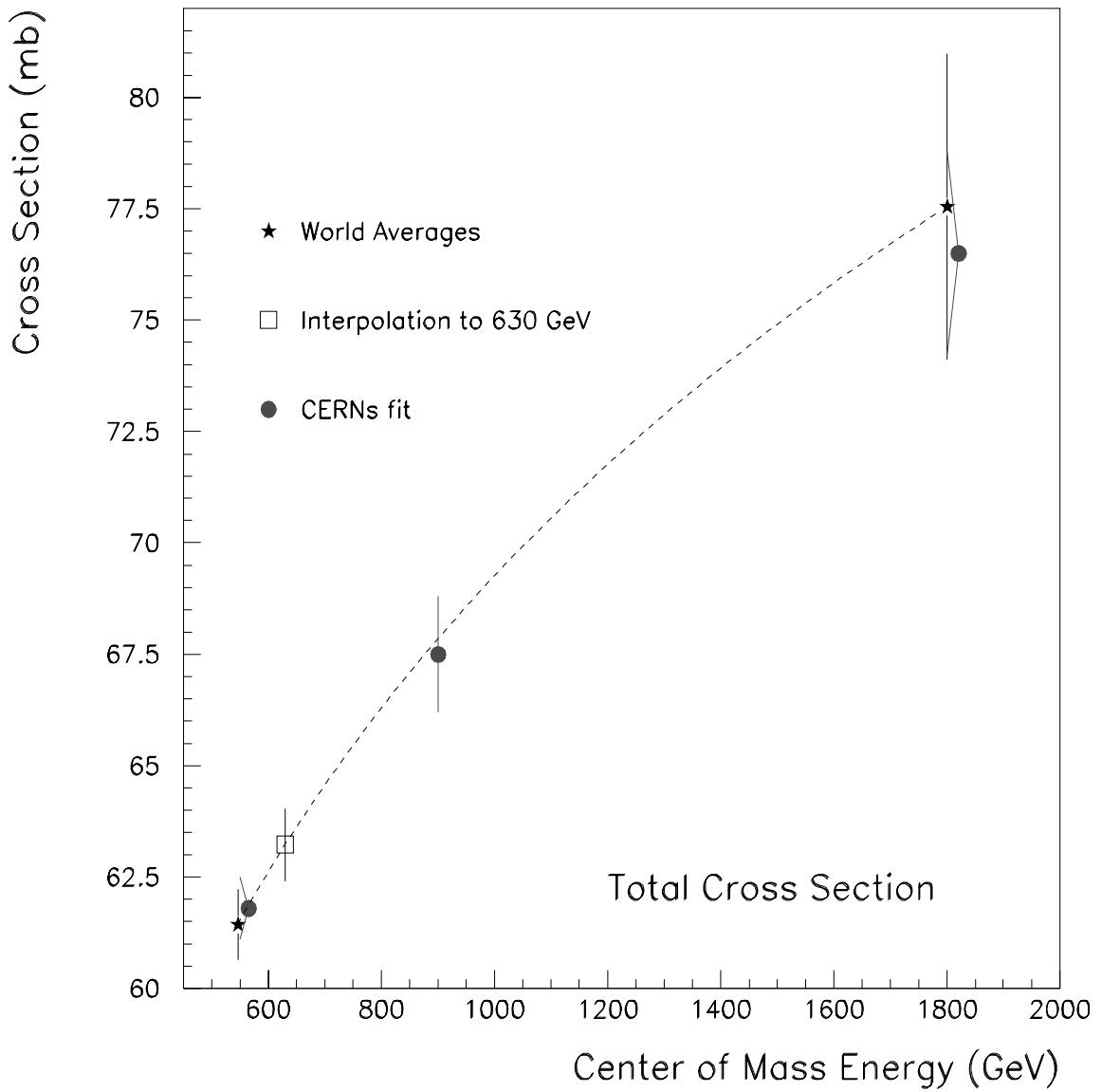
Figure 5.2: The world average total p$\overline{\text{p}}$ cross section at 546 and 1800 GeV (stars), interpolated to 630 GeV (square). The dashed line is the two parameter fit. The points from a best fit by CERN's UA4/2 Collaboration (circles) are included for comparison.

Final numbers from MBR and DTUJet
for Level 0 Acceptance at 630 GeV CM Energy

	TOTAL EVENTS IN SAMPLE	good FAST Z number	percent	stat error
DTUJet				
Single Diffractive, proton diffracted	5997	444	7.40%	0.34%
Single Diffractive, antiproton diffracted	6000	454	7.57%	0.34%
Double Diffractive	5999	4217	70.30%	0.59%
Hard Core	6000	5778	96.30%	0.24%
MBR				
Single Diffractive	5957	1102	18.50%	0.50%
Double Diffractive	5979	3946	66.00%	0.61%
Hard Core	5997	5704	95.11%	0.28%

		good SLOW Z number	percent	stat error
DTUJet				
Single Diffractive, proton diffracted	5997	514	8.57%	0.36%
Single Diffractive, antiproton diffracted	6000	527	8.78%	0.37%
Double Diffractive	5999	4324	72.08%	0.58%
Hard Core	6000	5829	97.15%	0.22%
MBR				
Single Diffractive	5957	1186	19.91%	0.52%
Double Diffractive	5979	4005	66.98%	0.61%
Hard Core	5997	5743	95.77%	0.26%

AVERAGES	FAST Z ACCEPTANCE	SLOW Z ACCEPTANCE
SINGLE DIFFRACTIVE	12.99% ± 6.95%	14.35% ± 0.73%
DOUBLE DIFFRACTIVE	68.15% ± 0.85%	69.53% ± 0.84%
HARD CORE	95.71% ± 0.37%	96.46% ± 0.34%

Table 5.4: Summary of geometric acceptance studies. FAST Z indicates the number and percentage of events with at least one particle passing through each Level Ø hodoscope. (The SLOW Z numbers, included for completeness, are germane to data triggers and luminosity studies, but not to the instantaneous luminosity measurement.)
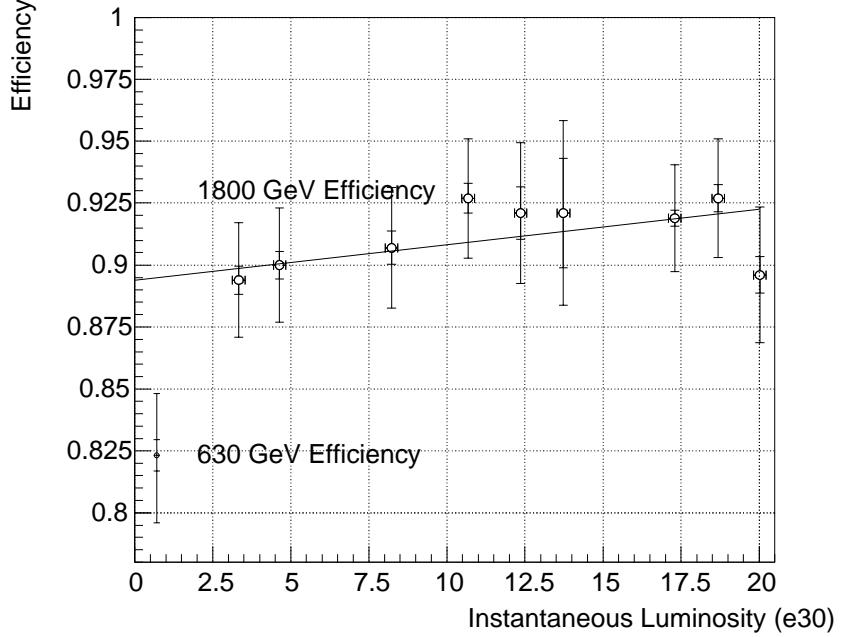
Figure 5.3: The Level Ø hardware efficiency at $\sqrt{s} = 1800$ and 630 GeV. The residual luminosity dependence is negligible over the luminosity range of the low–energy run ($1 \cdot 10^{28}$ to $3 \cdot 10^{30}$ cm$^{-2} \cdot$ sec^{-1}).

5.1.3   Level Ø Hardware Efficiency and Luminosity–Dependent Effects

Hardware Efficiency

The method used to evaluate the Level Ø hardware efficiency ($\epsilon_{\text{LØ}}$) is discussed at length in reference [28]. The scintillating tiles are least likely to detect events with very low particle multiplicity, resulting in a small luminosity dependence in $\epsilon_{\text{LØ}}$. Because the particle multiplicity of inelastic collisions at $\sqrt{s} = 630$ GeV is smaller than comparable events at 1800 GeV, the observed decrease in hardware efficiency is to be expected.

In Figure 5.3, the hardware efficiency found at 630 GeV lies approximately seven percent lower than the 1800 GeV points at similar luminosity. No attempt was made to include a luminosity dependence in the 630 number; the single point is used throughout the luminosity range ($1 \cdot 10^{28}$ to $2.6 \cdot 10^{30}$ cm$^{-2} \cdot$ sec^{-1}).
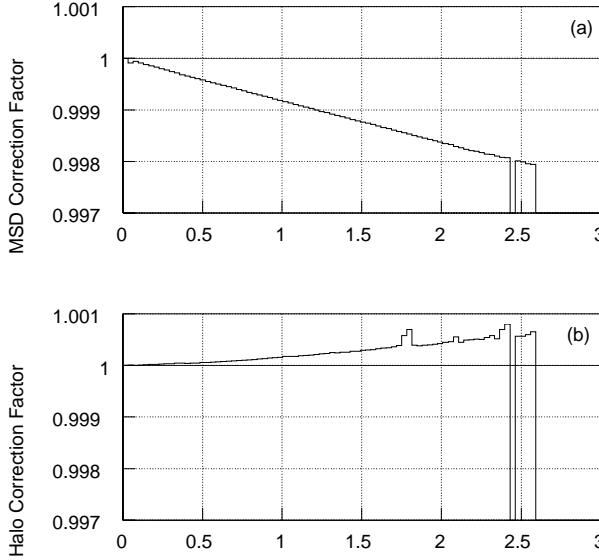
Figure 5.4: The (a) MSD correction and the (b) Halo correction as functions of instantaneous luminostiy. The corrections are each less than 0.2% and partially offset one another. Discontinuities in the halo correction are caused by unusually high halo rates in several isolated runs.

Multiple Single Diffractive Events

In Section 3, the calculation of the geometric acceptance assumed all events were single interactions. A single diffractive event has a low probability of firing both Level Ø hodoscopes because the trajectory of the non–fragmented particle usually remains within the beampipe. At high luminosities, two (or more) single diffractive events will occur simultaneously but in opposite directions with a calculable probability. Such an occurrence mimics a double diffractive event and shares the much higher acceptance. Although the expression for the luminosity given previously accounts for multiple interactions, it does so in a simple way that neglects the effect of multiple single diffractive events (MSD).

In high–luminosity environments, MSD effects can be significant. During the 630 GeV running period, the effect of MSD was much less pronounced (see Figure 5.4 (a)).
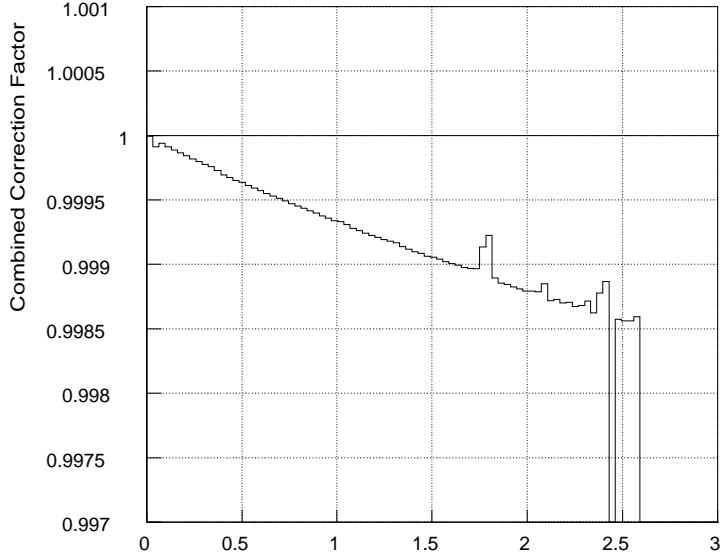
Figure 5.5: The combined MDS and Halo correction factor.

Beam Halo Correction

Particles orbiting within the Tevatron with a trajectory far from the nominal bunch center comprise beam halo. When the proton and antiproton beams are focused at the center of the detector, these halo particles can be deflected outside the beampipe and through the detector, distorting physics measurements. For this reason, "halo events" are rejected at the trigger level, with the unfortunate consequence of distorting luminosity measurements. The correction derived from measured halo rates is shown as a function of instantaneous luminosity in Figure 5.4 (b). (The effect of beam halo depends on both beam characteristics and luminosity, thus varying from run to run as highlighted by the discontinuities in Figure 5.4 (b). The correction is applied on a run–to–run basis, but the behavior of the correction is best viewed as a function of the stronger luminosity dependence.) The combined MSD and halo corrections are listed in Figure 5.5. The effect at all instantaneous luminosities is less than 0.15%.

$\epsilon_{\mathrm{SD}}\sigma_{\mathrm{SD}} + \epsilon_{\mathrm{DD}}\sigma_{\mathrm{DD}} + \epsilon_{\mathrm{HC}}\sigma_{\mathrm{HC}}$	40.081 ± 1.282 mb
$\epsilon_{\mathrm{L}\varnothing}$	0.8232 ± 0.0257
$f_{\mathrm{halo}} \cdot f_{\mathrm{MSD}}$	0.99924 ± 0.00200
$\sigma_{\mathrm{L}\varnothing}^{\sqrt{s}=630\,\mathrm{GeV}}$	32.97 ± 1.05 mb
compare to $\sigma_{\mathrm{L}\varnothing}^{\sqrt{s}=1800\,\mathrm{GeV}}$	46.7 ± 2.5 mb

Table 5.5: Results for the calculation of the luminosity monitor constant at $\sqrt{s} = 630$ GeV.

5.1.4 Luminosity Monitor Constant Summary

The luminosity monitor constant was calculated for $\sqrt{s} = 630$ GeV, considering changes in efficiency due to lower $p\overline{p}$ inelastic cross sections, differing particle kinematics, and luminosity–dependent considerations. The small run–dependent halo effect was included and the hardware efficiency of the scintillating hodoscopes was remeasured. A numeric interpolation of $p\overline{p}$ cross sections between $\sqrt{s} = 546$ and 1800 GeV was performed because no direct measurements are available. We find a final luminosity–weighted average $\sigma_{\mathrm{L}\varnothing} = 34.04 \pm 1.05$ mb, a fractional uncertainty of $\pm$ 0.0308.

The results of the individual components of the calculation are listed in Table 5.5 with the final result. Note that only the central values are listed, the MSD and beam halo corrections do vary slightly with instantaneous luminosity.

5.1.5 The Time–Integrated Luminosity

For cross section analyses, the integrated luminosity takes prime importance, setting the scale of the measurement. Strictly speaking, "integrated luminosity" is something of a misnomer, true only in the limit the time between beam crossings approaches zero. The luminosity sum is calculated for each trigger to account for individual prescales and deadtimes (*cf* Chapter 3).

The total time–integrated luminosity for the low–energy run, $537 \ \mathrm{nb}^{-1}$, was accumulated over three weeks. The individual luminosity exposure for the jet triggers of this analysis were listed previously in Table 3.2.

5.2 Data Selection Efficiency

Not all collected events contain valid jet data. Several different phenomena deposit energy in the calorimeter and may imitate a jet event:

- cosmic rays passing through the calorimeter during a beam crossing
- activity in the Main Ring
- beam halo (Tevatron noise)
- sparks or cascading noise in the calorimeter or read–out electronics
- electrons or photons misidentified as jets.

A set of criteria remove these background "fakes" from the sample. Called event and jet selection cuts, quality cuts, or simply "cuts," these criteria also remove some portion of the signal sample, resulting in a deficit in the measured cross section. With knowledge of the jet cut *efficiency* (denoted ϵ), a correction to the remaining jet sample eliminates the deficit, as in Equation 5.1. The selection cuts may invalidate an entire event, or only one of the jets within an event.

Each selection cut imposes a restriction on some jet or event variable. The efficiency of each cut is determined by the distribution of each variable before and after the cut; the binomial error formula (*cf* Appendix B) describes the statistical uncertainties of the efficiencies. The cut efficiencies are determined with a relatively pure jet sample to avoid background contamination in each distribution. The following subsections describe the selection criteria; a listing of the efficiencies is reserved for the summary at the end of this section.

5.2.1 Event Selection

Two event criteria validate jet events: the missing E_T cut and the vertex cut. The most powerful criterium in QCD physics at DØ, the missing E_T ($\not{E}_T$) cut removes most of the background due to cosmic rays and noise. The vertex cut does not remove background; instead, it ensures good E_T resolution for subsequent analysis.

The Missing E_T Cut

Cosmic rays striking the DØ calorimeter deposit large amounts of energy in the cells, similar to the energy deposits of hadronic jets. Unlike jets, the cosmic ray E_T is normally unbalanced. If, for instance, the cosmic ray strikes the calorimeter as in Figure 5.6, the lack of activity on the left–hand–side of the calorimeter results in $\not{E}_T$ of equal magnitude to the cosmic ray E_T. Even if the cosmic ray trajectory had passed through the exact center of the calorimeter (and the beampipe), the energy deposition pattern $\left(\frac{dE}{dx}\right)$ is inconstant, and usually results in large $\not{E}_T$. Some physics events result in (valid) non–zero $\not{E}_T$, but the dominant process in the inclusive jet cross section is the dijet channel ($\not{E}_T \approx 0$); decay channels with a single jet plus one other object (a photon, for instance) exhibit cross sections that are several orders of magnitude smaller (also $\not{E}_T \approx 0$). Exotic processes with expected non–zero $\not{E}_T$ occur even less frequently. Because QCD events with $\not{E}_T \approx 0$ dominate the inclusive jet cross section, a cut that limits the $\not{E}_T$ will not appreciably bias the data sample but will effectively remove cosmic ray backgrounds and noise.

Figure 5.7, the $\frac{E_T^{max}}{\not{E}_T}$ distribution, reveals an excess at unity over the smooth underlying shape. Here, E_T^{max} refers specifically to the jet in the event with greatest E_T (the "leading jet E_T"). Most events in the distribution lie to the right of the displayed region of the figure. The arrow indicates the position of the Missing E_T Fraction cut (sometimes denoted METFR) at 1.43. The efficiency is determined with the area under a best–fit Gaussian (which corresponds to the number of retained events, n), fit to the "signal interval" $[1.43, 4.0]$:

$$\epsilon_{METFR} = \frac{n + n'}{n + n' + l}. \tag{5.8}$$

Here, n' is the number of events with METFR greater than 4.0, and l is the area under the Gaussian between 0 and 1.43 (the estimated number of lost events). The binomial error formula determines the statistical uncertainty.

To estimate the magnitude of any systematic biases, a second fit is performed on the interval $[0.0, 4.0]$ with a double–Gaussian form, where the additional Gaussian is constrained
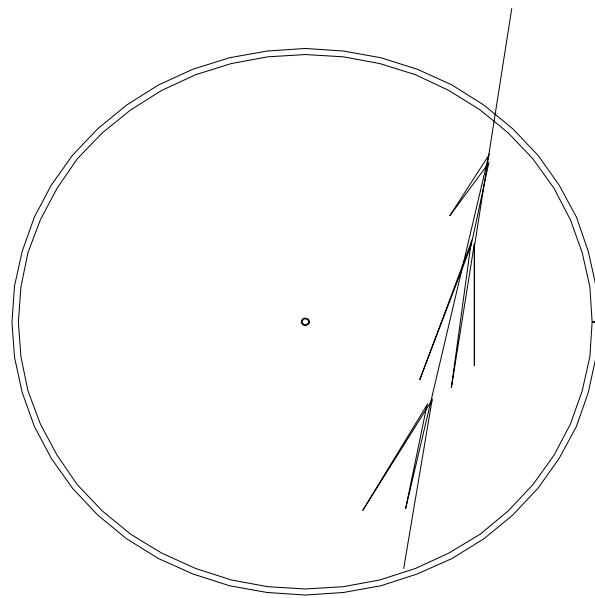
Figure 5.6: Illustration of a cosmic ray event (calorimeter viewed along its axis, beampipe in center). Some portion of the cosmic ray energy will be interpreted as a jet (or several jets).
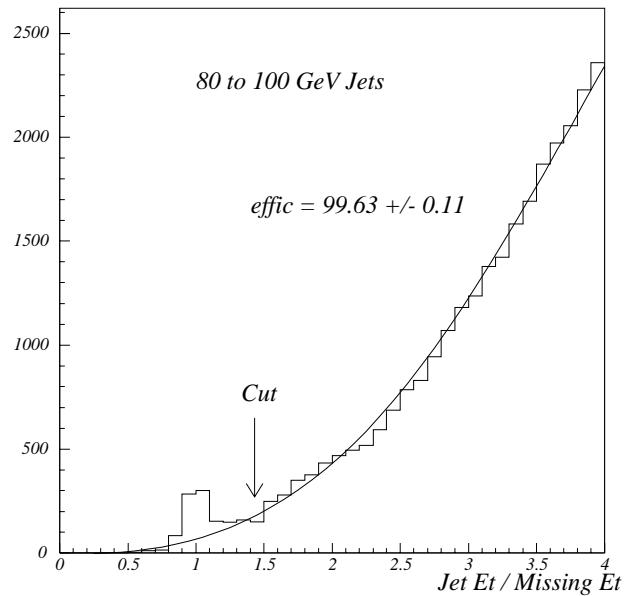
Figure 5.7: The Missing E_T Fraction

104

to have a mean of one. The double–Gaussian yields a poor χ^2, but has the advantage of modelling the observed distribution throughout the entire range. The efficiency is re-calculated from the new curve, and the difference from the nominal result (Equation 5.8) becomes the systematic error.

In events with very high–E_T jets, the $\not{E}_T$ cut loses some of its effectiveness. Occasionally, an analysis requires a "tighter" cut than usual, but never higher than 3.33. Other analyses require specific event topologies, rendering the $\not{E}_T$ cut useless.

Revertexing and the Vertex Cut

Because the length of the proton and antiproton bunches is non-zero, the interaction vertex frequently occurs off-center relative to the detector's nominal $z = 0$ point. During the low energy run, the Tevatron bunches maintained a typical length of 30 cm. The interaction vertex position, well-modeled by a Gaussian distribution, appears in Figure 5.8 for each of the three triggers used in the $\sqrt{s} = 630$ GeV analysis.

The high–luminosity environment at $\sqrt{s} = 1800$ GeV resulted in many multiple interac-tion events in the data set. Inherent in the presence of additional vertices is the possibility of selecting the wrong vertex as the primary for the event, resulting in an erroneous E_T calculation. The DØ reconstruction algorithm attempts to select the most likely primary vertex (or vertices) based on the highest multiplicity of tracks in the Central Drift Chamber, but the primary vertex does not always possess the highest multiplicity of tracks. To avoid mistakes in the case of multiple primary vertices, an offline revertexing algorithm resolves ambiguity by finding the vertex that minimizes the $\not{E}_T$. Because the $\not{E}_T$ is recalculated only approximately with jet balancing, the procedure is often called "(vector) $\mathcal{H}_T$ minimization," where the quantity $\vec{\mathcal{H}}_T$ is the vector sum* of all jet $\vec{E}_T$'s. Main Ring noise is usually not identified as a jet (see **Jet Selection** below); thus, $\vec{\mathcal{H}}_T$ is less sensitive to noise than the full $\not{E}_T$ calculation. In the limit that no electrons, photons, muons, or noisy cells appear in the event, $\vec{\mathcal{H}}_T = \not{E}_T$. As discussed in the previous subsection, the $\not{E}_T$ in QCD events is

---

* Some DØ analyses require a *scalar sum* of all jet E_T's, denoted $\mathcal{H}_T$. To avoid notational similarity, $\vec{\mathcal{H}}_T$ is sometimes denoted $\mathcal{S}_T$.
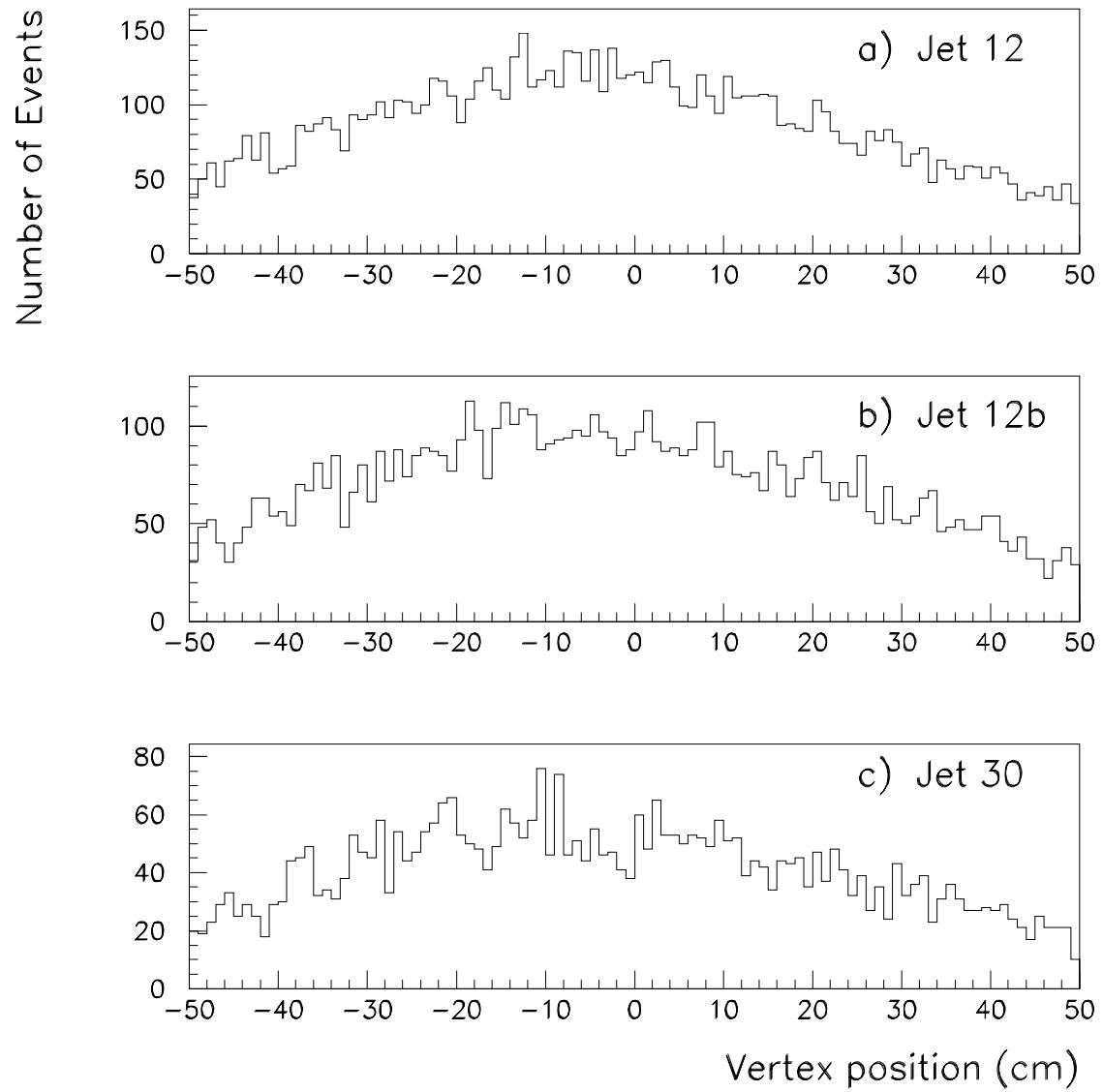
Figure 5.8: The event vertex position distribution for all events in the $\sqrt{s} = 630$ GeV cross section, subdivided by trigger.

approximately zero; thus, the correct vertex will have the least $\not{E}_T$ and an incorrect vertex will likely have significant $\not{E}_T$. The theoretical efficiency of revertexing is unity, and analysis of jet data has been unable to distinguish the real efficiency from that value; thus, no error is apportioned to this procedure. Revertexing decreases the $\sqrt{s} = 1800$ GeV cross section by approximately 5% through most of the spectrum, but at high values of E_T the decrease can approach $\sim 10 - 15\%$. Due to the paucity of multiple interactions at low luminosity, the effect of revertexing at $\sqrt{s} = 630$ GeV is negligible.

DØ's event reconstruction algorithms calculate jet E_T based on the event vertex; given the correct vertex, the accuracy of E_T measurements should not, in principle, be affected by z position of the vertex. The three-piece construction of the detector, however, results in a large change in material density near the ICR; an interaction far from $z = 0$ can result in a low–pseudorapidity jet showering through that region. A restriction of $|z| < 50$ cm applied to the data avoids degradation in jet E_T resolution (as discussed in the next chapter). Although removal of events with off-center vertices improves the precision of the remaining jet sample, the final cross section must account for all discarded events with an efficiency, ϵ_{vert}.

Unlike the rest of the quality criteria, the vertex cut does not remove background; therefore, the efficiency does not require a fit to the "signal" portion of the distribution. Instead, the number of accepted events over the total determines the efficiency, and the error is given by the binomial error formula without a systematic error estimate.

5.2.2 Jet Selection

The following criteria invalidate or accept single jets within an event. Rejection of one jet in an event does not necessarily invalidate any other jets in the same event. By design, these cuts remove both noise and physics objects which can imitate jets while retaining the maximum number of true hadronic showers.

The efficiencies (ϵ_i) for the following jet cuts are determined with a fit to the "signal" portion of each distribution. When extrapolated into the "background" region, the fit

provides an estimate of the number of good jets that are lost in the rejection region. The efficiency is then

$$\epsilon = \frac{n}{n+l},\tag{5.9}$$

where l is the estimated number of jets in the background region and n is the actual number of jets that pass the cut. Statistical uncertainty of the efficiency is determined with the binomial error formula

$$\Delta\epsilon_i = \sqrt{\frac{\epsilon \cdot (1-\epsilon)}{(n+l)-1}}.\tag{5.10}$$

To estimate the systematic uncertainty, the deviation of the original result from that of a second functional form in the signal region is added in quadrature to the binomial error.

The Electromagnetic Fraction Cut

Because electrons and photons interact with matter on relatively short distance scales, they tend to deposit all of their energy in the first few layers of the calorimeter (*cf* radiation lengths versus nuclear interaction lengths, Chapter 2). The fraction of all energy in the first few layers of the calorimeter effectively discriminates between electromagnetic and hadronic showers. The electromagnetic fraction (EMFR) of a jet candidate is defined as the fraction of the total E_T which lies in calorimeter layers EM1-EM4.

Jets emerge from the beampipe as clusters of hadronic particles, primarily composed of $\pi^{\pm}$ and π_0 mesons. Unlike the charged pions, the uncharged pions interact electromagnetically by rapidly decaying to two photons. Fluctuations may result in jets composed primarily of π_0's, thus resulting in losses of real jets with an EMFR cut.

Figure 5.9 displays the EMFR distribution for jet E_T between 140 and 160 GeV. Jets must possess an EMFR between 0.05 and 0.95 to satisfy the criteria. Very few jets lie in the excluded region; the Gaussian fit indicates an efficiency of 99.77%.

The Coarse Hadronic Fraction Cut

The Main Ring beampipe pierces the DØ calorimeter near the top; while Fermilab stacks protons and antiprotons, Main Ring beam losses appear as energy in the outermost layer of
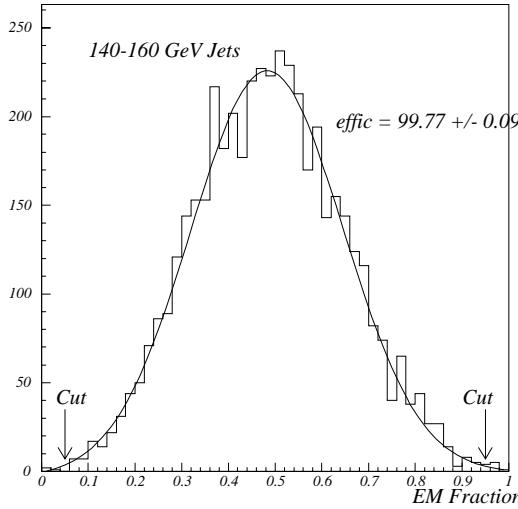
Figure 5.9: The EMFR distribution for a selected jet E_T range.

the DØ calorimeter (the coarse hadronic layer). The coarse hadronic E_T fraction (CHFR) is the ratio of the transverse energy in this outermost layer to that of the entire jet. The jet CHFR distribution (Figure 5.10), while primarily exponential in shape, displays activity at larger values. To eliminate jets contaminated with Main Ring energy, DØ analyses require a jet to have less than 40% of its entire E_T in the last layer.

The Hot–Cell Fraction Cut

Occasionally, electrical discharges in calorimeter cells contribute to jet E_T. These artificially hot cells can severely distort the cross section spectrum. Unfortunately, a jet can occasionally deposit a large fraction of its energy in a single cell. Hot–Cell Fraction (CelFR) is the E_T ratio of the first and second "hottest" cells in a jet. Figure 5.11 reveals the CelFR distribution as exponentially falling, with the cut criterium set at a value of ten. The two curves indicate the results of fits with slightly different parameterizations (to determine the systematic uncertainty). In low–statistics analyses, the cut criterium shifts from 10 to 20 to maximize jet statistics in the remaining sample, resulting in an increased efficiency.
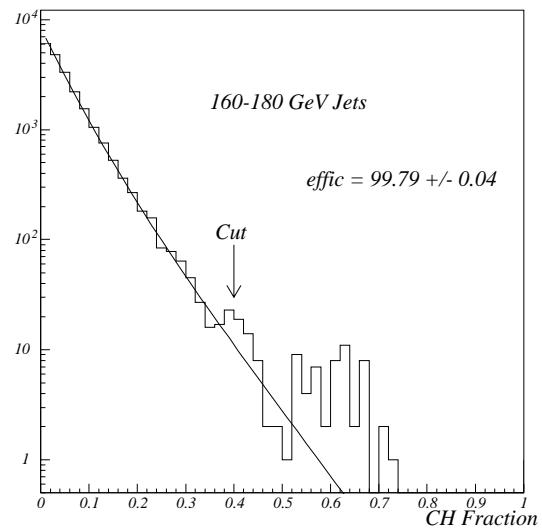
Figure 5.10: The CHFR distribution.
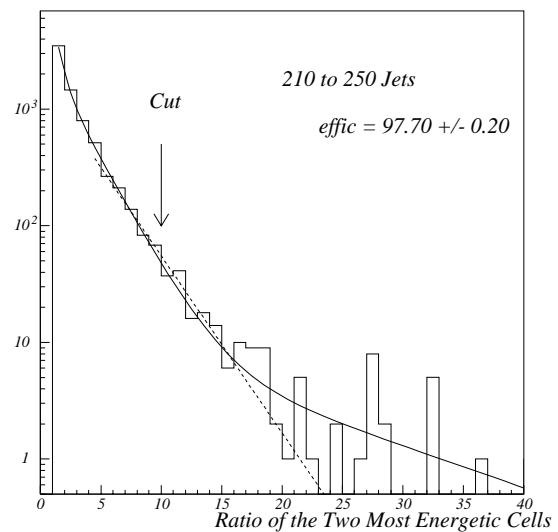
Figure 5.11: The CelFR distribution.
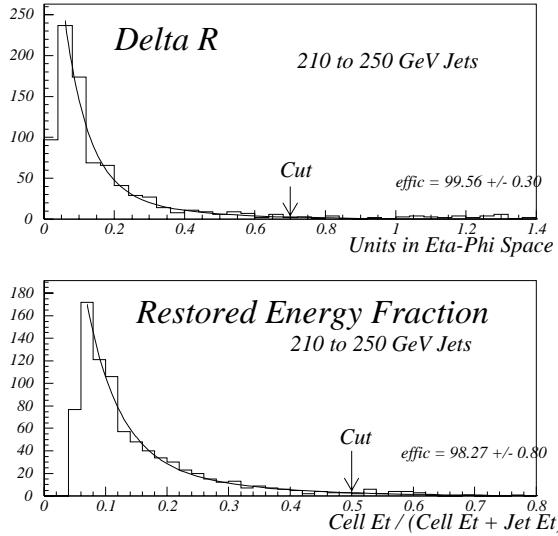
Figure 5.12: The cuts of the jet restoration procedure. (Top) Most AIDA cells lie within the $R = 0.7$ jet cone definition. (Bottom) Restoration of AIDA cells typically increases jet energy but never by more than a factor of two.

Cell Restoration

In an attempt to reduce the effect of hot cells during data–taking, the DØ collaboration implemented an algorithm that flagged the most energetic cells within jets; during data reconstruction, these "killed" cells were simply overlooked by the jet algorithm. The AIDA routine* successfully reduced the background rate for top quark and supersymmetry analyses, but inappropriately distorted the inclusive jet cross section by removing valid cells from high E_T jets. To correct the overzealous nature of the algorithm, the killed cells must be restored offline.

Jet restoration is accomplished in three steps. First, AIDA cells outside each jet's cone radius are removed from consideration (*i.e.*, they will continue to be ignored). This radius criterium is abbreviated "Del_R< 0.7." Second, a table of typically noisy cells is consulted; AIDA cells corresponding to known hot cells are removed from consideration. Third, each

---

* AIDA is both an acronym for **A**nomalous **I**solated **D**eposit **A**lgorithm and the name of an opera.

AIDA cell is added to the existing jet if the result will not exceed twice the original jet's E_T. This criterium is expressed "R_FRAC< 2.0." Figure 5.12 illustrates the measured efficiency of the procedure. After restoration, the jets must still satisfy the EMFR and CHFR cuts; the CelFR of a restored jet cannot be calculated without a new reconstruction, so the CelFR criterium is released in the case of a restored jet.

5.2.3 Data Selection Efficiency Summary

As a prerequisite to appearance in the inclusive jet cross section, all jet events must satisfy two criteria: the event must possess low $\not{E}_T$ relative to the leading jet E_T, and the vertex position must lie within 50 cm of the geometric center of the detector. Each jet in the cross section must satisfy three quality criteria: the jet must not have excessive EM activity, must not have excessive Main Ring activity, and must not have too much energy concentrated in a single calorimeter cell. Some jets, "damaged" during reconstruction, are restored according to another recipe.

Tables 5.6 and 5.7 list the efficiency of each jet criterium as measured for specific energy bins in the $\sqrt{s} = 1800$ GeV data set. The global jet efficiency is given by the product of jet selection efficiencies (EMFR, CHFR, CelFR, Del_R, R_FRAC) and event selection efficiencies (METFR), as listed in Table 5.8. By parameterizing the efficiency data, statistical uncertainties are minimized and each jet is corrected as it is added to the histogram. Figure 5.13 displays the parameterizations of the jet and event selection efficiencies.

5.3 The Raw Cross Section

The inclusive jet cross section at $\sqrt{s} = 630$ GeV consists of data collected with three triggers. The jet spectra for each trigger are displayed in Figure 5.14. Each of the three distributions exhibit two peaks. The trigger design causes the local maxima at high E_T: each trigger sample includes only events with at least one jet above the trigger threshold. Although the true jet distribution decreases monotonically in E_T, inefficiencies in trigger "turn–on" result in losses of jets with E_T near or somewhat higher than the trigger threshold, causing the

EMFR

Et bin	r	r'ı	n	effic	stat error	sys error	total error
60-80	21	75	38397	0.99875	0.00018	0.000703	0.000726
80-100	6.7	44	8097	0.996869	0.000621	0.002303	0.002386
100-120	12.3	27	31492	0.999376	0.000141	0.000233	0.000273
120-140	7.2	17	10451	0.998842	0.000333	0.000469	0.000575
140-160	3.65	10	4054	0.998316	0.000644	0.000783	0.001014
160-180	17.7	26	19063	0.998854	0.000245	0.000218	0.000328
180-210	12.1	23	10783	0.998372	0.000388	0.000505	0.000637
210-250	9.3	17	6576	0.998	0.000551	0.000585	0.000804
250-300	2.7	10	1862	0.99659	0.001351	0.00196	0.002381
300+	2.8	9	615	0.990407	0.003931	0.005041	0.006392

CHFR

Et bin	r	r'ı	n	effic	stat error	sys error	total error
60-80	162.4	300	31852	0.992741	0.000476	0.00216	0.002212
80-100	26.1	58	7580	0.994453	0.000853	0.002104	0.002271
100-120	83.3	103	28844	0.996771	0.000334	0.000341	0.000478
120-140	26.5	31	10122	0.99716	0.000529	0.000222	0.000574
140-160	3.6	10	4049	0.998321	0.000643	0.00079	0.001019
160-180	40	54	21640	0.997828	0.000316	0.000323	0.000453
180-210	34.1	45	12800	0.99691	0.000491	0.000426	0.00065
210-250	26.8	32	8344	0.996477	0.000649	0.000312	0.00072
250-300	8.6	14	2552	0.995572	0.001314	0.001058	0.001687
300+	3	7	779	0.993582	0.002861	0.002567	0.003844

CELFR

Et bin	r	r'ı	n	effic	stat error	sys error	total error
60-80	615	633	34278	0.981796	0.000722	0.000263	0.000768
80-100	126	146	7310	0.981395	0.00158	0.001368	0.00209
100-120	554	645	28077	0.978648	0.000863	0.001621	0.001836
120-140	201	206	9640	0.97889	0.001464	0.000259	0.001487
140-160	82	99	3751	0.975873	0.002505	0.002266	0.003378
160-180	454	464	19277	0.976189	0.001098	0.000259	0.001128
180-210	251	271	11084	0.976453	0.00144	0.000902	0.0017
210-250	172	186	6992	0.974399	0.001889	0.001001	0.002138
250-300	59	65	1844	0.966377	0.004198	0.001627	0.004502
300+	13	17	581	0.974182	0.006579	0.003442	0.007426

Table 5.6: Jet cut efficiencies at $\sqrt{s} = 1800$ GeV.

METFR

Et bin	r	r'ı	n	effic	stat error	sys error	total error
60-80	1126	940	766850	0.998653	4.19E-05	0.000121	0.000128
80-100	669	420	413975	0.998685	5.63E-05	0.000301	0.000306
100-120	748	410	508739	0.998862	4.73E-05	0.000332	0.000336
120-140	802	270	225779	0.997626	0.000102	0.001178	0.001183
140-160	545	225	107189	0.996408	0.000183	0.001493	0.001504
160-180	225	78	44011	0.996558	0.000279	0.00167	0.001693
180-210	125	62	23995	0.996103	0.000402	0.001313	0.001373
210-250	40	25	8698	0.996264	0.000654	0.000862	0.001082
250-300	22	9	2333	0.993356	0.001682	0.002786	0.003254
300+	5	12	733	0.988404	0.003954	0.004775	0.0062

RFRAC

Et bin	r	r'ı	n	effic	stat error	sys error	total error
60-80	22.7	28	1134	0.977646	0.00439	0.002337	0.004973
80-100	4	9	347	0.981268	0.007278	0.007205	0.010241
100-120	33.12	40	1789	0.979564	0.003345	0.001923	0.003858
120-140	3.6	13	705	0.988227	0.004062	0.006667	0.007807
140-160	0.89	5	292	0.989914	0.005847	0.007038	0.00915
160-180	10.7	22	1874	0.991275	0.002148	0.003015	0.003702
180-210	10.4	13	1224	0.990441	0.002781	0.001062	0.002977
210-250	8	21	835	0.982635	0.004521	0.007784	0.009002
250-300	3.1	8	307	0.981922	0.007604	0.00798	0.011023
300+	1.3	3	124	0.982661	0.011722	0.006855	0.013579

DEL_R

Et bin	r	r'ı	n	effic	stat error	sys error	total error
60-80	0.54	8	1756	0.997568	0.001175	0.002124	0.002428
80-100	0.21	1	380	0.998408	0.002045	0.001039	0.002294
100-120	1.34	5	1757	0.998196	0.001012	0.001042	0.001453
120-140	0.41	4	703	0.996863	0.002109	0.002553	0.003312
140-160	0.31	2	292	0.996045	0.003673	0.002894	0.004676
160-180	2.21	10	1856	0.996711	0.001329	0.002099	0.002484
180-210	1.4	4	1214	0.997776	0.001352	0.001071	0.001725
210-250	1.8	4	828	0.996498	0.002053	0.001329	0.002445
250-300	0.25	1	304	0.997944	0.002598	0.001234	0.002876
300+	0.68	1	123	0.993171	0.007426	0.001301	0.007539

Table 5.7: METFR efficiency and jet restoration efficiencies at $\sqrt{s} = 1800$ GeV.

114
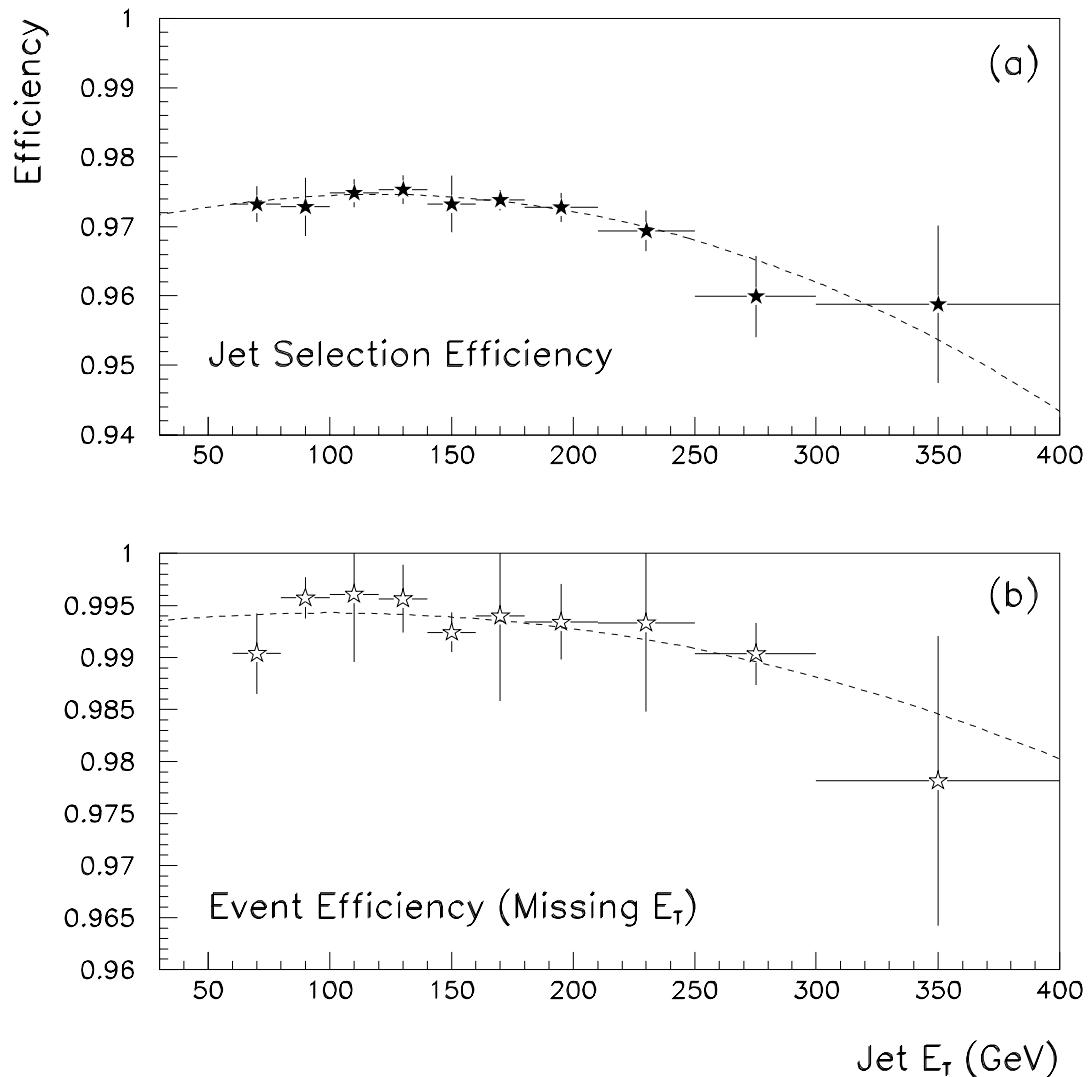
Figure 5.13: The jet and event cut efficiency for $\sqrt{s} = 1800$ GeV. Vertex cut efficiency is not included.

GLOBAL (all Jets)		
Et bin	effic	error +/-
60-80	97.3236	0.2569
80-100	97.2824	0.4205
100-120	97.4834	0.2035
120-140	97.5333	0.2083
140-160	97.3219	0.4086
160-180	97.3802	0.1492
180-210	97.2747	0.2052
210-250	96.9398	0.2943
250-300	95.9903	0.5882
300+	95.8802	1.1135

GLOBAL (all Jets)		with MET
Et bin	effic	error +/-
60-80	97.1925	0.2572
80-100	97.1544	0.4216
100-120	97.3725	0.2062
120-140	97.3018	0.2395
140-160	96.9723	0.4354
160-180	97.0450	0.2257
180-210	96.8956	0.2469
210-250	96.5776	0.3136
250-300	95.3525	0.6722
300+	94.7684	1.2745

Table 5.8: The global data selection efficiencies, before and after the missing E_T cut.

rounded appearance of the high E_T peak. The maxima at low E_T (~ 8 GeV) result from events that contain low E_T additional jets.

To form the inclusive jet cross section, a region of each trigger is selected to maximize statistical power while maintaining full trigger efficiency. Any given cross section bin receives contributions from one and only one trigger. The luminosity in any given bin is the luminosity exposure for that trigger, given in Table 3.2, page 60. The non–overlap of triggers ensures an unambiguous luminosity determination.

The inclusive jet cross section at $\sqrt{s} = 1800$ GeV was determined prior to the 630 GeV analysis. To facilitate the ratio calculation in x_T, the bin boundaries for the 630 GeV analysis were selected such that

$$E_T^{630} = \frac{315}{900} \cdot E_T^{1800},$$ (5.11)

i.e., such that the bin edges match in x_T–space. Most of the resulting bins are 3.5 GeV wide, but some bins have a GeV width of 7.0, 10.5, or more.

Figure 5.15 displays the raw cross section at $\sqrt{s} = 630$ GeV. The three different markers indicate the E_T region for each jet trigger. Horizontal lines indicate the bin widths, and vertical lines (mostly hidden by the markers) indicate the statistical uncertainty on each point. Markers are located in the center of each bin.
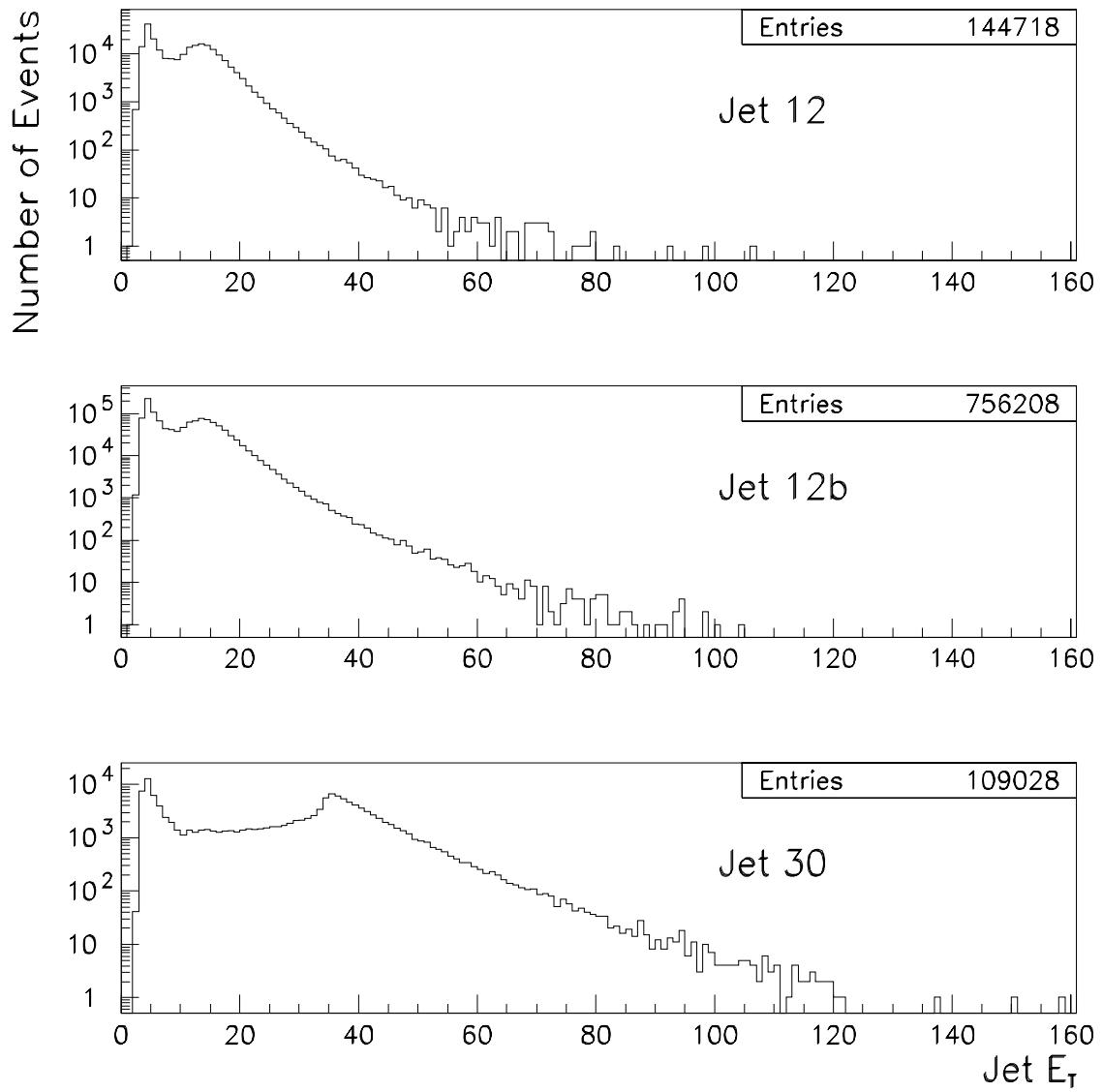
Figure 5.14: Number jets collected by each jet trigger, as functions of E_T. Each histogram bin is one GeV wide.
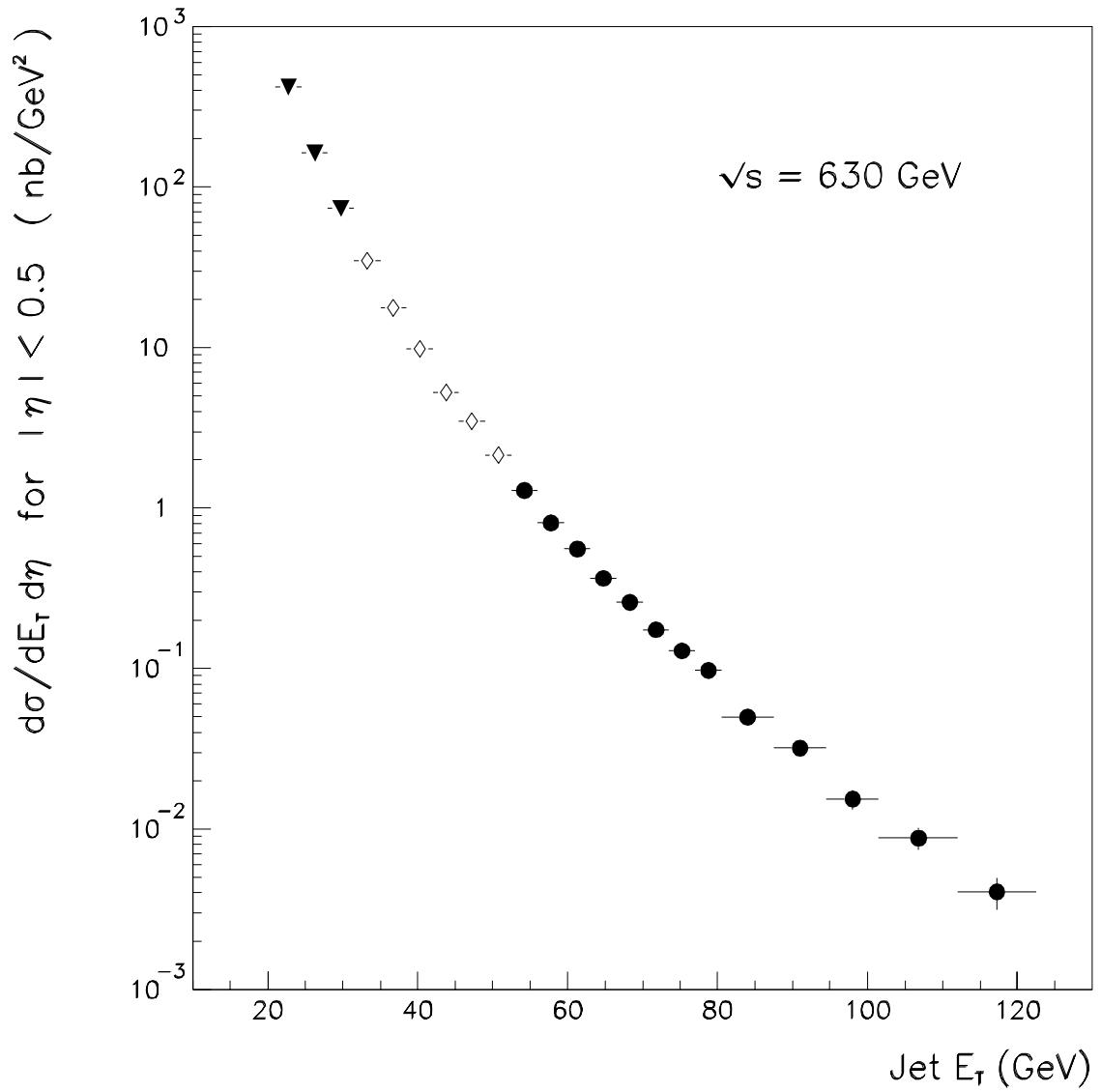
Figure 5.15: The "raw" inclusive jet cross section for $\sqrt{s} = 630$ GeV. Markers indicate the three jet triggers (shaded triangles: Jet 12, hollow diamonds: Jet 12b, black circles: Jet 30).

118

5.4 Summary

At the most basic level, the inclusive jet cross section analysis is a counting experiment, where the number of jets on an interval of E_T is scaled by the integrated luminosity, the selection efficiency, and the width of the bin in E_T and pseudorapidity. The end result describes the probability of observing a jet with particular transverse energy; in the units of high energy physics, this "differential cross section" has units of area/energy^2.

The luminosity is determined by the Level Ø counting rate, scaled by the p$\bar{\text{p}}$ inelastic cross section times the probability of detecting a p$\bar{\text{p}}$ interaction. The integrated luminosity is thus a measure of the number of chances that DØ might observe a jet event.

The selection efficiency describes how often a single jet or entire jet event is rejected on the basis that it appears to originate from noise or background effects. Several different criteria differentiate "good" jets from contamination and the efficiency of each must be calculated separately. The product of these efficiencies yield the total factor that corrects the jet cross section.

To measure the ratio of cross sections on a bin–by–bin basis, the width of the E_T "slices" must match between center–of–mass energies. Because the bin sizes must match in x_T units, the bins at $\sqrt{s} = 630$ GeV are roughly one–third the size of those at 1800 GeV.

Chapter 6

Unsmearing

**or, Correcting for the Effect of Finite Energy Resolution
in the Inclusive Jet Cross Section**

Stochastic variations in jet energy result in a distortion of the cross section E_T spectrum. Although jets may be mismeasured above or below the true E_T with equal frequency, a systematic shift in the cross section results. This effect, "smearing," results from the steeply falling nature of the E_T spectrum.

Consider a steeply falling distribution measured in five bins (Figure 6.1, top), assuming that "nature" determines the numbers of events in each bin, and also in bins to the left and right of the measured region. Assigning x as the measured quantity of each event, postulate that x is *always* mismeasured by ± 0.1, with a 50% probability of being mismeasured as larger than the true value and 50% probability of being mismeasured as smaller than the true value. As a result, some fraction of the events in each bin migrate to neighboring bins; both to the left and to the right (Figure 6.1, center). Because the bins decrease sharply in population as x becomes larger, more events migrate to the right than to the left across each bin border. The measured distribution may thus be significantly larger than the distribution determined by nature (Figure 6.1, bottom). In this example, the measured distribution differs from the true distribution by nearly a factor of two.

More realistically, a variable will be mismeasured to a *randomized* degree. The measured value is then displaced about the true value in a Gaussian distribution, rather than shifted
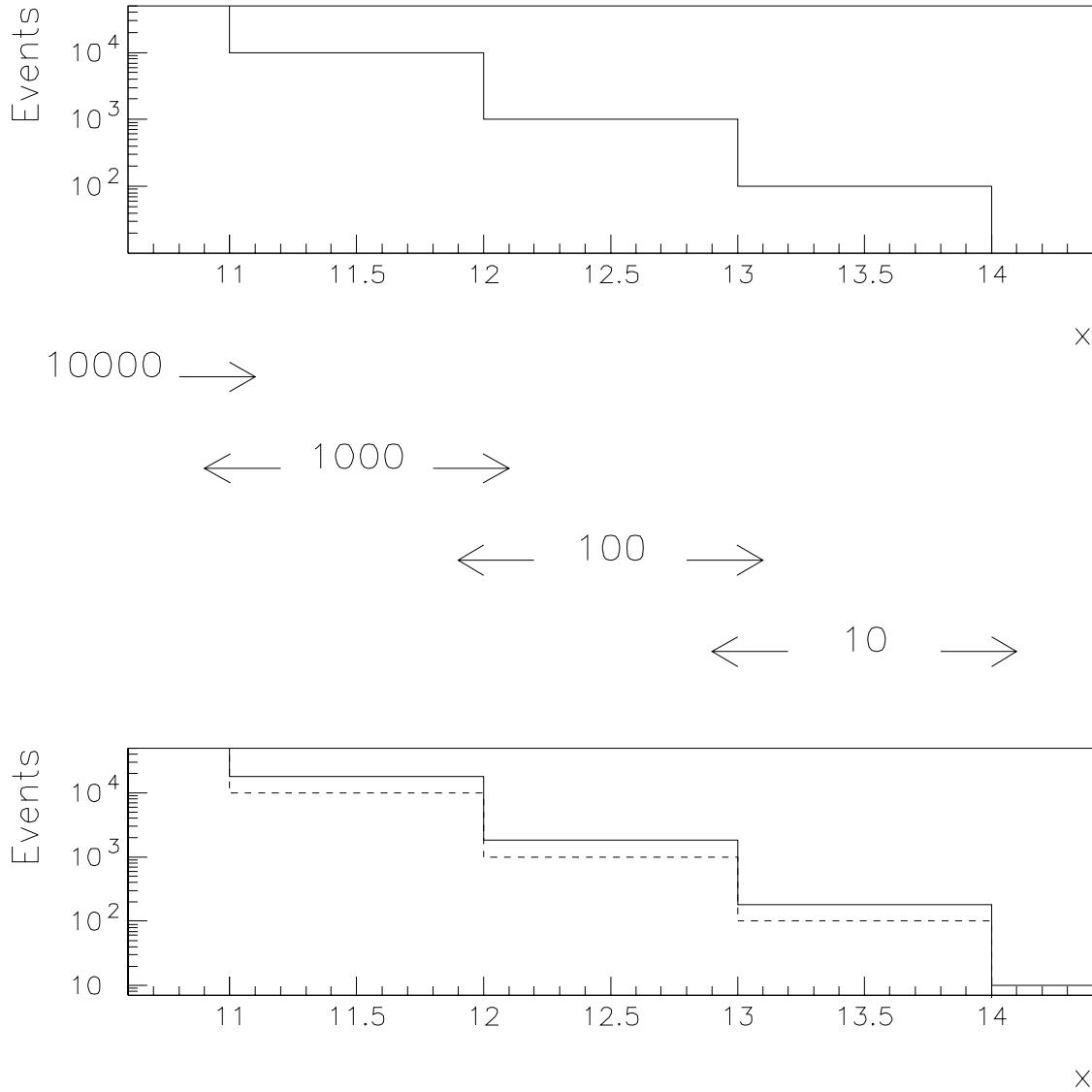
Figure 6.1: Illustration of the smearing effect. If the distribution of some variable x (Top) is mismeasured by 10%, a fraction of all events migrate across bin boundaries (Center). In the case of a steeply falling distribution, the resulting measured distribution (Bottom, solid line) is significantly larger than the true distribution (Bottom, dashed line).

by 10% as in the example. As an additional complication, the average displacement (the width of the Gaussian) need not remain constant as a function of the variable x. Such is the case with the mismeasurement of jet E_T in the inclusive jet cross section. The fractional mismeasurement, called the *jet E_T resolution*, is expressed as $\frac{\sigma_{E_T}}{E_T}$, where σ_{E_T} is the width of the Gaussian that describes the observed randomized displacements at a particular E_T.

The following sections describe the methods used to measure jet resolution and introduce the *unsmearing* technique. The error analysis follows the covariance techniques outlined in Appendix B. The resolution analysis is based on Reference [36], which documents the resolution calculations for the $\sqrt{s} = 1800$ GeV data. The reference also contains a preliminary result for $\sqrt{s} = 630$ GeV based on 18% of the full data sample; this chapter builds on the prior work.

6.1 Jet Energy Resolution

"The only limits are, as always, those of vision."
— James Broughton

The $\sqrt{s} = 1800$ GeV data set provides ample statistics for jet resolution measurements. Using the inclusive jet sample, the dijet asymmetry technique matches the two highest E_T jets in an event. Unfortunately, this data sample does not extend below 40 GeV, where resolutions change rapidly. This limitation complicates comparisons to the $\sqrt{s} = 630$ GeV sample.

In addition to stochastic calorimeter effects, the asymmetry measurement includes two extraneous contributions: biases from additional jets in an event, and the particle–level asymmetry inherent in the jet definition. The bias in the measurement is removed with an E_T–dependent correction as determined with data, while the particle–level asymmetry is removed with a Monte Carlo simulation.

6.1.1 Dijet Asymmetry Measurements

Also called the *dijet balance,* the dijet asymmetry is a measure of the degree to which the E_T's of the leading jets match. Because a $p\bar{p}$ collision initially has nearly zero transverse
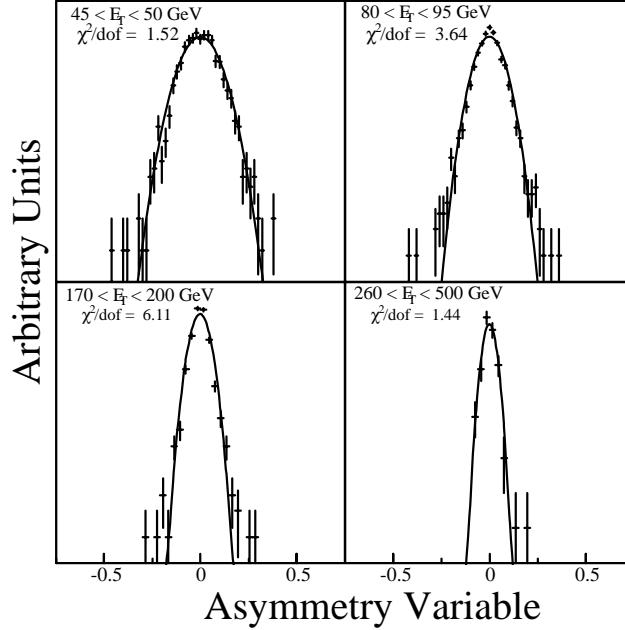
Figure 6.2: The observed dijet asymmetry for the central ($|\eta| < 0.5$) region, with $\sqrt{s} = 1800$ GeV. Scale is logarithmic. Simple Gaussian fits describe the data accurately.

momentum, a true dijet event must exhibit perfect E_T balance between jets. The dijet asymmetry provides a nearly direct measure of the E_T spread expected from a typical jet.

For notational convenience, define x and y as the E_T of the two jets in the event. The *dijet asymmetry* is then given by

$$A = \frac{x - y}{x + y}. \tag{6.1}$$

In the limit that $x \approx y \equiv E_T$ and $\delta x \approx \delta y \equiv \sigma_{E_T}$, the variance of the asymmetry in Equation 6.1 is simply related to the fractional transverse energy resolution:

$$dijet \; \frac{\sigma_{E_T}}{E_T} = \sqrt{2}\sigma_A, \tag{6.2}$$

where σ_A is the width of the A distribution, a smooth Gaussian (Figure 6.2).
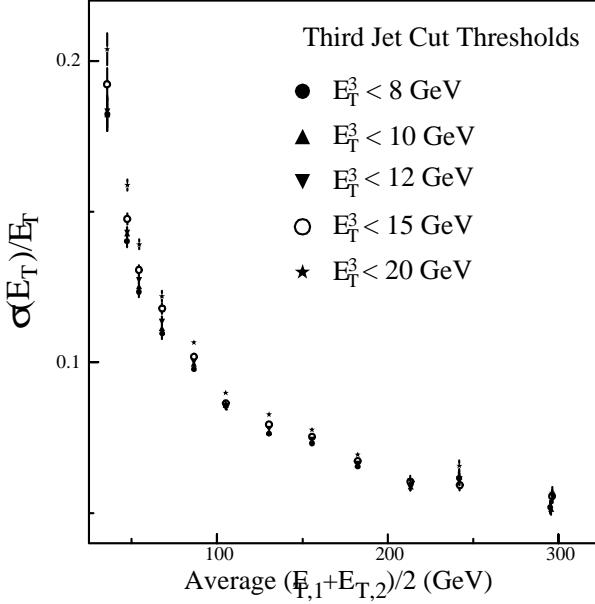
Figure 6.3: Asymmetry for different third–jet thresholds ($\sqrt{s} = 1800$ GeV).

6.1.2 The Soft Radiation Correction

Higher-order contributions can result in the production of three or more jets, destroying the balance of the two leading jets. Because the DØ reconstruction algorithm ignores jets with E_T less than 8 GeV, additional jets in an event may not be visible. Thus, the imbalance in the two observed jets cannot be entirely attributed to jet resolution effects—the spectrum of $\frac{\sigma_{E_T}}{E_T}$ must be corrected for the effect of undetected jets. QCD three–jet events dominate QCD events with four or more jets by factors of α_s, so this resolution analysis neglects the effect of more than one additional jet. With this approximation, the soft radiation correction is often termed the "third–jet bias" correction.

The correction is derived from an extrapolation [36] based on events with third jets of known E_T. The asymmetry of the leading two jets is measured as a function of the E_T of the third jet. The asymmetry data are then extrapolated to $E_T^{3rd} = 0$; the ratio of the asymmetry in dijet events (with an unknown number of third jets below the 8 GeV reconstruction threshold) and the extrapolated result provides a correction factor K. Figures 6.3, 6.4, and
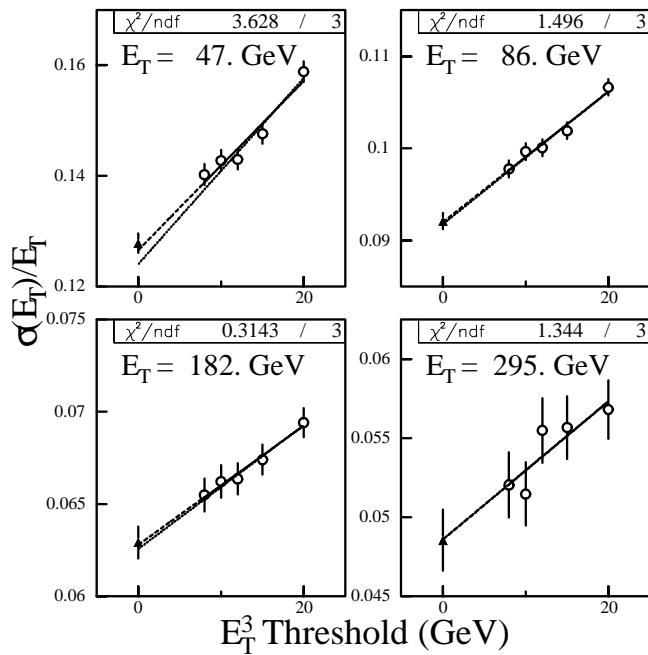
Figure 6.4: Extrapolation of asymmetry to a zero third–jet threshold. ($\sqrt{s} = 1800$ GeV.)
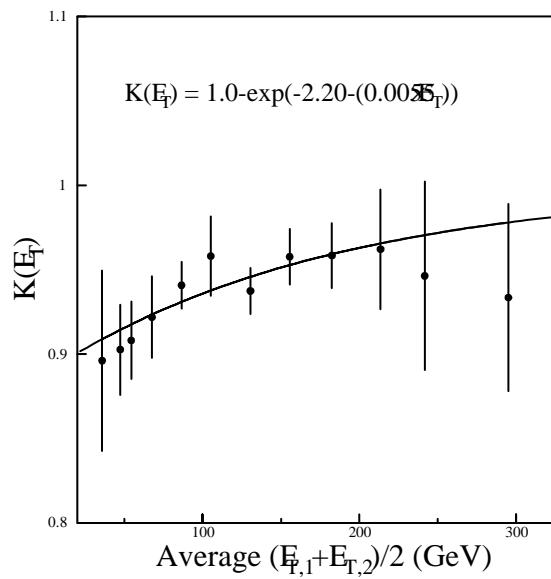
Figure 6.5: The soft radiation correction as a function of Jet E_T at $\sqrt{s} = 1800$ GeV.

6.5 show the results of this procedure for $\sqrt{s} = 1800$ GeV. Because third jets are relatively uncommon at $\sqrt{s} = 630$ GeV, the correction factor is approximately unity for that data set.

6.1.3 Particle–Jet Asymmetry

As mentioned briefly in Chapter 4, jets should be corrected back to the "particle level," a concept closely tied to the cone definition of jets. A cluster of particles emerging from the beampipe will have some spatial distribution and a cone drawn around their centroid may not include all particles in that cluster. Although particles outside the cone boundary are not by definition part of the jet, they nonetheless possess some fraction of the E_T required to balance other objects in the event. Occasional losses of particles outside the cone definition result in a "natural" dijet imbalance, the effects of which should *not* be removed from the cross section.

As with the showering correction in the energy scale chapter, the HERWIG Monte Carlo event generator provides a measure of the out–of–cone losses, and thus a measure of the particle–level asymmetry. Measuring the particle–jet imbalance and subtracting the result (in quadrature) from the data asymmetry (after the soft correction) isolates the true detector resolution. Figure 6.6 compares the soft radiation–corrected resolution to the particle–jet imbalance.

6.1.4 Resolution Parameterization

A three-parameter fit describes the final resolution data for $\sqrt{s} = 1800$ GeV,

$$\frac{\sigma_{E_T}}{E_T} = \sqrt{\frac{n^2}{(E_T)^2} + \frac{s^2}{E_T} + c^2},$$

(6.3)

as depicted in Figure 6.7. Table 6.1 lists the values of the fit parameters and the elements of their covariant uncertainty matrix. In this traditional fit, the first parameter simulates fluctuations with a constant magnitude for all jet E_T values; this "noise" term primarily describes the low E_T resolution. The second term, "sampling," describes the intermediate E_T range. The third parameter defines the asymptotic minimum of the asymmetry at
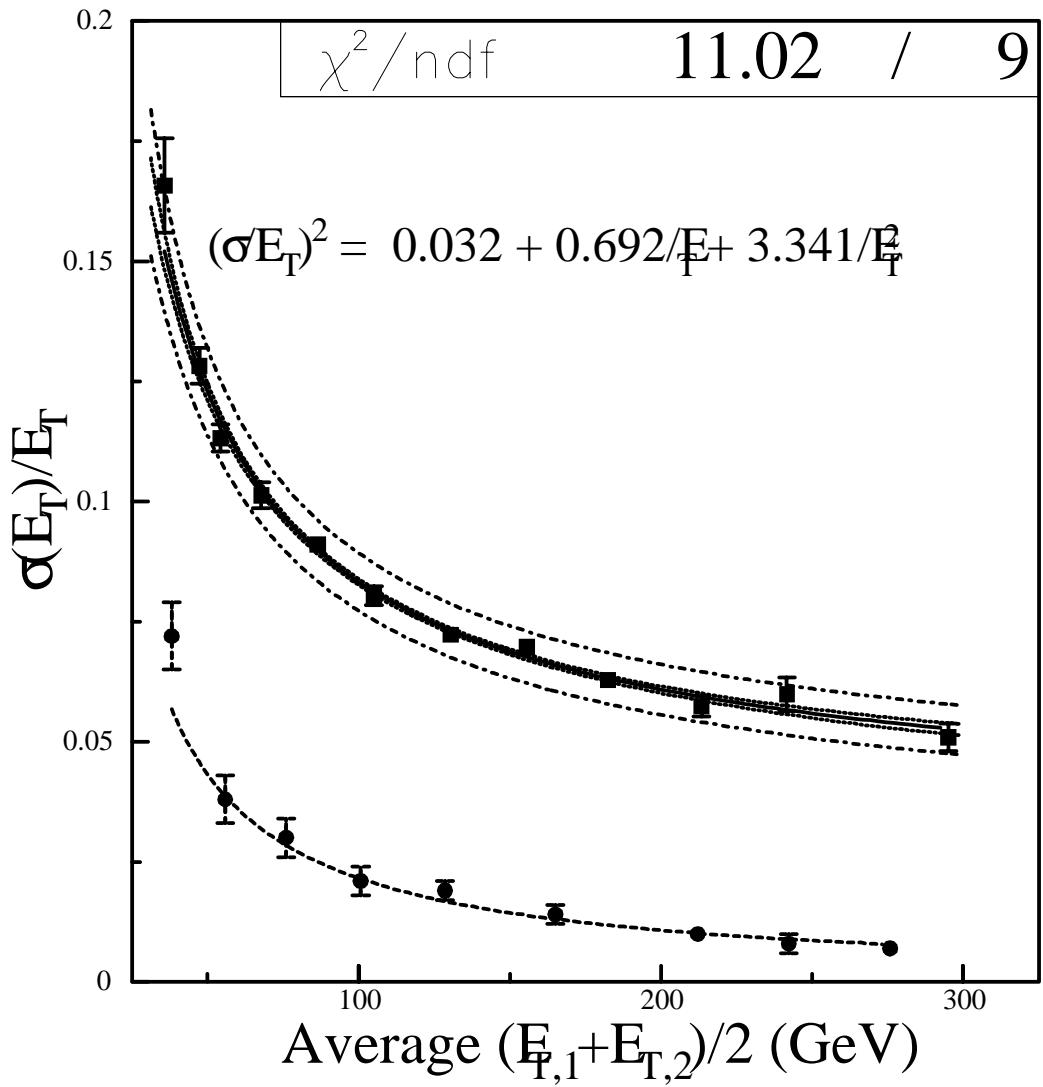
Figure 6.6: The jet E_T resolution curve after the soft radiation correction (upper set of points) with fit errors (shaded band) and systematic uncertainty (dash–dot line). The particle–jet correction (bottom set of points) will be subtracted in quadrature.

Parameter	Value	Error Matrix		
c	0.033	3.6×10^{-5}	-3.62×10^{-4}	0.0037
s	0.686	-3.62×10^{-4}	0.004225	-0.0486
n	2.621	0.0037	-0.0486	0.6561

Table 6.1: The parameters and covariant uncertainties of the 1800 GeV resolution fit. The fit yields $\chi^2 = 16.87$ for 9 degrees of freedom, or a 0.051% probability.

high E_T. Motivated by test beam results, the traditional parameterization contains the underlying assumption that jet E_T resolutions may be parameterized as though they were pion energy resolutions.

6.1.5 Modifications for 630 GeV

Although the 1800 GeV resolution data spans a wide range in E_T and results in a well–constrained fit, a fit to the sparse data at $\sqrt{s} = 630$ GeV cannot yield a similarly precise result. Two modifications to the basic asymmetry method supplant the otherwise insufficient data at 630 GeV: the inclusion of asymmetry data from photon–jet events and the "twin fit" technique. The former incorporates data from lower E_T than would be possible with dijet data alone, and the latter links the behavior of the resolution curves between center–of–mass energies. The following subsections detail these two modifications to the standard method.

Inclusion of Photon–Jet Asymmetry Measurements

The relative rarity of photon-jet events compared to dijet events and the limited running time at $\sqrt{s} = 630$ GeV provide low statistics for photon-jet asymmetry measurements above 30 GeV in E_T. The advantage of photon-jet measurements arises from trigger considerations. Because photon triggers are more sensitive to low-E_T events than jet triggers, the data sample can complement dijet measurements and extend knowledge of the jet resolution to much lower E_T than otherwise possible.

As described in the calorimeter section of Chapter 2, the DØ detector measures purely electromagnetic showers with much higher precision than hadronic showers. The energy res-
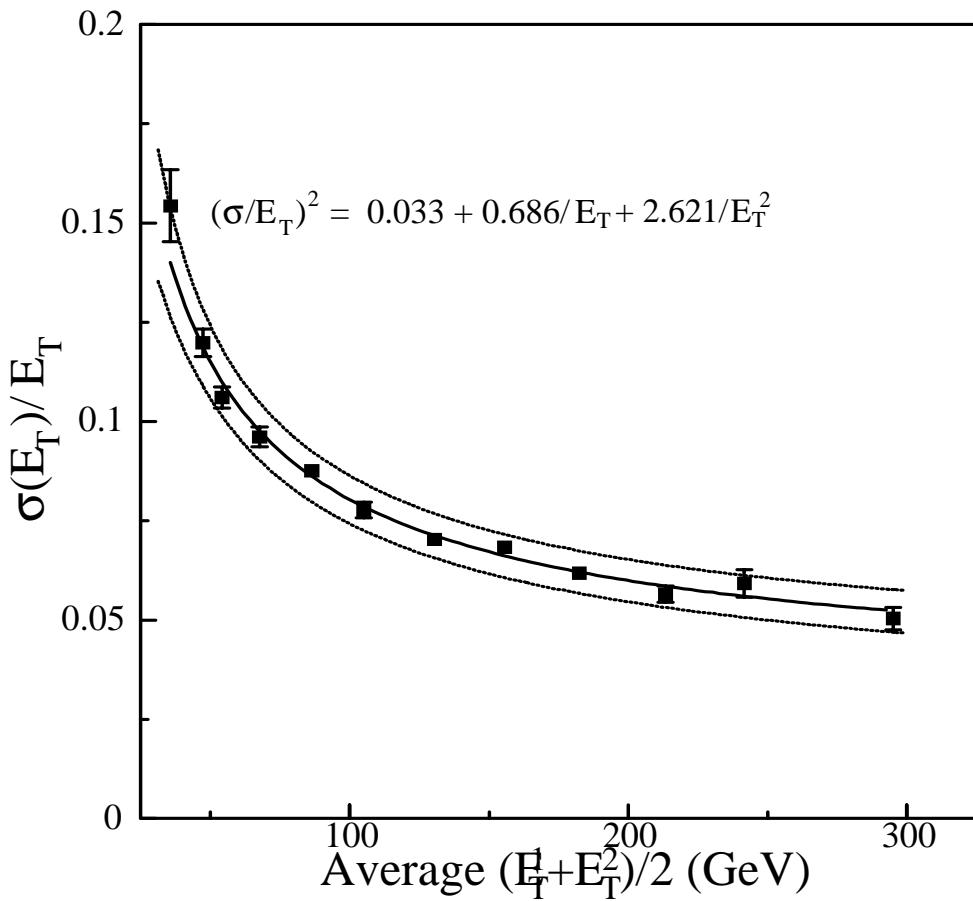
Figure 6.7: Fully–corrected resolution data for $\sqrt{s} = 1800$ GeV. The three–parameter fit (solid line) is well–constrained. Hatched lines indicate the systematic uncertainty, as described in a later section.
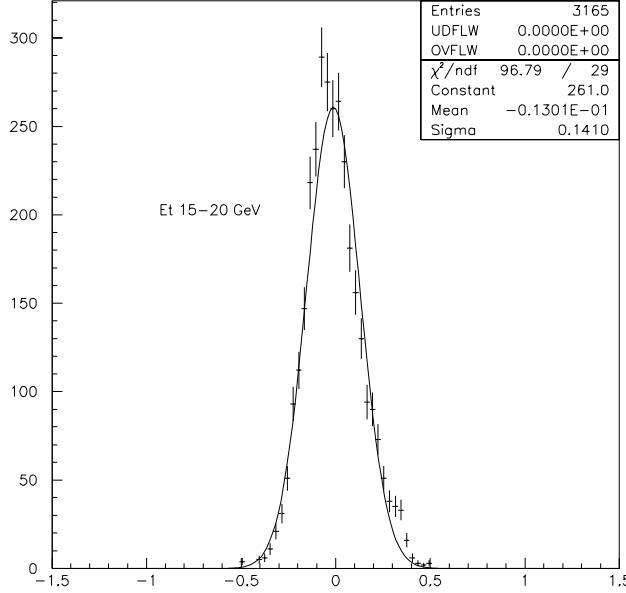
Figure 6.8: Distribution of photon-jet asymmetry for jet E_T between 15 and 20 GeV in the central region. Inset are the number of events, the χ/n, and the values of the fit parameters.

olution for photons is approximately 10 times better than that of a jet, allowing a convenient redefinition of Equation 6.1. The *photon–jet asymmetry* is defined as

$$photon\text{–}jet \ A = \frac{x-y}{y}, \tag{6.4}$$

where x and y are the photon and jet transverse energies, respectively. If one approximates $x \approx y \equiv E_T$ as before, and lets $\delta x \approx 0$, the standard deviation of the photon-jet asymmetry identically becomes the fractional jet resolution:

$$photon\text{–}jet \ \frac{\sigma_{E_T}}{E_T} = \sigma_A. \tag{6.5}$$

Figure 6.8 displays a typical distribution of photon-jet asymmetry.

As described in previous sections, the measured resolution is adjusted to reflect third-jet biases and the particle–jet asymmetry. The results bolster the low–statistics dijet results at $\sqrt{s} = 630$ GeV.

The Twin Fit Technique

Although the resolution data at 1800 GeV provide a well–constrained fit, the larger uncertainties of the 630 GeV data allow a large range of variation; independent parameterizations for the two data sets can actually cross one another at high values of E_T. The three parameters, c, s, and n, are highly correlated and can settle into this non–physical *crossing* behavior despite their common interpretation as "noise," "showering," and "constant" terms. The following method removes non-physical asymptotic behavior and much of the correlation between parameters by fitting both data sets simultaneously with shared parameters.

Dijet events fall into one of three categories: quark–quark, quark–gluon, or gluon–gluon final states. Gluons hadronize differently from quarks, having higher particle multiplicity (and somewhat lower individual particle E_T's). Variations in measured jet E_T depend on the quadrature sum of the individual particle fluctuations; thus, the DØ calorimeter measures jets with a different degree of precision, depending on whether the jet's parent was a gluon or a quark. Because the difference in resolution appears primarily at intermediate E_T and not at the asymptotes, the s parameter is re–expressed in terms of three components,

$$s \rightarrow s\left(x_T\right) = F_{qq}\left(x_T\right) \cdot s_{qq} + F_{qg}\left(x_T\right) \cdot s_{qg} + F_{gg}\left(x_T\right) \cdot s_{gg}, \tag{6.6}$$

where each final state category has its own "sampling" term, weighted by the fraction of all events represented by that final state. The final state fractions are functions of jet E_T. Alternatively, transformation to jet x_T reveals the commonality between center–of–mass energies (Figure 6.9), such that a single smooth curve describes the final state fractions of both data sets. After incorporation of Equation 6.6, the new resolution function takes the same form as previously, but with five parameters instead of three, and with three input distributions that are determined from Monte Carlo. These modifications allow a single parameterization to describe both $\sqrt{s}$ data sets simultaneously.

The results of this "twin fit" and the individual (traditional) fits are listed in Table 6.2; error matrices for these fits comprise Table 6.3. From the χ^2 probabilities, none of the fits exhibit overwhelming agreement, most likely because the point–to–point fluctuations
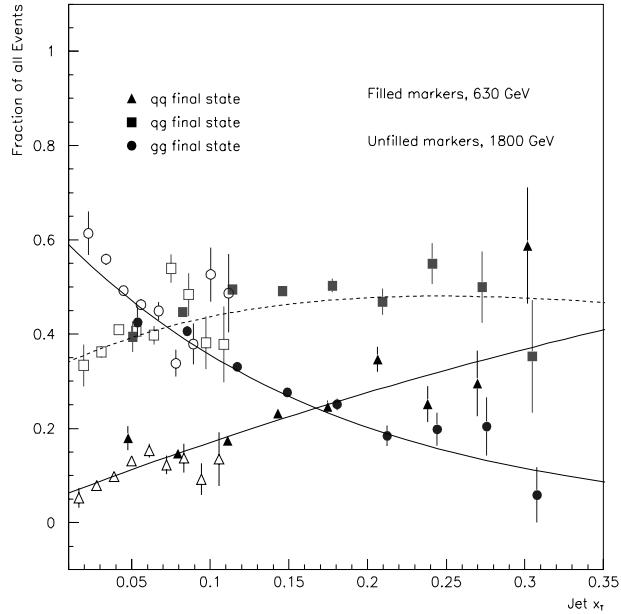
Figure 6.9: The fractional contribution of each final state to dijet events (HERWIG Monte Carlo and best fit parameterizations).

	χ^2/n	Parameter	Value	Simple Error
	15.18/9	c	0.031	0.00453
1800 GeV	= 1.69	s	0.704	0.0452
	$\rightarrow 0.086\%$	n	2.535	0.662
		c	0.0494	0.00325
Twin Fit	39.22/18	s_{qq}	2.93×10^{-7}	.0314
	= 2.18	s_{qg}	0.5448	.106
	$\rightarrow 0.002\%$	s_{gg}	1.117	.103
		n	0.000383	1.632
	16.93/8	c	0.048	0.0293
630 GeV	= 2.12	s	0.380	0.2776
	$\rightarrow 0.031\%$	n	2.836	0.635

Table 6.2: The parameters of the twin fit compared to individual fits.
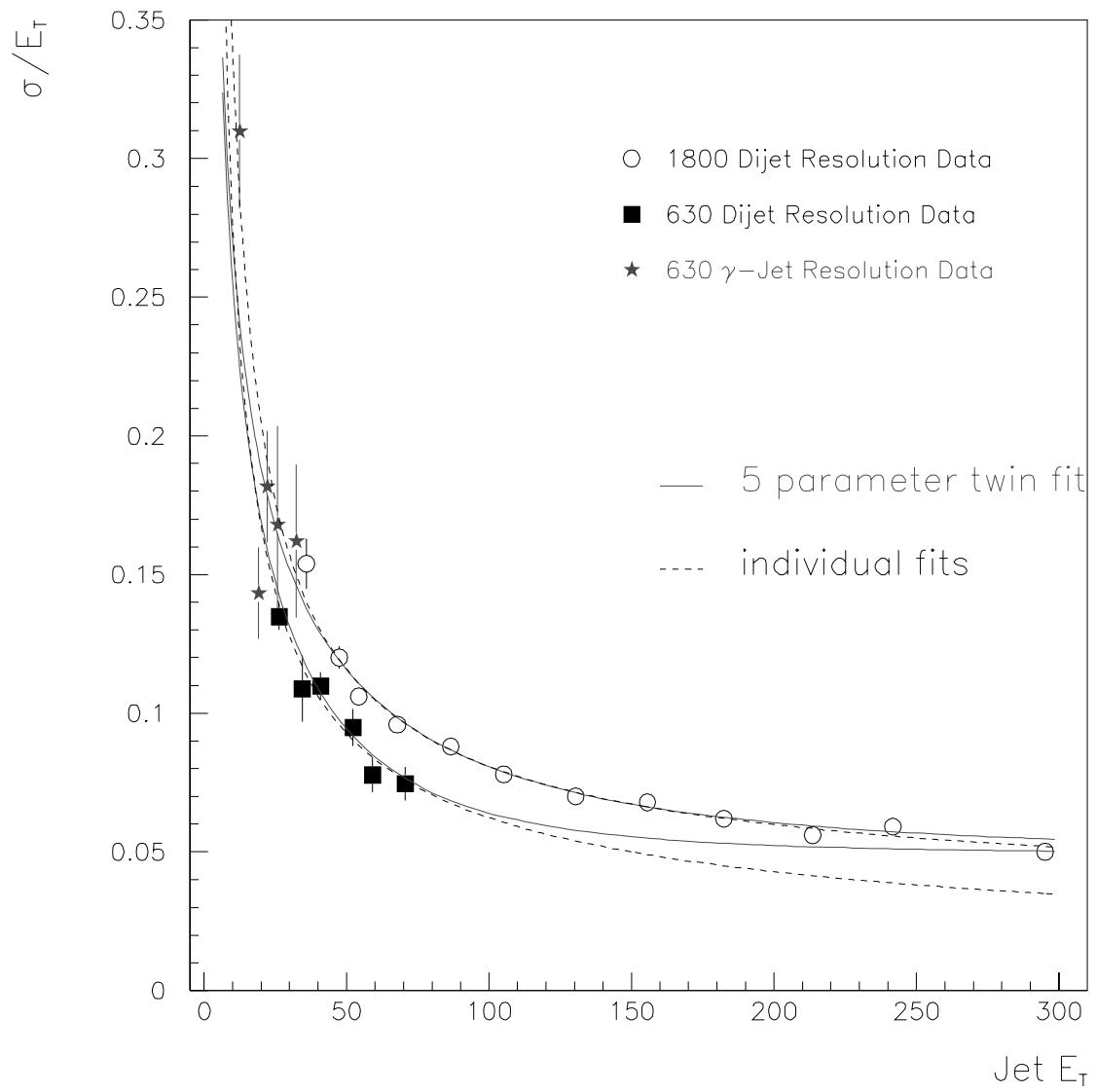
Figure 6.10: Results of the resolution fit procedure for both center–of–mass energies. Dashed lines indicate the best three–parameter fit for each data set. The five–parameter twin fit results in the solid lines.
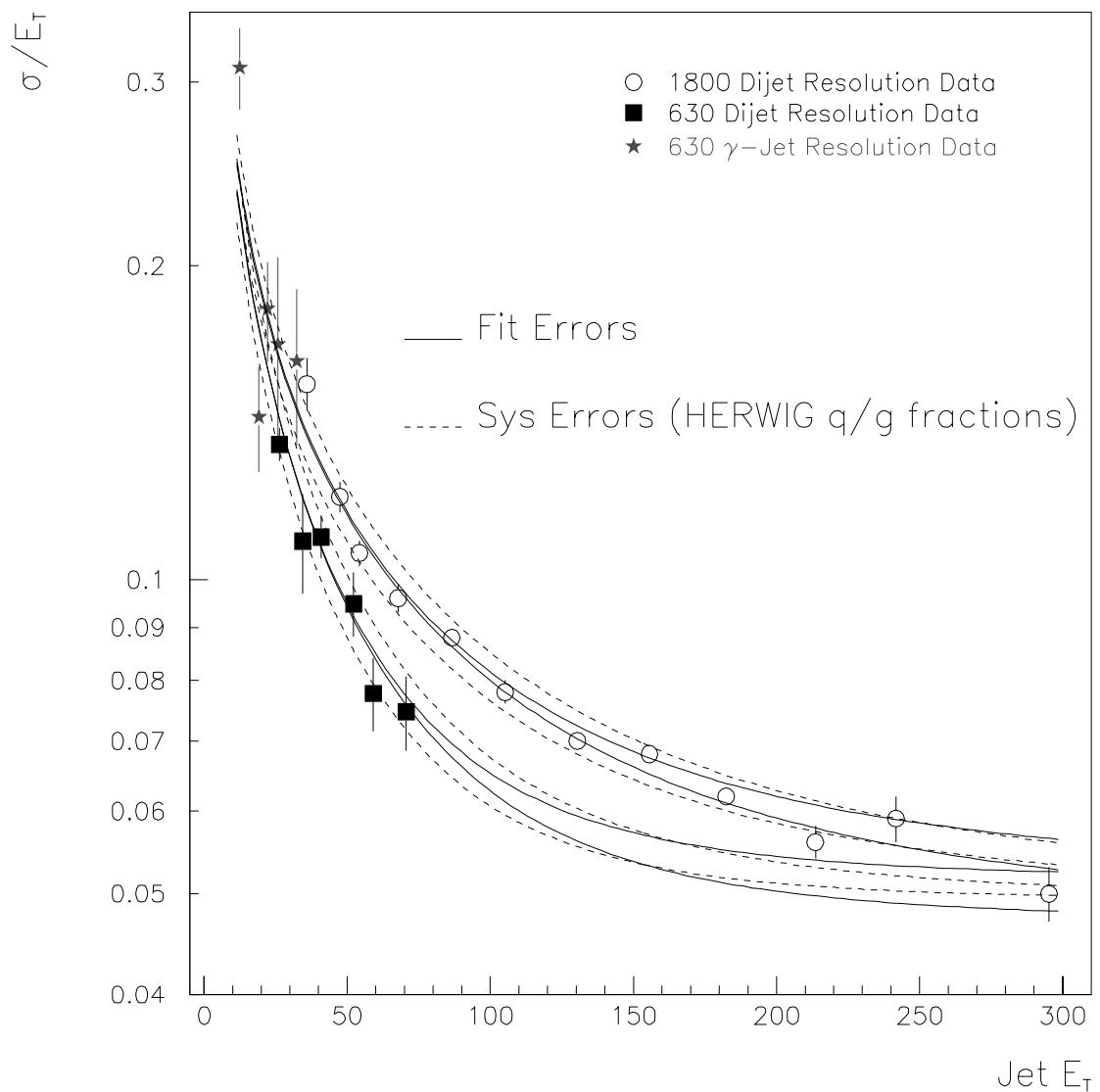
Figure 6.11: The uncertainty of the twin fit procedure. Solid lines demark the 1σ covariant fit uncertainty; dashed lines indicate the systematic shifts that result from a $\pm5\%$ change in the dijet parton fractions.

Error Matrix				
1800 GeV	2.05×10^{-5}	-1.93×10^{-4}	0.0024	
	-1.93×10^{-4}	0.00204	-0.0282	
	0.0024	-0.0282	0.438	
Twin Fit	5.02×10^{-6}	-2.14×10^{-4}	1.86×10^{-4}	-1.56×10^{-6}	4.85×10^{-6}
	-2.14×10^{-4}	1.13×10^{-2}	-1.06×10^{-2}	-5.94×10^{-4}	-1.82×10^{-4}
	1.86×10^{-4}	-1.06×10^{-2}	1.06×10^{-2}	3.26×10^{-4}	-1.00×10^{-5}
	-1.56×10^{-6}	-5.94×10^{-4}	3.26×10^{-4}	1.00×10^{-3}	-2.66×10^{-6}
	4.85×10^{-6}	-1.82×10^{-4}	-1.00×10^{-5}	-2.66×10^{-6}	2.66
630 GeV	8.6×10^{-3}	-0.00788	0.0164	
	-0.00788	0.0771	-0.170	
	0.0164	-0.170	0.404	

Table 6.3: Error matrices from the resolution fits.

are somewhat larger than the size of the statistical error bars. The parameterizations are illustrated in Figure 6.10. The twin fit results in a barely perceptible shift in the 1800 GeV resolution at or near 35 GeV (much lower in E_T than the 1800 resolutions have been used), but the 630 GeV parameterization shifts more perceptibly. Figure 6.11 depicts the uncertainties in the final parameterization. Solid lines indicate the fit errors, dashed lines indicate the maximum effect of shifting the quark–gluon fractions by ±5%. The semi–log scale distorts the low–E_T portion, but enhances detail at high values.

6.1.6 Monte Carlo Closure

To verify the resolution extraction methods, a Monte Carlo study compares events before and after the detector simulation. At the *calorimeter level*, jets experience simulated energy fluctuations. The energy of these so–called "cajets" can be compared to the original Monte Carlo jet at the *particle level* (a "pjet"). The difference between the pjet and the corrected cajet directly measures the calorimeter energy resolution. Alternately, the full asymmetry method determines the resolution *indirectly*, as described in the prior sections for data. The difference between the direct and indirect resolutions determines the validity and stability of the method.

Figure 6.12 illustrates the "closure" of the asymmetry method. Here, "pjet data" is a

direct resolution calculation,

$$\frac{\sigma_{E_T}}{E_T}_{\,pjet} = \frac{E_T^{pjet} - E_T^{cajet}}{E_T^{pjet}}. \tag{6.7}$$

The "cajet data" is the full asymmetry method. The difference between the two calculations does not lie preferentially above or below zero, indicating lack of significant bias in the method. Primarily less than 1%, the incomplete closure of the asymmetry method determines the magnitude of the systematic uncertainty, which is parameterized as

$$\Delta\left(\frac{\sigma_{E_T}}{E_T}\right)_{630\ \text{GeV}} = \frac{2.23}{E_T^2} + 0.0021, \tag{6.8a}$$

$$\Delta\left(\frac{\sigma_{E_T}}{E_T}\right)_{1800\ \text{GeV}} = \frac{14.1}{E_T^2} + 0.0024. \tag{6.8b}$$

The 68% probability curves do not enclose the points; rather, they enclose the residual difference of the mean of the points from zero.

6.1.7 Jet Resolution Summary

The single jet resolution describes the precision $\left(\frac{\sigma_{E_T}}{E_T}\right)$ with which the E_T of a jet may be determined after the energy scale correction. A three parameter fit describes the final resolution data for both $\sqrt{s} = 630$ and 1800 GeV,

$$\frac{\sigma_{E_T}}{E_T} = \sqrt{\frac{n^2}{(E_T)^2} + \frac{s_{eff}^2}{E_T} + c^2}. \tag{6.9}$$

The first parameter simulates fluctuations with a constant absolute magnitude for all jet E_T values; this "noise" term primarily describes the low E_T resolution. The second term, "sampling," describes the intermediate E_T range; because the resolution varies with the identities of the final state partons (quarks versus gluons) an *effective* sampling term must accommodate the weighted sum of these events. The third parameter defines the asymptotic minimum of the fractional resolution at high E_T.

Because the data at $\sqrt{s} = 630$ GeV cannot satisfactorily constrain the three–parameter fit alone, a "twin fit" technique links the resolutions between 630 and 1800 GeV. In this fit, the parameters cannot vary between data sets, allowing only the final state quark and
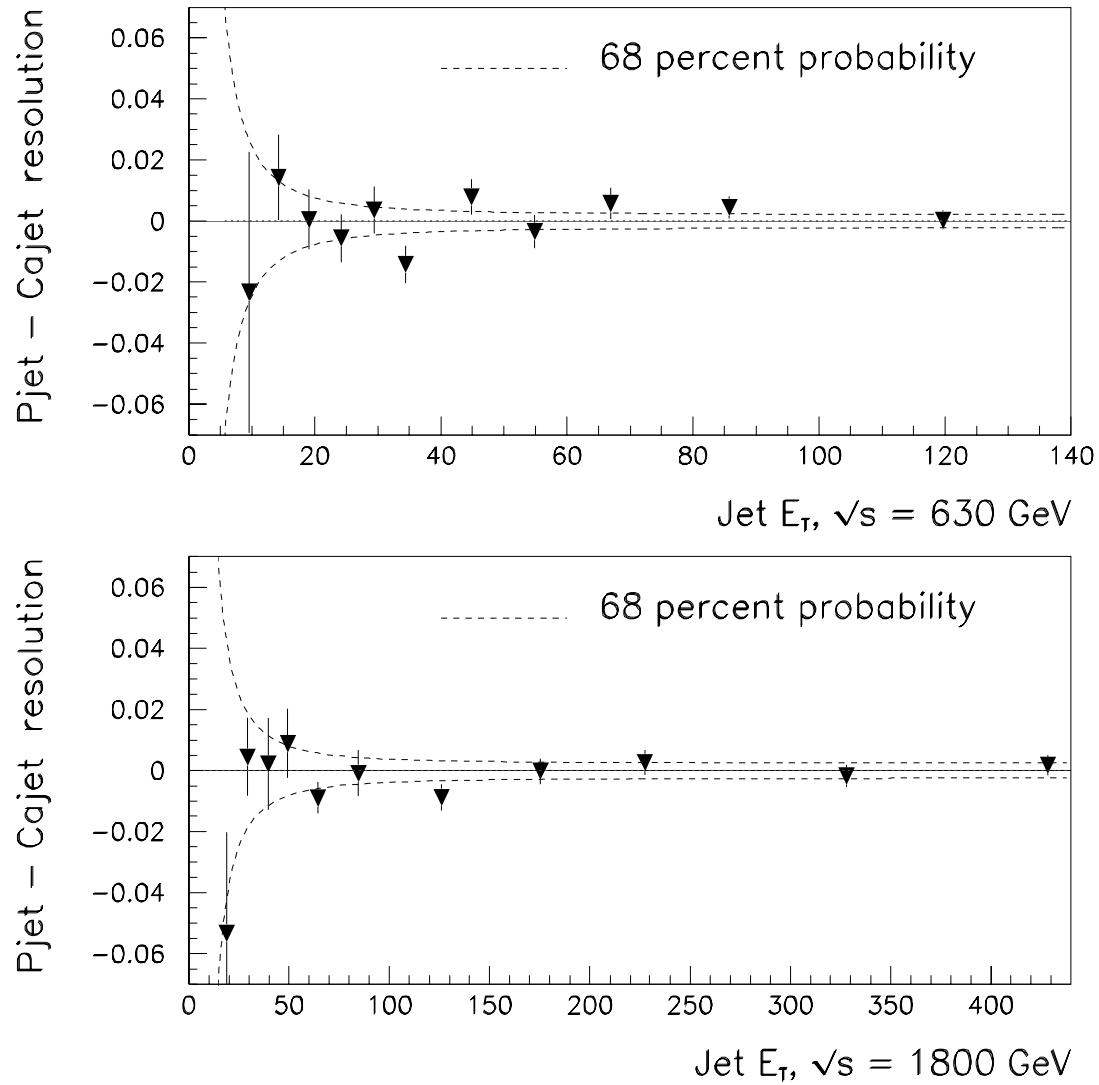
Figure 6.12: Resolution closure from HERWIG Monte Carlo simulation, both center–of–mass energies. *Cajets:* the full detector simulation and asymmetry method. *Pjets:* direct simulation of the particle level asymmetry. For most of the kinematic range, the degree of closure lies within a fraction of a percent.

gluon fractions to describe any observed differences. Uncertainties in the resolution determination include the covariance matrix from the fit and systematic uncertainty estimates to accommodate inaccuracies in the fractions of final state partons and inaccuracies inherent in the method.

6.2   The Process of Unsmearing

To correct the jet cross section for resolution effects, a smearing model must be created. To begin, postulate that the measured jet cross section results from the *convolution* of the measured jet E_T resolution and some "true" jet E_T spectrum. If the true spectrum is parameterized as

$$f\left(E_T\right) = e^A \cdot \left(E_T\right)^B \cdot \left(1 - \frac{E_T}{\sqrt{s}}\right)^D, \tag{6.10}$$

then this conjecture is expressed as

$$F\left(E_T\right) = \int g(E_T - E_T') \cdot f\left(E_T'\right)\ dE_T'. \tag{6.11}$$

Here, g is a Gaussian of width σ_{E_T}, as determined in the previous section. The integration must cover a sufficiently large range of E_T to allow ample opportunity for jets to smear into (or away from) the E_T point under study; three σ of the Gaussian should suffice. For 630 GeV, the integration ranges from 10 to 200 GeV; at 1800 GeV, the integration ranges from 10 to 600 GeV. To unsmear, the parameters of the ansatz f are varied to achieve the best fit between jet data and the smeared function F. The unsmearing correction factor, C_{smear} is then given by

$$C_{smear} = \frac{f\left(E_T\right)}{F\left(E_T\right)}. \tag{6.12}$$

Binwise multiplication of the raw cross section by the correction factor yields the final distribution.

$\sqrt{s}$	Parameter	Value	Error Matrix		
	A	37.64	6.36×10^{-3}	-1.64×10^{-3}	-9.58×10^{-3}
1800 (fb)	B	-5.122	-1.64×10^{-3}	4.24×10^{-4}	2.53×10^{-3}
	D	2.621	-9.58×10^{-3}	2.53×10^{-3}	1.62×10^{-2}
	A	23.07	2.32×10^{-2}	-8.77×10^{-3}	-5.84×10^{-2}
630 (nb)	B	-5.461	-8.77×10^{-3}	3.35×10^{-3}	2.28×10^{-2}
	D	6.175	-5.84×10^{-2}	2.28×10^{-2}	0.165

Table 6.4: Unsmearing parameters and errors. The cross section units are indicated.

The double–precision MINUIT package [47] performs the fitting and differentiation procedure. Data for each $\sqrt{s}$ energy are fit separately. Table 6.4 includes the final ansatz parameter values and the error matrix for both fits.

6.2.1 Unsmearing Uncertainties

Three sources contribute uncertainty to the unsmearing technique: the ansatz fit, the resolution parameter fit, and the resolution closure uncertainty. As described below, calculation of the uncertainty due to the ansatz fit follows the error matrix technique outlined in Appendix B, Section 2. The resolution fit uncertainty propagates into the unsmearing correction similarly, but less directly. Because, unlike the first two sources, the resolution closure uncertainties do not originate from a fit, the standard error propagation techniques will not accommodate them; thus a modification to the covariant error approach had to be invented for this analysis.

Because the ansatz appears in both the numerator and denominator of Equation 6.12, the fit uncertainty of the smeared ansatz alone is not relevant to the uncertainty in the cross section. Instead, computation of the covariant uncertainty in the cross section due to the ansatz fit requires knowledge of the partial derivatives of *the correction factor*. The integration of Equation 6.11 must be performed numerically, so partial derivatives of C_{smear} are not available in analytic form. To determine the fit errors, the partial derivatives with respect to each parameter are calculated numerically at each data point. The unsmearing

uncertainty at each point is then determined with

$$\Delta = \sqrt{\sum_i \sum_{j<i} \partial_i^2 \cdot \Delta_i^2 + 2Cov_{ij} \cdot \partial_i \cdot \partial_j} \tag{6.13}$$

where the ∂_i are the partial derivatives with respect to parameter i, the Δ_i are the standard deviations of each parameter in the fit, Cov_{ij} is the covariance between parameters i and j, and the indices run over the ansatz parameters A, B, and D. In Table 6.4, the diagonal elements are the Δ_i^2 and the off–diagonal elements are the covariances.

Next, the partial derivatives in the correction factor with respect to the resolution parameters are calculated at each point. Using Equation 6.13 again, these derivatives and the error matrix in Table 6.3 determine the uncertainty in the correction factor due to the resolution fit. For the resolution uncertainty propagation, the indices run over c, n, and the three s terms. Note that the resolution error matrix and the partial derivatives of the resolution parameters need not and do not originate from the same fit parameterization.

Finally, dummy constant terms of form $\frac{d_1}{(\mathrm{E_T})^2} + d_2$ in the fractional resolution (fixed at zero during the fit) are varied to find their partial derivatives. Specifically, the width of the Gaussian in Equation 6.11 takes the form

$$\sigma^2 = \left(\sqrt{c^2 x^2 + s_{eff}^2 x + n^2} + \frac{d_1}{x} + d_2 x \right)^2 \tag{6.14}$$

for purposes of error propagation. The variances for these two dummy parameters are precisely their magnitude in the Monte Carlo closure parameterization; thus, $d_1 = 0.0 \pm 2.0$ and $d_2 = 0.0 \pm 0.01$. A third dummy parameter is included in the quark–gluon final state parameterizations, such that

$$s_{eff} = (F_{qq}(\mathrm{x_T}) - d_3) \cdot s_{qq} + F_{qg}(\mathrm{x_T}) \cdot s_{qg} + (F_{gg}(\mathrm{x_T}) + d_3) \cdot s_{gg}. \tag{6.15}$$

The third dummy parameter, d_3, changes the relative magnitudes of the final state distributions. No variation is applied to the F_{qg} function because it does not vary as strongly as a function of $\mathrm{E_T}$, nor does it vary with pseudorapidity range. The third parameter is set to $d_3 = 0.0 \pm 0.05$, to accommodate fluctuations of the points in Figure 6.9, and to account for possible . Each dummy parameter is independent of all other parameters.

In essence, the error matrix approach is applied to all three sources of uncertainty. The technique outlined in this section is equivalent to defining an 11×11 error matrix

$$
V = \begin{pmatrix}
\Delta_A^2 & C_{AB} & C_{AC} \\
C_{AB} & \Delta_B^2 & C_{BC} \\
C_{AC} & C_{BC} & \Delta_D^2 \\
& & & \Delta_c^2 & C_{cs_{gq}} & C_{cs_{gg}} & C_{cs_{qq}} & C_{cn} \\
& & & C_{cs_{gq}} & \Delta_{s_{gq}}^2 & C_{s_{gq}s_{gg}} & C_{s_{gq}s_{qq}} & C_{s_{gq}n} \\
& & & C_{cs_{gg}} & C_{s_{gq}s_{gg}} & \Delta_{s_{gg}}^2 & C_{s_{gq}s_{qq}} & C_{s_{gg}n} \\
& & & C_{cs_{qq}} & C_{s_{gq}s_{qq}} & C_{s_{gq}s_{qq}} & \Delta_{s_{qq}}^2 & C_{s_{qq}n} \\
& & & C_{cn} & C_{s_{gq}n} & C_{s_{gg}n} & C_{s_{qq}n} & \Delta_n^2 \\
& & & & & & & & \Delta_{d_1}^2 \\
& & & & & & & & & \Delta_{d_2}^2 \\
& & & & & & & & & & \Delta_{d_3}^2
\end{pmatrix},
$$

(6.16)

where the diagonal contains the variance of all parameters, the off-diagonals hold the co-variance between parameters (denoted C), and all unfilled cells are zero. The elements of V, the partial derivatives of 6.12, and Equation 6.13 determine the unsmearing uncertainty as a function of E_T.

6.2.2 Final Correction Factor

Figure 6.13 depicts the unsmearing correction for both center–of–mass energies with the covariant uncertainties from all fits. The solid bands indicate resolution fit uncertainty alone; the hollow bands include the resolution fit and both systematic uncertainties. The error contribution from the unsmearing process totals less than 3% over the entire 1800 GeV E_T range, but for 630 GeV the errors become as large as 12%, the second–largest error (after the energy scale). For both $\sqrt{s}$ energies, the uncertainty in the ansatz fit alone yields a negligible error.

The results for 630 GeV and 1800 GeV differ dramatically for two reasons. First, the 630 GeV data set extends to lower E_T than does the 1800 GeV data set; at low E_T, the jet resolution worsens rapidly, resulting in a large smearing effect. Second, the 630 GeV cross section spectrum falls more steeply than does the 1800 GeV cross section, so an equal mismeasurement results in a larger distortion at 630 GeV.

6.3   Summary and Result

Whereas the energy scale corrects for the average jet mismeasurement, residual fluctuations about the average continue to distort the measured jet cross section distribution. The correction, called "unsmearing," requires knowledge of the degree of expected fluctuation for a given jet E_T. The jet E_T resolution, derived from E_T balance in dijet events, provides this knowledge.

The convolution of an ansatz function and the measured resolution describes the "raw" cross section. A best fit of the convolution to the observed jet cross section data estimates the jet resolution effect; the ratio of the convoluted ansatz and the bare ansatz yields the unsmearing correction factor. At $\sqrt{s} = 1800$ GeV, this correction is approximately 7% throughout the jet spectrum; for 630 GeV, the correction factor is greater than 15% and displays a strong E_T dependence. The change in the magnitude of the correction between center–of–mass energies results from both the different E_T ranges and the different slopes of the cross sections. The uncertainty on the procedure consists primarily of the uncertainties in the jet resolution measurements, not the convolution fits. The error matrices of the fits and a "constructed" error matrix for the resolution systematic combine to form a global error matrix that describes the covariant uncertainty in the correction factor.

Application of the correction factor to the inclusive jet cross section yields the distribution shown in Figure 6.14 ($\sqrt{s} = 630$ GeV data set). The solid line traces the NLO QCD prediction from JETRAD (with MRSA' as the input PDF). Similarly, Figure 6.15 depicts the corrected distribution at $\sqrt{s} = 1800$ GeV. Tables 6.5 and 6.6 list the bin edges in E_T and the corresponding cross sections and statistical uncertainties for each data set. The follow-
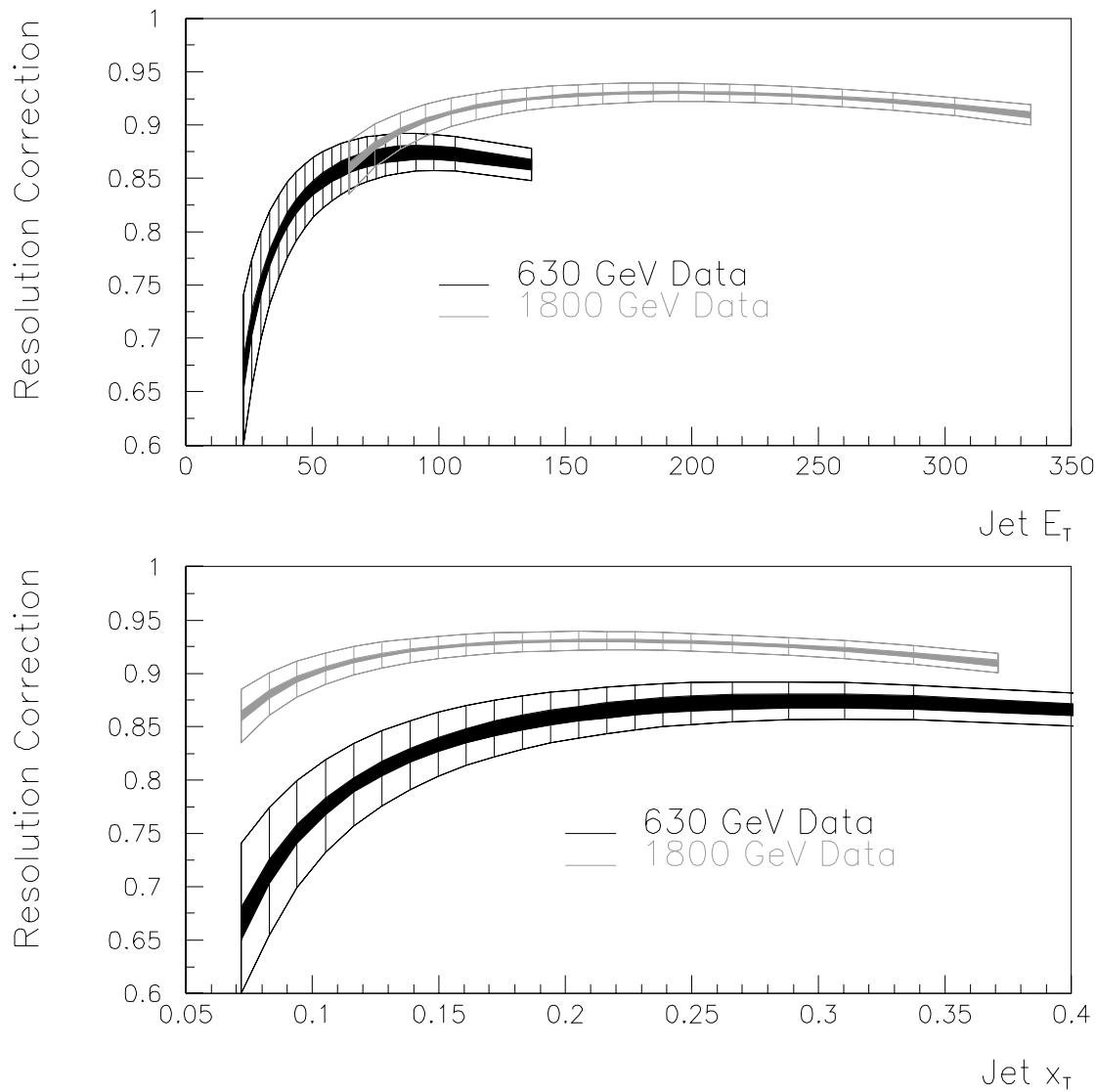
Figure 6.13: The correction factor for unsmearing. Solid bands: resolution fit uncertianty. Full band: fit and systematic uncertainties in quadrature.

$\sqrt{s}$	Bin Edges	(GeV)	Cross Section (nb/GeV)	Statistical Error
	21.0	24.5	290.6	3.7
	24.5	28.0	120.5	2.4
	28.0	31.5	55.2	1.7
	31.5	35.0	27.60	0.49
	35.0	38.5	14.19	0.35
	38.5	42.0	8.15	0.27
	42.0	45.5	4.28	0.20
	45.5	49.0	2.90	0.16
630	49.0	52.5	1.82	0.13
	52.5	56.0	1.098	0.024
	56.0	59.5	0.702	0.019
	59.5	63.0	0.485	0.016
	63.0	66.5	0.317	0.013
	66.5	70.0	0.230	0.011
	70.0	73.5	0.1572	0.0092
	73.5	77.0	0.1128	0.0078
	77.0	80.5	0.0833	0.0067
	80.5	87.5	0.0434	0.0034
	87.5	94.5	0.0272	0.0027
	94.5	101.5	0.0134	0.0019
	101.5	112.0	0.0076	0.0012
	112.0	196.0	0.00055	0.00011

Table 6.5: Inclusive jet cross section and statistical errors for 630 GeV.

ing chapter discusses the systematic uncertainties of the cross section calculations; Chapter 8 provides a full data–to–theory comparison for each cross section and the dimensionless ratio of cross sections.

144
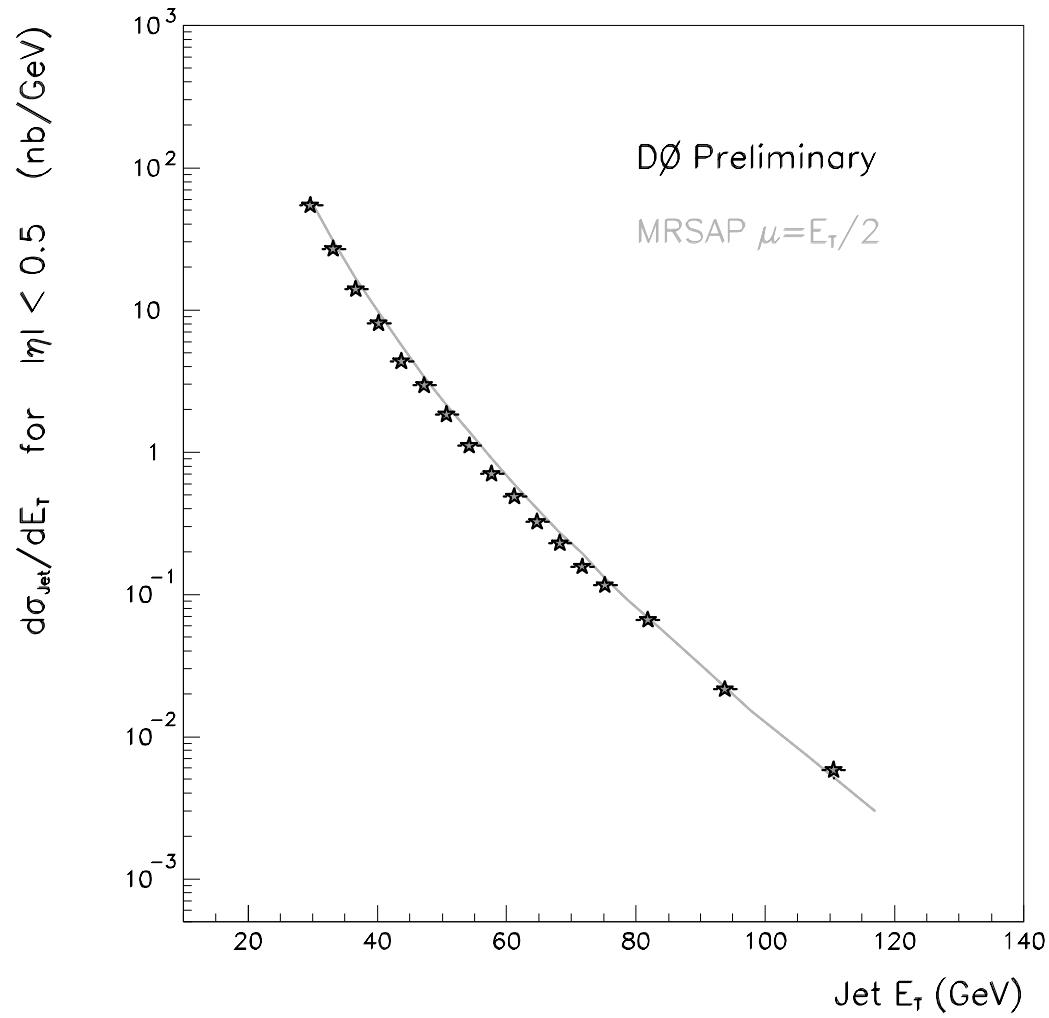
Figure 6.14: The final inclusive jet cross section at 630 GeV (stars). The solid line indicates the NLO QCD prediction (PDF and μ scale indicated).
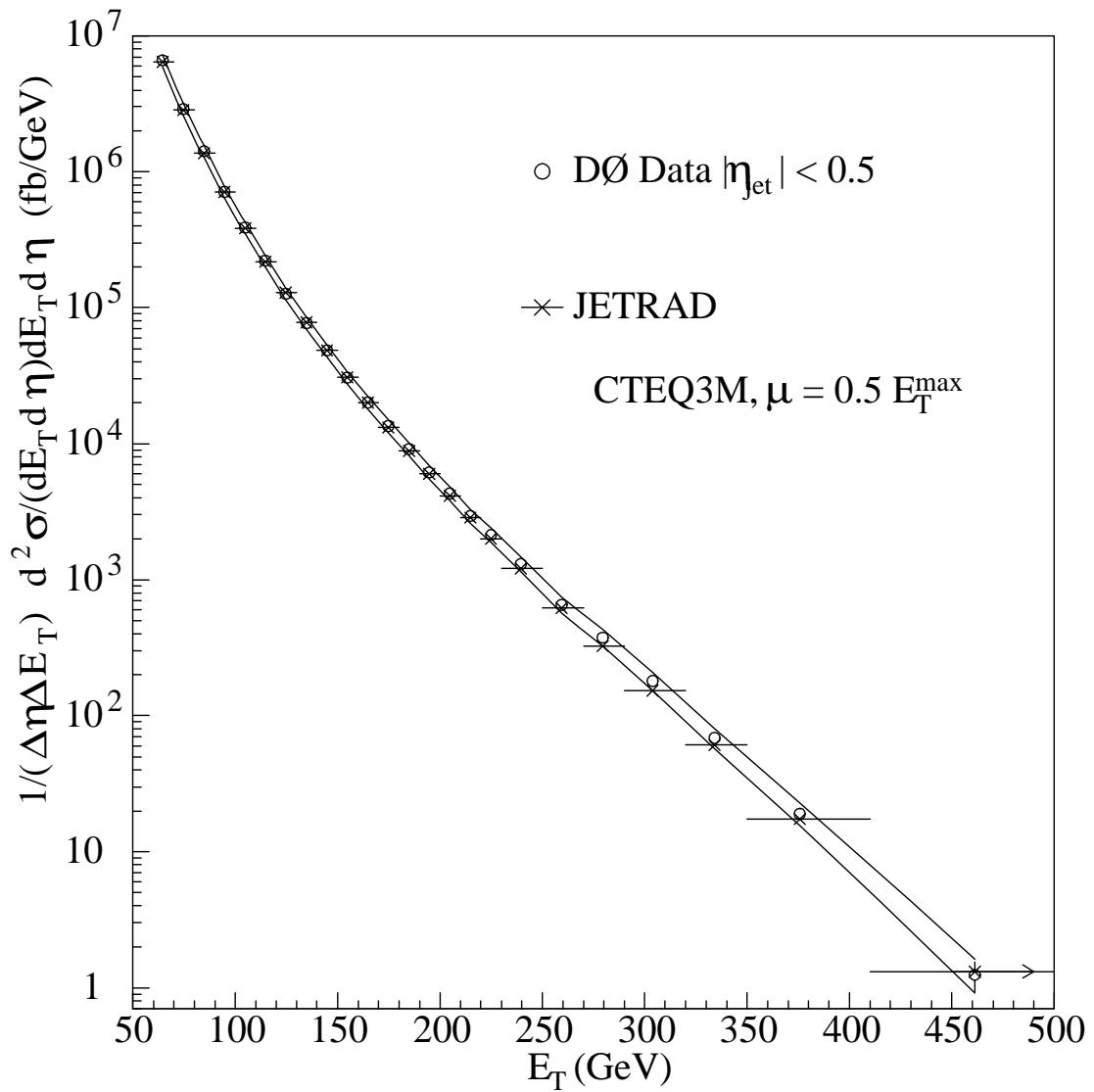
Figure 6.15: The final inclusive jet cross section at 1800 GeV (circles). The solid lines indicate systematic uncertainties.

$\sqrt{s}$	Bin Edges	(GeV)	Cross Section (fb/GeV)	Statistical Error
1800	60	70	$6.59{\times}10^6$	$0.04{\times}10^6$
	70	80	$2.90{\times}10^6$	$0.03{\times}10^6$
	80	90	$1.41{\times}10^6$	$0.02{\times}10^6$
	90	10	$7.07{\times}10^5$	$0.04{\times}10^5$
	100	110	$3.88{\times}10^5$	$0.03{\times}10^5$
	110	120	$2.21{\times}10^5$	$0.02{\times}10^5$
	120	130	$1.27{\times}10^5$	$0.02{\times}10^5$
	130	140	$7.70{\times}10^4$	$0.04{\times}10^4$
	140	150	$4.86{\times}10^4$	$0.03{\times}10^4$
	150	160	$3.07{\times}10^4$	$0.02{\times}10^4$
	160	170	$2.00{\times}10^4$	$0.02{\times}10^4$
	170	180	$1.34{\times}10^4$	$0.01{\times}10^4$
	180	190	$9.12{\times}10^3$	$0.10{\times}10^3$
	190	200	$6.15{\times}10^3$	$0.09{\times}10^3$
	200	210	$4.29{\times}10^3$	$0.07{\times}10^3$
	210	220	$2.93{\times}10^3$	$0.06{\times}10^3$
	220	230	$2.14{\times}10^3$	$0.05{\times}10^3$
	230	250	$1.30{\times}10^3$	$0.03{\times}10^3$
	250	270	$6.54{\times}10^2$	$0.20{\times}10^2$
	270	290	$3.77{\times}10^2$	$0.15{\times}10^2$
	290	320	$1.79{\times}10^2$	$0.08{\times}10^2$
	320	350	$6.82{\times}10^1$	$0.52{\times}10^1$
	350	410	$1.89{\times}10^1$	$0.19{\times}10^1$
	410	560	$1.24{\times}10^0$	$0.31{\times}10^0$

Table 6.6: Inclusive jet cross section and statistical errors for 1800 GeV.

Chapter 7

Uncertainties in the Ratio of Jet Cross Sections

> *"Knowledge rests not upon truth alone,*
> *but upon error also."*
> — Carl Jung

Because jet cross section spectra decrease sharply as functions of E_T, apparently small uncertainties for a single jet become large in the measurement of the jet cross sections. The advantage of a ratio calculation between the two center–of–mass (CM) energies is the cancellation of large portions of the errors. In this case, "ratio" refers to the cross section at 630 GeV over the cross section at 1800 GeV. Although error cancellation between jets of like E_T at different $\sqrt{s}$ is conceptually simple, two considerations prevent a direct ratio calculation. First, the limited run time at 630 GeV yielded a small number of jets above 60 GeV in E_T (where the 1800 GeV jet cross section begins); any ratio with 1800 GeV would be statistically limited above 100 GeV, and (short of rebinning the 1800 data) would consist of only six data points. Second, the ratio of *dimensionless* cross sections is easier to explain theoretically, because the differences between parton distribution functions become negligible in that framework. The dimensionless jet cross section is the spectrum of $E_T^4 \cdot E \frac{d^3\sigma}{d^3p}$ versus x_T. In terms of collider variables, this spectrum is $\frac{E_T^3}{2\pi} \cdot \frac{d^2\sigma}{dE_T d\eta}$ versus $\frac{2}{\sqrt{s}}E_T$. Cross section comparison in this form also addresses the statistical limitations; in x_T, the statistics in the bins at 630 GeV match those at 1800 with the exception of only the last few bins, maximizing the measureable region of the distribution. In the x_T measurement, however,

148

uncertainties which might cancel identically for like E_T's cancel less completely.

The cancellation of uncertianties in the ratio represents the true stength of this analysis; all error considerations have been concentrated into this chapter.* The origins of the following uncertainties may be found in prior chapters, so brief descriptions will appear here in cases where errors are treated simply. Energy scale and luminosity errors, being more complicated, receive fuller treatment. For reference, Appendix B provides a short primer on error analysis.

For the uncertainty in the ratio, all errors are separated into one of three categories, depending on the correlation (ρ) as a function of E_T or, as importantly, the correlation between $\sqrt{s}$ energies:

- $\rho = 1$: "Completely correlated," indicating that a 1σ fluctuation in an error at a particular E_T implies a 1σ fluctuation at all other E_T (Figure 7.1). In the ratio, a fractional error at 630 GeV, $\pm\Delta_1$, and its completely correlated analog at 1800 GeV, $\pm\Delta_2$, yield a fractional ratio uncertainty of magnitude

$$\Delta_{ratio}^{\rho=1} = \frac{1 \pm \Delta_1}{1 \pm \Delta_2} - 1, \tag{7.1}$$

  where the signs of the two cross section errors are always the same. Note that if Δ_2 is greater than Δ_1, the sign of the ratio uncertainty will be the opposite of the signs of the cross section errors.

- $\rho = \rho(E_{T_1}, E_{T_2}) = [-1, 1]$: "Partially correlated," possessing a varying degree of correlation in E_T, resulting from the covariance matrix of a fit. A 1σ fluctuation thus implies a less than unit fluctuation elsewhere (Firgure 7.2); negative ρ indicates the shifts will have opposite directions at the two points. This type of error is the most complicated to calculate and propagate through the ratio.

- $\rho = 0$: "Uncorrelated," statistical in nature or otherwise independent of one another. Some small errors with unknown (but probably positive) E_T correlation are treated as uncorrelated for simplicity and because such treatment is conservative. The simple quadrature addition formula for the two *fractional* errors Δ_1 and Δ_2 is

$$\pm\Delta_{ratio}^{\rho=0} = \sqrt{(\Delta_1)^2 + (\Delta_2)^2}. \tag{7.2}$$

In most cases, complete correlation in E_T for one CM energy implies complete correlation between $\sqrt{s}$ energies, but exceptions exist and will be highlighted in the following sec-

---

* Major portions of this chapter were originally published as DØ Note 3423, "Calculation of Uncertainties in the Ratio of Jet Cross Sections at 630 and 1800 GeV," J.Krane, April 9, 1998.
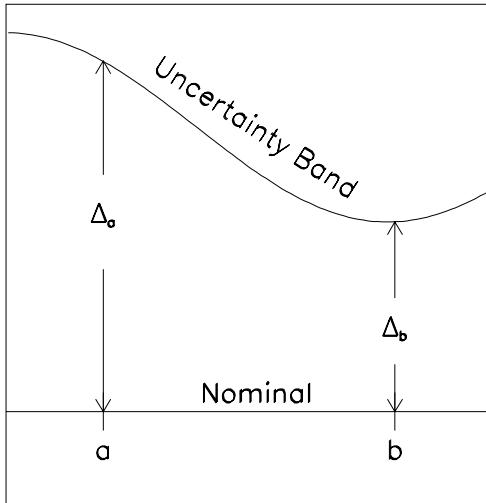
Figure 7.1: Example of an error band relative to some nominal distribution (illustrated here with a flat line). If the errors at points **a** and **b** are *completely correlated,* then a one standard deviation (1σ) mistake Δ_{a} at the first position necessarily results in a 1σ mistake Δ_{b} at the second position.

tions. The final section includes a graphical depiction of the x_{T} distributions of all ratio uncertainties.

The end result of this chapter, an "uncertainty band" around the cross section data points, represents one standard deviation of allowed shifts in the data points. Unlike the statistical "error bars," where any given point can fluctuate without affecting the likely position of the other points, a *systematic* shift of one point implies a likely new position for all other points. Although this *covariance* between points is difficult to present visually, it can be described with a matrix, as in the final section.

This chapter is arranged in five parts. The first section discusses luminosity uncertainties, including speculative results from Fermilab experiment E811. Sections two and three incorporate the uncertainty from data selection criteria and the unsmearing procedure. The most complicated portion of the error analysis resolves the interplay of the energy
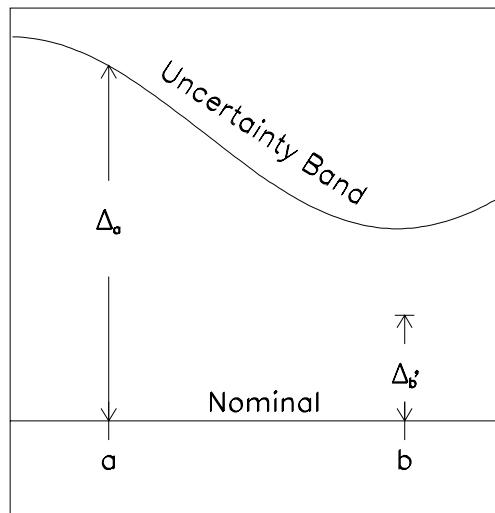
Figure 7.2: If the errors at points **a** and **b** are *partially correlated,* then a full 1σ mistake Δ_a at the first position results in a smaller than 1σ mistake $\Delta_\mathrm{b'}$ at the second position. As illustrated here, the correlation factor is 0.55.

scale correction between the two $\sqrt{s}$ data sets. Although the discussion becomes lengthy, sophisticated treatment of the energy scale uncertainty in section four yields more error reduction than the combined total of all other uncertainties. Section five presents the final covariance matrix.

7.1   Luminosity Uncertainties

The luminosity calculation at $\sqrt{s} = 630$ GeV shares many common uncertainties with the calculation at 1800 GeV. Both calculations consist of three distinct ingredients: the geometric acceptance of the Level Ø hodoscopes, the Level Ø hardware efficiency, and the p$\bar{\text{p}}$ inelastic cross section. The magnitudes of these uncertainties are listed in Table 7.1.

The largest contribution to the luminosity uncertainty at 1800 GeV originates in the World Average (WA) p$\bar{\text{p}}$ total cross section. The p$\bar{\text{p}}$ cross section at 630 GeV was determined with a fit to the values at 1800 and 546 GeV; the covariant uncertainty from the fit (a "partially correlated error") determines the error on the 630 cross section (Figure 7.3). A 1σ shift in the mean value of the 1800 cross section directly impacts the central value of the 630 cross section, resulting in a sympathetic shift of unequal magnitude but like direction. The magnitude of the shift at 630 GeV, subtracted in quadrature from the covariant interpolation error, defines two error components: the shift, which is completely correlated with the 1800 cross section error, and the remainder, which will be added in quadrature with the other independent luminosity errors. The uncertainty components in the WA elastic and single–diffractive p$\bar{\text{p}}$ cross sections seperate with the same procedure. Because the uncertainties of these three cross sections contribute to the total luminosity uncertainty non–linearly, Table 7.1 reports only the final results; the special treatment of the partially correlated luminosity uncertainty makes the result difficult to calculate from the information in the table alone.

Two Monte Carlo minbias event generators (MBR and DTUJET) determined the geometric acceptance of the Level Ø hodoscopes. The difference in acceptance between the two MC results was cited as a source of systematic uncertainty for each $\sqrt{s}$. The consistent
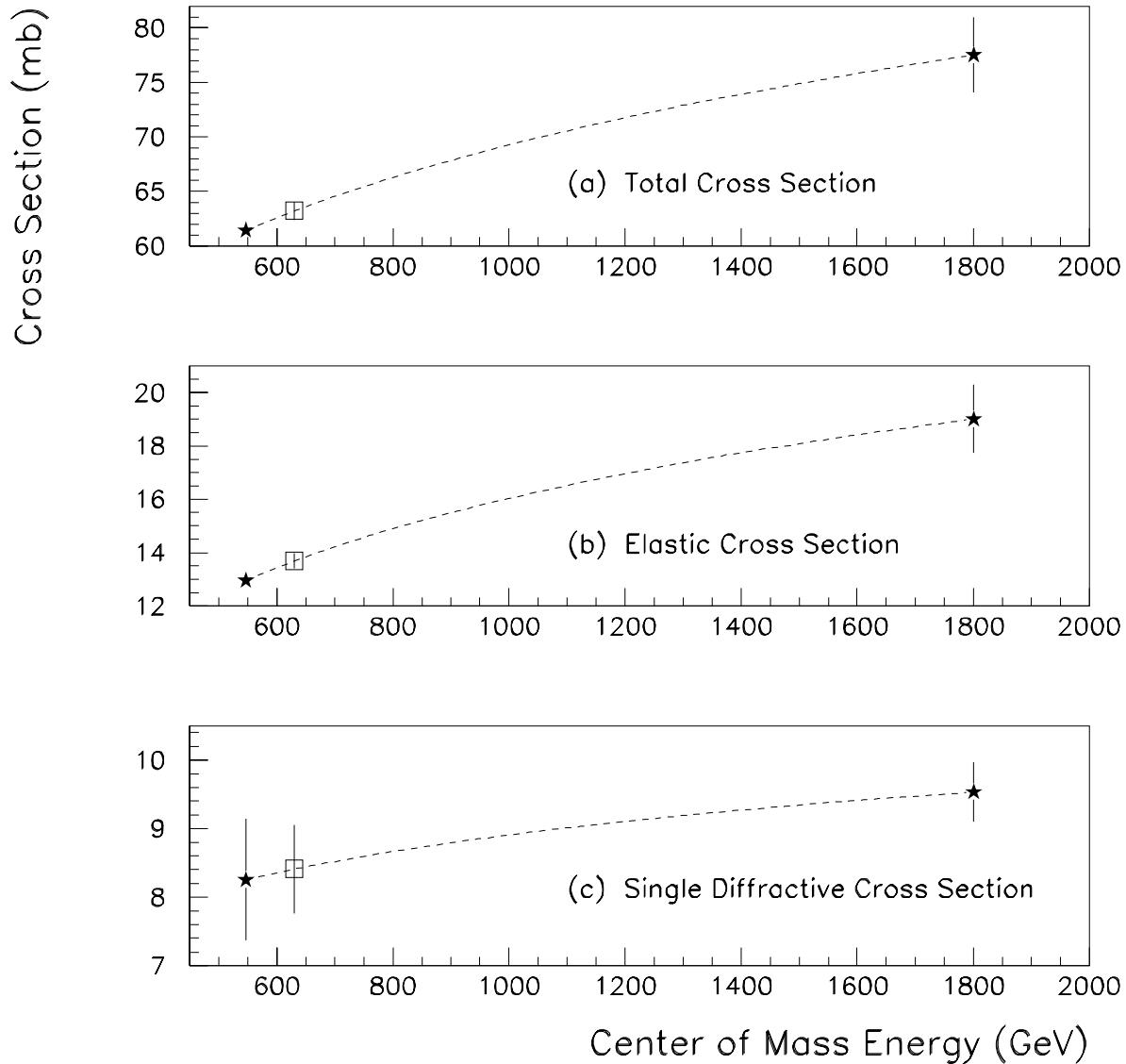
Figure 7.3: The three fits to the World Average p̄p cross sections. A fluctuation of the 1800 GeV point directly influences the interpolated value at 630 GeV, particularly in the case of the total cross section (a).

Source of	Uncertainty (Percent)		
Uncertainty	$\sqrt{s} = 1800$ GeV	$\sqrt{s} = 630$ GeV	Ratio
Original Uncertainty	5.32	3.17	
World Average p$\bar{\text{p}}$ cross sections only	4.41	1.48	+1.66 −1.47
Remaining Uncertainty	2.97	2.80	
Hardware efficiency (systematic)	2.10	2.47	+0.362 −0.378
Geometric Acceptance ("hard–core" systematic)	1.96	1.19	+0.785 −0.755
Uncorrelated Remainder*	0.754 + 0.70	0.756	±1.64
All sources*	6.1	3.17	+2.49 −2.31

Table 7.1: Uncertainties in the luminosity calculation. *Includes filter matching error.

behavior of each generator relative to the other between CM energies indicates that the systematic uncertainty may be considered completely correlated. The systematic error at each CM energy yields the ratio error listed in Table 7.1 with the use of Equation 7.1. The statistical portions of acceptance uncertainty must be added in quadrature for the ratio. Although the geometric acceptance of the Level Ø hodoscopes to diffractive processes must be considered in luminosity calculations, the uncertainty of the non-diffractive acceptance (the so-called "hard–core" acceptance) dominates. The small uncertainty contributions from the diffractive acceptances, despite their (positive) partial correlations, will be considered to be independent of one another and added in quadrature for the ratio.

A zerobias study determined the hardware efficiency of Level Ø. Examination of the analog charge sums from one Level Ø hodoscope when the other hodoscope received a hit in coincidence with a beam crossing reveals a large pedestal peak and a smooth underlying distribution. The analog sum from one hodoscope without hits in time on the other exhibits only the pedestal peak. To estimate the efficiency, the (normalized) pedestal peak from the second distribution is subtracted from the first. The uncertainty in the method lies in the determination of the number of events that hit the hodoscope but produce a small signal, such that the charge sum remains in the pedestal region. Because the same estimation of

this number appears in the calculation of the luminosity at both $\sqrt{s}$ energies, the errors are completely correlated. Table 7.1 lists the systematic uncertainty in the hardware efficiency for both CM energies and the ratio uncertainty as calculated with Equation 7.1.

Because of anomalies in the luminosity between sets of data collected by different triggers, the 1800 GeV jet cross section differs slightly in normalization from trigger to trigger. The cross section for each trigger was normalized [38] to JET_MAX (trigger versions V9 and V10). This "trigger matching" procedure adds a linear 0.7% uncertainty to the luminosity calculation, as indicated in the bottom row of Table 7.1.

Summary of Luminosity Uncertainty

The partial correlation in the uncertainties of the three World Average cross sections (at each CM energy) results from the interpolation procedure. The degree of correlation was isolated by shifting the 1800 GeV points by 1σ and finding the corresponding shift at 630 GeV. The hardware efficiency and geometric acceptances each had systematic uncertainties that were considered to be completely correlated. The remaining uncertainties were added in quadrature.

Presently, experiment E811 at Fermilab is processing their data for new determinations of the total and elastic $p\bar{p}$ cross sections. Some sources indicate the results will agree with E710 data and not with the CDF measurement, resulting in a small shift to the World Average at $\sqrt{s} = 1800$ GeV and the fitted result at 630 GeV. Although the unpublished E811 numbers should not be incorporated into the final result, an estimate of the effect is warranted. Because the new results affect both the total and elastic cross sections, competing effects result in a luminosity change at 1800 GeV of only -3%. The change in 630 GeV measurement is smaller yet; the final shift in the ratio is negligible.

7.2 Jet and Event Selection Uncertainties

For 1800 GeV, the total uncertainty for jet cut efficiencies, the $\not{E}_T$ cut efficiency, and the vertex cut efficiency totals 1%. An independent study at 630 GeV determined cut uncer-

Uncertainty		Value
1800 GeV	all selection efficiencies	1% below 350 GeV
		2% above 350 GeV
630 GeV	Jet cuts	0.12 to 0.41%
	$\not{E}_T$ cut	0.03%
	vertex cut	0.006%

Table 7.2: Uncertainty from jet and event selection.

tainties that were smaller yet (Table 7.2). Despite some similarities in methodology, these errors are all considered independent of one another in the ratio and are thus added in simple quadrature (Equation 7.2). The selection criteria are described in Chapter 5, in [39], and in [40].

7.3 Resolution and Unsmearing Uncertainties

Uncertainty in the unsmearing correction is dominated by the uncertainty in the jet resolution measurement, which is itself dominated by the systematic uncertainties. The systematic uncertainties are assumed uncorrelated between the center–of–mass energies, as are the fitting errors. The magnitudes of the resolution and unsmearing uncertainties are illustrated in Figure 7.8 at the end of this chapter.

7.4 Energy Scale Uncertainties

When queried, the jet energy scale algorithm (CAFIX version 5.1) reports the uncertainty of its correction, which is always less than $\sim 3\%$ for the E_T range of this analysis. Figure 7.4 illustrates the individual components of the per jet uncertainties from the energy scale for both center–of–mass energies. The steeply falling nature of the inclusive jet cross section magnifies the effect of energy scale uncertainties to at least 8%, and sometimes as large as 25%. Although the energy scale error estimates, as determined with the data, are statistically significant in many regions of the inclusive jet cross section, limited statistics in some E_T bins decrease the accuracy of the error estimate markedly. Additionally, cancellation of errors in the ratio of jet cross sections requires more intimate knowledge of the initial states
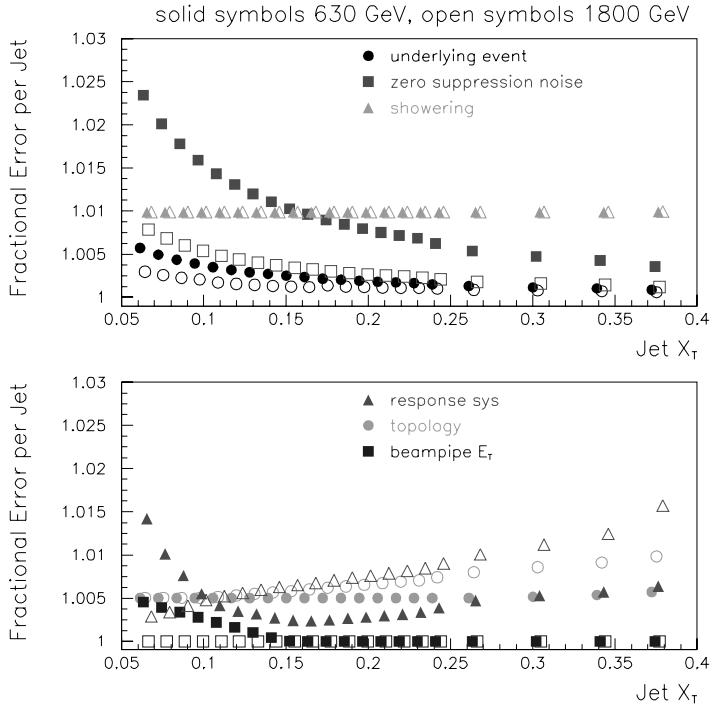
Figure 7.4: The jet–by–jet uncertainties in the energy scale correction. Filled markers indicate the uncertainties in the 630 GeV data set; unfilled markers indicate 1800 GeV.

of the jets than provided by the data.

The Monte Carlo study described in this section addresses both concerns. The following subsections describe the algorithm that generates the Monte Carlo sample, the analysis of the Monte Carlo output, and the results of the analysis. This Monte Carlo technique determines the total energy scale uncertainty of both the inclusive jet cross section and the ratio of cross sections; *i.e.*, the following algorithm handles all aspects of energy scale error.

7.4.1 Code Description

The event generator performs several steps for each $\sqrt{s}$ and each cross section bin in x_T, fully described in list format below. First, it generates a sample of jets with a spectrum that matches that observed in data. Second, it closely imitates true running conditions by simulating luminosity, vertexing, and smearing effects; thus, the energy scale corrections of

each Monte Carlo jet will closely match the corrections in real data. Third, the uncertainties from the energy scale corrections are acquired. Finally, the weighted average errors and correlations in each bin combine to form an error matrix.

Monte Carlo Jet Generation

The jet E_T distribution must be identical to the observed (smeared) jet cross section in data. The routine:

1. Randomly generates the initial parton momenta x_1 and x_2 to find the scale of the collision (dijet mass $= \sqrt{x_1 \cdot x_2 \cdot s}$, for example).

2. Finds the corresponding p_T and other kinematic quantities for both of the final state partons (which result in jets).

3. Smears the jets according to the known resolution functions and then selects one jet at random.

4. Ensures that the selected jet falls within the desired x_T bin and $-0.5 < \eta_{jet} < 0.5$ (or starts over)

5. Generates a *weight* for the jet, to reproduce the jet cross section's steeply falling spectrum, using either of

   - a theoretical weight* based on CTEQ4M and the scale of the collision, or
   - an experimental weight based on the ansatz from unsmearing

Simulation of Vertex Position, Luminosity, and Mi_Tool Values

These quantities are all required by the energy scale correction algorithm, called CAFIX (v5.1), or NT_CAFIX.

1. A Level 2 trigger is assigned to the jet based on its E_T (corresponding to the actual E_T region of each trigger in the data)

2. The vertex distribution from that trigger is sampled to find a vertex position

3. The instantaneous luminosity distribution for that trigger is sampled to assign a luminosity

4. The MI_RUN1 or MI_630 distribution for that trigger and that luminosity is sampled to find a random MI_TOOL value.

---

* The theoretical weight is extracted from CERN's PDF library.

The Energy Scale Uncertainty

Because the generated jet distribution already represents the energy scale corrected jet E_T, and because the response correlation is given in terms of the energy before the response correction, the energy scale algorithm must be run "in reverse" to find the uncertainty.

1. The jet is "uncorrected" to a best guess measured E_T
2. NT_CAFIX corrects the jet
3. If the new corrected E_T is not the original Monte Carlo E_T, the process is repeated with a better guess for the measured E_T until convergence
4. NT_CAFIX is asked for the errors on the jet correction. The errors are categorized by their degree of correlation in energy or E_T. Again, the categories are:

    - Uncorrelated errors (errors that are statistical in nature, or errors whose correlations are not known)
    - (Completely) correlated errors (typically "method" errors)
    - partially correlated errors (from the fit of the response curve)

The Covariance of the Error

The published energy scale note [43] contains a correlation matrix for the response fit, parameterized as a function of jet energy. Because the energy scale corrections for both CM energies use the same response correction, the correlation matrix is valid at both energies. The *covariance* between (for instance) a jet at 630 GeV and a jet at 1800 GeV is extracted with a two-dimensional interpolation of this discrete matrix. The weighted average of the jet correlations, the magnitude of the response uncertainty, and the magnitude of the jet cross sections determine the covariance of the uncertainty in the ratio. A similar process determines the completely correlated and uncorrelated error components in the energy scale.

The ratio of inclusive jet cross sections is given by

$$R = \frac{\sigma^{630}}{\sigma^{1800}},\tag{7.3}$$

where the σ indices indicate the dimensionless cross sections in x_T for 630 and 1800 GeV. The elements of the covariance matrix are

$$C_{ij} = \left\langle \hat{\rho}_{ij}\, \delta R_i\, \delta R_j \right\rangle,\tag{7.4}$$

where $\hat{\rho}$ expresses the correlation between the x_T bins i and j, and the errors in the ratio δR may be expressed as

$$\delta R_i = \frac{\partial R_i}{\partial \sigma_i^{630}}\, \delta\sigma_i^{630} + \frac{\partial R_i}{\partial \sigma_i^{1800}}\, \delta\sigma_i^{1800}, \tag{7.5}$$

an expression similar to the total derivative of calculus. Here, the two partial derivatives possess opposite signs:

$$\frac{\partial R_i}{\partial \sigma_i^{630}} = \frac{1}{\sigma_i^{1800}} = \frac{R_i}{\sigma_i^{630}} \qquad \text{and} \qquad \frac{\partial R_i}{\partial \sigma_i^{1800}} = \frac{-\sigma_i^{630}}{\left(\sigma_i^{1800}\right)^2} = -\frac{R_i}{\sigma_i^{1800}}. \tag{7.6}$$

Defining $x \equiv x_T$ for conciseness of notation, each $\delta\sigma$ in Equation 7.5 may be expanded in terms of jet energy:

$$\delta\sigma_i^a = \frac{\partial \sigma_i^a}{\partial x_i}\delta x_i^a = \frac{2}{a}\sin\theta_i \cdot \frac{\partial \sigma_i^a}{\partial x_i}\, \delta E_i^a \tag{7.7}$$

The covariant cross section error is now expressed in terms of jet energy, the jet colatitude, the center–of–mass energy (a), and the slope of the dimensionless cross section. The final expression for the covariance matrix elements becomes

$$C_{ij} = \sum_{a,b}\sum_{kl} q \cdot \frac{2}{a}\sin\theta_k \cdot \frac{2}{b}\sin\theta_l \cdot \frac{R_k}{\sigma_k^a}\frac{\partial \sigma_k^a}{\partial x_k} \cdot \frac{R_l}{\sigma_l^b}\frac{\partial \sigma_l^b}{\partial x_l} \cdot \left\langle \rho_{kl}^{ab}\, \delta E_k^a\, \delta E_l^b \right\rangle, \tag{7.8}$$

where a and b indicate center–of–mass energies, and ρ_{kl}^{ab} is the correlation between the two jets whose energies fall in bins k and l, originating from the data sets at $\sqrt{s} = a$ and b. A factor that accounts for the negative sign in Equation 7.6, $q = 1$ when $a = b$, and $q = -1$ otherwise. The bracket notation indicates the expectation over the entire bin; in practical terms, the weighted average quantities of a large jet sample in each bin determine the bracketed quantity. The summations indicate the four relevant correlations, visually described in Figure 7.5.

As mentioned previously, interpolation of a correlation matrix determines the values of ρ_{kl}^{ab} for the response error. For the completely correlated errors, all ρ's take the value of unity; for the uncorrelated errors, all ρ's are zero except for the special case $a = b$ and $k = l$, where the value is unity.
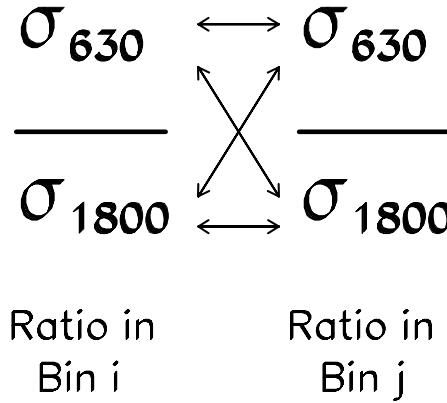
Figure 7.5: Correlations between two ratio bins i and j. Arrows indicate the four possible correlation (ρ) terms. The uppermost arrow would be $\rho_{ij}^{630-630}$, while the "$\searrow$" arrow is $\rho_{ij}^{630-1800}$.

The analysis code computes the covariance matrix for each of the three cases element by element. The simulation results are reported in three 22×22 matrices whose diagonal elements are the squared uncertainties at each x_T point, and whose off–diagonal elements determine the covariance between x_T points. Equation 7.8 represents the most complicated aspect of the uncertainty calculation: cancellation in the ratio of the energy scale errors.

7.4.2 Energy Scale Uncertainty Results

The following results were generated with 280,000 events in each x_T bin. Figure 7.6 compares the total Monte Carlo result with the uncertainty reported in the 630 GeV data set. The results agree well, but the Monte Carlo points clearly exhibit a statistical advantage.

The energy scale uncertainties, divided by degree of correlation, are displayed in Figure 7.7; the curves include all cancellation effects observed in the ratio. The major contribution originates from the partially correlated response error but receives a nearly equal contribution from the completely correlated components at low values of x_T. The full
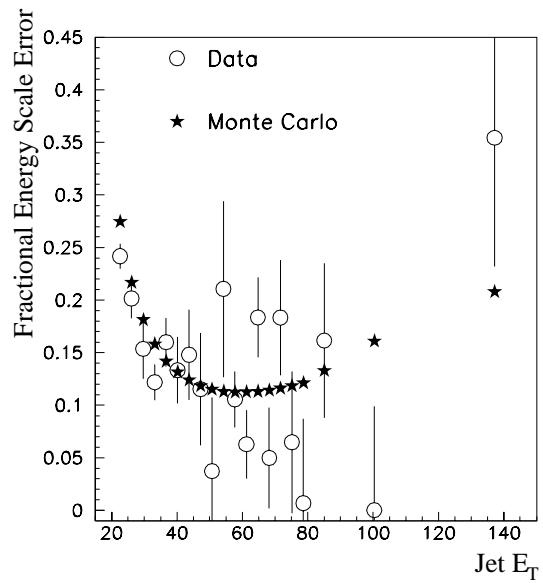
Figure 7.6: Comparison of Monte Carlo results (total uncertainty at 630 GeV) with the uncertainty reported in data.
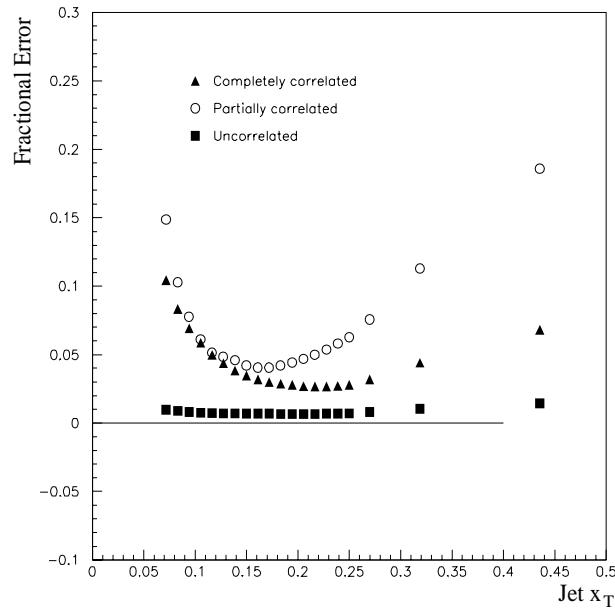

Figure 7.7: Energy scale uncertainties in the ratio of cross sections, divided by category.

Error Source	Correlation in		Comments
	√s energy	Jet E	
Luminosity	partial	1	
filter match	0	1	1800 GeV only
Event cuts	0	0	
Jet cuts	0	0	
Resolution			
fits	partial	1	Twin Fit
closure	0	0	
quark/gluon fractions	1	1	
Unsmearing fits	0	1	
Energy Scale			
Zsp model	1	1	
response fit	1	partial	
response at 630 GeV	0	1	Limit of verification
out-of-cone	1	1	
response background	1	1	
topology bias	1	1	
MPF acceptance	1	1	
underlying event	0	1	
cryostat matching	1	1	
Change of units	0	0	

Table 7.3: Error correlations in the ratio of cross sections. "0" indicates no correlation, "1" indicates complete correlation.

covariance matrix, presented in the next section, includes the energy scale, unsmearing, luminosity, and all other uncertainties.

7.5   Final Uncertainty in the Ratio

The individual uncertainties of the earlier sections fall into several classifications, summarized in Table 7.3. Cancelation of uncertainties only materializes when the errors are completely correlated between center–of–mass energies.

To help interpret the total covariance matrix for the ratio of cross sections, Figure 7.8 depicts the square root of the diagonal elements, by individual component. The uncertainty in the energy scale correction dominates at each end of the spectrum; resolution and contributions from other sources (primarily luminosity uncertainty) become important at

intermediate values of x_T. The 22×22 covariance matrix itself takes the form

$$\bar{\mathsf{V}} = \begin{pmatrix} \Delta_1^2 \cdot \partial_1^2 & \rho_{12}\Delta_1\Delta_2\partial_1\partial_2 & \rho_{13}\Delta_1\Delta_3\partial_1\partial_3 & \\ \rho_{21}\Delta_2\Delta_1\partial_2\partial_1 & \Delta_2^2 \cdot \partial_2^2 & \rho_{23}\Delta_2\Delta_3\partial_2\partial_3 & \cdots \\ \rho_{31}\Delta_3\Delta_1\partial_3\partial_1 & \rho_{32}\Delta_3\Delta_2\partial_3\partial_2 & \Delta_3^2 \cdot \partial_3^2 & \\ & \vdots & & \ddots \end{pmatrix}. \qquad (7.9)$$

Dividing each row and column of the covariance matrix by the square root of its diagonal element reveals the correlation matrix; the diagonal elements are by definition unity, and the off–diagonals range from -1 to 1. Figure 7.9 represents the elements of the correlation matrix with the height of its lego blocks.

The covariance matrix allows very discriminating comparisons to the NLO QCD predictions described in Chapter 1. Given a prediction for the ratio of cross sections or an individual cross section, the level of agreement is determined with

$$\chi^2 = (D - T)^\text{T} \; \bar{\mathsf{V}}^{-1} \; (D - T). \qquad (7.10)$$

Armed with the covariance matrix for the ratio and both cross sections individually, the next chapter presents the findings of this analysis.
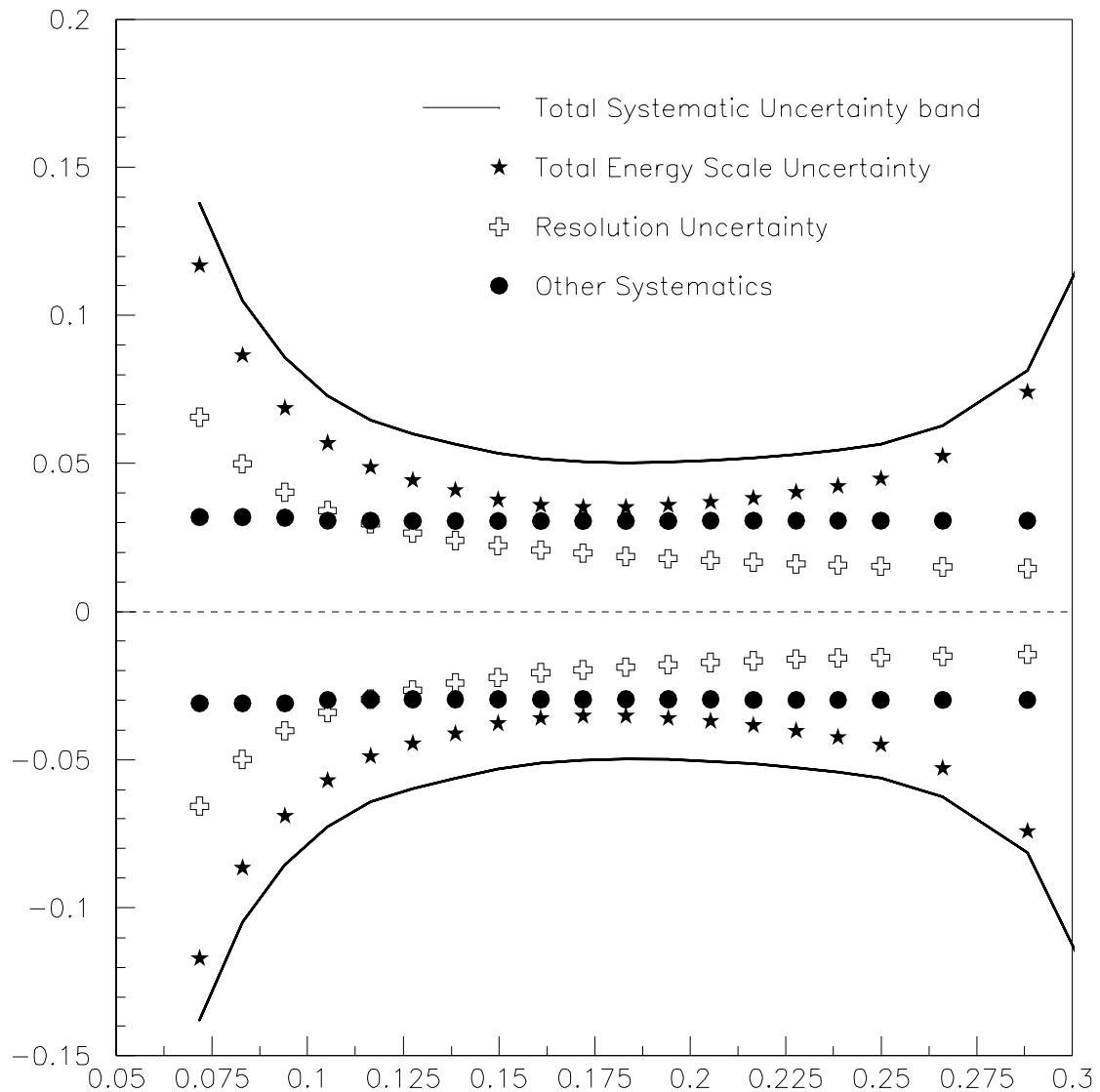
Figure 7.8: All errors in the ratio of inclusive jet cross sections, as a function of x_{T}. Uncertainty from the energy scale dominates the spectrum.
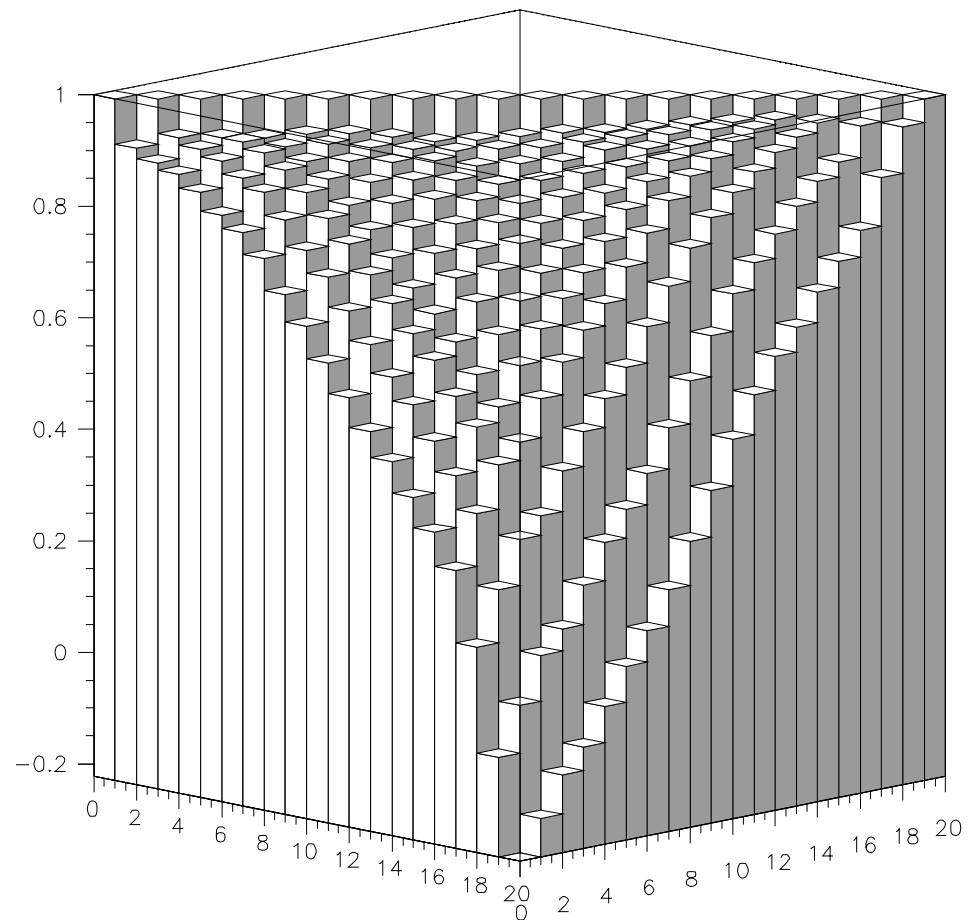
Figure 7.9: Rendition of the correlation matrix for the ratio of cross sections. Axes indicate the bin numbers. The "ridgeline" is formed by the uncorrelated uncertainties, which appear only on the diagonal of the matrix.

Chapter 8

Results and Comparison to Theoretical Predictions

> *"Many a beautiful theory is spoiled by an ugly fact."*
> — Aldous Huxley

This final chapter reports the results of the inclusive jet cross section at $\sqrt{s} = 630$ GeV and the ratio of dimensionless cross sections between $\sqrt{s} = 630$ and 1800 GeV. The first section reintroduces the four parameters in the theoretical predictions; the second section compares the observed jet cross section to NLO QCD predictions with several representative choices of renormalization scales, fragmentation scales, PDF's, and values of R_{sep}. Differences between data and theory are qualitatively discussed and a full χ^2 analysis is presented. The final section provides some discussion of the results and summarizes this dissertation.

8.1 Theoretical Parameters

Recall that the QCD predictions of this dissertation extend to next–to–leading–order ($\mathcal{O}(\alpha_s^3)$). Although such calculations inherently contain many uncertainties, the usual practice in HEP is to consider the theory to be *errorless* for any given set of input parameters; the variation of the theory is explored by making several comparisons with different parameter values. Four different parameters describe the choices available to the QCD prediction.

First, the prediction varies with different values of the renormalization scale, required to replace divergent integrals with finite integrals in the calculation. Normally, the scale μ is set to some factor times the maximum jet E_T in the event; *i.e.,* $\mu = c \cdot E_T^{max}$. The

inclusive jet cross section increases as the constant c varies from very low values to $c = 0.5$, then decreases again for larger values. Although there is no theoretical preference [44] for $c = 0.5$, this saddle–point behavior in the cross section makes it attractive aesthetically.

The factorization scale, a second indeterminate parameter, determines what percentage of the prediction is calculated perturbatively, versus the fraction that is determined empirically in the PDF. For simplicity, and because its variations result in lesser effects, this scale, μ_f, is typically set equal to the renormalization scale.

The third source of theoretical uncertainty, the PDF depends on both renormalization and fragmentation scales, on the input data from prior experiments (some of which conflicts), and on the collaborations responsible for preparing "commercial" PDF's. Only two of the purveyors of PDF's, CTEQ and MRS, receive treatment in this chapter.

Finally, an empirical parameter, R_{sep}, determines the maximum separation permitted between a parton and its radiated daughter parton before they result in separate jets. In essence, this factor describes an *effective* cone diameter $(d = R_{sep} \cdot R)$ for parton "jets," which is smaller than the calorimeter definition of $2R$. This parameter was determined by the DØ Collaboration to have a best value of $R_{sep} = 1.3$ because it best reproduces [8] the event–by–event behavior of the calorimeter.

8.2   Results

The steeply falling cross section distributions for both $\sqrt{s}$ energies span more than five orders of magnitude. Because absolute comparisons become difficult over such large scales, the comparisons of this section concentrate on the *fractional deviation*, defined

$$D(x_i) = \frac{f(x_i) - t(x_i)}{t(x_i)}, \qquad (8.1)$$

where the $f(x_i)$ are the cross section values in the data at bin points x_i, and $t(x_i)$ are the theoretical predictions at those same points.
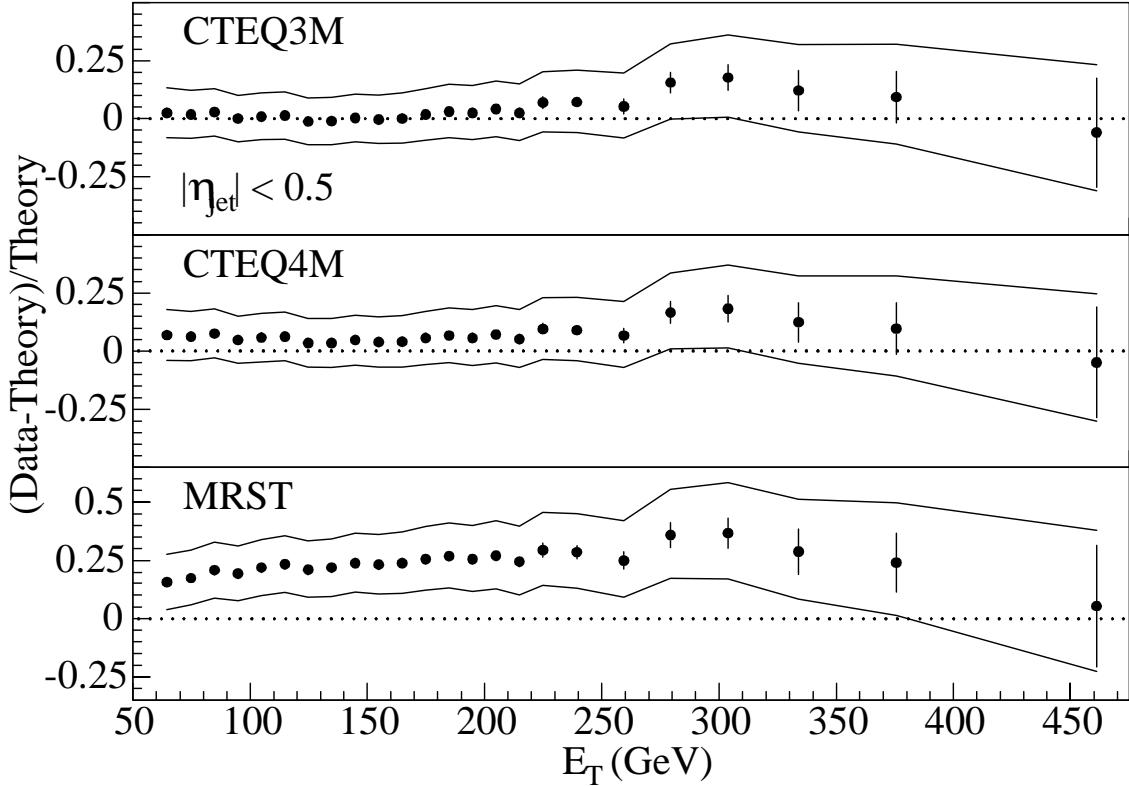
Figure 8.1: Fractional deviation of the inclusive jet cross section at $\sqrt{s} = 1800$ GeV and selected NLO QCD predictions.

8.2.1   Results at $\sqrt{s} = 1800$ GeV

The 1800 GeV cross section, depicted in Figure 8.1, agrees well with the theoretical predictions. Visually, the cross section is reasonably proximate to all predictions without regard to variation in the theoretical details.* The covariance matrix for 1800 GeV quantifies the level of agreement, as indicated in Tables 8.1 and 8.2. In most cases, the cross section and NLO QCD prediction are at least 50% likely to be the same distribution. The second table reports the results for a slightly different pseudorapidity range, to facilitate comparisons to other publications.

The dichotomy between the normalization difference in the visual comparison to MRST

---

* Because the EKS predictions do not differ substantially, this subsection treats JETRAD predictions exclusively.

Renormalization	$\mathbf{E}_{\mathrm{T}}^{max}$		$\mathbf{E}_{\mathrm{T}}^{jet}$	
Scale	χ^2	prob.	χ^2	prob.
0.25	14.8	92.6%	19.8	70.8%
0.5	19.4	73.0%	22.2	56.7%
1.00	16.8	85.7%	18.1	79.8%

Table 8.1: χ^2 comparisons for the 1800 GeV cross section, varying the renormalization scale.

PDF	$|\eta| < 0.5$		$0.1 < |\eta| < 0.7$	
	χ^2	prob.	χ^2	prob.
CTEQ3M	23.9	46.7%	28.4	24.4%
CTEQ4M	17.6	82.2%	23.3	50.2%
CTEQ4HJ	15.7	89.9%	20.5	66.8%
MRSA$'$	20.0	69.7%	27.8	26.9%
MRST	17.0	84.9%	19.5	72.5%

Table 8.2: Additional χ^2 comparisons for the 1800 GeV cross section, varying PDF.

and the acceptable χ^2 result highlights the danger of visual methods in the case of highly correlated uncertainties. In the case of the 1800 GeV cross section, the normalization of the distribution changes with very little χ^2 penalty, but the shape remains largely invariant. As a result, the relative normalization of data and theory are less important than the final shape of the spectrum once normalization has been established, allowing MRST to agree more strongly with the data than CTEQ3M, which apparently requires no normalization change.

8.2.2 Results at $\sqrt{s} = 630$ GeV

Now consider the fractional deviation between theory* and the 630 GeV inclusive jet cross section. Although Figure 8.2 exhibits a slight normalization difference, the large systematic uncertainties ensure satisfactory agreement with the NLO QCD prediction. Table 8.3 lists the resulting χ^2 values for several PDF's and renormalization scales. Here again, the factorization scale has been set equal to the renormalization scale for convenience. As with the cross section at $\sqrt{s} = 1800$ GeV, the prediction for $\mu = \frac{1}{2}\mathrm{E}_{\mathrm{T}}$ appears to be slightly disfavored by the data, and CTEQ4HJ yields the best agreement.

---

* Again, all predictions in this subsection were generated with JETRAD.

PDF	Renormalization Scale	χ^2	prob.
CTEQ3M	$2 \cdot E_T$	18.5	55.4%
	E_T	28.1	10.8%
	$E_T/2$	39.2	0.63%
	$E_T/4$	15.8	72.9%
CTEQ4HJ	$E_T/2$	24.4	22.5%
MRSA$'$	$E_T/2$	44.1	0.14%
CTEQ4M	$E_T/2$	30.3	6.68%

Table 8.3: χ^2 comparisons for the 630 GeV cross section, compared to several predictions.
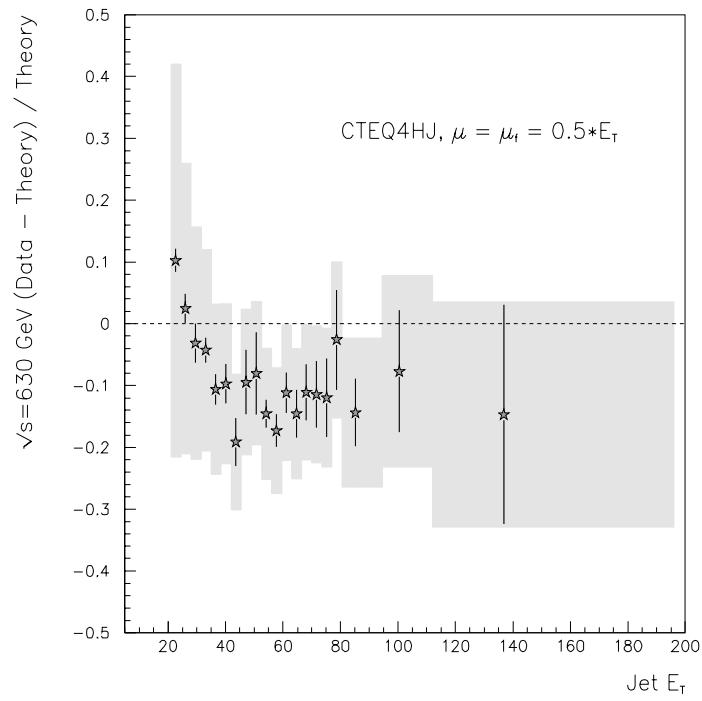
Figure 8.2: Comparison of the 630 GeV inclusive jet cross section and a NLO QCD prediction. Shaded regions encompass the systematic errors, vertical bars indicate the statistical uncertainty.

8.2.3   Results for the Ratio of Dimensionless Cross Sections

The ratio of dimensionless cross sections enjoys several advantages over the individual measurements. First, the error cancelation is significant, as seen in the previous chapter. Second, the change in the ratio with varying PDF's becomes smaller for EKS predictions and becomes negligible (Figure 8.3) for the JETRAD predictions. As experimental data accumulates, the best–fit PDF's change; thus, this analysis is insensitive to the part of the NLO prediction that lies in continuous flux. As an additional benefit, renormalization scale differences are muted somewhat (Figure 8.4). The final result is very sensitive to shortfalls inherent in the theory, whether they result from effects that are neglected in the calculations or from new physics.

Table 8.4 lists the χ^2 distributions for the ratio of cross sections and selected theoretical predictions. In all cases, the factorization scales are equal to the listed renormalization scale, which use the E_T^{max} convention. Unlike the individual cross sections, the ratio of cross sections does not agree with any given NLO QCD prediction; the χ^2 probability is less than 8% in every case; for the choice $\frac{E_T}{2}$, the probability corresponds to more than three standard deviations. As was evident in Figure 8.3, the three listed PDF's yield similar results. The sole exception, EKS, with CTEQ3M, $\mu = \mu_f = \frac{1}{4}E_T^{max}$, yields a probability of 11%; this is the only combination of theoretical parameters that lies within one standard deviation of the data. All other parameter sets for EKS result in predictions that yield poor χ^2 values (Figure 8.5). This single differing result may indicate that small renormalization scales can pull the EKS calculation out of a perturbative region, and that the agreement between data and prediction results more from chance than from accuracy.

8.3   Discussion

As evinced by the low probabilities in the previous section, the level of agreement between data and NLO QCD predictions is less than satisfactory. Because there exist four free parameters in the NLO QCD prediction, the predicted ratio of cross sections possesses some flexibility that has not yet been explored. Figure 1.11, Page 22, depicts the fractional change
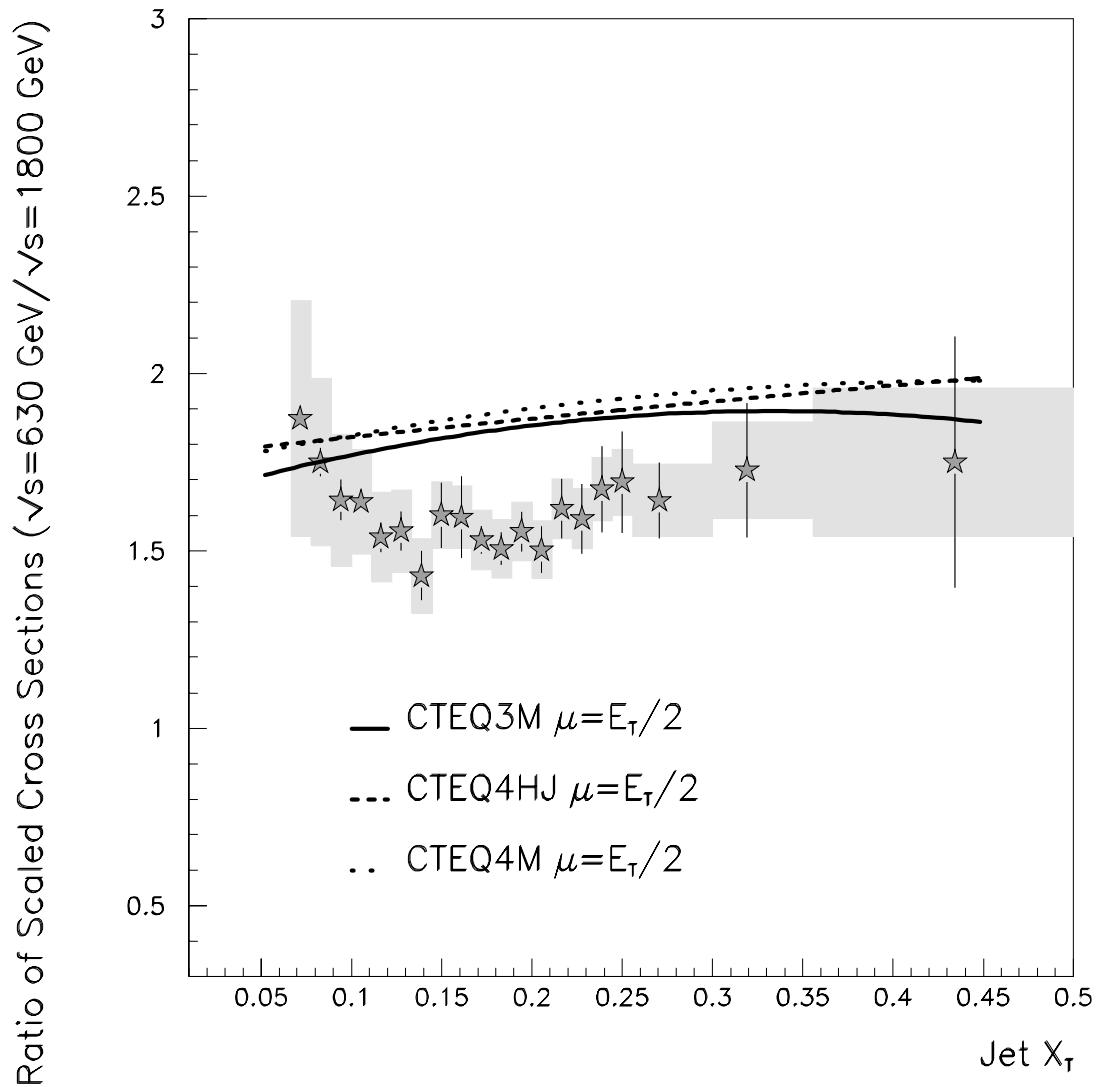
Figure 8.3: The ratio of dimensionless cross sections and NLO QCD predictions with various parton distribution functions.
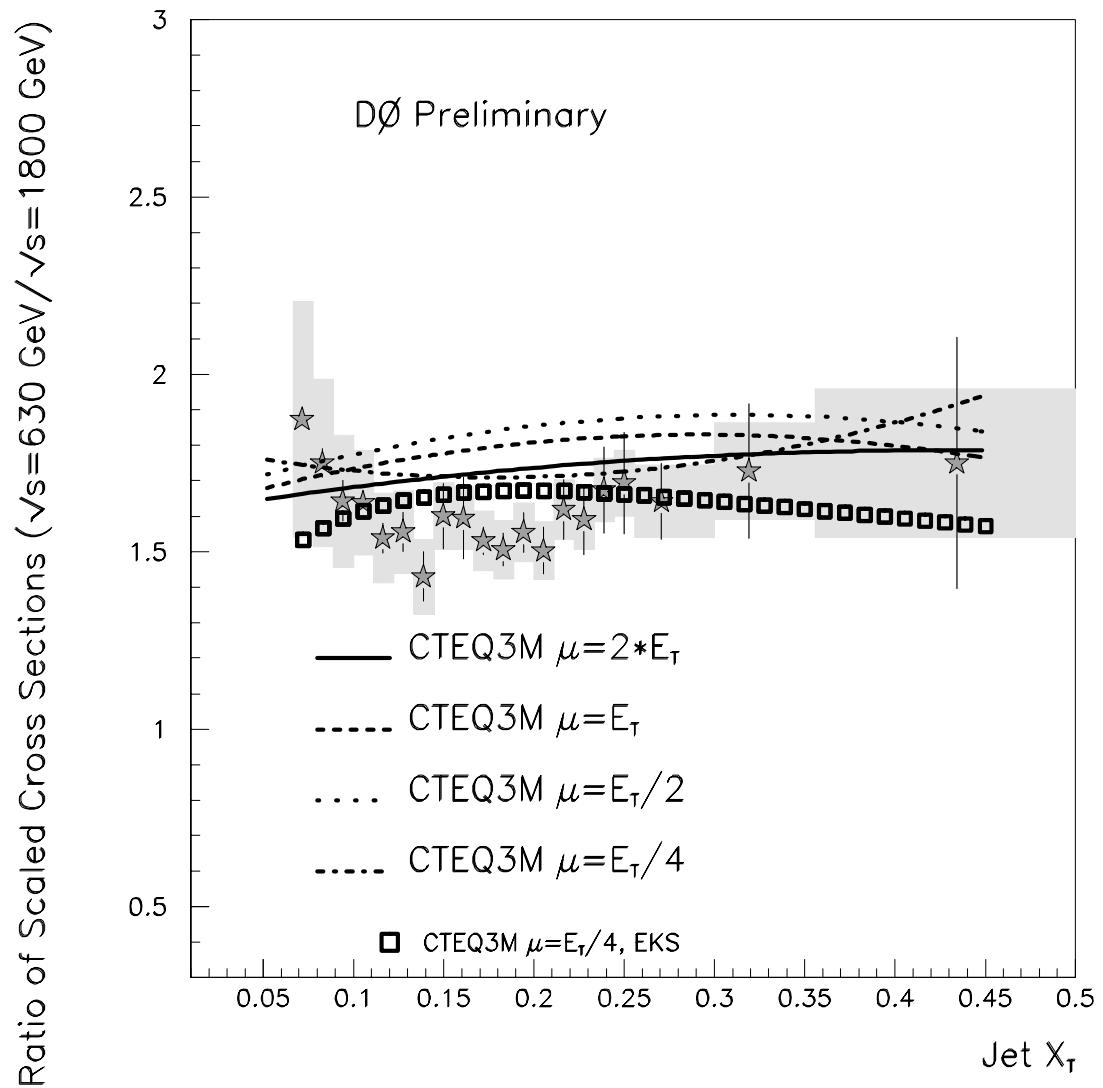
Figure 8.4: The ratio of dimensionless cross sections, versus predictions with various renormalization scales.

PDF	Renormalization Scale	χ^2	prob.
CTEQ3M	$2 \cdot E_T$	29.9	7.19%
	E_T	41.8	2.91%
	$\frac{3}{4} E_T$	51.1	0.02%
	$E_T/2$	50.8	0.02%
	$E_T/4$	30.9	5.66%
CTEQ4HJ	$E_T/2$	51.7	0.01%
MRSA$'$	$E_T/2$	56.6	0.002%
CTEQ3M, EKS	$E_T/4$	27.9	11.0%

Table 8.4: The χ^2 comparisons for the ratio of cross sections.
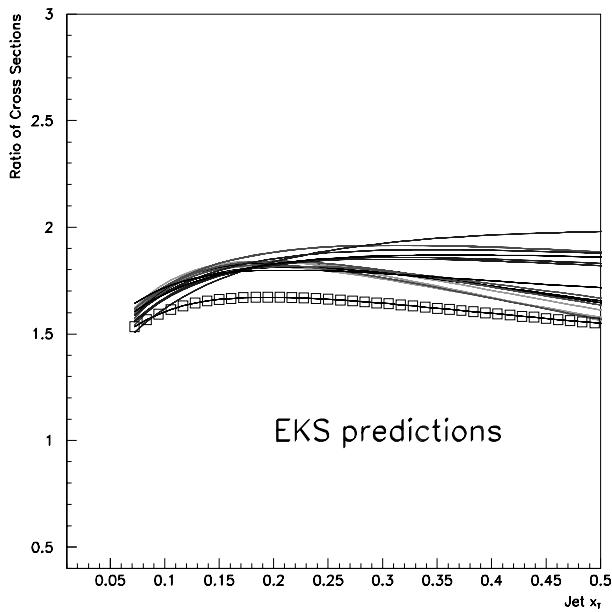
Figure 8.5: Ratio of dimensionless cross sections generated with EKS and many combinations of the four parameters. Only one combination yields an acceptable χ^2 value (highlighted with markers).

PDF	Renormalization		χ^2	prob.
	630	**1800**		
	$2 \cdot E_T$	$E_T/2$	10.9	94.7%
CTEQ3M	E_T	$E_T/2$	28.5	9.84%
	$E_T/4$	$E_T/2$	12.1	91.3%

Table 8.5: Additional χ^2 comparisons for the ratio of cross sections. Here, the renormalization scale is mismatched between CM energies.

in the cross section ($\sqrt{s} = 630$ GeV) with respect to variations of any one of the parameters; Figure 8.6 presents the analogous changes in the ratio. In each case, the fractional variation is reduced in the ratio. (Note that none of the shifts in the figure reproduce the 15% change observed with the specific choice $\mu = \mu_f = \frac{1}{4} E_T^{max}$.) Although large shifts may still be induced with parameter changes, none of the individual shifts reproduce the difference observed between the predictions and the data. This section explores different possibilities that may describe the data.

Different renormalization scales could be selected for the different center–of–mass energies: an unconventional solution that remains within the bounds of NLO QCD (Figure 8.7). Theoretically, there is no implicit need for identical scales at $\sqrt{s} = 630$ GeV and 1800 GeV, but a variable renormalization scale may be too inelegant for the scientific community to accept. Nonetheless, the resulting χ^2 probabilities indicate remarkably good agreement (Table 8.5).

Alternately, new calculational techniques could remove possible deficiencies in the prediction. The first of these methods has been proposed [45] by Balitskiĭ, Fadin, Kuraev, and Lipatov. The BFKL formalism treats the nonperturbative physics of soft hadronic radiation by introducing a *pomeron* exchange diagram. The pomeron, a composite object, consists of a gluon that radiates several final state gluons (Figure 8.8). This "gluon ladder" represents a resummation of leading energy logarithms to all orders of QCD. Unfortunately, the resummation procedure introduces yet another free parameter to the prediction: the Regge scale, μ_R.

A recent BFKL calculation, applied to the leading–order QCD processes, [46] spans the
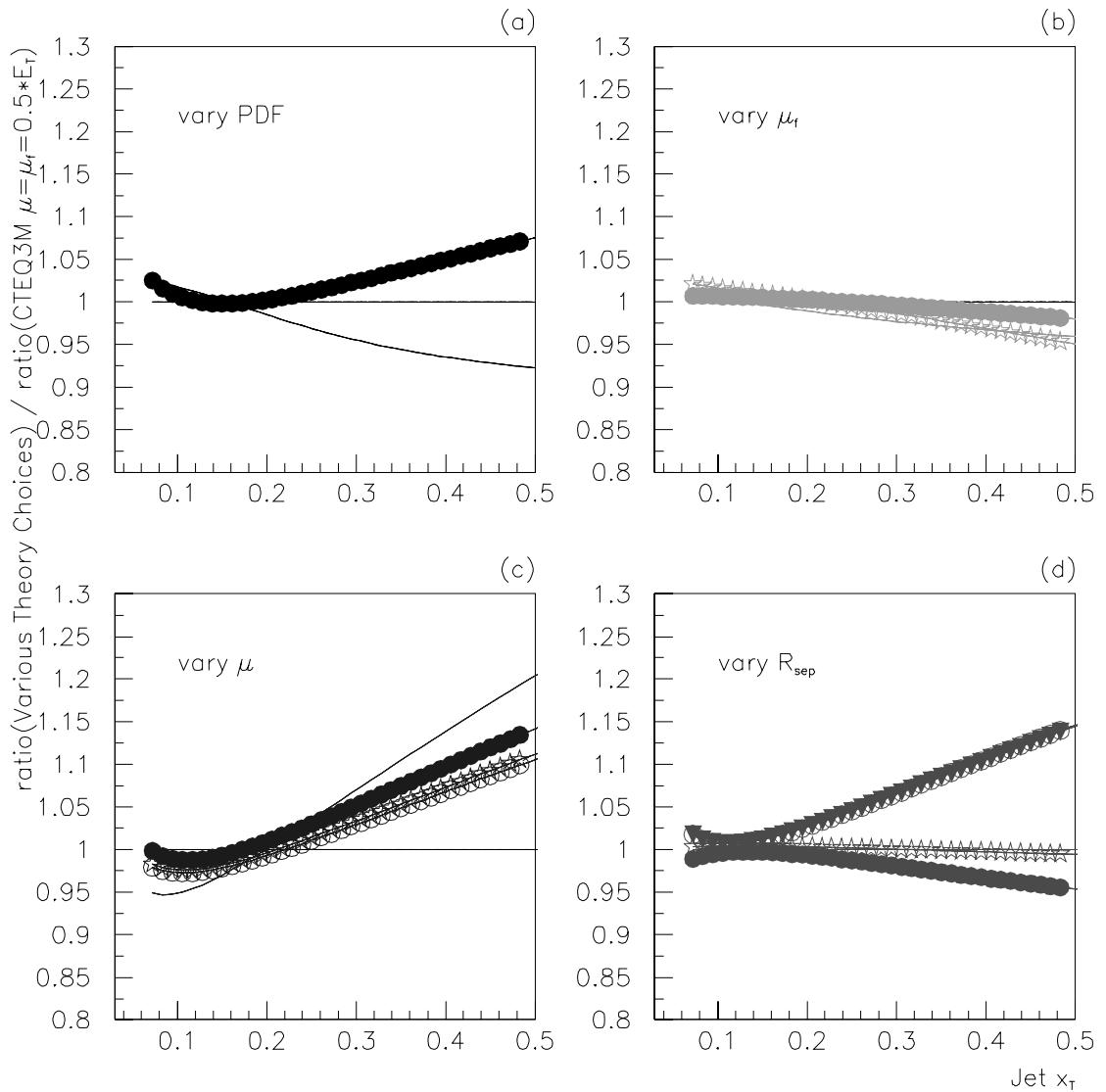
Figure 8.6: Theoretical uncertainties in the NLO QCD predition for the ratio, resulting from (a) changes in PDF, (b) changes in renormalization scale, (c) changes in factorization scale, and (d) changes in the R_{sep} parameter.
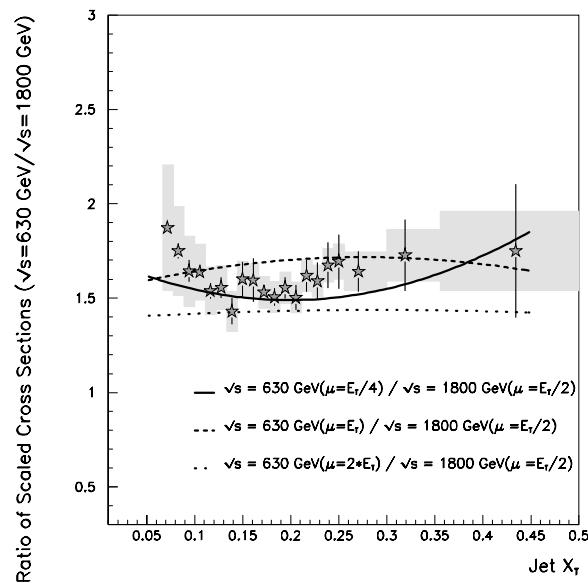
Figure 8.7: Ratio of cross sections, different renormalization and factorization scales for each CM energy.
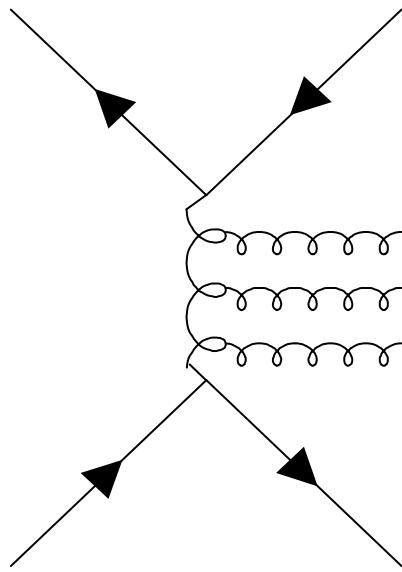

Figure 8.8: Illustration of the BFKL "gluon ladder". Although only three radiated gluons appear in this diagram, the BFKL formalism sums over infinitely many radiated gluons.
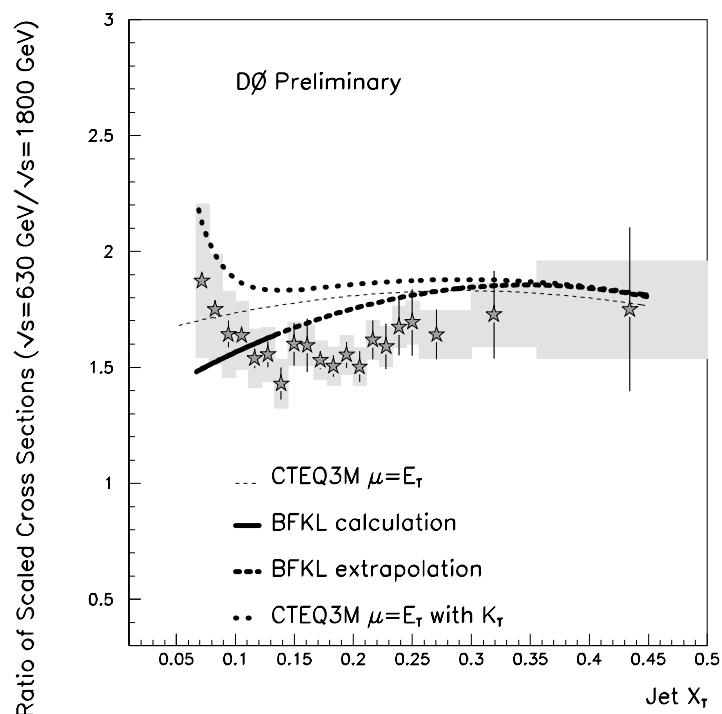
Figure 8.9: The ratio of cross sections relative to augmented QCD predictions.

low x_T region. Computing–power limitations prevent analytic extension beyond $x_\mathrm{T} \gtrsim 0.13$, but the BFKL prediction rapidly converges to the standard NLO prediction as x_T increases. Figure 8.9 compares the BFKL prediction to the measured ratio of cross sections; the dashed line represents an extrapolation of the BFKL prediction throughout the region of data. For this prediction, $\mu = \mu_f = \mathrm{E_T}$, $\mu_R = \frac{1}{2}\mathrm{E_T}$, the PDF is CTEQ4L, and $R_{sep} = 2.0$. This particular combination of parameters was not available for the NLO prediction, but a similar PDF with the same μ and μ_f is included in the figure for comparison. The extrapolated prediction indicates that a fuller BFKL treatment could reproduce some of the normalization differences between the data and NLO QCD, but may not model the low x_T behavior.

A second augmentation to NLO QCD, "k_T smearing," is currently a hypothesis and not an analytic prediction. The low x_T behavior of the ratio may arise from soft gluon radiation. Current NLO QCD calculations do not include soft radiative corrections, where the partons can emit low–energy gluons nearly colinearly. This soft radiation can be included with an *ad hoc* correction to the standard perturbative prediction by adding a small quantity of transverse energy, called k_T, to the outgoing partons during the calculation. This randomized "kick" to the outgoing partons inflates the lowest portions of the inclusive jet cross section in much the same way as the smearing from jet energy resolution. In Figure 8.9, the hatched line indicates the effect of a Gaussian–distributed kick with width 3 GeV. The normalization differences remain throughout most of the x_T range, but the rise in the prediction at the low end is similar to the rise observed in the data. Because k_T effects would result in an observed dijet asymmetry, it is not clear how much k_T would survive the unsmearing process, so the predicted change in Figure 8.9 may be an overestimate.

Because the ratio of cross sections isolates the high–order effects of QCD without masking them with the leading–order behavior, the final and possibly best explanation for the deviation of the ratio from the QCD prediction stems from the truncation of the calculation at NLO. Although the augmentive techniques discussed in this section could explain the observed difference to some degree, these additions at best approximate a full $\mathcal{O}(\alpha_s^4)$
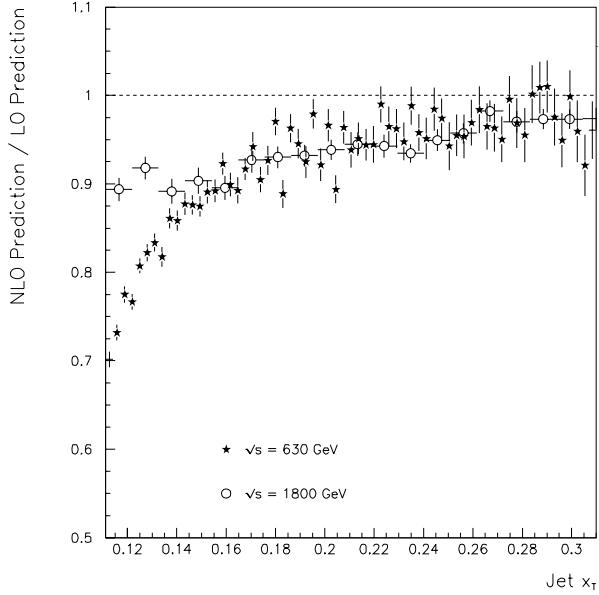
Figure 8.10: The effect of the $\mathcal{O}(\alpha_s^3)$ term in the QCD jet cross section prediction, for both center–of–mass energies. Distributions were generated with JETRAD.

calculation. Significant computational power requirements prohibit a NNLO calculation at this time, but the ratio of NLO to leading–order could provide an insight to the magnitude of the effect (Figure 8.10). For jet x_{T} greater than 0.15, the $\mathcal{O}(\alpha_s^3)$ term generates the same effect without regard to center–of–mass energy. The difference from LO is small, so an additional perturbative term cannot induce much additional change. The behavior at low x_{T} differs markedly, but only for $\sqrt{s} = 630$ GeV; because the jet energies become very small, greater sensitivity to α_s terms should be expected. Note that the x_{T} range spanned by the Monte Carlo simulation in Figure 8.10 does not extend as low as the data, the difference between LO and NLO in the first data bin could be as large as 70%. Although the shape of the distributions in Figure 8.10 are suggestive, definitive conclusions must await a full calculation.

A study of event topology provides additional evidence of the need for additional terms in the QCD prediction. Consider Figure 8.11, which plots the fraction of events with two jets (three jets, *etc.*) as a function of jet E_{T} ($\sqrt{s} = 630$ GeV). Approximately 10% of
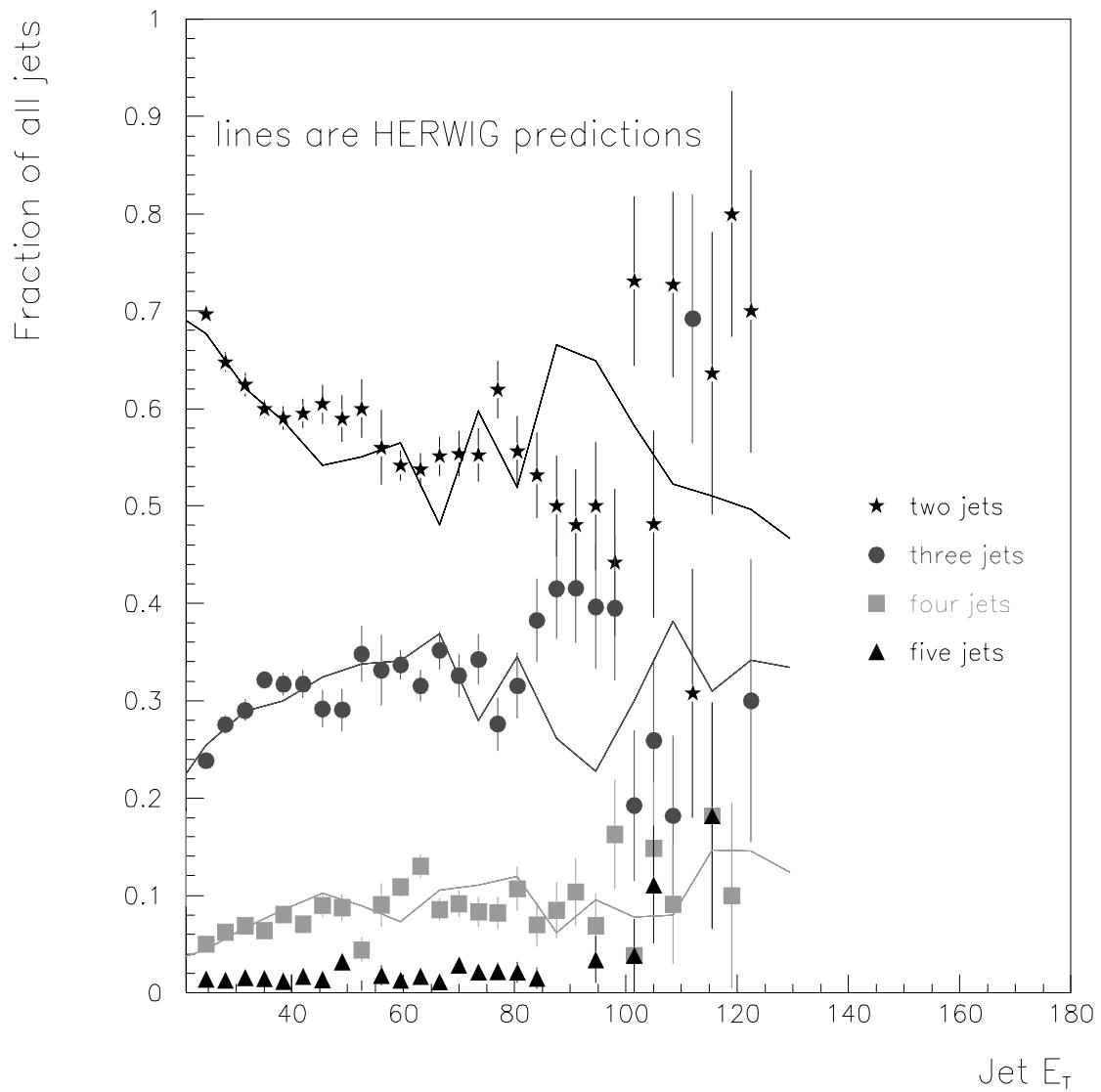
Figure 8.11: Number of jets per event as a function of Jet E_T. Lines indicate the HERWIG Monte Carlo prediction.

all events contain four jets. Because an additional (radiated) jet generally "steals" its E_T from its parent jet, the predicted cross section would decrease if it could accommodate the possibility of fourth jets. Note that NLO calculations cannot contain more than three jets; thus, NLO QCD can neither describe the observed jet topology nor the normalization of the cross section to better than 90%. In contrast, HERWIG models final–state radiation with a fragmentation function, and initial–state radiation with a "reverse evolution" technique. The internal workings of HERWIG are empirical and not analytic, so the output event topology mimics data very closely (solid lines in the figure). Although HERWIG is useful for detector studies, it cannot provide a meaningful comparison of basic theory to physics results.

In Figure 8.11, the number of dijets increases at low values of jet E_T while the number of three–jet and four–jet events decreases over the same range. This effect results from increased frequency of jet merging; low–E_T jets tend to lie closer to their radiated jets. Although this effect should, in principle, be modelled by the R_{sep} parameter, no similar behavior appears in Figure 8.6(d). The low–E_T feature of the ratio may imply either a failure of R_{sep} or a severe underestimation of the number of radiated jets in NLO QCD.

8.4   Summary

This dissertation provides the most precise measurement of inclusive jet cross sections to date. For the first time, a full error analysis describes the relationship of the binwise uncertainties with one another. Use of the χ^2 comparison test quantitatively describes the level of agreement between the measured distribution and the NLO QCD predictions. For both $\sqrt{s} = 630$ and 1800 GeV, the cross sections display no significant deviations from the NLO QCD predictions.

The ratio of dimensionless cross sections enjoys significant error reduction relative to the cross section measurement alone. While the cross section errors range from 10 to 25%, the ratio uncertainties become as small as 5%. The uncertainties in the ratio of cross sections are less correlated than the cross section uncertainties; therefore, the ratio measurement

Bin Edges	in x_{T}	Point Position	Ratio	Statistical Error	Systematic Error
0.067	0.077	0.072	1.87	0.029	0.339
0.077	0.089	0.083	1.75	0.041	0.239
0.089	0.100	0.094	1.64	0.057	0.188
0.100	0.111	0.105	1.64	0.032	0.148
0.111	0.122	0.116	1.54	0.042	0.126
0.122	0.133	0.127	1.56	0.055	0.115
0.133	0.144	0.139	1.43	0.070	0.104
0.144	0.156	0.150	1.60	0.091	0.093
0.156	0.167	0.161	1.60	0.115	0.087
0.167	0.178	0.172	1.53	0.038	0.083
0.178	0.189	0.183	1.51	0.046	0.081
0.189	0.200	0.194	1.55	0.056	0.081
0.200	0.211	0.205	1.50	0.066	0.081
0.211	0.222	0.216	1.62	0.083	0.084
0.222	0.233	0.228	1.59	0.099	0.085
0.233	0.244	0.239	1.67	0.122	0.089
0.244	0.256	0.250	1.69	0.144	0.092
0.256	0.300	0.271	1.64	0.107	0.101
0.300	0.356	0.319	1.73	0.189	0.136
0.356	0.622	0.434	1.75	0.354	0.209

Table 8.6: The ratio of dimensionless jet cross sections.

is more sensitive to normalization differences between data and the predicted result. The observed normalization difference results in a less than 8% probability that the data and NLO calculations describe the same distribution. The difference can be accommodated by varying the renormalization scale between center–of–mass energies. Several augmentations to the NLO prediction show some promise, but the perturbative behavior of QCD indicates that an $\mathcal{O}(\alpha_s^4)$ prediction could provide satisfactory agreement without any additions to the standard QCD formalism.

The size of the covariance matrix prevents publication, but an ASCII–format text file will appear on the DØ Collaboration web page. The final ratio bins, ratio values, and binwise uncertainties appear in Table 8.6.

Appendix A

Coordinate Systems, Units, and Variables for HEP

> *"Differing weights and differing measures—the* Lord
> *detests them both."*
>
> — Proverbs 20:10

A collider detector requires several different coordinate systems to conveniently specify hardware locations, physics results, and beam mechanics. The DØ collaboration uses four primary systems: Cartesian (x, y, z), cylindrical (r, ϕ, z), spherical (r, ϕ, θ), and a modified spherical system using transverse energy, pseudorapidity, and azimuth (E_T, η, ϕ). The fourth coordinate system defines direction and energy magnitude rather than three dimensional position. In all cases, the systems are right-handed with positive z assigned to the direction of the proton beam (south at the DØ collision point). Thus, the x-axis points inward toward the center of the Tevatron and positive y-axis points vertically upward. The colatitude θ becomes zero along the z-axis, and ϕ becomes zero along the x-axis.

A.1 Natural Units

As a standard of high energy physics, all quantities are scaled by the two fundamental constants of relativistic quantum mechanics: Planck's constant

$$\hbar = \frac{h}{2\pi} = 1.055 \times 10^{-34} \text{ J} \cdot \text{sec} \tag{A.1}$$

Quantity	Units
mass (m), momentum (mc), energy (mc^2)	GeV
length ($\hbar$/mc), time ($\hbar$/mc^2)	GeV^{-1}
charge ($\sqrt{\hbar c}$)	(dimensionless)

Table A.1: Physical quantities expressed in terms of natural units.

and the speed of light in vacuum

$$c = 2.998 \times 10^8 \, \frac{\text{m}}{\text{sec}}. \tag{A.2}$$

With the selection of units such that these quantities become dimensionless (*i.e.* $\hbar$, $c \equiv 1$), all quantities may be easily expressed in terms of energy (Table A.1), typically electron-Volts because the mass of the proton is approximately 1 GeV.

As an exception to the convention, cross sections are expressed in terms of *barns*, where

$$1 \, \text{b} = 1 \times 10^{-28} \, \text{m}^2. \tag{A.3}$$

This area-like quantity is related to natural units by the relation

$$1 \, \text{GeV}^{-2} = 0.389 \, \text{mb}. \tag{A.4}$$

A.2 Variables for Collider Physics

For any two–body interaction, the initial 4–momenta* form the Mandelstam variable

$$s = (p_A + p_B)^2, \tag{A.5}$$

which is Lorentz invariant (*i.e.*, the numerical value is independent of the frame of reference). The total center–of–mass energy of the colliding system is given by $\sqrt{s}$, and each particle has center–of–mass energy

$$E_A = \frac{s + m_A^2 - m_B^2}{2\sqrt{s}}. \tag{A.6}$$

At Fermilab, both colliding particles have the same mass, so each has energy $\frac{\sqrt{s}}{2}$, which is sometimes called the "beam momentum."

---

* The four–dimensional momentum vector takes the form $p = (E, \, p_x, \, p_y, \, p_z)$.

Although the transverse component of a scalar quantity may at first seem like a strange concept, E_T is simply defined as the total energy of a particle or group of particles multiplied by the sine of the angle between the energy deposit and the beampipe; loosely, the "transverse energy" is the component of the energy which is orthogonal to the beam direction:

$$E_T = E \sin \theta. \tag{A.7}$$

This quantity is used interchangeably with the more properly formulated transverse momentum, p_T. Because the calorimeter measures energy rather than momentum, and because the masses of the particles that comprise a jet are not measured, transverse energy better describes the observed quantity. In some sections of Chapter 4, $\vec{E}_T$ will be used as a vector for convenience of notation to indicate the magnitude E_T with azimutial direction $\hat{\phi}$.

Because the initial particles in the beams have negligible transverse momentum components, by conservation of momentum, the $\vec{E}_T$ sum of all objects in an event is zero. Some particles escape through the detector without depositing energy; thus creating "missing $\vec{E}_T$," denoted $\vec{\rlap{E}}_T$.

The variable *rapidity* is defined as

$$y = \frac{1}{2} \ln \frac{E + p_z}{E - p_z}, \tag{A.8}$$

where E and p_z indicate total energy and longitudinal momentum. While rapidity is not Lorentz invariant, the first derivative of the rapidity does satisfy this condition; thus, the shape of a rapidity distribution will not change with a boost* in the longitudinal direction. This is a crucial consideration at a hadron collider because the fraction the beam momentum possessed by the inital state partons varies from event to event.

In the limit that $p \gg m$, the rapidity may be re-written in terms of $\cos \theta = \frac{E_z}{E}$ to become

$$\eta = \frac{1}{2} \ln \frac{\cos^2 \frac{\theta}{2}}{\sin^2 \frac{\theta}{2}} = -\ln \left(\tan \frac{\theta}{2} \right). \tag{A.9}$$

While this expression is strictly identical to the rapidity only for massless particles (where

---

* "Boost" indicates that the rest frame of the collision is not identical to the laboratory frame.

$E \approx p$), it is a good approximation for highly relativistic particles. Thus, η is called the *pseudorapidity.*

In a p$\bar{\text{p}}$ collision, the vertex does not in general appear at the center of the detector. As a result, coordinates must be redefined with the zero point at the vertex of the event, not at the center of the detector. At times both detector and "physics" coordinates must be used, the detector quantities are then differentiated with subscripts (*e.g.* η_d denotes detector pseudorapidity).

For collider detectors, values of pseudorapidity close to zero ($|\eta| \lesssim \{0.5 - 0.8\}$ for DØ) are referred to as *central* and large values are termed *forward.* Note that the term *forward* usually applies to large negative pseudorapidity as well; in most analyses, the directions are not distinguishable so there is no "backward" region of the detector. Refer to the calorimeter schematic on page 49 (Figure 2.16) for a depiction of pseudorapidity.

A.3   Calculation of Jet Variables

The DØ experiment uses a "fixed cone" jet definition: each jet consists of all cell energies within a radius

$$R = \sqrt{(\phi_0 - \phi)^2 + (\eta_0 - \eta)^2}, \tag{A.10}$$

where ϕ_0 and η_0 are the coordinates of the jet centroid. Because each jet deposits energy in many detector cells, an algorithm for E_T summation must be defined. Additionally, several non-equivalent methods exist to determine the pseudorapidity and azimuth of the jet centroid. DØ adheres to the following conventions, where the summations occur over calorimeter cells:

$$\text{E}_\text{T}^{jet} = \sum_i \text{E}_{\text{T}i} = \text{E}_i \sin\theta_i, \tag{A.11}$$

$$\phi^{jet} = \tan^{-1}\left(\frac{\sum_i \text{E}_{y_i}}{\sum_i \text{E}_{x_i}}\right), \text{ and} \tag{A.12}$$

$$\theta^{jet} = \tan^{-1} \frac{\sqrt{\left(\sum_i E_{x_i}\right)^2 + \left(\sum_i E_{y_i}\right)^2}}{\sum_i E_{z_i}}, \tag{A.13}$$

where

$$\begin{aligned} E_{x_i} &= E_i \sin\theta_i \cos\phi_i \\ E_{y_i} &= E_i \sin\theta_i \sin\phi_i \\ E_{z_i} &= E_i \cos\theta_i. \end{aligned} \tag{A.14}$$

The pseudorapidity of the jet is determined with Equations A.13 and A.9. Although other algorithms (*e.g.*, Snowmass) result in slightly different quantities, the differences are negligible in the central region. For completeness, the Snowmass definitions are included below.

$$\text{Snowmass } E_T^{jet} = \sum_i E_{T_i} = E_i \sin\theta_i, \text{ as above, but} \tag{A.15}$$

$$\text{Snowmass } \phi^{jet} = \frac{\sum_i E_{T_i} \cdot \phi_i}{\sum_i E_{T_i}}, \text{ and} \tag{A.16}$$

$$\text{Snowmass } \eta^{jet} = \frac{\sum_i E_{T_i} \cdot \eta_i}{\sum_i E_{T_i}}. \tag{A.17}$$

Appendix B

Propagation of Errors

"Sometimes we may learn more from a man's errors,
than from his virtues."
— Henry Wadsworth Longfellow

With any measurement, the degree of certainty to which the nominal value is known is as important as the value itself. The following sections detail the steps necessary to properly calculate the uncertainty of many quantities and several methods of propagating error through a calculation. In the discussion, y_i represents the measured values of some quantity at generalized x_i positions. The "true" distribution being measured is sometimes represented by $f(x)$, although f and g are also used more generally in other discussions.

B.1   Statistical Errors and Binomial Errors

In a standard counting experiment, the statistical uncertainty on a number N is simply

$$\Delta N = \sqrt{N}. \tag{B.1}$$

The fractional error on the number is given by

$$\frac{\sqrt{N}}{N}. \tag{B.2}$$

For a quantity derived from the number (*e.g.*, an event rate, given by N per unit time), the statistical portion of the fractional uncertainty remains the same, as given by Equation B.2. The absolute statistical uncertainty would be given by Equation B.1, divided by the

time. Such a calculation also requires a systematic uncertainty that expresses the precision of the time measurement.

A different method describes the uncertainty of a data *selection*. Given an event sample with N events where some number of events a pass a selection criteria, the *efficiency* is expressed as

$$\epsilon = \frac{a}{N}, \tag{B.3}$$

and the statistical error is given by the *binomial error formula*

$$\Delta\epsilon = \sqrt{\frac{\epsilon \cdot (1 - \epsilon)}{N - 1}}. \tag{B.4}$$

By Equation B.4, the uncertainty range about the efficiency remains bounded by the physical region (*i.e.*, never leaves the interval $[0,1]$). Unfortunately, even for small values of N the errors can be too small to accommodate possible method biases. Usually, experimenters add a systematic error to the binomial uncertainty to avoid underestimation of errors (as in Chapter 5).

B.2 Quadrature Addition of Errors

This simple procedure requires knowledge of the degree of correlation between errors. The formula for the uncertainty on a function $f(x)$, based on the known variances of parameters a, b, c, ..., is given by

$$
\begin{aligned}
(\Delta f(x))^2 &= \left(\frac{\partial f}{\partial a}\right)^2 (\Delta a)^2 + \left(\frac{\partial f}{\partial b}\right)^2 (\Delta b)^2 + \left(\frac{\partial f}{\partial c}\right)^2 (\Delta c)^2 + \cdots \\
&\quad + 2\rho_{ab}\frac{\partial f}{\partial a}\frac{\partial f}{\partial b}\Delta a \Delta b + 2\rho_{ca}\frac{\partial f}{\partial c}\frac{\partial f}{\partial a}\Delta c \Delta a + 2\rho_{bc}\frac{\partial f}{\partial b}\frac{\partial f}{\partial c}\Delta b \Delta c + \cdots,
\end{aligned}
\tag{B.5}
$$

where ρ_{ij} is the *correlation* between parameters i and j, and the one–sigma standard deviations are Δa, *etc.* In the case of uncorrelated parameters ($\rho_{ij} = 0$), Equation B.5 simplifies to

$$\Delta f(x) = \sqrt{\left(\frac{\partial f}{\partial a}\right)^2 (\Delta a)^2 + \left(\frac{\partial f}{\partial b}\right)^2 (\Delta b)^2 + \left(\frac{\partial f}{\partial c}\right)^2 (\Delta c)^2 + \cdots}. \tag{B.6}$$

With Equation B.6, it is easy to verify that for a simple ratio $R(x) = \frac{f(x)}{g(x)}$ with uncorrelated uncertainties,

$$\frac{\Delta R(x)}{R(x)} = \sqrt{\left(\frac{\Delta f(x)}{f(x)}\right)^2 + \left(\frac{\Delta g(x)}{g(x)}\right)^2}, \tag{B.7}$$

and for the comparative *fractional deviation* $D(x) = \frac{f(x)-g(x)}{g(x)}$, the uncertainty is similarly expressed as

$$\Delta D(x) = \frac{f(x)}{g(x)} \cdot \sqrt{\left(\frac{\Delta f(x)}{f(x)}\right)^2 + \left(\frac{\Delta g(x)}{g(x)}\right)^2}. \tag{B.8}$$

The formulae in this section apply equally well to discrete functions $f(x_i)$ as to continuous functions.

When fitting functions to data points, software packages frequently use a chi-square minimization algorithm. Most fitting packages will produce a covariance matrix (an "error matrix"), whose diagonal elements are the squares of the parameter errors (the *variances*), and whose off-diagonal elements are the *covariances* of the parameters. For a three parameter fit, the error matrix is given by

$$V = \begin{pmatrix} (\Delta a)^2 & \rho_{ab}\Delta a\Delta b & \rho_{ac}\Delta a\Delta c \\ \rho_{ba}\Delta b\Delta a & (\Delta b)^2 & \rho_{bc}\Delta b\Delta c \\ \rho_{ca}\Delta c\Delta a & \rho_{cb}\Delta c\Delta b & (\Delta c)^2 \end{pmatrix}. \tag{B.9}$$

In the (usual) case of parabolic errors, the error matrix is symmetric about the diagonal, because $\rho_{ba} = \rho_{ab}$. (For the diagonal elements, ρ_{aa} is identically unity.) The matrix form is easily generalized to additional parameters. When combined with a function's partial derivatives, the matrix elements of V are precisely the factors required by Equation B.5.

B.2.1   Advanced Work with Covariance

In some cases, an analysis requires the covariance of a function *to itself*. Then, the individual elements of a matrix $\bar{V}$ may be expressed as the product of two total derivatives and a correlation. Here the overbar notation indicates inclusion of the derivatives in the matrix;

194

additionally, the rows and columns indicate different values of x in some function $f(x)$:

$$\bar{V}_{ij} = \begin{pmatrix} (\Delta f(x_1))^2 \left(\frac{\partial f(x_1)}{\partial x_1}\right)^2 & \rho_{12} \, \Delta f(x_1) \, \Delta f(x_2) \frac{\partial f(x_1)}{\partial x_1} \frac{\partial f(x_2)}{\partial x_2} \\ \rho_{12} \, \Delta f(x_1) \, \Delta f(x_2) \frac{\partial f(x_1)}{\partial x_1} \frac{\partial f(x_2)}{\partial x_2} & (\Delta f(x_2))^2 \left(\frac{\partial f(x_2)}{\partial x_2}\right)^2 \\ & & \ddots \end{pmatrix}. \quad \text{(B.10)}$$

The formulation of the error matrix in this section should not be confused with Equation B.9.

To illustrate the technique, suppose that the error matrix for the inclusive jet cross section is required for a systematic error that varies as a function of jet energy.* If the cross section consists of 20 points, then the matrix must have 20 rows and 20 columns; the square roots of the diagonal elements are identically the errors of each cross section point. In the matrix, the correlations describe the dependence between different E_T points rather than between different parameters. For any given bin in the cross section, $\sigma(E_T)$, the total derivative with respect to the energy is

$$\delta\sigma(E_T) = \frac{\partial\sigma}{\partial E_T} \frac{\partial E_T}{\partial E} \delta E = \frac{\partial\sigma}{\partial E_T} \sin\theta \, \delta E, \quad \text{(B.11)}$$

and the elements of the covariance matrix in Equation B.10 may be expressed

$$\bar{V}_{ij} = \left\langle \rho_{ij} \delta\sigma_i \delta\sigma_j \right\rangle = \rho_{E_i E_j} \cdot \frac{\partial\sigma}{\partial E_{T_i}} \sin\theta_i \, \delta E_i \cdot \frac{\partial\sigma}{\partial E_{T_j}} \sin\theta_j \, \delta E_j. \quad \text{(B.12)}$$

For a less elementary example, consider the dijet mass, $M = \sqrt{2E_1 E_2 (1 - \cos\theta_{12})}$, a function of two jet energies and the angle between the jets. Assuming the uncertainty is *only* a function of jet energy, the "total derivative" is

$$\delta M = \frac{\partial M}{\partial E_1} \delta E_1 + \frac{\partial M}{\partial E_1} \delta E_1 \quad \text{(B.13a)}$$

$$= \frac{1}{M} \left(E_1 \delta E_2 + E_2 \delta E_1 \right) \left(1 - \cos\theta_{12} \right), \quad \text{(B.13b)}$$

where the $\delta\cos\theta_{12}$ term has been set to zero. The matrix elements are then

$$\bar{V}_{ij} = \left\langle \rho_{ij} \delta M_i \delta M_j \right\rangle = \frac{1}{M_i M_j} \left(1 - \cos\theta_{12_i} \right) \left(1 - \cos\theta_{12_j} \right) \times \quad \text{(B.14)}$$

$$\left(E_{1_i} E_{1_j} \cdot \left\langle \rho_{ij}^{22} \delta E_{2_i} \delta E_{2_j} \right\rangle + E_{2_i} E_{1_j} \cdot \left\langle \rho_{ij}^{12} \delta E_{1_i} \delta E_{2_j} \right\rangle + \right.$$

$$\left. E_{1_i} E_{2_j} \cdot \left\langle \rho_{ij}^{21} \delta E_{2_i} \delta E_{1_j} \right\rangle + E_{2_i} E_{2_j} \cdot \left\langle \rho_{ij}^{11} \delta E_{1_i} \delta E_{1_j} \right\rangle \right).$$

---

* This scenario is a simplified example of the energy scale uncertainty described Chapter 7: the response is correlated in jet energy, but the jet cross section is a function of E_T.

The principle difficulty in the use of Equation B.10 lies in the acquisition of the correlations between bin points. This information is not readily available from most fitting routines.

B.3   Useful Formulae

Very often a weighted average value describes a sample more accurately than a simple average. Given a set of weights w_i and measurements y_i, the average is found with

$$\mu = \frac{1}{\sum_i w_i} \cdot \sum_i w_i \, y_i. \tag{B.15}$$

The uncertainty on the average is given by

$$\Delta\mu = \frac{1}{\sqrt{\sum_i w_i}}. \tag{B.16}$$

This technique was used extensively in Chapter 8, where the w_i represented the values of the jet cross section at each x_i, and the y_i were (for instance) the uncertainties of jet energies due to the response correction. Use of Equation B.15 allowed events generated with a flat distribution to properly model bins with steeply falling distributions.

Another use for Equation B.15, the so–called "World Average," estimates the mean value of several measurements with different uncertainties. The average μ of several measurements y_i with different variances σ_i^2 is calculated with

$$\mu = \frac{1}{\sum_i \frac{1}{\sigma_i^2}} \cdot \sum_i \frac{y_i}{\sigma_i^2}, \tag{B.17}$$

and the resulting (one standard deviation) uncertainty on the mean is

$$\Delta\mu = \frac{1}{\sqrt{\sum_i \frac{1}{\sigma_i^2}}}. \tag{B.18}$$

This technique determined the $p\bar{p}$ cross sections and errors for the luminosity determination in Chapter 5.

Least Squares (the χ^2 Goodness of Fit Test)

To perform simple consistency checks, one may use a χ^2 test. To test the agreement between a set of N data points $y_i(x_i)$ with uncertainties σ_i versus some function $f(x)$, the simple *chi-square* is given by

$$\chi^2 = \sum_i^N \frac{(y_i(x_i) - f(x_i))}{\sigma_i^2}. \tag{B.19}$$

For a more elaborate comparison, use the error matrix and vectors containing the differences:

$$\chi^2 = (\mathsf{y} - \mathsf{f})^{\mathrm{T}} \, \bar{\mathsf{V}}^{-1} \, (\mathsf{y} - \mathsf{f}) . \tag{B.20}$$

where $\bar{\mathsf{V}}^{-1}$ is the inversion of Equation B.12. This form for χ^2 correctly accounts for any correlations between errors and is used to good effect in Chapter 8. If the correlations of σ_i between the x_i are zero, the matrix $\bar{\mathsf{V}}$ is diagonal, and Equation B.20 is equivalent to the simpler form of Equation B.19.

An often useful quantity, the *reduced chi-square* may be computed with

$$\frac{\chi^2}{d} = \frac{\chi^2}{N - p}. \tag{B.21}$$

Here, $d = N - p$ represents the number of *degrees of freedom* in the problem; N is the number of points y_i, and p is the number of parameters in the functional form $f(x)$. A lookup table, an example of which can be found in the PRD manual, describes the confidence level associated with a given $\frac{\chi^2}{d}$. While smaller values of a reduced chi-square indicate better agreement, for $d > 10$, statistical fluctuations normally prevent a reduced chi-square value much smaller than unity; values between 0.75 and 1.25 are normal and expected. Many software routines (including Microsoft Excel) can compute the likelihood precisely from χ^2 and d, but the $\frac{\chi^2}{d} \approx 1$ rule provides a useful order–of–magnitude gauge.

The Log Likelihood

An alternative to the χ^2 likelihood, the log likelihood is largest when the agreement is best. Unlike the chi-square value, the numerical value of the log likelihood has no meaning at

the best–fit point [47] and can change with a change of the units in which the problem is expressed.

In most cases, errors follow a Gaussian distribution—they are symmetric about the nominal value. In the case of small numbers of events, a Poisson distribution yields a better estimate of the uncertainty. To the eye, the Poisson distribution appears to be a Gaussian skewed to the left. For both distributions, the log likelihood that a number of data points are consistent with a function $f(x)$ is the natural logarithm of their respective probability distributions:

$$\text{Gaussian } G \;=\; \frac{1}{\sqrt{2\pi}\cdot\sigma}\exp\left(\frac{-\left(y-\mu\right)^2}{2\sigma^2}\right), \tag{B.22}$$

$$\text{Gaussian likelihood } L_G \;=\; -\sum_i^N\left(\ln\left(\sigma_i\cdot\sqrt{2\pi}\right)+\frac{\left(y_i-\mu\right)^2}{2\sigma_i^2}\right), \tag{B.23}$$

and

$$\text{Poisson } P = \frac{\mu^n e^{-\mu}}{n!}, \tag{B.24}$$

$$\text{Poisson likelihood } L_P \;=\; \sum_i^N\left(n_i\cdot\ln\mu-\mu-\ln\left(n!\right)\right) \tag{B.25a}$$

$$=\; \sum_i^N\left(n_i\cdot\ln\mu-\mu-\ln\Gamma\left(n+1\right)\right). \tag{B.25b}$$

Here, N is the total number of measurements, μ is the average y value of the measurements, and n (Poisson) is the number of events on a particular interval of x. In the best fit calculation, the substitution $\mu \rightarrow f(x_i)$ compares the measured values (y or n) to the function. For the Poisson distribution, the variance $\sigma^2 = \mu$. For large values of N, the expressions for the Gaussian and the Poisson distributions become equivalent.

B.4   For Further Reading

While many textbooks present statistical methods at various levels of difficulty, relatively few frame their discussions in terms which are useful to experimenters. Two exceptions are worth mentioning here.

The **Physical Review D** Review of Particle Physics contains a section on probability and a section on statistical inference. Both sections relate their discussions to specific problems encountered in HEP.

The most useful and surprising resource was the MINUIT user's manual, available from the CERN webpages (Reference [47] of this dissertation). It clearly and concisely described difficult concepts, such as the covariance matrix and how it is calculated. Because the manual describes the use of a software package, its discussions are results–oriented and framed in terms of the FORTRAN computing code.

Appendix C

The Total W Boson Cross Section

> *"Here is the simple but powerful rule: always give*
> *people more than they expect to get."*
> — Nelson Boswell

The brevity of $\sqrt{s} = 630$ GeV running at the Tevatron limited the integrated luminosity and total number of events collected. Despite statistical limitations, a DØ calculation of the total W boson cross section contributes to the precision of the World Average value and provides corroborative weight to the luminosity measurement of Chapter 5.

For simplicity, only the W $\rightarrow e\nu$ channel was investigated, using techniques developed during the prior full–energy running period. The signature for W boson events in this channel is a single electron and large missing E_T, the presence of a jet is allowed. Figure C.1 presents a sample of W boson production mechanisms.

The total W $\rightarrow e\nu$ cross section is given by

$$\sigma_{W \rightarrow e\nu} = \frac{N\left(1 - f_{QCD}\right) - N_{Z\ fake}}{\epsilon_{ID} \cdot A \left(1 + \frac{A_{W \rightarrow \tau\ fake}}{A}\right) \cdot \int \mathcal{L}\ dt}, \tag{C.1}$$

where the number of W candidate events, N, less background events from QCD and Z boson sources, is scaled with the integrated luminosity ($\mathcal{L}$), the electron identification efficiency (ϵ_{ID}), and the fiducial acceptance (A) of the DØ detector. A small acceptance correction accommodates W decays in the tau channel that might mimic the electron signal. The luminosity calculation for the W events is completely equivalent to the discussion in Chapter 5; the remaining elements of the cross section calculation are briefly described below.
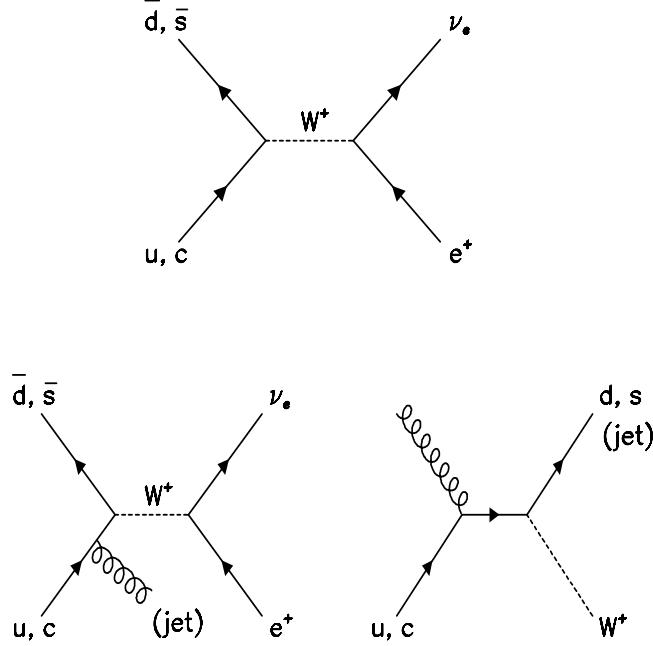
Figure C.1: Some possible W→ $e\nu$ mechanisms. Although the diagrams specify W^+ production, there exists a conjugate set of diagrams that result in W^- production.

C.1   Run Conditions

All W events were collected with the EM1_EISTRKCC_MS-LNR trigger. The complicated name reflects the various trigger criteria:

- EIS: Electromagnetic object in the calorimeter, shape consistent with an electron, isolated from other objects
- TRKCC: If the electron is in the CC, require associated track in CD
- MS: missing E_T greater than 15 GeV in the event
- EM1: electron with E_T greater than 20 GeV

The DØ detector collected a total of 376 events with this trigger, which had a total luminosity exposure of 490.0 nb^{-1}. Although the W trigger was never prescaled, it was not present on the trigger list throughout the run.

C.2   Data Selection and Efficiencies

Three offline criteria select W boson events from the collected sample: there must exist one and only one electron ($E_T > 25$ GeV) in the event, the electron must lie in a fiducial

region of the detector, and the event must possess at least 25 GeV of missing E_T. The following subsection describes the efficiencies associated with the electron cuts and the $\not{E}_T$ cut. Because W boson events trigger the Level Ø detector somewhat less reliably than do minbias or QCD events, the luminosity measurement requires a small correction: the Level Ø trigger efficiency*. The fiducial cut will be described in a later section.

C.2.1 Electron Identification Efficiency

The electron efficiency reflects the detector's ability to resolve tracks and electromagnetic clusters. The most powerful criterium demands that the electron shower develop similarly to test–beam electrons, as described by the shower's energy "shape" in the electromagnetic portion of the calorimeter. To remove contamination from jets, the energy deposit must lie primarily in the first few calorimeter layers and have little energy outside a narrow region. Electrons only distinguish themselves from photons by their ionization trail through the central detector, so a tracking requirement demands an track CD that points from the vertex to the energy deposit.

H-Matrix Chi-Squared $\left(\chi^2_{\mathrm{HM}} \right)$

Electrons passing through the EM calorimeter layers leave characteristic energy signatures. A template for typical electrons was built from a combination of test-beam data and Monte Carlo electron simulations. This template is expressed in terms of 41 electron observables:

- the energy fraction in EM layers 1, 2, and 4,
- the energy fraction in each cell of a 6x6 grid in EM layer 3,
- the logarithm of the cluster energy,
- vertex z position.

A covariance matrix M expresses the typical electron shower shape, where

$$\mathrm{M}_{ij} = \frac{1}{N} \sum_{n=1}^{N} \left(x_i^n - \bar{x}_i \right) \left(x_j^n - \bar{x}_j \right) \tag{C.2}$$

---

* The Level Ø *trigger efficiency* defined here should not be confused with the Level Ø *hardware efficiency* of Chapter 5.

for each combination of observable i and j. All electron candidates are rated according to the inverse of the covariance matrix, denoted $H = M^{-1}$:

$$\chi^2_{\text{HM}} = \sum_{i,\,j=1}^{41} \left(x_i^c - \bar{x}_i\right) H_{ij} \left(x_j^c - \bar{x}_j\right).$$ (C.3)

A cleanly measured electron yields a very small value [48] for χ^2_{HM}. As a DØ standard, electrons candidates must have a chi-squared value less than 100.0.

Electromagnetic Energy Fraction (EMFR)

Electromagnetic interactions consume an electron's energy within the first few layers of the calorimeter. Because the resulting shower should be almost entirely contained in the EM section, the EMFR for electrons is required to be greater than 0.95. This cut is the complement of the requirement defined in Chapter 5 for jets.

Isolation

The isolation fraction cut restricts the amount of energy that can surround an electromagnetic cluster, removing the possibility that a cluster of π^0 mesons within a jet can mimic an electron. The isolation fraction is defined as

$$f_{iso} = \frac{E^{Tot}_{R=0.4} - E^{EM}_{R=0.2}}{E^{EM}_{R=0.2}},$$ (C.4)

where $E^{Tot}_{R=0.4}$ is the total energy in a 0.4 radius cone and $E^{EM}_{R=0.2}$ is the energy in the first eight layers of the calorimeter (lying within a smaller "isolated cone" of radius 0.2). For good electrons, $f_{iso} \leq 0.15$.

Track match significance

For electrons, a track in the CD should align with the EM energy deposit. The level of agreement between track and energy cluster is calculated by projecting the track into the calorimeter and comparing its position with that of the EM shower centroid. Using cylindrical coordinates, the track match significance is expressed as

$$S_{trk}^{CC} = \sqrt{\left(\frac{r\,\Delta\phi}{\sigma_{r\phi}}\right)^2 + \left(\frac{\Delta z}{\sigma_z}\right)^2} \text{ or} \tag{C.5a}$$

$$S_{trk}^{EC} = \sqrt{\left(\frac{\Delta\phi}{\sigma_\phi}\right)^2 + \left(\frac{\Delta r}{\sigma_r}\right)^2}. \tag{C.5b}$$

Here, the Δ terms represent the differences in positions and the σ terms describe the uncertainties in the positions. The uncertainties result from calorimeter position resolution, tracking resolution, and the track extrapolation procedure. For good electrons in the CC, $S_{trk}^{CC} \leq 5.0$; in the EC, $S_{trk}^{EC} \leq 10.0$.

Fitting the Efficiencies

Traditionally, a study of Z boson events determined the electron efficiency. Because the short run time produced only ten to twenty Z boson events, the efficiency of the electron selection criteria could not be studied independently at $\sqrt{s} = 630$ GeV; instead, the efficiencies were drawn from the well–measured [?] 1800 GeV data sample. The W boson identification efficiency, ϵ_W, consists of the product of the efficiencies of the selection criteria above and a small correction factor that removes correlation* biases.

The efficiency, ϵ_W, varies as a function of the instantaneous luminosity, electron pseudorapidity, and the number of jets in the event. Figure C.2 (top) displays the measured efficiencies for $\sqrt{s} = 1800$ GeV. The value of ϵ_W is higher in the central calorimeter than in the end calorimeters, and ϵ_W is larger for "clean" events (when no jets are present). At 1800 GeV, jets with E_T greater than 25 GeV accompany approximately 8% of all W events; at 630 GeV, all events are clean. With the assumption that the efficiency for the inclusive sample may be written

$$\epsilon_W = \frac{N^{no\,jets}}{N}\,\epsilon_W^{no\,jets} + \frac{N^{at\,least\,1\,jet}}{N}\,\epsilon_W^{at\,least\,1\,jet}, \tag{C.6}$$

simple algebra isolates the clean–event efficiency, $\epsilon_W^{no\,jets}$, as depicted in Figure C.2, bottom. Note the change in labeling of the x–axis. Neglecting pileup effects in the calorimeter, sup-

---

* Z boson events contain two electrons; the identification probability of one electron is correlated with the probability of identifying the other.
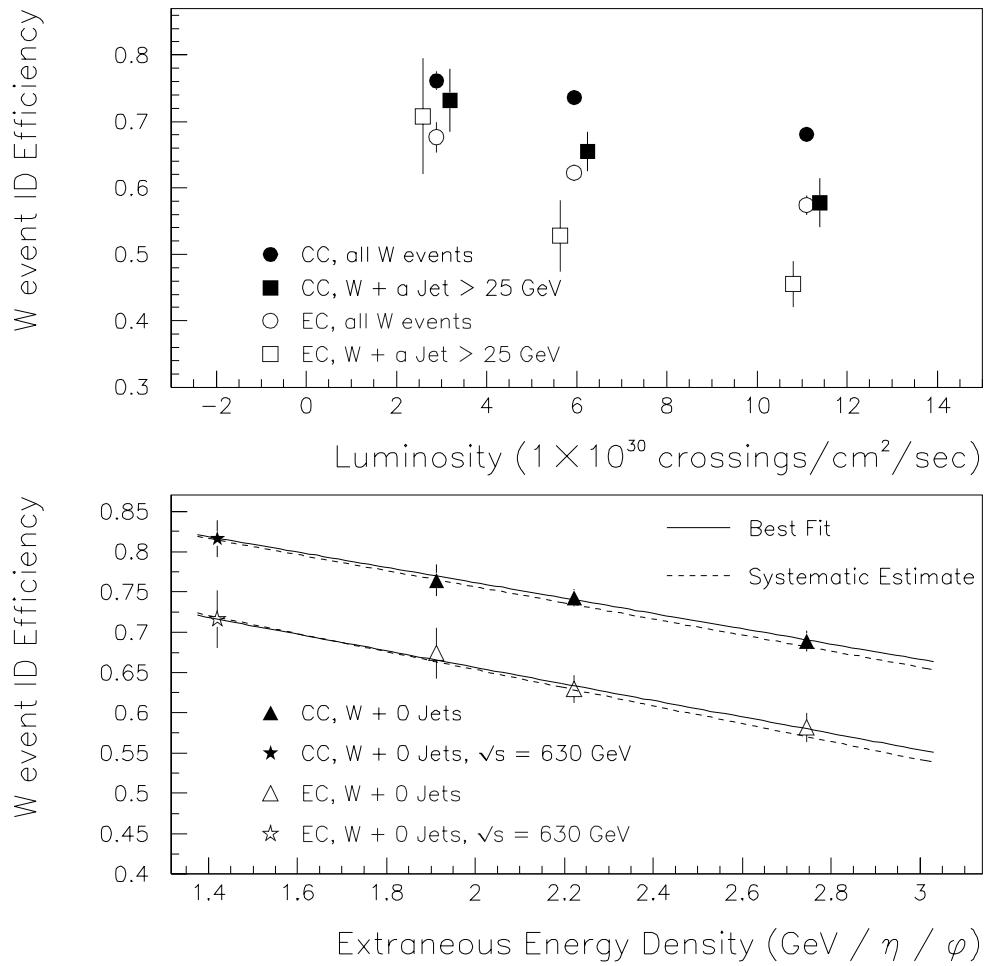
Figure C.2: Efficiency of W event selection criteria. (Top) Efficiencies versus luminosity for the CC and EC, for all events and for the subset of events with an accompanying jet. (Bottom) The extracted efficiency for W event selection with zero accompanying jets. Stars indicate the efficiency for the 630 GeV data set.

pression noise, underlying event, and additional interactions provide the extraneous energy of an event. Because noise and underlying event are constant, the luminosity–dependent behavior must result from additional interactions. The number of expected interactions per beam crossing rises linearly with luminosity; thus, using the measurements [43] of the DØ energy scale correction, the luminosity values map linearly to extraneous energy densities. In the figure, the efficiencies have been extrapolated to the average extraneous energy density found at $\sqrt{s} = 630$ GeV. Comparison of the x–axes in the bottom and top of the figure reveal that a simple zero–luminosity limit would not be sufficient.

The uncertainty on the extrapolated point results from the covariant fit uncertainty. As an additional check, the inclusive efficiencies were extrapolated to 630 GeV (dashed line in the figure). The result exhibits complete consistency with the nominal technique, the residual difference forms the systematic uncertainty. The final W selection efficiency is 0.808 ± 0.0241.

C.2.2 Trigger Efficiencies

Additional event losses can result from requirements in the trigger. First, the online Level Ø requirement mistakenly excludes some W boson events because the beam remnants fail to trigger the hodoscope arrays. For the 1800 GeV data set, the Level Ø trigger efficiency is 0.986. At 630 GeV, the average Level Ø hardware efficiency differs, as depicted in Figure 5.3, page 97. The Level Ø trigger efficiency should scale with the ratio of the values in the figure. Evaluating the function at a luminosity of $7 \times 10^{30} \frac{crossings}{cm^2\ sec}$, the Level Ø trigger efficiency becomes

$$\epsilon_L = 0.986 \cdot \frac{0.823}{0.905} = 0.897 \pm 0.00854^{stat} \pm 0.00619^{sys} \tag{C.7}$$

The systematic uncertainty dominates the size of the error bar on each point in Figure 5.3, the inner marks delineate the statistical portion of the total. Because the source of the systematics is identical [28][37] for both center–of–mass energies, the uncertainties are completely correlated and mostly cancel in the ratio.

As with the offline selection, the trigger requirements for electrons should become more efficient at $\sqrt{s} = 630$ GeV than at 1800 GeV, where the efficiency is 0.995%. Possible improvement in this efficiency was neglected but the uncertainty was tripled, from 0.001 to 0.003. The $\not{E}_T$ cut efficiency receives the same treatment: no change in nominal value (0.9928), tripled error (now 0.0033).

A simple vertex requirement near $|z| < 100$ cm ensured proper E_T calculation. The precise vertex position could be determined by any of three methods: reconstruction algorithms, PELC bank, or a cluster algorithm. Because low luminosity minimizes mis-vertexing effects, all three methods yield the same result for the 630 GeV data set; thus, the differences in the vertexing methods need not be discussed.

C.3 Backgrounds

Due to the rarity of W events, significant numbers of background events contaminate the sample, as categorized [49] in Table C.1. QCD multijet events, the most copious contaminant of the W sample, result from one jet depositing a large fraction of its energy in the EM calorimeter while the detector mismeasures the E_T of a second jet. Such events imitate the electron-plus-$\not{E}_T$ signature of the W boson. Additionally, if a Z boson decays to two electrons, sometimes one of the leptons will be lost in a poorly instrumented region of the calorimeter, resulting in a second way to imitate the W signal. Alternately, if the Z boson decays to two τ leptons, the decay process $\tau \to e\nu$ can result in a fake signature. The third background arises from real W bosons decaying in the tau channel with the lepton misidentified as an electron. Although the intermediate state was indeed a W boson in this case, the event would be inappropriately included in the W$\to e\nu$ channel.

The values in Table C.1 were calculated for the $\sqrt{s} = 1800$ GeV data sample and would be somewhat inappropriately applied at $\sqrt{s} = 630$ GeV. Although the shift in center-of-mass energy should cause little change in the background fractions, the shift is most likely non-zero and should, in principle, be reexamined. The W boson data at 630 GeV will be statistics-limited, and so recalculation of backgrounds was deemed too time consuming to

Background Source	Location	Fraction of sample
Multijet	CC	$(4.1 \pm 1.0)\%$
	EC	$(12.8 \pm 3.0)\,\%$
Z→ee,$\tau\tau$		$(0.983 \pm 0.295)\%$
W→$\tau\nu$		$(2.14 \pm 0.21)\%$

Table C.1: List of background sources to W events for the 1800 GeV data sample.

Central Cross Sections	1800 GeV	630 GeV
$\sigma_{Jet,\,\mathrm{E_T}>25}$ (nb)	8056 ± 1710	700.4 ± 148.5
$\sigma_{\mathrm{W}\to e\nu}$ (nb)	2.382 ± 0.058	0.747 ± 0.05
ratio	3382	937.6

Table C.2: The predicted total cross sections for W boson production and jet production at two center-of-momentum energies.

be worthwhile. Because the Z and W background cross sections scale with $\sqrt{s}$ in exactly the same way as does the W $\to e\nu_e$ signal, the background fraction from these sources should remain entirely unchanged.

The QCD background is, to first approximation, proportional to the ratio of the QCD jet cross section to the W cross section. Because finite energy resolution in the calorimeter distorts jet cross sections, a theoretical QCD prediction was smeared with the measured jet energy resolution values of the DØ detector. Table C.2 lists the relevant total cross sections at the two center-of-momentum energies. The theoretical jet cross sections were created with the CTEQ4M parton distribution function. The DØ Collaboration determined [49] the W boson cross section at $\sqrt{s} = 1800$ GeV; the value for 630 GeV is a NLO prediction.

The ratio $\frac{\sigma_{Jet}}{\sigma_{\mathrm{W}}}$ changes by a factor of 0.28 ± 0.1132, indicating the multijet background for $\sqrt{s} = 630$ GeV should be 1.15% in the central region and 3.58% in the EC. Most of the uncertainty in this scaled jet background results from the uncertainty in the QCD cross section predictions.

C.4   Fiducial Acceptance

Electrons in the ICR are frequently mismeasured or lost due to the coarseness of EM segmentation or lack of EM modules; therefore, candidates in the area subtended by the

ICR are excluded from consideration. Generated during a Monte Carlo study, Figure C.3 shows the fraction of electrons lost in the detector as a function of physics pseudorapidity. The ICR losses, while quite evident, are softened by the mismatch between η and η_d due to non-zero vertex positions. The high–pseudorapidity regions of the end calorimeters are also excluded because segmentation becomes coarse [50] in that region. Further, longitudinal seams between EM modules in the CC distort electron measurements; therefore, electrons within 0.01 radians of a module boundary are excluded from the data sample. Losses in these so-called "ϕ-cracks", of order 10%, do not vary with pseudorapidity but rather with the azimuthal position within a cell (Figure C.4). Because the incomplete EM coverage of the calorimeter results in non-unity acceptance, the cross section measurement is performed only in the well-behaved regions of the calorimeter, with a smooth correction for the electrons that fall outside the fiducial region.

A Monte Carlo study determines the acceptance of the DØ calorimeter. First, a theoretical prediction for the W cross section, as a function of both rapidity and transverse momentum, defines a "grid" of cross sections. A detector simulation processes events drawn from this smooth cross section distribution to determine the final number of events that are "visible" to the analysis. The fraction of electrons from W decays that remains in the fiducial region is 0.5213, nearly 10% higher than the acceptance at $\sqrt{s} = 1800$ GeV.

C.5 Result

Searches of the 630 GeV data set reveal 130 candidate events. The luminosity (490.0 nb^{-1}) and parameters in previous sections determine the total W boson cross section in the electron channel:

$$\sigma_{W \to e\nu} = 0.6585 \pm 0.0583^{stat} \pm 0.0301^{sys} \text{ nb.} \qquad (C.8)$$

In terms of percentage error, the statistical and systematic components are $\pm 8.9\%$ and $\pm 4.6\%$ respectively, for a quadrature total of $\pm 10.0\%$. The systematic error reported in Equation C.8 includes the $\pm 3.04\%$ uncertainty contribution from the luminosity determi-

Figure C.3: Lost electrons as a function of pseudorapidity. The most inefficient portions of the detector will not be included in the fiducial region.

Electron Acceptance without Fiducial Cuts
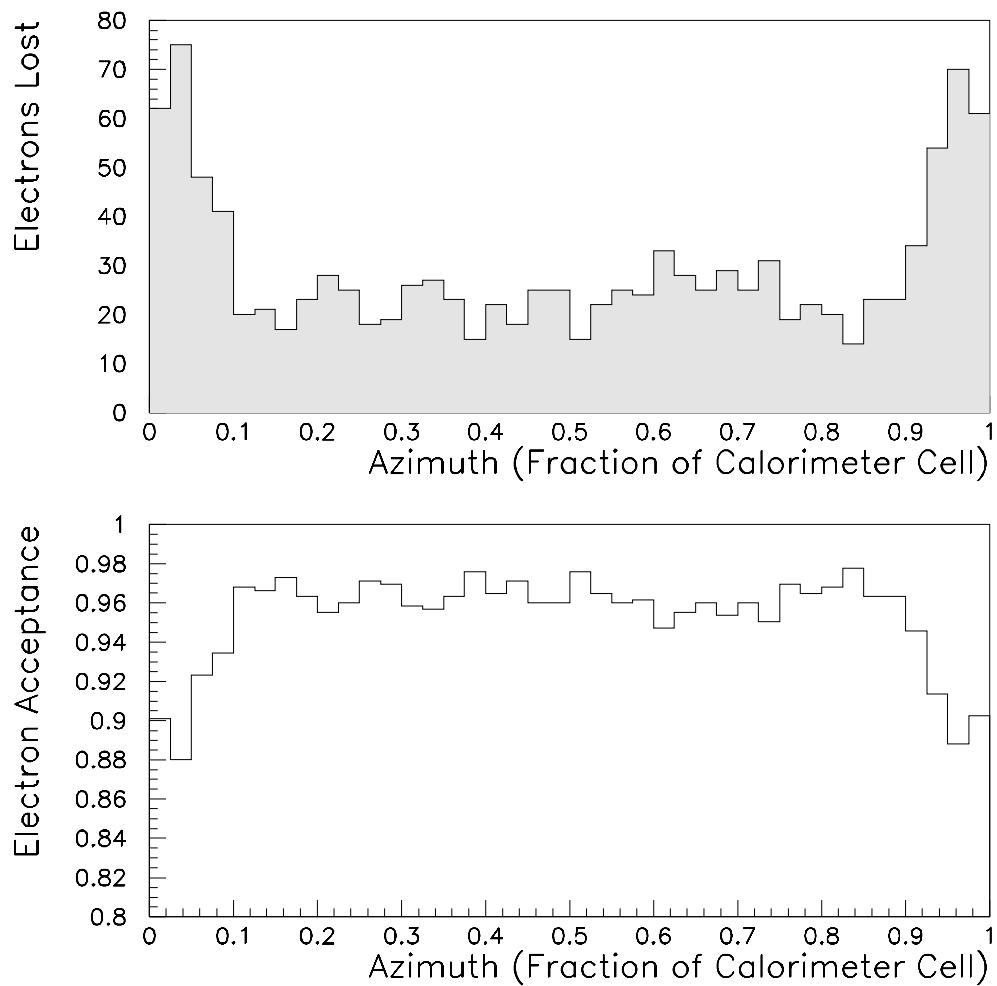
Figure C.4: Lost electrons as a function of azimuthal position within a calorimeter cell. Acceptance suffers near cell boundaries.

Source	$\sigma_{\mathrm{W}\rightarrow e\nu}$ at $\sqrt{s} = 630$ GeV (nb)
UA1 (1987)	0.630 ± 0.11
UA2 (1992)	0.711 ± 0.04
Prior World Average	0.702 ± 0.038
DØ (1998)	0.6585 ± 0.0657
World Average	0.691 ± 0.032
Theory	0.714 to 0.762

Table C.3: Total W cross section times branching ratio compared to prior experiments.

nation. Without considering luminosity, the systematic error reduces to ± 0.0225 nb or $\pm 3.4\%$.

With or without the reduced uncertainty, the total W boson cross section is consistent with both theory and previous experiments; thus validating the DØ luminosity calculation at $\sqrt{s} = 630$ GeV. Figure C.5 compares the cross section results with NLO theoretical predictions and the results of the UA1 [51] and UA2 [52] experiments, while Table C.3 lists the numerical values of these results. The DØ measurement shifts the "World Average" total W$\rightarrow e\nu$ cross section lower by 1.5%, while improving the precision of the measurement by 15%.
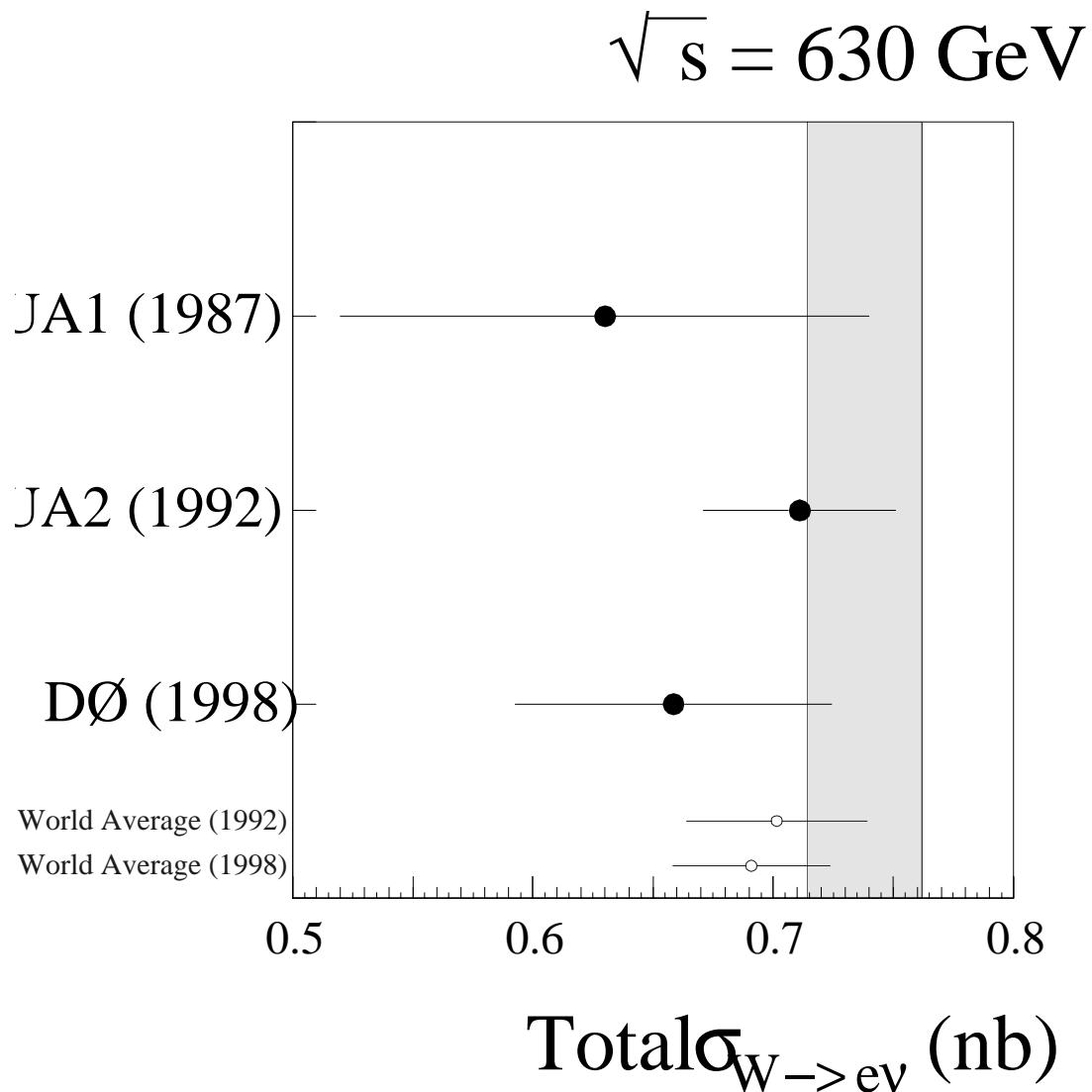
Figure C.5: The DØ W→ $e\nu$ cross section measurement at $\sqrt{s} = 630$ GeV compared to the results from UA1, UA2, and theory (shaded band). The open circles indicate the world average before and after inclusion of DØ's result.

References

[1] M. Gell-Mann, *Phys. Lett.* **8**, 214 (1964).

[2] D. Griffiths, *Introduction to Elementary Particles,* John Wiley & Sons, Inc., 1987, Pg. 97.

[3] V. Barger and R. Phillips, *Collider Physics,* Frontiers in Physics Lecture Note Series, Addison-Wesley Publishing Company, 1987.

[4] A.D. Martin, R.G. Roberts, W.J. Stirling, and R.S. Thorne, "Parton Distributions: a New Global Analysis," hep-ph/9803445 v2, 21 April 1998, (the MRST parton distribution function).

[5] J. Botts, J.G. Morfin, J.F. Owens, J. Qiu, W.K. Tung and H. Weerts, Phys. Lett. **B304**, 159 (1993),
H.L. Lai, J. Botts, J. Huston, J.G. Morfin, J.F. Owens, J. Qiu, W.K. Tung and H. Weerts, Phys. Rev. **D51**, 4763 (1995),
H.L. Lai, J. Huston, S. Kuhlmann, J.F. Owens, D.E. Soper, W.K. Tung and H. Weerts, Phys. Rev. **D55**, 1280 (1997)

[6] A.D. Martin, R.G. Roberts, and W.J. Stirling, Phys. Lett. **B354**, 155 (1995), and Phys. Lett. **B387**, 419 (1996).

[7] M. Gluck, E. Reya and A. Vogt, Z. Phys. C 53, 127 (1992), Phys. Lett. **B306**, 391 (1993), and Z. Phys. C 67, 433 (1995).

[8] B.Abbott, M.Bhattacharjee, D.Elvira, F.Nang, H.Weerts, The R_{sep} Committee, "Fixed Cone Jet Definitions in DØ and R_{sep}," DØ Note 2885, March 1996.

[9] H.L.Lai, *et al.*, The CTEQ Collaboration, "Global QCD Analysis and the CTEQ Parton Distributions," Phys. Rev. **D51** (1995) 4763-4782.

[10] W.T.Giele, E.W.N. Glover, and D.A.Kosower, Phys. Rev. Lett. **73**, 2019 (1994).

[11] B.Abbott, I.A.Bertram, M. Bhattacharjee, G. Di Loreto, V.D. Elvira, R. Hirosky, T. Joffe-Minor, J. Krane, F. Nang, "An investigation of uncertainties in the QCD NLO predictions of the inclusive jet cross section in $\bar{p}p$ collisions at $\sqrt{s} = 1.8$ TeV and 630 GeV," Euro. Phys. J. **C5** 4 (1998), pp. 687-692.

Chapter 2

[12] J.Alitti, *et al.,* The UA2 Collaboration, "Inclusive jet cross-section and a search for quark compositeness at the CERN $\bar{p}p$ Collider," Phys. Lett. **B257**, 232 (1991).

[13] J.Thompson, "Introduction to Colliding Beams at Fermilab*,"* Fermilab Tech. Memo. TM-1909, October 1994.

[14] S.Abachi *et al.*, The DØ Collaboration, Nucl. Intr. Methods **A338** (1994) 185-253.

[15] A.R. Clark, *et al.*, Nucl. Intr. Methods **A315**, 243 (1992).

[16] D. Green, Fermilab, *The Physics of Particle Detectors*, unpublished textbook, Graduate Student Association Summer School, Aug. 1997.

[17] A.R. Clark, *et al.*, Nucl. Intr. Methods **A279**, 243 (1989).

[18] C. Fabjan, *Calorimetry in High Energy Physics*, Experimental Techniques in High-Energy Nuclear and Particle Physics, World Scientific Publishing Co. Pte. Ltd., 1991, pp. 257-324, and R. Wigmans, *High Resolution Hadron Calorimetry*, Nucl. Instrum. Methods, **A265**, pp. 273-290 (1988).

[19] S. Snyder, "The DØ Detector*,"* DØ Note 2500, March 16,1995.

[20] M. Abolins, *et. al.*, Nucl. Intr. Methods **A280**, 36 (1989).

Chapter 4

[21] Private communication with Daniel Elvira.

[22] J.Krane, "A Multiple Interaction Tool for $\sqrt{s} = 630$ GeV," DØ Note 3265, April 15, 1997.

[23] J.Pumplin, "Hard underlying event correction to inclusive jet cross sections", hep-ph/9708464.

Chapter 5

[24] J.Bantly, K.Epstein, J.Fowler, G.S.Gao, R.Hlustick, R.E.Lanou, F.Nang, R.Partridge, L.Wang, and H.Xu, IEEE Trans. on Nucl. Sci. **41**, 1274 (1994).

[25] F. Abe *et al.*, the CDF Collaboration, "Measurement of the p$\bar{\text{p}}$ Total Cross Section at $\sqrt{s} = 546$ and 1800 GeV", Phys. Rev. **D50** (1994) 5550.

[26] N. Amos *et al.*, "A Luminosity Independent Measurement of the p$\bar{\text{p}}$ Total Cross Section at $\sqrt{s} = 1.8$ TeV", Phys. Lett. **B242**, 158 (1990).

[27] J.Bantly, A.Brandt, R.Partridge, J.Perkins, D.Puseljic, "Improvement to the DØ Luminosity Monitor Constant," Fermilab Tech. Memo. TM-1930, 1995 and DØ Note 2544, December 29, 1995.

[28] J.Bantly, J.Krane, D.Owen, R.Partridge, L.Paterno, "DØ Luminosity Monitor Constant for the 1994-1996 Tevatron Run," Fermilab Tech. Memo. TM-1995 and DØ Note 3199, 1 Feb. 1997.

[29] D. Bernard, *et al.*, the UA4 Collaboration, "The Cross Section of Diffraction Dissociation at the CERN SPS Collider", Phys. Lett. **B186**, 2, March 5, 1987.

[30] M. Bozzo, *et al.*, "Measurement of the Proton-Antiproton Total and Elastic Cross Sections at the CERN SPS Collider", the UA4 Collaboration, Phys. Lett. **B147**, number 4, 5, November 8, 1984.

[31] C. Augier, *et al.*, UA4/2 Collaboration, "Predictions on the total cross section and real part at LHC and SSC", Phys. Lett. **B315**, pp. 503-506, 1993.

[32] G. Chiarelli, for the CDF Collaboration, "Measurement of p$\bar{\text{p}}$ Elastic and Total Cross Section at $\sqrt{s} = 546$ and 1800 GeV at CDF", FERMILAB-Conf-93/360-E.

[33] P.Aurenche, *et al.*, Phys. Rev. **D45** (1992) 92. See also, F.W.Bopp, *et al.*, Z. Phys. **C51** (1991) 99.

[34] A.Jonckheere, "Proceedings of the Argonne National Laboratory Detector Simulation Workshop", August 1987. See also F.Carminati, *et al.*, "GEANT User's Guide", CERN Program Library (Dec 1991).

216

[35] S.Abachi *et. al,* the DØ Collaboration, Nucl. Instrum. Meth. **A338**, 185 (1994).

Chapter 6

[36] M.Bhattacharjee, "Jet Energy Resolutions," DØ Note 2887, May 22, 1996.

Chapter 7

[37] J.Krane, J.Bantly, D.Owen, "The DØ Luminosity Monitor Constant for $\sqrt{s} = 630$ GeV," Fermilab-TM-2000 and DØ Note 3222 April 15, 1997.

[38] B.Abbott, *et. al,* The DØ Collaboration, "The Inclusive Jet Cross Section in $\bar{p}p$ Collisions at $\sqrt{s} = 1.8$ TeV," submitted to Phys. Rev. Lett. 20 July, 1998, and also G.Blazey and R.Hirosky, "The DØ Inclusive Cross Section," DØ Note 3276, April 14, 1998.

[39] L.Baboukhadia, G.Blazey, D.Elvira, F.Nang, M.Shupe, "Standard Jet Cuts and their Efficiencies for Run1b DØ Collider Data," DØ Note 3407, 2 March, 1998. (This paper uses jet criteria that are not identical to the ones in Chapter 5 or Reference [38] but it can provide additional discussion.)

[40] A.Goussiou, "Jet Sample Selection at $\sqrt{s} = 630$ GeV," DØ Note 3364, December 1, 1997.

[41] I.Bertram, M.Bhattacharjee, J.Blazey, S.Y.Choi, D.Elvira, A.Goussiou, R.Hirosky, J.Krane, J.Perkins, and R.Snihur, "Single Jet Resolutions at DØ for Run 1," DØ Note 33XX, 21 January 1997. (Available in draft form on the web www-d0.fnal.gov/~bertram/d0_private/qcd_resolutions/resolutions.html.)

[42] As suggested by Mark Strovink.

[43] B.Abbott, *et al.,* The DØ Collaboration, "Determination of the Absolute Jet Energy Scale in the DØ Calorimeters," Submitted to Nucl. Inst. Meth. and Elsevier Preprint. Also described in Chapter 4.

Chapter 8

[44] B.Abbott, I.A.Bertram, M.Bhattacharjee, G.Di Loreto, V.D.Elvira, R.Hirosky, T.Joffe–Minor, J.Krane, and F.Nang, "An Investigation of Uncertainties in the QCD NLO Predictions of the Inclusive Jet Cross Section in $\bar{p}p$ Collisons at $\sqrt{s} = 1800$ GeV and 630 GeV," hep-ph/9801285, 13 Jan. 1998, to be published in Eur. Phys. J. C.

[45] L.N. Lipatov, Sov. J. Nucl. Phys. **23**, 338 (1976), E.A.Kuraev, L.N.Lipatov, and V.S.Fadin, Sov. Phys. JETP **44**, 443 (1976), *ibid.*, **45,** 199 (1977), Ya.Ya.Balitskiǐ and L.N.Lipatov, Sov. J. Nucl. Phys. **28**, 822 (1978), L.N.Lipatov, Sov. Phys. JETP **63**, 904 (1986).

[46] V.T.Kim and G.B.Pivovarov, Phys. Rev. D **37,** 57 1998.

Appendix B

[47] F.James, "Minuit Function Minimization and Error Analysis," CERN Program Library Long Writeup D506, Version 94.1, 1994.

Appendix C

[48] P.Grudberg, *Measurement of the W and Z Boxon Production Cross Sections in $p\bar{p}$ Collisions at $\sqrt{s} = 1.8$ TeV with the DØ Detector,* Ph.D. Thesis, 1997.

[49] B.Abbott, *et. al*, The DØ Collaboration, *A Measurements of $\sigma(p\bar{p} \rightarrow W + X) \cdot B(W \rightarrow e\nu)$ and $\sigma(p\bar{p} \rightarrow Z + X) \cdot B(Z \rightarrow ee)$ and Their Ratio*, to be submitted to Phys. Rev. D, (1998).

[50] P.Grudberg, "Cross Section Measurements of W and Z Bosons to Electrons at DØ: Event Selection and Efficiency Studies", DØ Note 2316, 31 October 1994.

[51] UA1 Collaboration: C. Albajar *et al.*, *Phys. Lett.* **B198**, 271 (1987).

[52] UA2 Collaboration: J. Alitti *et al., Phys. Lett.* **B276**, 365 (1992).

Index

THE RATIO OF INCLUSIVE JET CROSS SECTIONS AT
$\sqrt{s} = 630$ GeV AND $\sqrt{s} = 1800$ GeV

This dissertation presents an analysis of hadronic jet production from proton-antiproton collisions at two center–of–mass energies. Measurements were performed in the central region ($|\eta| < 0.5$) of the DØ detector at Fermi National Accelerator Laboratory (Batavia, IL). Results are compared to next–to–leading–order QCD predictions generated with JETRAD and EKS Monte Carlo. Several techniques reduce the uncertainty in the ratio of cross sections to as low as 5%. The observed normalization difference results in a low probability that the data and predictions describe the same distribution.